Towards a cyclostratigraphic framework of the Upper Cretaceous Chalk Group in the Dutch offshore

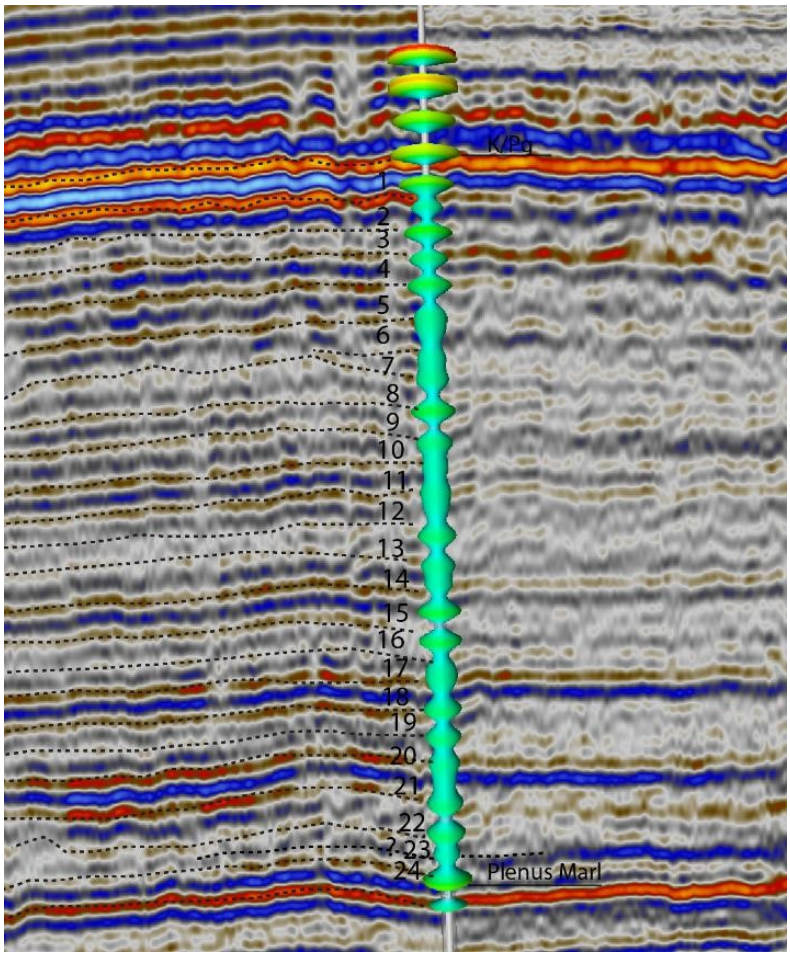

Michiel C.M. Arts │Earth Sciences Masterthesis│ Utrecht 2017

Research: University Utrecht, faculty of Geosciences, Michiel C.M. Arts

Editorial: Michiel C.M. Arts

Design and production: Michiel C.M. Arts

Cover image: Top image, Photo of core A12-02 taken core repository TNO Zeist (photo by author). Bottom image well G10-02 with the filtered 50m 1200-kyr cycle. Left of well, seismic signal filtered on 50m period with cycles indicated. Right of well, unfiltered seismic image (seismic survey Z3NAM1997A).

Towards a cyclostratigraphic framework of the Upper Cretaceous Chalk Group in the Dutch offshore

Author:

Michiel Christianus Martinus Arts

Studentnumber:3847411

Email: m.c.m.arts@students.uu.nl

and

Michiel025@live.nl

Under supervision of:

Dr. Frits J. Hilgen

Universiteit Utrecht The Netherlands

Second supervisor:

Dr. Geert-Jan Vis

TNO, Geological Survey of the Netherlands

Universiteit Utrecht

Masterthesis Geosciences

Utrecht | 2017

Abbreviations

DT: Sonic (slowness)

DRHO: Bulk Density Correction (g/cm3)

Ecc: Eccentricity

EHA: Evolutive Harmonic Analysis

eASM: Evolutive Average spectral misfit

FCO: First common occurrence

FCOD: First common occurrence datum

FO: First occurrence

FOD first occurrence datum

GR: Gamma ray

Hz: Hertz

K: velocity gradient

Kyr: Kilo-years (thousands of years)

K/Pg: Cretaceous/Palaeogene

LAP: log association parameter

LCO: Last common occurrence

LCOD: Last common occurrence datum

LO: Last occurrence

Ma: Mega-annum (age in Millions of years)

MTM: Multitaper method

Myr: Million years (duration in millions of years)

NPHI: Neutron Porosity

OAE: Ocean Anoxic Event

OWT: One-way travel time

ppm: Parts per million

RHOB: Bulk density (g/cm3)

SI: supplementary information

SSTVD: Subsea true vertical depth

TWT: Two-way travel time

TVD: True vertical depth

Vint: internal velocity

V0: Instantaneous velocity at zero meters

Vshale: Volume of shale (% or fraction 0-1)

VSP: Vertical seismic profile

XRF: X-ray refraction fluorescence

Elements

As: arsenic

Au: gold

Ca: calcium

C: carbon

Co: cobalt

Cr: chromium

Cu: copper

Fe: iron

Hg: mercury

K: potassium

Mn: manganese

Mo: molybdenum

O: oxygen

Ni: nickel

Pb: lead

Th: thorium

Ti: titanium

Rb: rubidium

S: sulphur

Sc: scandium

Se: selenium

Sr: strontium

U: uranium

V: vanadium

W: tungsten

Zn: zinc

Zr: zirconium

Abstract

The current geological timescale has already been astronomically calibrated down to the early Campanian. This study evaluated the Danian to Cenomanian Chalk Group in the Dutch offshore on the Schill Grund Platform as a possible extension for the astronomically calibrated timescale. The Schill Grund Platform in the Dutch offshore is one of the few areas where the Chalk Group is relatively undisturbed and virtually complete. Spectral analysis on well-logs by van der Molen (2004) already showed promising cyclostratigraphic results for the Schill Grund Platform. Van der Molen (2004) also proposed a non-tectonic origin for some of the seismic reflectors on the Schill Grund Platform.

An integrated petrophysical, seismic, biostratigraphic and core material based approach was used to investigate the presence of Milankovitch cycles on the Schill Grund platform. The EHA, Blackman-Tukey transformation and Redfit spectral analyses of the well-logs in depth domain showed consistent peaks for the 4-6, ~8, 15-22 40-60, ~105, 125-160 and 300-400 m periods. Based on eASM results and the (bio)stratigraphic constraints the 15-22 m period is interpreted as the 405-kyr eccentricity cycle and was subsequently used for a depth-time conversion. Spectral analysis in the depth and time domain led to the identification of cycles with periods of 100, 200, 300, 405, 700-1000, 1200, 2400, 3500 and 9500-kyr. The 100, 405, 1200, 2400, 3500-kyr periods could be readily assigned to an orbital cycle, but the assignment of an orbital cycle to the 200, 300, 700-1000 and 9500-kyr cycles is more problematic. The enigmatic presence of the 1200 and 2400-kyr cycles could hint to an episode of chaotic resonance between the orbits of Earth and Mars. No definite orbital phase-lithology relationship exists for the Chalk Group in the North Sea Basin, which results in two tuning options; an eccentricity minimum and an eccentricity maximum tuning option. The 1200, 2400 and 3500-kyr (40-60, ~105 and 125-160 m periods) cycles are also registered in the spectral analysis of the seismic trace data. The filtering of the seismic trace and well data of the 1200 and 3500-kyr cycles (in the depth domain) display a good fit with the seismic record and an astronomical modulation of the reflector pattern is therefore likely.

XRF, core observations, well-logs and literature indicate that the Chalk Group has two different depositional settings; a cool water detrital/anoxic setting with marl deposition and an oxic warm water chalk deposition. The two settings can be explained by an upwelling or a stagnation model. The upwelling model is linked to the eccentricity maximum tuning option and the stagnation model is linked to the eccentricity minimum tuning option. The upwelling model is preferred over the stagnation model due to more evidence in literature for the upwelling model, the presence of *Prasinophyte* algae in the core of well A12-02 and the phase relationship between the biostratigraphy and the filtered gamma ray log data of well A12-02.

The cyclostratigraphic framework enabled a long-distance correlation of stage boundaries across the Schill Grund Platform, a re-evaluation of the ages assigned to the CK sequence stratigraphic boundaries of van der Molen (2004) and a re-evaluation of the ages assigned to the formation boundaries of the Chalk Group in the Dutch offshore.

Table of contents

1. Introduction

The development of the Astronomical Time Scale (ATS) is one of the great advances in modern geochronology. Periodic variations in the Earth's orbit and tilt relative to the Sun influences Earth's climate and are recorded in the sedimentary record. These cyclic sediments can be exploited as a geologic 'clock' and can be used to create a timescale based on a numerically calculated solution for the different orbital cycles and hence the creation of the ATS. The ATS provides continuous time information for sections were other geological time information techniques such as radiometric dating or biostratigraphy are unsatisfactory.

The geological timescale has been astronomically calibrated down to the latest Campanian (Batenburg et al., 2014; Husson et al., 2011). From the latest Campanian downwards the Upper Cretaceous record consists of incomplete and/or floating timescales (Hinnov and Hilgen, 2012). The Chalk Group in the Dutch Offshore on the Schill Grund platform will be investigated for the existence of astronomical cycles and if these cycles can be used for the extension of the astronomical calibration of the geological timescale. The Chalk Group succession on the Schill Grund Platform stretches from the Danian to Cenomanian and contains possible tie-points to the K/Pg boundary and the Plenus Marl (Ocean Anoxic Event 2 (Jarvis et al., 2006; Schlanger et al., 1987b)). Ocean Anoxic Event 2 (OAEII) is a globally recognized event and thus an excellent tie-point for future research. Ocean Anoxic Event 2 itself is also a source of (cyclostratigraphic) discussion (Batenburg et al., 2016; Lanci et al., 2010; Laurin et al., 2016; Mitchell et al., 2008; Sprovieri et al., 2013). A tuned record down to Ocean Anoxic Event 2 can provide new insights in the relationship between this event and astronomical cycles.

The Chalk Group on the Schill Grund Platform in the Dutch offshore has a virtually complete Danian to Cenomanian succession (Van der Molen, 2004) and has been a structurally separate area from at least the early Carboniferous (Geluk et al., 2007). The unique tectonic history of the Schill Grund platform resulted in a gradual thermal subsidence during the late Cretaceous with only a minor impact of the late Cretaceous inversion phases and its associated salt movement phases (Ten Veen et al., 2012). Spectral analysis of well-logs from the Schill Grund platform by van der Molen (2004) already showed promising results. The seismic sequence stratigraphic framework boundaries of the Chalk Group defined by van der Molen (2004) are expressed as continuous parallel reflectors on the Schill Grund Platform. A non-tectonic control on the reflector pattern was proposed by van der Molen (2004).

For the Schill Grund platform an integrated petrophysical, seismic, biostratigraphic and core material based approach will be used to investigate the presence of Milankovitch cycles. Biostratigraphic data will be re-evaluated to identify the K/Pg boundary and other stage boundaries. The possible presence of cycles in the well-logs and seismic data will be investigated by using the Blackman-Tukey, Redfit, MTM and EHA spectral analysis techniques. The biostratigraphic age constraints in combination with the eASM and spectral analysis results should lead to a hypothesis in which the stable 405-kyr eccentricity cycle (Laskar et al., 2011a) can be assigned to a period in the depth domain. The 405-kyr eccentricity cycle will be extrapolated to infer ages for other identified cycles. The 405-kyr eccentricity cycle will be used to perform conversion from the depth to the time domain. A tuning of the 405-kyr bandpassed record to an astronomical solution of La2010 (Laskar et al., 2011a) will be used to give preliminary ages for the Chalk Group on the Schill Grund Platform. Visual observations and XRF data from the core of well A12-02, well-logs and literature will be used to give a palaeoclimatological explanation for any observed cyclicity. The palaeoclimatological explanation will be used to interpret the relationship between the lithology, the filtered records, the orbital phase and stratigraphic events. The new cyclostratigraphic framework will enable the evaluation of the seismic data of the Schill Grund platform from a seismic-cyclostratigraphic point view. A cyclostratigraphic framework will also enable a long distance correlation of stage boundaries across the Schill Grund Platform and a re-evaluation of the ages of the CK sequences of van der Molen (2004) and the formation boundaries of the Chalk Group in the Dutch offshore.

2. Geological setting

2.1 Tectonostratigraphic evolution of the Dutch offshore

For this research, the tectonostratigraphic history of the Dutch North Sea is divided into 9 tectonostratigraphic phases. The division into 9 phases is based on the work of Doornenbal and Stevenson (2010) and Wong et al. (2007) and references therein. The 9 tectonostratigraphic phases are indicated in the tectonostratigraphic cross-section of Figure 1. An extra South-North tectonostratigraphic intersection can be found in the supplementary information (SI)10.1.3 Figure 68. A general sedimentary succession for the different structural elements in the Netherlands can be observed in S.I. 10.1.4 Figure 68.

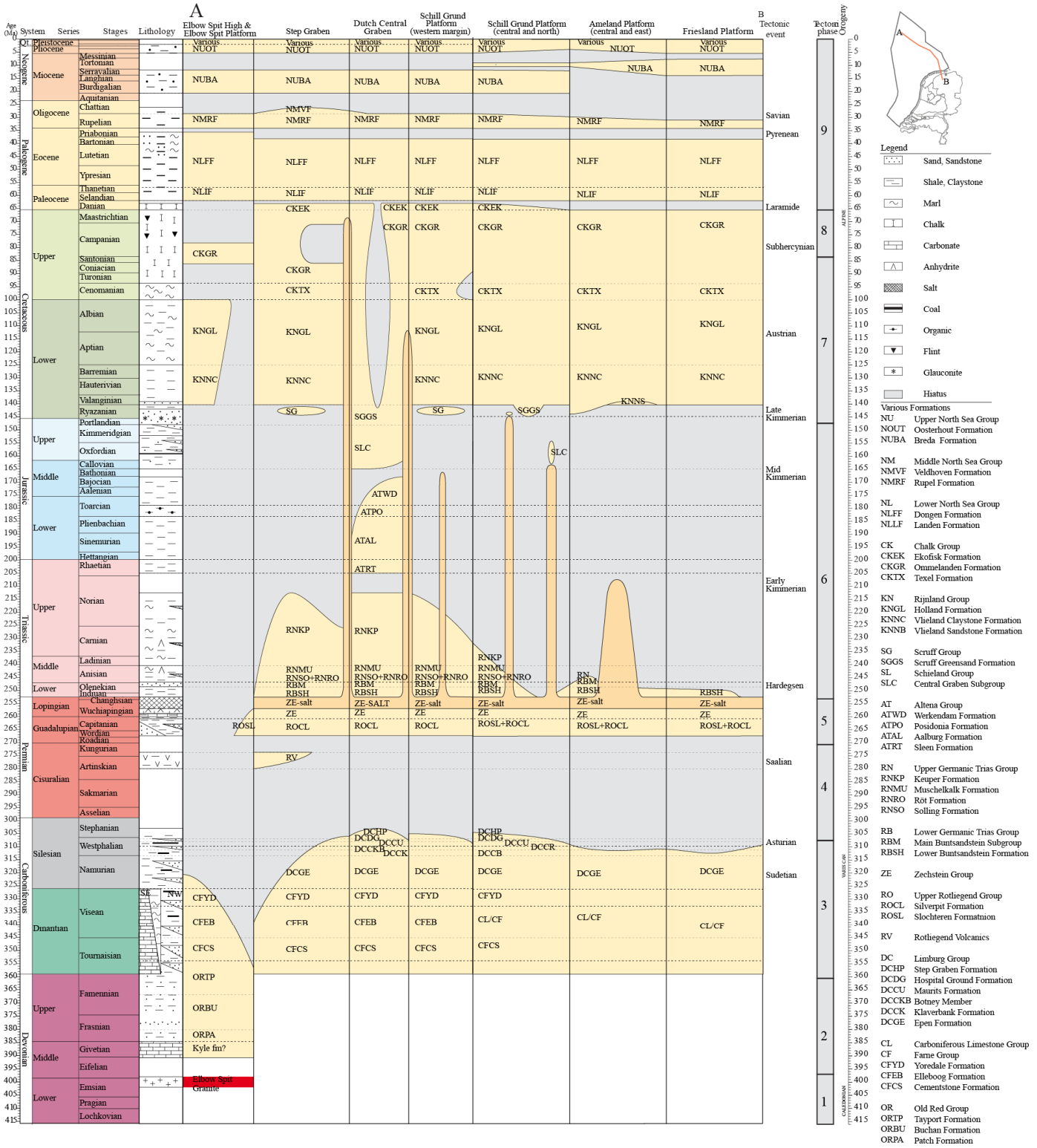

Figure 1. Schematic cross-section across the Northern-Dutch offshore. Modified after TNO (2011).

2.1.1 Laurussian amalgamation and Caledonian orogeny

During the late Ordovician the Netherlands and the Dutch North Sea were located on the Avalonia continent. Avalonia collided with the Baltic continent during the late Ordovician to early Silurian (Torsvik and Rehnström, 2003). the combined Avalonia-Baltica continent collided with Laurentia during the middle Silurian and early Devonian, which led to the creation of the continent of Laurussian and the Caledonian orogen (de Jager, 2007; De Vos et al., 2010; Geluk et al., 2007; Pharaoh et al., 2010). The collisions created multiple NW-SE and N-S running fault trends. These fault trends were often reactivated during later tectonic events.

2.1.2 Post Caledonian extension

During the Devonian half grabens formed in the Netherlands in response to back-arc extension in the Rhenohercynian Basin to the south-east of the Netherlands (Ziegler, 1990). Deposition of carbonate reef build-ups took place on top of horst blocks while shale deposition occurred in the grabens (Bełka et al., 2010; Geluk et al., 2007). During the Late Devonian, the carbonate system was replaced by the siliciclastics of the Old red Banjaard Group (Geluk et al., 2007). The siliciclastic system was in turn replaced by the lower Carboniferous Limestone Group (Geluk et al., 2007; Kombrink et al., 2010). Deposition of the carbonate facies of the Limestone Group was centred on top of structural highs. These highs include the Cleaver Bank platform, the Schill Grund Platform, the Texel-Ijsselmeer high, the Groningen platform and the Peel-Maasbommel complex. In-between the carbonate platforms a shaly starved basin facies was deposited. Lower Carboniferous siliciclastic sediments are observed in the adjacent UK sector. These siliciclastic sediments are also assumed to be present in the northernmost part of the Dutch offshore (Geluk et al., 2007).

2.1.3 Variscan orogeny

The collision of the Laurussia and Gondwanan continents during the late Carboniferous led to the formation of the Pangean continent and the Variscan orogeny. The Netherlands was located just north of the Variscan orogeny in a foreland basin in which a thick sedimentary package was deposited (Kombrink et al., 2010; van Buggenum and Den Hartog Jager, 2007). The creation of this foreland can be seen in a shift from carbonate deposition in the early Carboniferous to a fully clastic deltaic deposition in the late Carboniferous. The Variscan orogen also led to a further structuration of the area by the creating of NW-SE trending faults.

2.1.4 Variscan Orogenic Collapse

The Variscan orogen collapsed during the latest Carboniferous and early-middle Permian. Wrenching and upwarping of the Variscan orogenic foreland led to uplift and subsequent erosion (Gast et al., 2010; Geluk, 2007a). The Variscan orogenic collapse led to the creation of NW-SE trending faults. The Lower Rotliegend volcanics and clastics were deposited in the Dutch central graben area and the Ems Low during the orogenic collapse.

2.1.5 Sag basin

After the Variscan collapse a sag phase ensued, which lasted from the late Permian to early Triassic. Sedimentation occurred within an arid continental environment punctuated by multiple marine transgressions. The Upper Rotliegend Group was deposited from the middle to early late Permian. The Upper Rotliegend Group consists of the fluvial and aeolian sediments of the Slochteren Formation which interfingers with the playa lake sediments of the Silverpit Formation (Gast et al., 2010; Geluk, 2007a).

A connection with the Barents Sea was established during the late Permian which led to the creation of a hypersaline inland sea. The Zechstein Group was deposited in and around this inland sea (Geluk, 2007a; Peryt et al., 2010) . The Zechstein Group consists of 5 evaporitic cycles (Z1 to Z5) with an unconformable claystone on top. The Evaporitic cycles consist of evaporites, carbonate (platforms) and clayey/shaly sediments, which are the result of an intermittent connection to the Barents Sea. Sabkha and fluvial conditions prevailed to the south of the Central Netherlands Basin. Minor fault movement related to the initiation of the breakup of Pangea and onset of the Uralic orogeny occurred during the deposition of the Rotliegend and Zechstein Group. The fault movement manifested itself in the formation of half grabens in pull apart type basins.

The Lower Germanic Trias Group below the Hardegsen unconformity is part of the transition from the sag basin to the failed rift phase. The deposition of the Lower Germanic Trias Group was influenced by the Hardegsen tectonic phase

which occurred in 4 pulses. The Hardegsen tectonic phase created some minor fault movement and subsidence in the central graben which progressively restricted sedimentation to the structural lows. The Lower Germanic Trias Group consists of the lower and main Buntsandstein Formations (Bachmann et al., 2010; Geluk, 2007b). The lower Buntsandstein consists of fine grained lacustrine sandstones and clay-siltstones stacked into fining upwards cycles. Towards the south of the Netherlands the lower Buntsandstein sediments changes to sandstones and conglomerates. The main Buntsandstein Formation is dominated by fluvial facies in south while aeolian sandstones and clayey siltstones dominate as a playa lake setting in the north (Bachmann et al., 2010; Geluk, 2007b).

2.1.6 Failed rift

A failed rift phase occurred in the early Triassic to early Cretaceous times. Small scale rifting already started during the early Triassic with the onset of the Hardegsen tectonic event. The large-scale rifting associated with the Kimmerian tectonic phases took place from the middle Triassic to Late Jurassic. During the Kimmerian tectonic phases many of the Palaeozoic faults were reactivated which led to the formation of deep basins. Sedimentation was restricted to these deep basins while erosion occurred on the platforms and highs. The phases in between the rift phases are characterized by regional thermal subsidence. Rifting induced salt movement started during the Kimmerian phases and led to the formation of salt domes, pillows, ridges and pillars. Salt movement was largest in the basins while only salt pillows formed on the highs and platforms (Ten Veen et al., 2012).

The Upper Germanic Trias Group above the Hardegsen Formation consists of the Solling, Röt, Muschelkalk and Keuper Formations (Bachmann et al., 2010; Geluk, 2007b) . The Solling Formation consists of a basal sandstone covered by clay/siltstones. During the deposition of the Röt Formation a connection with the Tethys Ocean was established via the Silesian-Moravian gateway (Bachmann et al., 2010; Geluk, 2007b). Phases with a restricted connection to the Silesian-Moravian gateway initiated the deposition of evaporitic sediments. The Röt Formation consists of clay/siltstones intercalated by evaporitic layers (Bachmann et al., 2010; Geluk, 2007b). Towards the south the deposition of the Röt Formation gets progressively more dominated by sandstones. The Muschelkalk Formation consists of a lower carbonate, a middle evaporitic and an upper carbonate unit (Geluk, 2007b). The Keuper Formation is strongly affected by Kimmerian I rifting and its associated salt movement (Geluk, 2007b). The Keuper consists of 4 members; the Lower Keuper Member which consists of claystones alternating with fine grained sandstones and coals with an anhydrite on top, the Main Keuper Member consists of an alternation of evaporates and claystones, the Middle Keuper claystone Member consists of claystones and the post Kimmerian I rifting Red Keuper consists of a lower evaporite and an upper claystone and dolomite.

The Altena Group is separated from the Upper Germanic Trias Group by an unconformity associated with the early Kimmerian II rifting phase (Lott et al., 2010; Wong, 2007). The deposition of the Altena Group took place in-between the Early Kimmerian and the end of the Mid Kimmerian tectonic phase. The distribution of the Altena is confined to the rift basins. Tectonic activity associated with the mid Kimmerian phase led to the creation of the Central North Sea dome, which created uplift and subsequent erosion the northern Dutch offshore The Altena Group consist of marine claystones, marine silt/mudstones and greensands.

The Schieland, Scruff and Niedersachsen Groups were deposited from the mid Kimmerian tectonic phase to the late Kimmerian pulse II. The Schieland Group is subdivided into the Central graben, Delfland, Scruff and Niedersachsen Subgroups. The Central Graben Subgroup is an alternation of sandstones, claystones and coal beds and was deposited in the Dutch central graben and Terschelling Basin. The Central Graben Subgroup was heavily influenced by the post mid-Kimmerian uplift and erosion. The Delfland Subgroup is an alternation of sandstones and claystones with thin intercalations of dolomite and coal beds. The Delfland Subgroup was deposited in the Vlieland Basin, Central Netherlands Basins, Broad Fourteens Basin, West Netherlands Basin and Roer Valley Graben. The Scruff Subgroup consists of marine claystones (locally bituminous) intercalated by thin carbonate and glauconitic to argillaceous sandstone beds and was deposited in the Dutch Central Graben, Terschelling Basin and the northern part of the Vlieland Basin (Herngreen and Wong, 2007; Wong, 2007). The Niedersachsen Subgroup was deposited in the Lower Saxony Basin and consist of claystones intercalated by marls and limestones and has evaporite layers in the lower part (Herngreen and Wong, 2007; Wong, 2007).

2.1.7 Thermal sag

During the early Cretaceous, rifting halted and a post-rift thermal sag phase started. The combination of the thermal sag phase and a global eustatic sea-level rise led to an overstepping of the basin margin (Herngreen and Wong, 2007; Van der Molen, 2004; Vejbæk et al., 2010). The Schieland, Delfland, and Niedersachsen Subgroup sediments were interfingered and overstepped by the marine Valanginian to Aptian Rijnland Group sediments. The Rijnland Group sediments can be dived into the proximal Vlieland Sandstone Formation which consists of shallow marine sandstones and the distal Vlieland claystones which consists of claystones with minor amounts mica and lignitic matter. The Aptian to Cenomanian part of the Rijnland Group consist of the Holland Formation which consists of marls, claystones and greensands which were deposited in a middle to outer-neritic environment. A rise in sealevel led to progressively less continental influence and subsequently less clastic input into the basin, which initiated the transition from the argillaceous claystone dominated Rijnland Group to the open marine carbonate facies of the Chalk Group.

2.1.8 Alpine inversion

During the Late Cretaceous the northward movement of Africa led to the creation of the alpine orogen which manifested itself in the North Sea Basin as multiple inversion phases (Herngreen and Wong, 2007; Van der Molen, 2004; Vejbæk et al., 2010). Deposition of the Chalk Group carbonates continued in the late Cretaceous to Palaeogene, but the deposition and re-deposition was heavily influenced by multiple inversion phases. The northern Dutch offshore was characterized by a S/W tilting during the Turonian (Van der Voet, 2015). Major subsidence took place in the eastern Dutch offshore during the Coniacian to Santonian (Van der Molen, 2004). Two inversion pulses occurred in the Campanian to Maastrichtian in the Dutch Northern offshore (Van der Voet, 2015). The Step Graben and western Dutch Central Graben were inverted in the first phase. The Elbow Spit Platform was inverted during the second phase. The inversion in combination with the inherent instability of the chalk sediments leads to erosion and redeposition, which manifested itself as slumping and channel formation. The inversion phases also led to a renewed phase of salt movement in the Dutch offshore (Ten Veen et al., 2012).

2.1.9 Siliciclastic shift

The Laramide tectonic phase occurred during the latest Cretaceous/early Palaeogene. (Knox et al., 2010; Wong et al., 2007b). This tectonic phase caused inversion and a shift from a carbonate to siliciclastic dominated depositional environment. The siliciclastic sedimentation continued until the present day. Major erosional hiatuses were created by inversion related to the late Eocene Pyrenean phase and the Oligocene-Miocene Savian phase.

2.2 The Chalk Group

2.2.1 Stratigraphic subdivision

The Chalk Group is divided into 4 parts, which are the: the Texel Formation, the Plenus Marl Member , the Ommelanden Formation and the Ekofisk Formation (Figure 2) (van Adrichem Boogaert and Kauwe, 1997; Van der Molen, 2004). The German, Danish, UK and Norwegian sectors often have different names for these formations, but the main boundaries are often the same (see Figure 2).

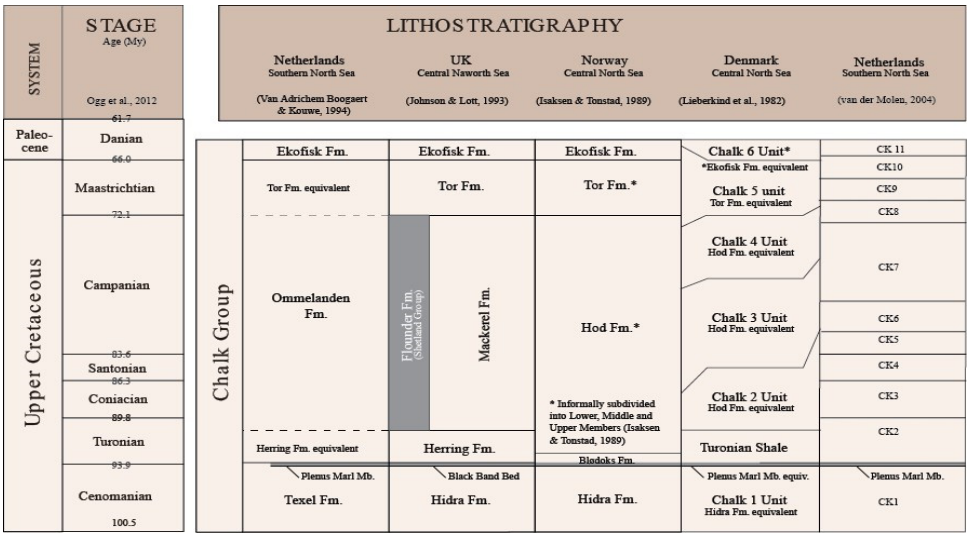

Figure 2. Stratigraphic subdivision of the Chalk Group from van der Molen and Wong (2007)

2.2.1.1 Texel Formation

The Texel Formation consists of white to beige marly chalks and limestones and can be identified by a decrease in sonic and gamma ray and an increase in the density reading. The Texel Formation reaches a maximum thickness of ~60m on the Schill Grund Platform (Van der Molen, 2004). The top of the Texel Formation is defined by the Plenus Marl. Within the Texel Formation there is the Texel greensand Member, which is a glauconitic sand body, which was deposited at the basinal edges of the North Sea Basin (Herngreen and Wong, 2007). The occurrence of the greensand Member on the Schill Grund Platform is not mentioned in literature nor found in any of the well-logs or well reports.

2.2.1.2 Plenus Marl Member

The Plenus Marl Member consists of dark-grey and locally black calcareous bituminous claystone. The Plenus Marl is up to 10 metres thick and is the North Sea equivalent to AOEII and therefore placed around the Cenomanian-Turonian boundary (Schlanger et al., 1987b). The Plenus Marl is characterized by a large peak in the gamma ray log a smaller peak in the sonic log and a decrease in the density log (Van der Molen, 2004).

2.2.1.3 Ommelanden Formation

The Ommelanden Formation is an alternation between white to beige chalks and more clay rich light-olive-green to grey chalks. The chalk is generally fine-grained, but in places resembles more of an argillaceous limestone. Flint nodules are common within this formation. The Ommelanden Formation is characterized by a decrease in the gamma ray and sonic values with depth. The top of the Ommelanden Formation is defined as either the K/Pg boundary or a large shift towards higher Gamma ray and sonic values. The Ommelanden reaches thicknesses of up to ~1100 metres on the Schill Grund Platform.

2.2.1.4 Ekofisk Formation

The Ekofisk is the Danian part of the Chalk Group (van Adrichem Boogaert and Kauwe, 1997; Van der Molen, 2004). The formation consists of an alternation of white chalks and grey/green clay rick laminated chalks. Nodular and bedded flint layers and glauconite beds are also present. The Ekofisk Formation is often subjected to re-sedimentation and is characterized by high amplitude reflectors. The gamma ray and sonic logs often show an increase in sonic and gamma ray values and a more internal erratic variation than the Ommelanden Formation. The top of the Ekofisk is defined by a gradual increase in the shale content, which can be observed by an increase in the gamma ray and sonic values. The maximum thickness of the Ekofisk Formation in the Dutch offshore is around 120 metres (Van der Molen, 2004).

2.2.2 Biostratigraphic background

The northern Dutch offshore contains 15 wells from which the biostratigraphic data is used as a biostratigraphic background framework for this research (for location see S.I. 10.1.5 Figure 70). Of the 15 wells in this study 13 wells have foraminifera-based biostratigraphic data that is from the 70's and 80's which was updated using the most recent biostratigraphic literature ((Bergen and Sikora, 1999; Gradstein and Waters, 2016; Hardenbol et al., 1998) and https://www.dinoloket.nl/sites/www.dinoloket.nl/files/file/DRW-0289.pdf). The biostratigraphic data was updated to the NCF zonation of Gradstein and Waters (2016). Emphasis was placed on the LO's of species rather than their FO's because the biostratigraphies are based on cutting records. During drilling cuttings flow up through the well bore and the first event which is recorded is the LO of a species. A FO can significantly vary in depth due to residual cuttings surfacing after the bulk of a drilled layer is pumped to the surface. The resulting ages for the boundaries and their sedimentation rates in-between these boundaries can be seen in Table 1. For a table with all the LO and FO's species see S.I. 10.1.6 Table 2.

2.2.2.1 Well A12-02

Well A12-02 has new data which is based on dinoflagellate research by Dr. D. Munsterman (TNO-GDN). The results indicated that the K/Pg boundary in located in between 2037.5 and 2032.55 m MD. A 63.5-66 Ma age range for the sample at 2032.55 m was based on Townsend (2016). The age range was based on the FOD *Damassadinium californicum* (66 Ma), the FOD *Senoniasphaera inorata* (66 Ma), the LOD *Senoniasphaera inorata* (63.5 Ma) and the Absence *Palynodinium grallator* (LOD 65 Ma). The 66.89-67.88 Ma age range for the sample at 2037.5 m was also based on Townsend (2016). The LCOD of *Palynodinium grallator* (abundance of 43% of total amount of dinoflagellate cysts) is coupled to a super abundance event which has an age range of 66.89 to 67.88 Ma.

2.2.2.2 Well G11-1

For the German sector one nanoplankton-based biostratigraphy was available from well G11-1 on the Schill Grund Platform (Köthe, 2007)(location: http://nibis.lbeg.de/cardomap3/#). The whole Cenozoic down to the K/Pg boundary was the subjected to the study of Köthe (2007). The K/Pg boundary was identified at 1600 m as calcareous nanoplankton zone CC26, which was identified by the presence of *Nephrolithus frequens* and *Cribrosphaerella daniae.* Both nanoplankton species have their LO and FO in CC26 (Bolli et al., 1989). To correlate the biostratigraphy of well G11-1 to the nearby wells in the Dutch offshore the well was transposed on to seismic line SNST87N10a. The corresponding seismic horizon was then tracked into the 3D dataset of the Dutch sector.

			well	sedrate m/Ma	well	sedrate m/Ma	well	sedrate m/Ma	well	sedrate m/Ma	well	sedrate m/Ma	well	sedrate m/Ma	well	sedrate m/Ma
			G17-01	G17-01	G16-02	G16-02	F15-01	F15-01	F18-03	F18-03	F02-03	F02-03	A18-01	A18-01	B14-01	B14-01
Boundary	Age (Ogg et al., 2012)	Definition	depth		depth		depth		depth		depth		depth		depth	
Maastrichtian Palaeocene	66	Top NCF 19	1493-1500		1580		1655		1512		1522		2280		1990-2010	
Campanian Maastrichtian	72.1	Top NCF17	1756	41.96721311	1750	27.868852 46	1925	44.26229508	1660	24.26229508	1574	8.524590164			2104	18.68852459
Santonian Campanian	83.6	Top NCF 15	2237	41.82608696	2056	26.60869565	2385/2400	41.30434783	1884	19.47826087						
Coniacian Santonian	86.3	Top NCF 13														
Turonian Coniacian	89.9	middle NCF 13														
Cenomanian Turonian	93.9	bottom NCF 12 OAE2	2480	31.97368421	2170	11.06796117	2748	33.78640777	2092	523	not present		2446	5.949820789	no present	
Albian Cenomanian	100.5	Top NCF 8	2560	12.12121212					2172	12.12121212						
Aptian Albian	113	Top NCF 5														
Barremian Aptian	125	Middle NCF 4 LO Gavellinella barremiana & LO Conorodtalites intercedens	2609	2			2840	2.958199357								
Hauterivian Barremian	129.4	Top NCF 2	2646	8.409090909												
Valanginian Hauterivian	132.9	Bottom NCF 1	2719	20.85714286			2935	12.02531646								
Berriasian/Ryazanian Valanginian	139.8	No definition														

			well	sedrate m/Ma	well	sedrate m/Ma	well	sedrate m/Ma	well	sedrate m/Ma	well	sedrate m/Ma	well	sedrate m/Ma		
			A12-01	A12-01	B17-02	B17-02	F12-01	F12-01	M01-01	M01-01	M07-01	M07-01	F09-02	F09-02		
Boundary	Age (Ogg et al., 2012)	Definition	depth		depth		depth		depth		depth		depth			
Maastrichtian Palaeocene	66	Top NCF 19	2120		1950/2013		1460		1400		1435		1570			
Campanian Maastrichtian	72.1	Top NCF17			2205	41.80327869	1640	29.50819672			1635	32.78688525				
Santonian Campanian	83.6	Top NCF 15									1795/1835	29.56521739	1620	2.840909091		
Coniacian Santonian	86.3	Top NCF 13														
Turonian Coniacian	89.9	middle NCF 13														
Cenomanian Turonian	93.9	botom NCF 12 OAE2	2705?	20.96774194	2653	20.55045872	1960	14.67889908	1694	10.53763441	2052	24.95145631	not present			
Albian Cenomanian	100.5	Top NCF 8							1720	3.939393939	2130	11.81818182				
Aptian Albian	113	Top NCF 5					1970	0.523560209			2145	1.2				
Barremian Aptian	125	Middle NCF 4 LO Gavellinella barremiana & LO Conorodtalites intercedens			2781	4.115755627	1985	1.25	1800	3.265306122	2160/2185	3.333333333				
Hauterivian Barremian	129.4	Top NCF 2							1950	34.09090909						
Valanginian Hauterivian	132.9	Bottom NCF 1														
Berriasian/Ryazanian Valanginian	139.8	No definition														

Table 1. Results re-evaluation of biostratigraphic data. Re-evaluation based on (Bergen and Sikora, 1999; Gradstein and Waters, 2016; Hardenbol et al., 1998) and https://www.dinoloket.nl/sites/www.dinoloket.nl/files/file/DRW-0289.pdf. The NCF zonation is based on Gradstein and Waters (2016)

2.2.3 Sealevel and palaeo-temperature

The Deposition of the Chalk Group coincided with a global eustatic sealevel highstand, increased CO_2 concentrations and elevated temperatures linked to increased sea-floor spreading rates (Larson, 1991a, 1991b). In the late Albian global sealevel rose to ~205– 215 m above present day mean sealevel (Haq, 2014). During the early Cenomanian, sealevel remained stable and only varied by ~20 m. From the late Cenomanian to early Turonian global sealevel rose to the highest level of the Cretaceous at ~240–250 m above present day mean sealevel. Global sealevel fell by ~60 m during the Turonian. From the Coniacian to Campanian global sealevel remained stable and only varied by ~20 m. The sealevel gradually fell by ~40 to 50 m during the Maastrichtian, which resulted in a global sealevel at ~190–200 m above present day mean sealevel at the end of the Cretaceous. The gradual sealevel fall continued during the Danian.

The palaeotemperature records of the Chalk Group closely mimic the global sealevel trend. The temperature increased from the Albian to the Cenomanian-Turonian anoxic event 2 (OAEII) and reached the highest temperatures of the whole late Cretaceous during AOEII (Jenkyns et al., 1994). After OAEII the temperature gradually decreased only to increase

at the end of the Cretaceous. This temperature increase was due elevated levels of greenhouse gasses released by the Deccan traps volcanism (Chenet et al., 2009; Friedrich et al., 2005; Thibault et al., 2015; Thibault and Husson, 2016).

2.2.4 Water depth

There is still no consensus regarding the water depth of the European Epicontinental Sea in which the Cretaceous chalk was deposited. Håkansson et al. (1974) interpreted chalk as being deposited in a shallow epicontinental sea with only deepest areas outside the photic zone (<250m). According to Håkansson et al. (1974) an interpretation for the depth of the biomicrite chalk facies is difficult due to the rapid transition from the near shore greensands, sandstones and biocalcarenites to the deeper water biomicrites. Kennedy (1987) estimated the water depth between 300-600 m. Van der Molen (2004) estimated water depths from hundred to thousand metres for the Danish-Norwegian Central graben. Zijlstra (1995, 1994) reaches no definite conclusion but notes the absence of benthic organisms in the chalks of the Limburg area. According to Hudson (1967) the absence of aragonite indicates that the chalk was deposited at depths at which aragonite can dissolve. Hudson (1967) also notes that that the Chalk Group facies was at least deposited below storm wave base and estimates a depth range between 200 and 400 m. Bathurst (1975) indicates that the hardgrounds in the chalk are formed during a lowstand at a minimum of 50m depth while the chalk ooze facies is formed during a highstand and was deposited at ~200m depth. Glennie (1998) indicates that the Chalk Group was deposited at least below the storm wave base (>50m). Rasmussen and Sheldon (2015) used a benthic planktonic ratio to arrive at a water depth of 200-800 for the Danish central graben. It was noted by Rasmussen and Sheldon (2015) that the benthic/planktonic ratio carries a high degree of uncertainty due to the interpretation of anoxic bottom waters, which affects the benthic/planktonic ratio. For the Paris Basin (Lasseur et al., 2009) documented the variability of the chalk facies from a near shore to below wave base setting and assigned different facies features to different depth intervals. Mitchell et al. (2010) compiled data for a general depth model with a minimum and maximum water depths for the boreal realm (Figure 3). Both depth models are deemed accurate enough for tidal current modelling of the Bohemian Basin but no further emphasis was placed on the evaluation of the regional water depth model.

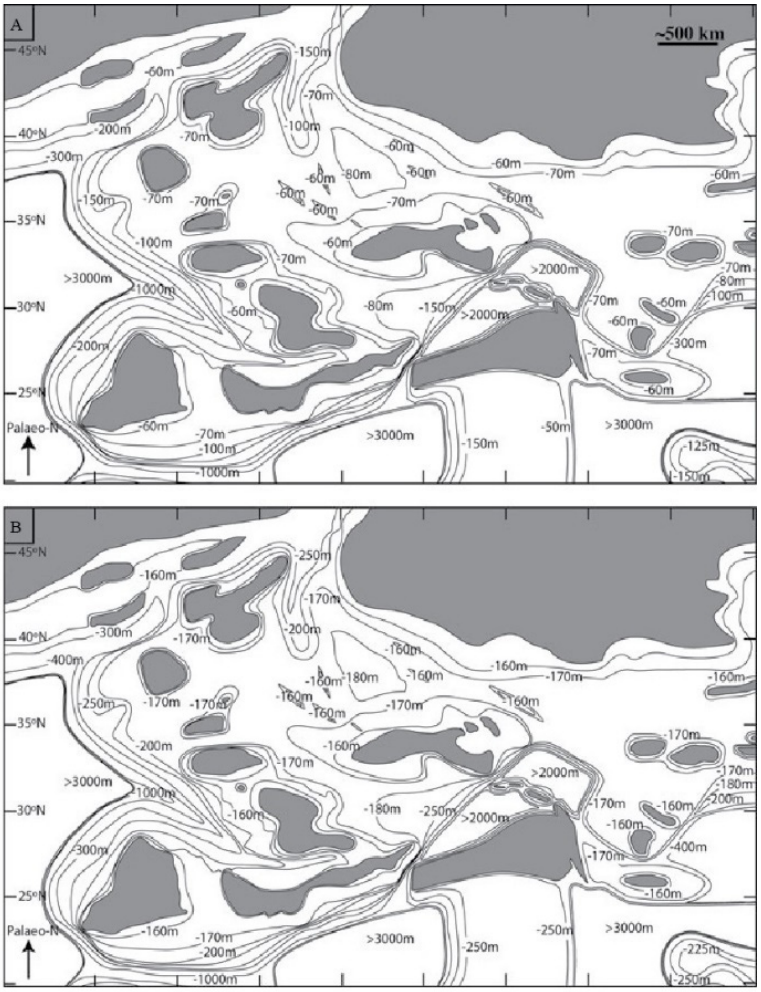

Regional palaeobathymetries for the Mid-Cretaceous European Epicontinental Sea showing major isobaths for (A) minimum and (B) maximum depth scenarios. Dark grey areas are emergent regions.

Figure 3. Minimum and maximum water depth estimates for the European Epicontinental sea. From Mitchell et al. (2010).

2.2.5 Sedimentation rate

The sedimentation rate of the chalk is highly variable depending on the location. For the shallow seas in the Limburg area, Zijlstra (1994) estimated a sedimentation rate between 10 and 100+ mm/kyr. Boussaha et al. (2016) estimated a sedimentation rate of 10-70 mm/kyr for the Danish Basin. Tucker and Wright (1990) gave a general sedimentation rate of 150-250 mm/kyr for the Chalk Group in the North Sea area. Håkansson et al. (1974) gave a general sedimentation rate for the Chalk Group of 150 mm/kyr. For the Chalk Group in Germany the sedimentation rates are 22-33 mm/kyr (Voigt and Schönfeld, 2010), 45-50 mm/kyr (Niebuhr and Prokoph, 1997), 25-52 mm/kyr (Niebuhr et al., 2001) and 41–54 mm/kyr (Niebuhr, 2005). For the Danish central graben Damholt and Surlyk (2004) estimated a sedimentation

rate of 20–30 mm/kyr, while Perdiou et al. (2016) estimated a sedimentation rate of ~10 mm/kyr. For the Dutch offshore van der Molen (2004) estimated sedimentation rates of 50-70 mm/kyr.

2.2.6 Chalk composition

The main constituent of the Chalk Group is calcium carbonate, which reaches concentrations of 96-99% (Van der Molen, 2004), 2004). The carbonate fraction mainly consists of coccolithophore remains ((Håkansson et al., 1974) and Figure 7), but also contains foraminifera, calcispheres, echinoids, bivalves, sponges, brachiopods and bryozoans (Tucker and Wright, 1990). The main non-carbonate components are clay and flint (Kennedy, 1987).

2.2.6.1 Coccolithophores

The main constituent of the chalk carbonate fraction are the remains of coccolithophores (Figure 4). Coccolithophores are unicellular eukaryotic phytoplankton (algae) (Figure 4). Coccolithophores consist of a Protoplasm and a Periplasm cell covering made of scales (coccoliths), which can be made from organic and non-organic (carbonate) material (Pienaar, 1994). The coccolith disks are formed on an organic baseplate or an organic matrix. Coccolith calcite consists of low-mg calcite. Multiple functions have been ascribed to coccoliths, such as increased protection, environmental buffering, more efficient nutrient uptake, act as a transition layer in between the cell and the seawater, increase photosynthesis efficiency by carbonate precipitation, enhanced nutrient uptake by increasing the sinking rate, increased motility or play a role in regulating the light entering the cell (Young, 1984). Coccolithophores are transported to the sea bottom in the form of faecal pellets or marine snow (Kennedy, 1987; Steinmetz, 1994a). Coccolith remains pass through alimentary canals of zooplankton and are then incorporated in faecal pellets. Marine snow is an amorphous particulate made of different components (organic, non-organic and detrital) that stays together by intermolecular, intramolecular, atomic forces, surface tension, organic cohesion or electrostatic force. On the seabed, the marine snow and faecal pellets are reworked and disintegrate into clay to silt sized mud ((Fabricius et al., 2007) and see Figure 5).

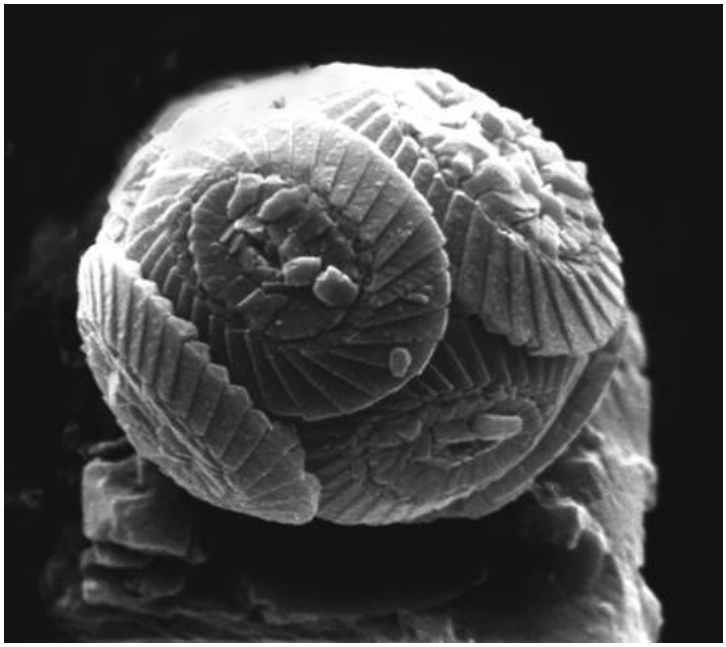

Figure 4. SEM from a Coccosphere (http://www.ucl.ac.uk/GeolSci/micropal/calcnanno.html), Species: Watznaueria barnesae (Black and Barnes, 1959; Perch Nielsen, 1968), Age: Early Bajocian-Maastrichtian, Location: Speeton, UK

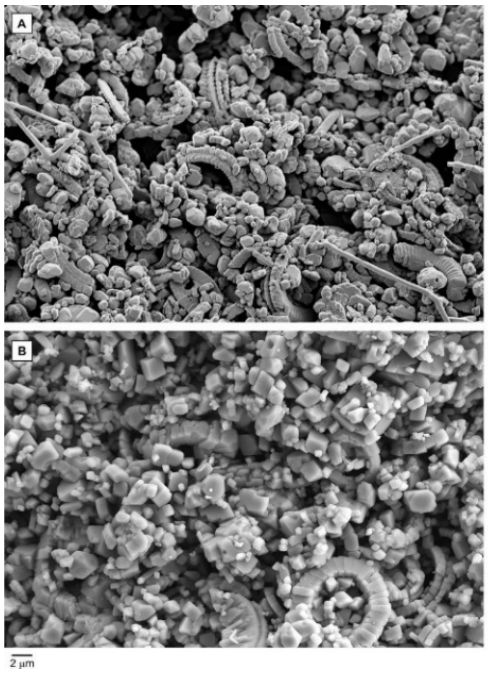

Figure 5. Scanning electron microscope images of Chalk from the Norwegian Central graben. From Fabricius (2007).

2.2.6.2 Non-carbonate fraction

2.2.6.2.1 Clay layers

Although the chalk consists of mainly pure chalk, some layers are so enriched in clay that they have an almost sapropel like appearance (Gale et al., 1999). The clay layers mainly consist of clays with minor amounts of quartz and pyrite (Anderskouv and Surlyk, 2011; Stage, 2001a). There are four hypothesises for the formation of these clay layers. The first hypothesis is that these clay layers are of a detrital origin (Deconinck and Chamley, 1995; Jeans, 1968; Jeans et al., 2001; Kennedy, 1987; Lindgreen et al., 2008, 2002; Stage, 2001a; Wray, 1999; Wray et al., 1996; Wray and Wood, 1998). The low concentration of clay minerals in the chalk is attributed to the high sealevel during the late Cretaceous, which reduced detrital input. The second hypothesis is that these layers formed in situ. The clay mineral montmorillonite is hypothesised to have been precipitated from pore waters within the chalk substrate (Deconinck and Chamley, 1995; Jeans, 1968). The third hypothesis is that at least some clay layers are the result of the weathering of volcanic ash layers (Deconinck and Chamley, 1995; Gale et al., 1999; Sumbler, 1999; Voigt and Schönfeld, 2010; Wray, 1995; Wray et al., 1996; Wray and Gale, 2006; Wray and Wood, 1998) The weathering of the ash layers would have created clay layers rich in the mineral smectite. The origin of these ash layers is proposed to originate from volcanism related to the Atlantic opening, but Deconinck and Chamley (1995) note that multiple huge ash falls are needed to create the proposed volcanogenic smectite layers which are present over large areas. The argument of Deconinck and Chamley (1995) therefore casts doubt on the volcanic origin for most of the clay layers. The fourth hypothesis is that these clay layers formed by dissolution (Lindgreen et al., 2008). At burial depths of more than 1 km migration of solutions through permeable chalk layers would have led to the dissolution of chalk and the enrichment in clay particles.

2.2.6.2.2 Flint layers

The formation of flint layers is more localized in comparison to clay layers (Arthur et al., 1986; Cottle, 1989; Hart, 1987; Zijlstra, 1995, 1994). Flint layers are an early-stage diagenetic feature linked to precipitation of silica within or slightly below the anoxic redox zone in the sediment interface (Zijlstra, 1994, 1995). The source of the silica is unknown but sponges, radiolarians or diatoms have been put forward as a source for silica (Hart, 1987). The concentration of flint into distinct layers might be the result of orbitally controlled productivity cycles changing the silica-carbonate ratio in sediments (Zijlstra, 1995, 1994). Diagenesis would have further concentrated the silica in the silica enriched beds (Arthur et al., 1986; Hart, 1987; Zijlstra, 1994, 1995). Zijlstra (1994, 1995) postulated that the longer sediment resided at the surface the more it is enriched in silica and flint beds are thus inferred to be related to periods of low sedimentation rates. Cyclic patterns in flint bands are thus linked to changes in the sedimentation rate.

2.2.7 Reworking of the chalk

The Chalk Group has been reworked and redeposited from micro to macro scales, which leads to the formation of chalk sediments with varying types of morphology (Figure 6,7 and 8). Varying topography and proximity to the shore impacts the composition and the appearance of chalk (Figure 8), while currents and mass movements further modified the appearance of the chalk (Figure 7). Tucker and Wright (1990) observed bioturbation features Chondrites, Zoophycos and Planolites throughout the Chalk Group and Thalassinoides in a shallow(er) setting. van der Molen (2004) identified a large-scale channel feature in a 2D seismic lines of the eastern Schill Grund Platform. This channel feature continues on into the German part of the Schill Grund Platform where it was mapped in 3D by Surlyk et al. (2008). Large channel features have also been studied in the Norwegian-Danish central graben (Back et al., 2011; Gennaro and Wonham, 2014; Van Buchem et al., 2017). Gennaro and Wonham (2014) suggests that the channel systems from the Norwegian-Danish Central graben to the Schill Grund Platform are a local expression of a single large north to south flowing bottom current system. Multiple smaller channels have been observed on the Step graben and Dutch Central graben (Van der Voet, 2015). Large slumping/mass flow deposits are observed in the Dutch Central graben and Norwegian-Danish central graben (Gennaro et al., 2013; Van Buchem et al., 2017; Van der Voet, 2015). Many layers of redeposited chalk are thought to be mass flows triggered by active faulting due to the alpine inversion affecting the area (Glennie, 1998; Kennedy, 1987; Van Buchem et al., 2017). Mass transportation and channel features can also be seen originating from halokinesis induced palaeo-highs in the Danish Central graben (Arfai et al., 2016; Gennaro et al., 2013). Turbidite, debrite and mudflow facies associations are also observed in the Danish Central graben (Anderskouv and Surlyk, 2011). Oval shaped depressions in the Ekofisk Formation in the Danish graben have been identified as pockmarks, which were reworked by bottom currents (Arfai et al., 2016; Masoumi et al., 2014).

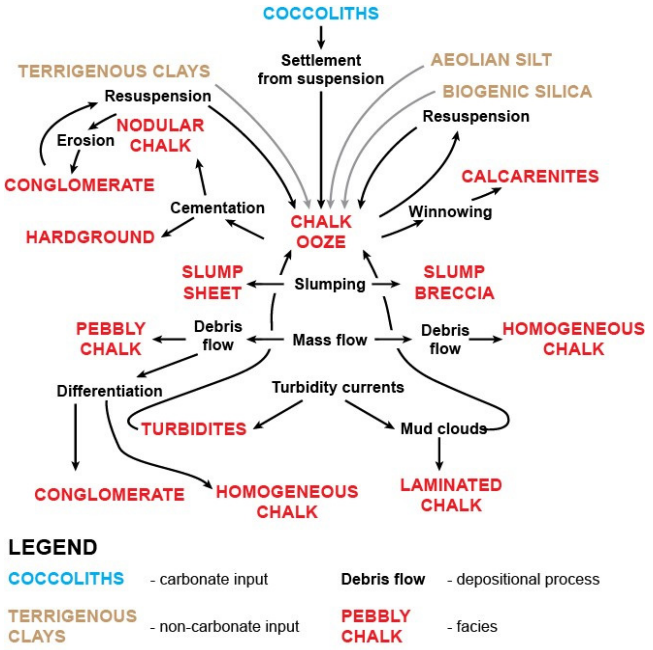

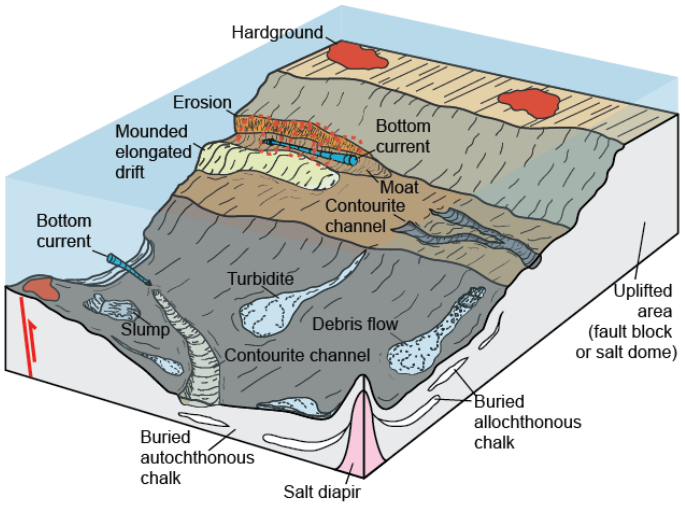

Depositional model of chalk in the Central Graben (modified from taylor & Lampré, 1987; Surlyk & Lykke-Andersen 2007)

Figure 6 Depositional system and reworking. From Gennaro (2011)

Figure 7. Different reworking and depositional features present in the chalk. From Gennaro (2011)

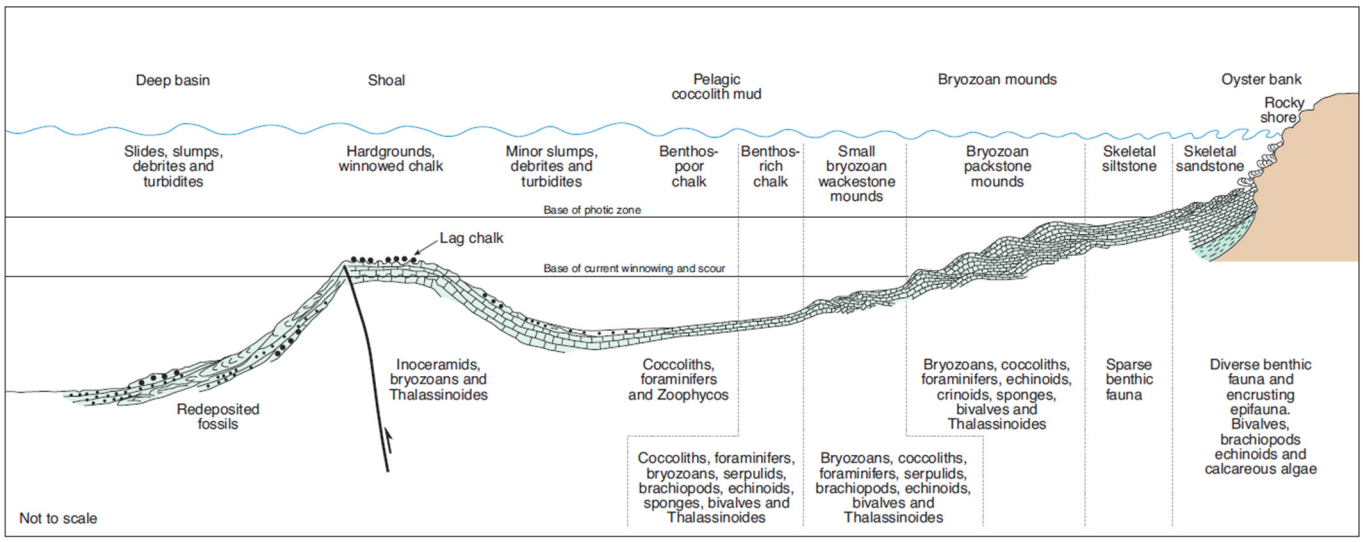

Figure 8. Different facies expression of chalk with proximity to the coast and water-depth. Model from Evans et al, (2003).

3. Material and methods

3.1 Focus Area

The focus area of this thesis was the Schill Grund Platform. The main reason for the focus on this area is the completeness of the stratigraphic record. Van der Molen (2004) subdivided the Chalk Group into 11 seismic sequences (CK1 to CK11). These seismic sequences include the whole Chalk Group spanning from the Cenomanian (CK1) to Danian (CK11). Van der Molen (2004) created maps, which indicated the areal extent thickness and seismic character of the different seismic sequences. The CK seismic sequence coverage maps were simplified and stacked on top of each other to arrive at figure 9, which indicates where the stratigraphy is complete. Three areas have a complete Cenomanian to Danian stratigraphy. These areas are the Winterton high, Central Offshore Platform-Vlieland Basin and the Schill Grund Platform. Of the three areas, the Schill Grund Platform has the largest areal extent and the most data available (well-logs, biostratigraphy and seismic data, table 9, Figures 153 and 154). Another factor favouring the decision towards the Schill Grund Platform was the unique history of this area. The area has been a stable structural high since the early Carboniferous (Geluk et al., 2007). The absence of thick Permian or Triassic salt packages in combination with relative minor tectonic movement during the rifting phases prevented the large-scale mobilization of salt and thus created a relative flat topography on which the Chalk Group could be deposited. The stable subsidence regime in the late Cretaceous created a virtually complete stratigraphy in contrast to other areas of the Dutch offshore, which were heavily impacted by multiple inversion phases.

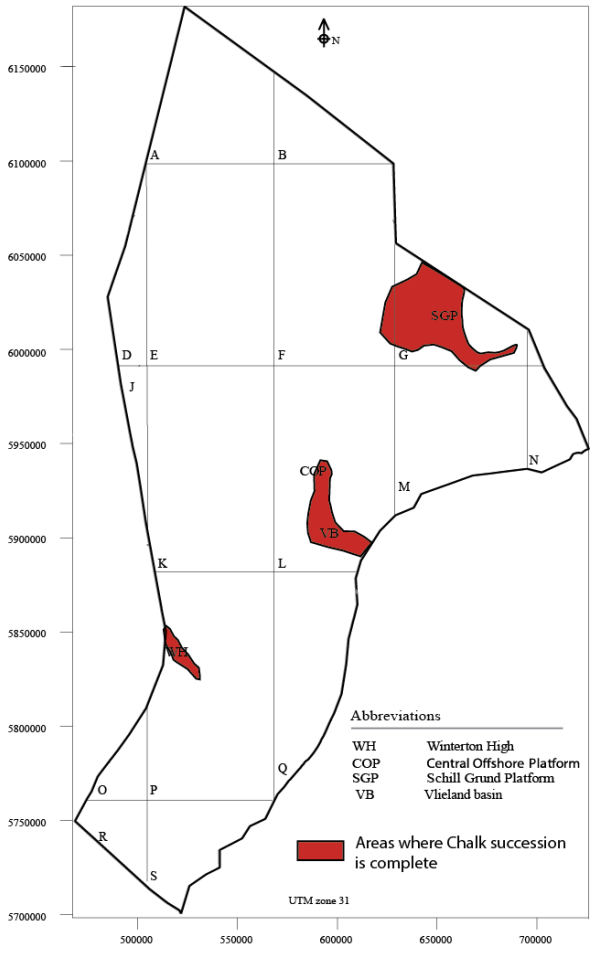

Figure 9. Locations according to van der Molen (2004) *where seismic sequences CK1 to CK11 are all present (i.e. where the Chalk Group succession is most complete.)Modified from* van der Molen (2004)

3.2 Dataset

The dataset consists of well-logs, checkshots, well reports, (bio)stratigraphy reports, cores, 3D seismic cubes, 2D seismic lines and vertical seismic profiles (VSP)'s. For locations of the used well and seismics see S.I. 10.18.1 and S.I. 10.18.3 for figures 153 and 154. See S.I. 10.18.2 table 9 for a table with all the wells with their available well-logs, biostratigraphy and processing techniques which were used on these records. The existence of orbital cycles in the well logs was investigated using spectral analysis (Blackman Tuckey, Redfit, MTM and EHA analysis) and the sedimentation rate was calculated using the eASM function in R statistics. The 3D and 2D seismics was used for well to well correlation and look for the potential existence of longer time-scale Milankovitch cycles in the seismic trace patterns. (Bio)stratigraphic data was used to provide age constraints in the form of the K/Pg boundary and other stage boundaries. The seismic data was depth converted with the help of TNO's velmod-2. The time-depth relationship was quality checked with help of seismic to well ties. The discovered Milankovitch cycles were identified and tied to the well-logs and seismics to investigate the completeness of the stratigraphic record, which could provide a possible connection to the CK sequences of van der Molen (2004). For the handling of the seismic and well-log data the Petrel 2014, R statistics, ARDI executor Analyseries and Past software packages were.

3.2.1 Well-data and well reports

The gamma ray (GR) and sonic travel time/slowness (DT) logs were the main petrophysical measurements used in this study. The gamma ray log measurements are available for almost every well and could be used for a relatively straightforward facies and climate interpretation. The sonic log is an important log for coupling the well-logs to seismic dataset. Density (RHOB, DRHO), Porosity (NPHI), and Spectral gamma ray records were used when they could provide additional insights. Checkshot data was used to establish a time-depth relationship and the deviation files were used to give the wells their curvature. Well reports were mainly used for their biostratigraphic information and to check for anomalies found in the dataset. Composite well-logs were also used to check for anomalies in the datasets.

3.2.1.1 Well-log resolution

Worthington (1990) created the log association parameter (LAP), which is a non-dimensional factor which indicates if the well-log resolution is sufficiently high for a cycle to be registered by a logging tool. Table 3 was created using the LAP formula (equation 1), Figure 12 and Table 4. Table 3 shows the minimum sedimentation rates for each orbital cycle and the minimum cycle length of any cycle to be registered by the different logging tools.

LAP= log association parameter

LAP quantifies if a given cycle can be detected in a log

$$LAP = \left(\frac{s * \tau}{2 * h}\right) * 10^{-6}$$

s= sedimentation rate (m Ma^-1)

τ= cyclic period (years)

h= log sensitivity (m)

LAP > 1 implies good cyclic resolution of the targeted periodicity

LAP = 1 implies critical resolution

LAP < 1 implies unresolved cyclicity

Equation 1. Log association parameter input parameters and formula

Table 3 data from Worthington (1990)			
	Tool intrinsic resolution (m)	Log sensitivity (m)	Log parametric resolution (m)
Gamma ray	0.2-0.3	0.3-0.4	0.6-0.75
Density	0.4	0.25-0.3	0.45-0.6
Induction	2.1-2.4	0.75-0.9	1.2-1.5 (conductive beds) 10 (resistive beds)

Table 3. Resolution and sensitivity of Gamma ray, Density and Induction.

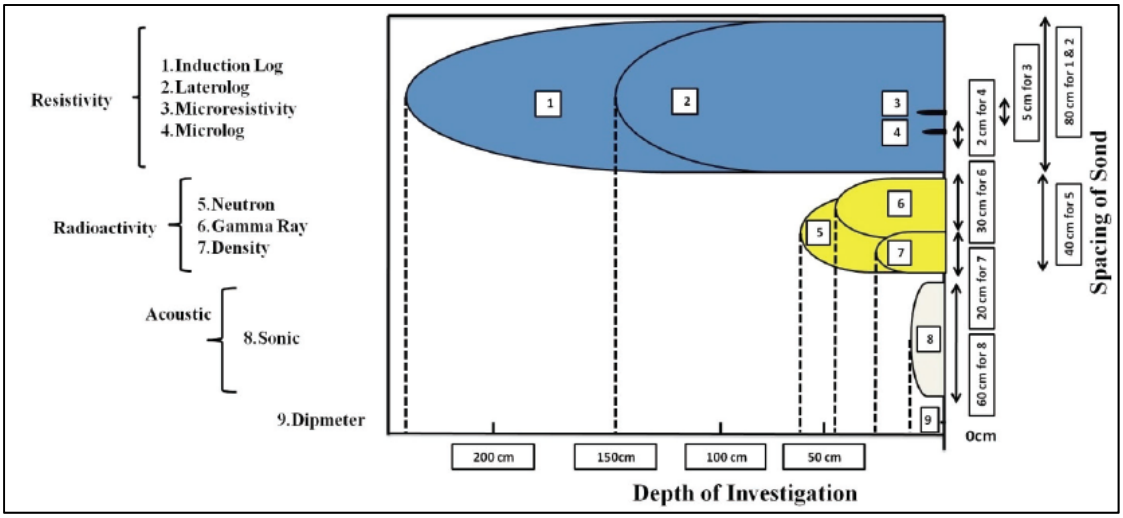

Figure 12. Depth of investigation and spacing of receiver (log sensitivity (m)). From Darling (2005)

Table 4.	Precession	Obliquity	100-kyr ecc.	405-kyr ecc.	
	min sedrate mm/kyr	min sedrate mm/kyr	min sedrate mm/kyr	min sedrate mm/kyr	min cycle length (m)
dipmeter	0	0	0	0	0
sonic	120	60	24	5.93	2.4
density	40	20	8	0.20	0.8
gamma ray	60	30	12	0.30	1.2
neutron	80	40	16	0.40	1.6
induction log	160	80	32	0.79	3.2
laterolog	160	80	32	0.79	3.2
microresistivity	10	5	2	0.05	0.2
microlog	4	2	0.8	0.02	0.08

Table 4. Minimal sedimentation rate required for different cycles to be registered by different petrophysical measurements and minimal length of any cycle to be registered by different petrophysical measurements.

3.2.2 Gamma ray log

A gamma ray logging tool measures the natural gamma rays emitted by the radioactive isotopes of uranium, thorium and potassium (Ellis and Singer, 2007; Serra, 1984). The gamma ray signal is standardized to GRAPI = 8*238Uppm + 4*232Thppm + 16*39K% (Ellis and Singer, 2007). For the gamma ray log a base level background radiation was interpreted as pure carbonate deposition (around ~5-10 API units). Spikes in the gamma ray log were interpreted as being enrichened in either organic or detrital material (Ellis and Singer, 2007; Serra, 1984). To estimate the shale content the Gamma-ray was converted to Vshale (shale percentage) (Vshale=((GR shale-GR)/(GR shale-GR Shale minimum))*100) (Ellis and Singer, 2007). The Vshale itself was corrected with the Larionov (1969) Mesozoic rocks correction function (Larionov, 1969). For the Chalk Group of the Schill Grund Platform the percentage of shale varies between 2% and 20%.

3.2.3 Sonic

The sonic log measures the time it takes a sound wave to travel through the rock from the transmitter to two or more receivers (Ellis and Singer, 2007; Serra, 1984). The path the wave takes is influenced by Snell's law while the speed of the wave through a medium is governed by elastic properties of the rock/fluid mixture and its density embodied in the Wood-Biot-Gassman equations. The P-wave velocity through a clean carbonate is much higher than through clays and shales (Mavko, 2005). The shale content is the main factor governing the expression of the sonic log, because the two main constituents of the chalk are carbonate and shale.

3.2.4 Porosity

The main log used to estimate the porosity is based on the neutron log. The adsorption of neutrons by a formation correlates to the hydrogen content of a rock because neutron slow-down is most effective by hydrogen atoms (Serra, 1984). The incoming signal at the detector is therefore the inverse of the hydrogen content (hydrogen index) of the formation. The neutron log was used as a tool to estimate the porosity, because hydrogen is mainly present as pore waters. No hydrocarbons are present in the Chalk Group on the Schill Grund Platform and the shale content of the Chalk Group is low and thus hydrogen atoms will only be present as water in the pore space.

3.2.5 Seismic data

The seismic dataset consists of 3D-seismic cubes 2D lines and VSP's (provided by TNO). Most of the 3D seismic cubes are in the North Sea (European) zero phase convention and this polarity convention was consequently used in this thesis. In the North Sea (European) zero phase normal polarity convention an increase in impedance is represented as a negative amplitude (blue in Petrel default seismic display setting) and a decrease in impedance is represented as a positive

amplitude (red in Petrel default seismic display setting). The North Sea zero phase polarity was checked for all the seismic data and when needed the phase of the seismic data was shifted to closer resemble North Sea (European) zero phase. VSP surveys were used to further investigate the tie in between the well-logs and the seismic signal. Surfaces indicating the bottom of different stratigraphic groups in the Dutch subsurface are also available in TWT and TVD at http://www.nlog.nl. For a map with all the used 2D and 3D seismic data see S.I. 10.18.3 figure 154.

3.2.5.1 Seismic resolution

The maximum vertical resolution of seismic data is ¼ of the seismic wavelength (Nanda, 2016; Sheriff and Geldart, 1995). The wavelength could be calculated from with help of the formulae; Wavelength =Velocity/frequency (Nanda, 2016; Sheriff and Geldart, 1995). The interval velocity of the Chalk Group on the Schill Grund Platforms is ~3900m/s (Figure 10). The frequency in Hz was acquired with the help of the Petrel inspector option, which gives the spectrum of the seismic data at a specific location on a seismic line (see Figure 11). A quick investigation showed that all the seismic cubes on the Schill Grund Platform have similar spectra for the Chalk Group. The Chalk Group on the Schill Grund Platform has a maximum frequency of ~65Hz and a minimum frequency of ~12.5Hz, which results in a maximum vertical resolution of (3900(m/s)/65(Hz))/4=~15m and a minimum vertical resolution of 3900(m/s)/12.5(Hz)≈310m.

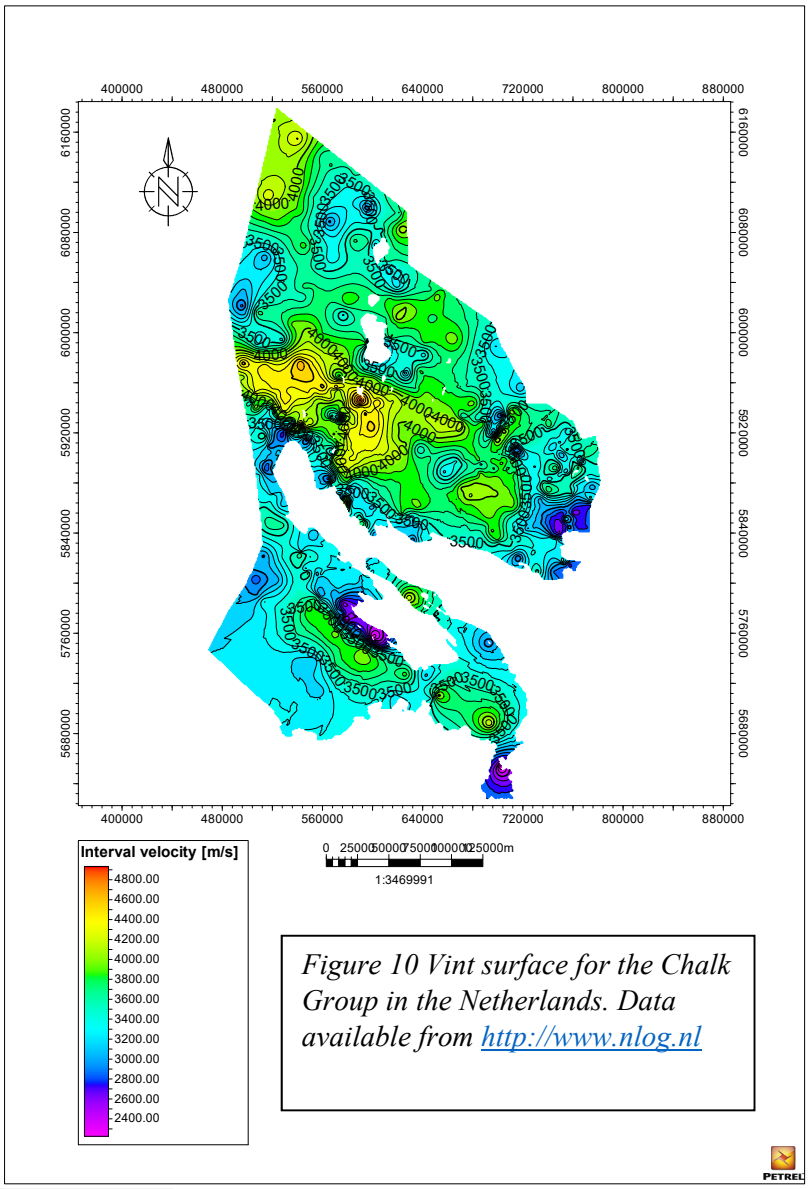

Figure 10 Vint surface for the Chalk Group in the Netherlands. Data available from http://www.nlog.nl

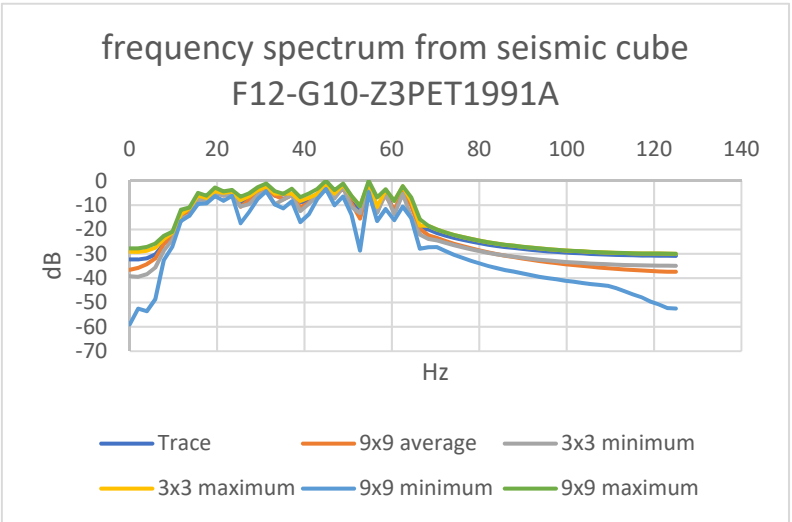

Figure 11 seismic point spectrum from the Chalk Group interval from seismic cube F12-G10-Z3PET1991A

3.2.5.2 Velmod-2

The Velmod-2 velocity model consists of velocity and depth (TVD and TWT) surfaces made by TNO (van Dalfsen et al., 2007) (available on http://www.nlog.nl). This model gives accurate depth predictions for the tops and bottoms of different zones, but internal velocity differences were not accounted for. A trend in which the velocity decreases towards the top of the Chalk Group could be identified in the sonic logs. This trend could be attributed to the compaction/reduction of porosity of the sediment at greater depths (Van der Molen, 2004). The interval velocity distribution caused reflector thickness to be overestimated for the top of the Chalk Group while the thickness of reflectors was underestimated for the Chalk Group. The seismic reflector thickness difference is one of the caveats of the internal velocity surface velocity model and could only be solved by creating a V0*K model. Creating a new V0*K model for the Dutch offshore was beyond the scope of this thesis. The 3D seismic cubes were time-depth converted using TNO velmod-2 and an additional correction was applied with the help of well tops.

3.2.5.3 Seismic to well tie

The seismic to well tie option in Petrel enables a coupling between the well-logs and the seismic data and enables the extraction of traces (for trace extraction process see S.I. 10.15*)*. A synthetic log created from the sonic log in the North Sea normal polarity scheme indicates that the steepest part of a slope has the largest impedance contrast and thus a peak or through was created in the seismic signal (Figure 13). A positive slope indicates a decrease in the impedance while a negative slope indicates a decrease in the impedance. With a zero phase North Sea normal polarity this means that where the slope is negative there is a negative reflector (Blue reflector in Petrel standard colour scheme) and when the slope is positive there is a positive reflector (Red reflector Petrel standard colour scheme). A peak in the gamma ray and sonic logs thus corresponds to an S-crossing in the seismic record and a through in the logs corresponds to an Z-Crossing (see figure 13). Peaks in the sonic and gamma ray log represent minima or maxima in the orbital cycles and thus it was important to keep in mind that not the peaks or throughs in the seismic record represent peaks in the orbital cycles but the S and Z-crossings do.

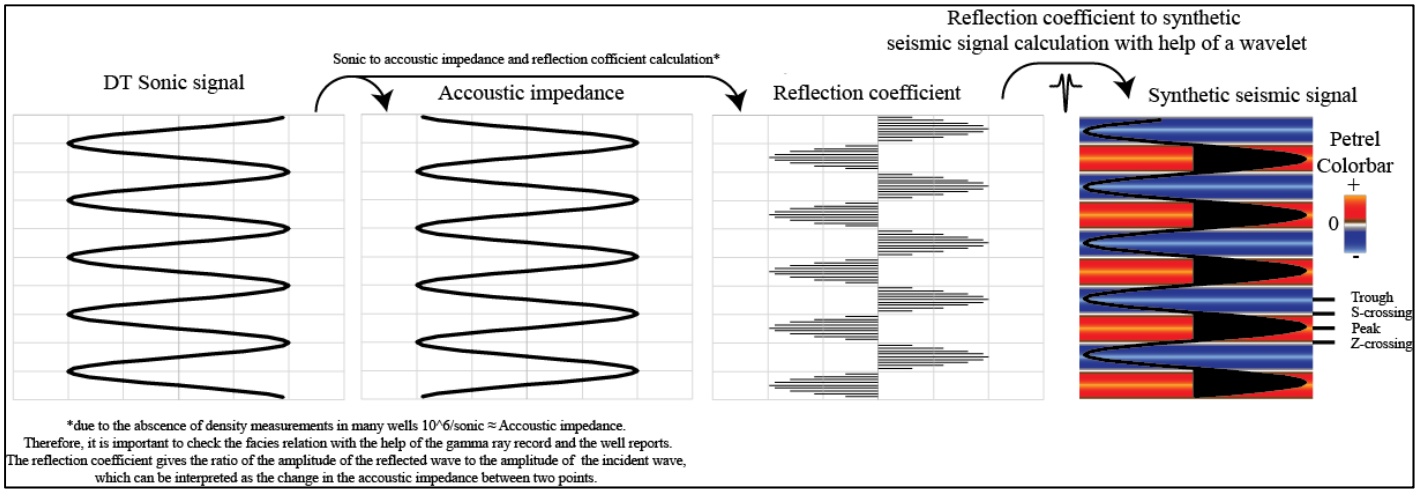

Figure 13. Schematic seismic to well tie

3.2.6 XRF and core plug data

The XRF measurements were conducted with a handheld Thermo Scientific Niton XL3t X-ray Fluorescence analyser (borrowed from palaeomagnetic lab Fort Hoofddijk Utrecht University) on the core of well A12-02 at the TNO core repository at Zeist in December 2016. The XRF analyser was set on soil mode with the filters main and low selected. Soil mode with the selected filters measured the elements; Mn, Fe, Co, Ni, Cu, Zn, As, Se, Rb, Zr, Mo, W, Au, Hg, Pb, Sr Th, U S, K, Ca, Sc, V, Ti and Cr. The filters were each used for a specific amount of time: main 20 seconds and low 30 seconds. The measuring interval was ~30 cm and was measured near previously sampled core-plugs on which porosity and permeability measurements were conducted by the NAM in 1983 (http://www.nlog.nl). The measuring position near the core plug locations makes a comparison between the XRF measurements and the previously measured porosity and permeability values more straightforward and reliable. A total of 169 measurements were conducted

including a measurement of the standard NIST2780 every ~15 measurements. The standard was measured to rule out possible erroneous deviations in the measurements. The results of the XRF analysis were in relative concentrations of the different elements converted parts per million (ppm) with an error value. Measurements lower than the error of 2σ were automatically excluded by the Thermo Scientific Niton XL3t X-ray Fluorescence analyser. The samples and core plug measurements were resampled in R statistics at an 0.1m interval so that the data could be directly compared to the well-log data (GR, DT, Sonic derived density and (neutron) porosity) of well A12-02

3.2.7 Core material

Core material from wells A12-02, A18-02 and F06-02 was inspected at the TNO core-repository in Zeist (December 2016). Core photos are also available for the cores from wells A12-02, A18-02 and F06-02 (http://www.nlog.nl). The cores of wells A18-02 and F06-02 were of inferior quality so only core A12-02 was studied in more detail. The core from well A12-02 was inspected as part of the Biostratigraphy and XRF study. The core covers ~45 metres of stratigraphy and is virtually complete. The core spans from the top part of the Ommelanden Formation to the bottom part of the Ekofisk Formation. Latest Cretaceous to early Danian ages were expected based on well-tops and well-reports. The visual inspection and core photos enabled a detailed study of features such as chert nodules, colour, laminations, bioturbation and stylolites, which were not observed in the well-logs.

3.3 Software

3.3.1 Petrel

The Petrel software platform was used to visualize, process, and interpret the geophysical and petrophysical data. Petrel was used to convert the seismic data from the time to the depth domain, which was done using the velmod-2 velocity model of TNO. Seismic to well ties were used as a quality check on the time-depth relationship. The bandpass filtered data series was displayed in Petrel to compare them to the unfiltered data-series and the seismic data. The 3D-seismics were in turn frequency filtered to highlight a possible coupling of well-log parameters to the seismic data set. The seismic trace data was extracted from the well-trajectory using the seismic to well tie option and frequency analysis was performed on the extracted data and the dominant frequencies were filtered and evaluated. Seismic attributes were used to identify redeposition features such as slumps, channels and pockmarks in the Chalk Group (S.I. 10.3).

3.3.2 R statistics

Astrochron (Meyers, 2014) was the main package used within the R software suite. The evolutive harmonic analysis (EHA) command was used to identify orbital frequencies. The evolutive Average Spectral Misfit (eASM) command was used to calculate the optimal sedimentation rate by comparing the ratios between the spectral peaks in the depth domain and predetermined astronomical cycles. The track frequency function was used to transform EHA spectra into a sedimentation rate curve. With the help of the sedimentation rate the depth domain could be converted to the time-domain. The bandpass filter was used to filter frequencies in the time and depth domain.

3.3.3 Analyseries

Initial cyclostratigraphic analysis was conducted using the Blackman-Tukey spectral analysis of Analyseries (Paillard et al., 1996). The main use of the Blackman-Tukey analysis was to make a quick assessment of the spectral characteristics of different records.

3.3.4 Past

The Past toolkit was used to create periodograms following the Redfit spectral analysis method (Schulz and Mudelsee, 2002). The Past toolkit also created confidence intervals for the Redfit periodograms. The confidence intervals were used to give a statistical significance to spectral peaks. The confidence intervals are based on the chi-squared statistical test. The chi-squared test is based on a theoretical spectrum of the red noise. The Chi-squared confidence values are based on the AR1 model which consists, of 1000 Monte Carlo simulations of the red noise signal.

3.3.5 SSA-MTM toolkit

The SSA-MTM toolkit (Ghil et al., 2002) of the University of California, Los Angeles was used to conduct spectral analysis using the Multitaper Method. The MTM-Toolkit also calculates confidence intervals, which gives statistical significance to the spectral peaks.

4. Results

4.1 Seismic to well tie

Multiple synthetic to well tie studies were performed to check the time-depth relationship and the relation between the well-logs and the seismic signal (see S.I. 10.18.2 table 9). The seismic to well tie does contain a few issues. The first issue is the establishment of a time-depth relationship for the wells (seismic time (TWT)). There were only checkshot surveys available for wells G10-02, G10-01 and G14-05. All other well have a time-depth relationship based on the sonic log. To check the validity of the time-depth relationship the TWT surfaces of Formation/Group boundaries were compared to the corresponding well-tops in the wells (TWT surfaces available at http://www.nlog.nl). Wells in which the time-depth relationships were deemed satisfactory were further used for the seismic to well tie. Shifting the time-depth relationship in synthetic seismics did not significantly improve the overall time-depth relationship and was therefore not used in the seismic to well ties in this study. Most of the wells do not have a density record for the Chalk Group, which hinders the calculation of absolute values for the acoustic impedance. The result of the non-absolute acoustic impedance value does have an influence on the reflection coefficient, because in the ideal scenario both density and the sonic logs are accounted for. Even though the density records are missing the sonic (DT) record still has a good correlation with the seismic data (Figure 14). The gamma ray log (GR) has a weaker correlation to the seismic data. For the seismic to well ties in the time-depth converted seismic data, there is an over-estimation of the thickness of layers/reflectors at the top of the Chalk Group while at the bottom of the chalk the layers/thickness of the reflectors are underestimated. These over and underestimations were expected which is one of the caveats of the Velmod-2 model (chapter 3.2.5.2).

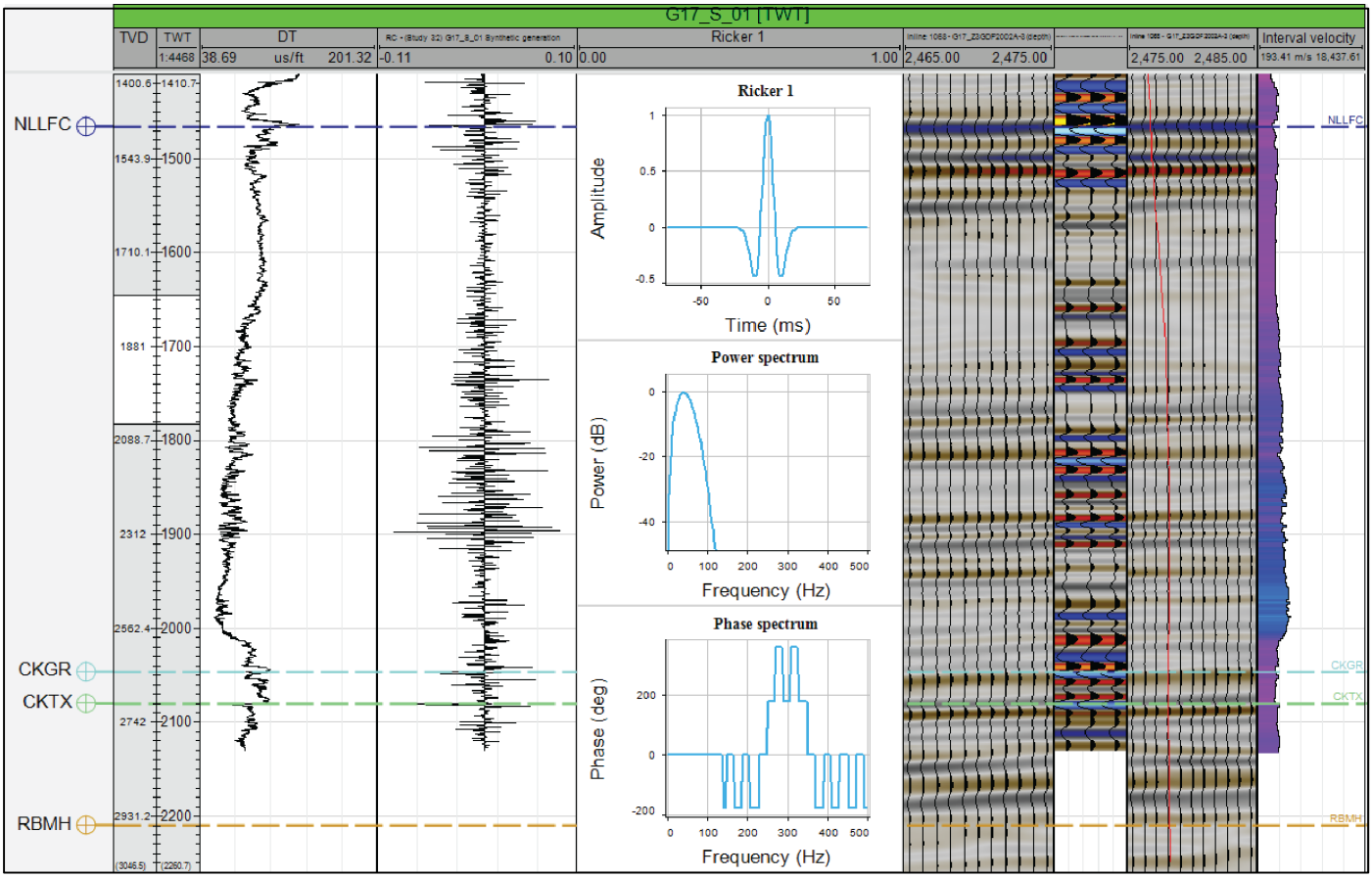

Figure 14. Synthetic well G17-S-01

4.2 Seismic signature of the K/Pg boundary

The K/Pg boundary is not distinct enough to be picked up by the logging tools and it thus does not generate a seismic reflector. If the stratigraphy is complete then biostratigraphy indicates that the K/Pg boundary is located at a S-wave crossing above the third peak below the top of the Chalk Group. In the Petrel standard colour scheme, the location of the K/Pg boundary is observed as a white line above the third red reflector of the Chalk Group (Figure 15). The location of the K/Pg within the seismic reflectors is constant and can be traced throughout the Northern Dutch offshore (for Schill Grund Platform see S.I. 10.14 Figure 126). When a section gets condensed the K/Pg boundary is located within a trough (red reflector in Petrel standard seismic colour scheme with zero phase European polarity). The shift from S-wave to trough can be seen in the seismic cross-section of wells F12-02 to F15-01 to G10-3 (see S.I. 10.14 Figure 125).

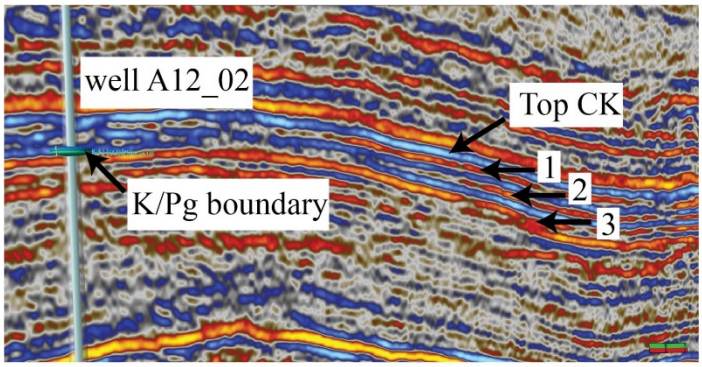

Figure 15. well A12-02 with location of the K/Pg boundary based on biostratigraphy. The Top CK reflector is based on a coupling between the seismic data and the well-logs. A sharp increase in the sonic and gamma ray readings indicated the transition from the Ekofisk Formation to the Lower North Sea group and subsequently indicated the Top CK reflector. Seismic data from seismic line

4.3 Petrophysical logs

4.3.1 Gamma ray

The Chalk Group shows a general trend in which the gamma ray values steadily increase inversely with depth (see Figure 16). This increase in the gamma ray signal can be attributed to a decrease in the carbonate productivity or an increase in sediment flux. If the general trend in the gamma ray log is linked to an increase in the background sediment flux, then the formula (increased sedimentation rate =100-(100-Vshale minimum) / (100-vshale /100)) can be used to give the percentage of increase in sedimentation rate. For example, well G10-02 has a ~12% increase in the sedimentation rate towards the top of Chalk Group. Similar percentages were calculated for other wells of the Schill Grund Platform. Superimposed on the general trend are multiple smaller and larger scale fluctuations. These fluctuations have range in period from mere metre scale fluctuations up to 15 to even 50 m fluctuations.

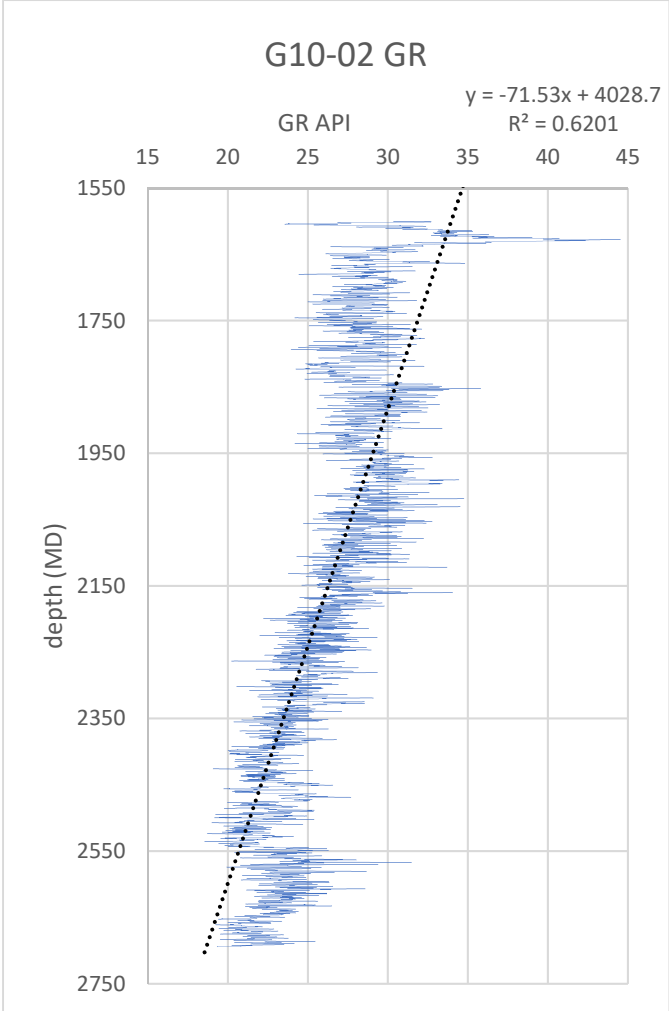

Figure 16. Well G10-02 GR record with trendline.

4.3.2 Sonic

When the sonic (DT) log is plotted against the gamma ray GR there is a positive correlation (Figure 17). The positive correlation is attributed to the fact that the shale content of the Chalk Group heavily influences both the GR and DT logs.

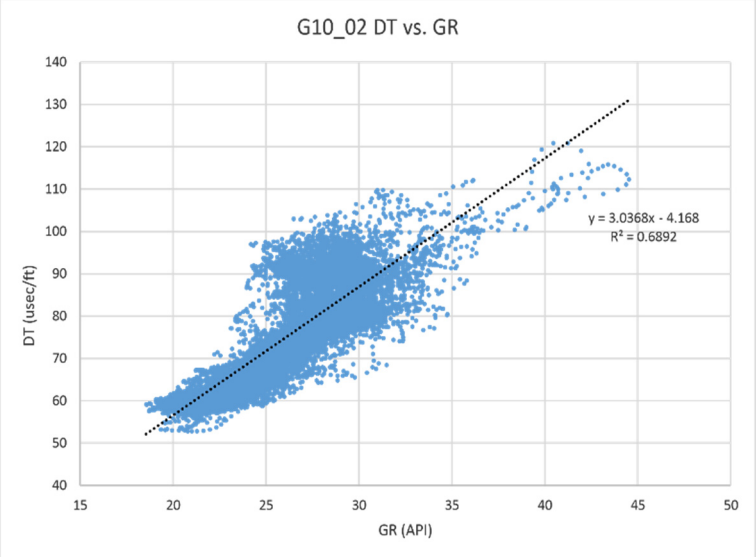

Figure 17. Well G10-02 sonic vs gamma ray with trendline

4.3.3 Sonic vs Density vs Vshale

The Sonic travel time was converted into Sonic derived density with the help of Gardener's relation (Gardener et al., 1974). This density record was compared to the available density logs. The density logs have similar values (±0.1 gr/cm^3) and is thus deemed accurate to be used. If the depositional system is assumed to be a 2-component system consisting of shale/clay and Chalk then the density can be approximated from Vshale with the formula Vshaledensity = ((100-Vshale) *density Calcite) + (Vshale*density shale). A comparison between these two derived densities shows a diverging trend (Figure 18). The Sonic derived density and Vshaledensity has a good fit at the bottom of the Chalk Group, but the Vshaledensity decreases only slightly towards top of the Chalk Group while the Sonic derived density decreases with a larger factor. The disparity between the Vshale density and (sonic) density is attributed to the general compaction trend which influences porosity and subsequently the density (Japsen, 1998; Van der Molen, 2004). A compaction factor = ((Vshaledensity-sonic derived density)/sonic derived density*100) was calculated to indicate the disparity between the two calculated densities. In well G10-02 the compaction factor at bottom of the Chalk Group is virtually zero, while at the top of the Chalk Group the compaction factor reaches more than 15%. Similar compaction factors were calculated for the other wells on the Schill Grund Platform. Superimposed on the general compaction trend are multiple smaller and larger scale fluctuations. These fluctuations have range in period from mere metre scale fluctuation to fluctuations up to 15 m to even 50 m.

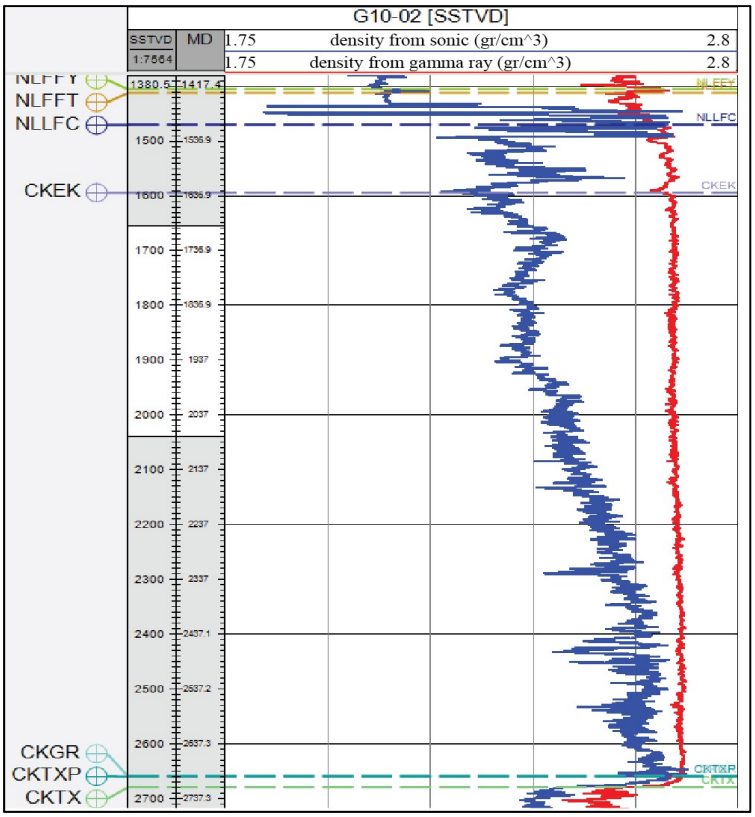

Figure 18. Well G10-02 Sonic density vs gamma ray density

4.3.4 Porosity

Neutron porosity will therefore approximate the true porosity. A clear correlation between the gamma ray and porosity can be seen in the lower part of the chalk while a diverging trend is seen towards the top of the Chalk Group (Figure 19). This relationship is also shown by cross plotting Vshale and porosity (Figure 20). There is a correlation between the porosity in the 1800-2381 m interval (Figure 20), but there is no clear correlation between the Vshale and the porosity in the 1800-1442 m interval (Figure 20). The non-correlation in the top part of the Chalk Group is due to the general compaction trend in the North Sea which influences the porosity of the Chalk Group (Japsen, 1998; Van der Molen, 2004). Superimposed on the diverging trend porosity also contains multiple smaller and larger scale fluctuations. These fluctuations have range in period from mere metre scale fluctuation to fluctuations up to 15 m to even 50 m.

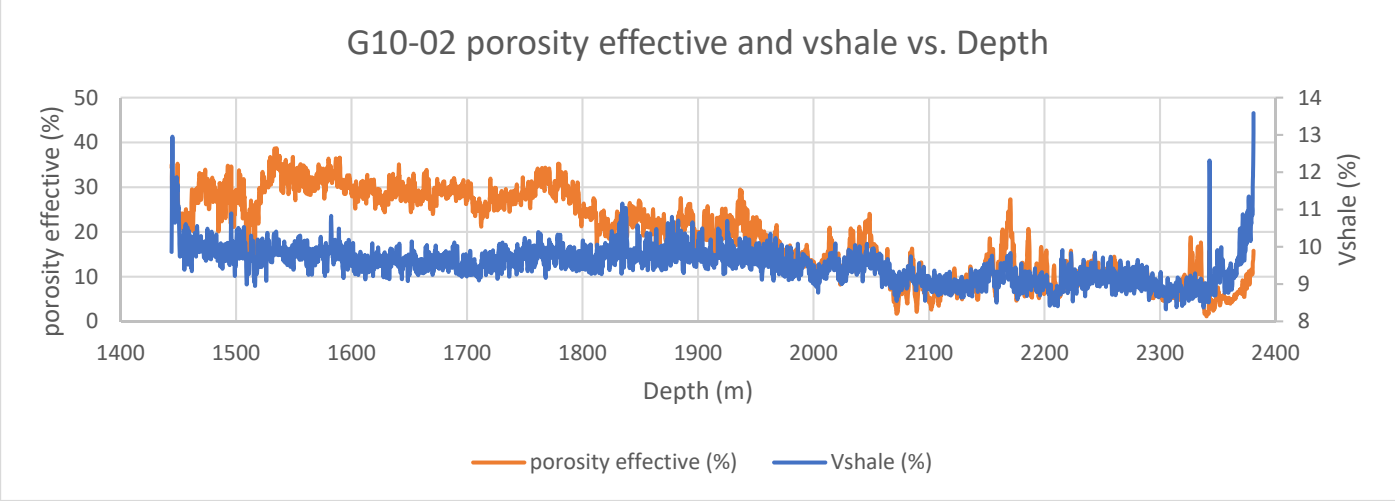

Figure 19. Porosity and Vshale plotted against depth

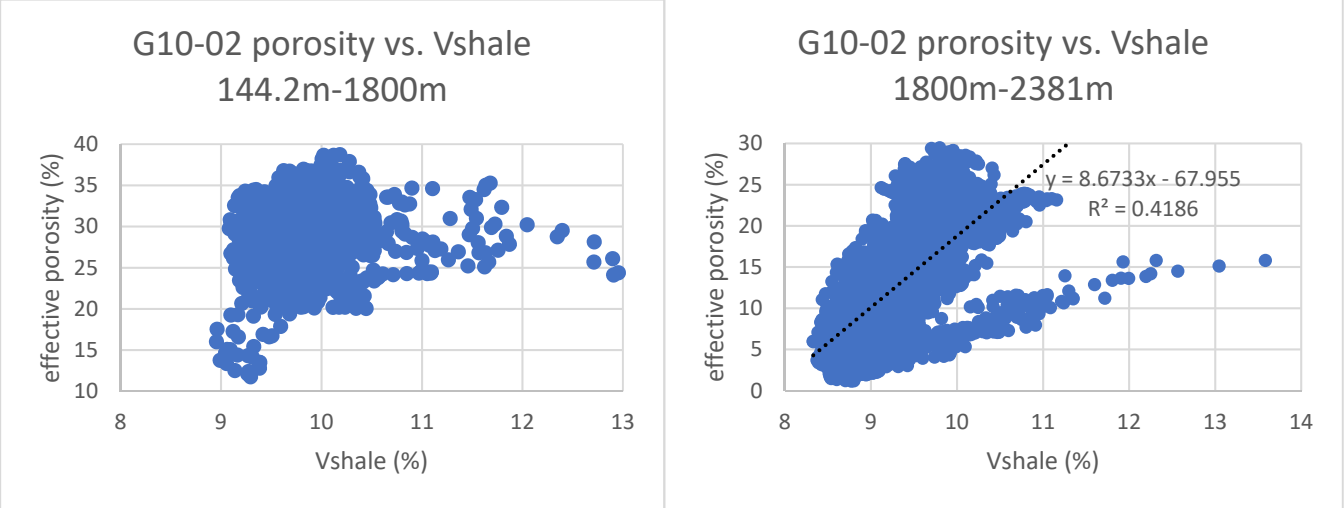

Figure 20. G10-02 Porosity Vshale cross plots, left plot G10-02 1442-1800m interval and right plot 1800-2381m interval. Note the deviation trendline from the general trendline in G10-02 porosity vs. Vshale 1800m-2381m.

4.3.5 Spectral gamma ray

For the Schill Grund Platform 3 wells with spectral gamma ray data are available (wells G14-A-02, G17-S-01 and G10-03). The data from well G10-03 are not used for this research, because the concentration of most of the uranium measurements was negative. The negative concentration of uranium is most likely a measuring error of the tool. G14-A-02, G17-S-01 do also contain negative uranium measurements, but most of the uranium measurements are positive and thus the data was considered accurate enough to be used. The negative values were replaced in Microsoft excel with a zero value. The gamma ray values were re-calculated using the formulae GRAPI = 8*238Uppm + 4*232Thppm + 16*39K% (Ellis and Singer, 2007).

The gamma ray signal can be interpreted as being the result of enrichment of either organic or detrital material (Ellis and Singer, 2007; Serra, 1984). Uranium can be interpreted as a proxy for TOC, suboxic, anoxic, sulphidic or reducing conditions, while potassium and thorium can be used as proxies for detrital input (Ellis and Singer, 2007; Serra, 1984; Stephen et al., 2007). The Th/K ratio is indicative of the type of clay mineral present (Schlumberger, 20013) and the Th/U ratio is indicative of redox conditions and proximity to the shoreline (Adams et al., 1958). Ellis and Singer (2007) indicate that there often is a positive correlation between clay minerals and thorium and potassium concentration while no correlation can be observed with uranium. The correlation between clay minerals and thorium is often larger, because potassium is also incorporated in non-clay minerals such as feldspars.

The source of the potassium signal often originates from potassium rich alkali feldspars and micas (Serra, 1984). During diagenetic alteration feldspars are dissolved and potassium is then transported in its ionic form. Micas can also release part of their potassium content during alteration to illite, montmorillonite and mixed layers I-M. Under temperate, humid conditions muscovite will dissolve and form kaolinite. Potassium ions are transported by rivers to the sea in humid regions, while in arid regions the potassium remain within the altered minerals. Potassium ions can be adsorbed to the surface of clay platelets get absorbed by plants and get incorporated in organic compounds.

In sedimentary rocks thorium is mainly contained in minerals, such as monazite and zircon, which are highly resistant to both chemical and physical alteration (Salminen et al., 2005). Any thorium released by weathering is often quickly adsorbed to clay minerals. According to Serra (1984) thorium can be found in three settings which are; adsorbed to clay platelets, in acidic igneous rocks such as cinerites and bentonites, in beach-sands and in fluvial sediments enriched in heavy minerals such as monazite, zircon and xenotime.

According to Serra (1984) there are 8 ways uranium can precipitate and accumulate in sediments. 1: in the presence of organic matter uranium is adsorbed form a uranyl solution. In the presence of organic matter and under acidic conditions Uh+ is reduced to U4+, which forms urano-organic complexes or chelates. Organic matter may also act as a reduce and convert UO+ into an insoluble quadrivalent ion. 2: Platy minerals adsorb uranium or platy minerals enable the formation of schoepite by hydrolysis of uranyl ions. 3: under reducing anaerobic environment bacteria reduce and precipitate uranium from a uranyl solution. 4: Uranium replaces calcium to create carbonate-fluorapatite. 5: under acidic conditions ($2.5 < pH < 4$) uranium will precipitate. 6: under reducing conditions ($0 > Eh > -400$ mV) uranium will precipitate. 7: uranium adsorbs to materials such as amorphous silica, alumina-(silicates) and coals under reducing environment. 8 : during diagenesis uranium, may also accumulate by adsorbing to clay particle or accumulate in phosphates, zircon, sphene, monazite, allanite, biotite, xenotime, sediments or in organic matter of humic origin (Serra, 1984). Uranium can also adsorb to coccolithophore platelets which further hinders the environmental interpretation for the element (Levin et al., 2015). Uranium can also be fixed in uranyl-tricarbonate during the formation of carbonate minerals (Adams et al., 1958).

The uranium, potassium and thorium values of both wells are cross plotted against its Vshale values (Figures 21 and 22). Thorium correlates positively to Vshale (Figure 21). Potassium also correlates positively to Vshale, but the data point spread around the trendline is larger than that of thorium (Figure 21). Uranium has no correlation in well G17-S-01, but in well G14-A-02 uranium has a positive correlation albeit is minor (Figure 21). The clay mineral composition can be deduced by plotting the thorium concentration against the potassium concentration, (Figure 22) (Schlumberger, 20013). The clay mineral composition of both wells is the same and consists of an assemblage of montmorillonite, illite, micas and glauconite. The thorium/potassium ratio was plotted against the thorium/uranium ratio to give the trend of the mineral composition against the origin of uranium (Figure 22) (Adams et al., 1958; Schlumberger, 20013). Both wells show a similar spread in which most of the data-points are within the fixed marine to shallow marine domain and

only a minor amount of data points is located within the continental-marine transition area and the leached continental area.

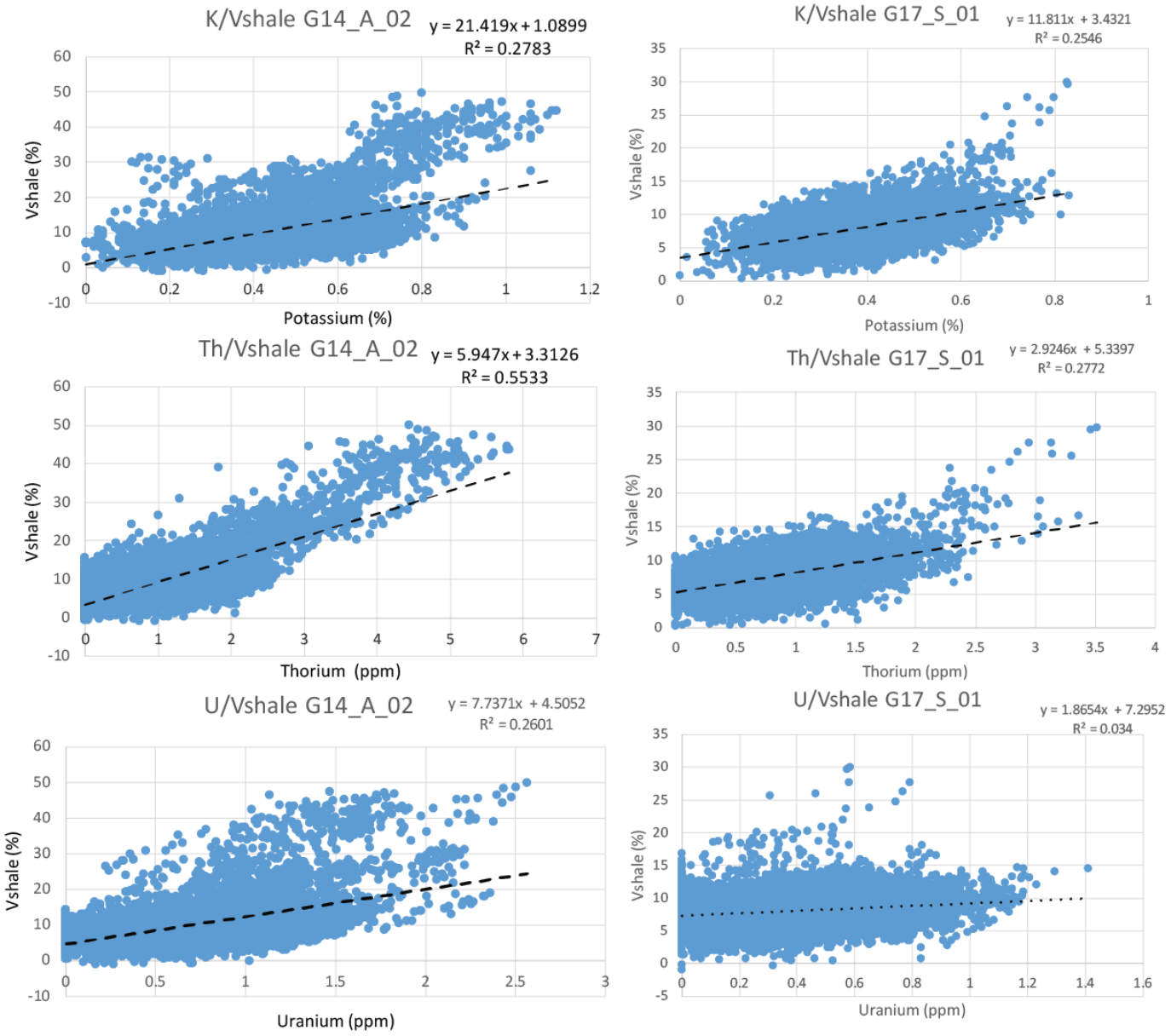

Figure 21. Cross plots spectral gamma ray wells G14-A-02 and G17-S-01

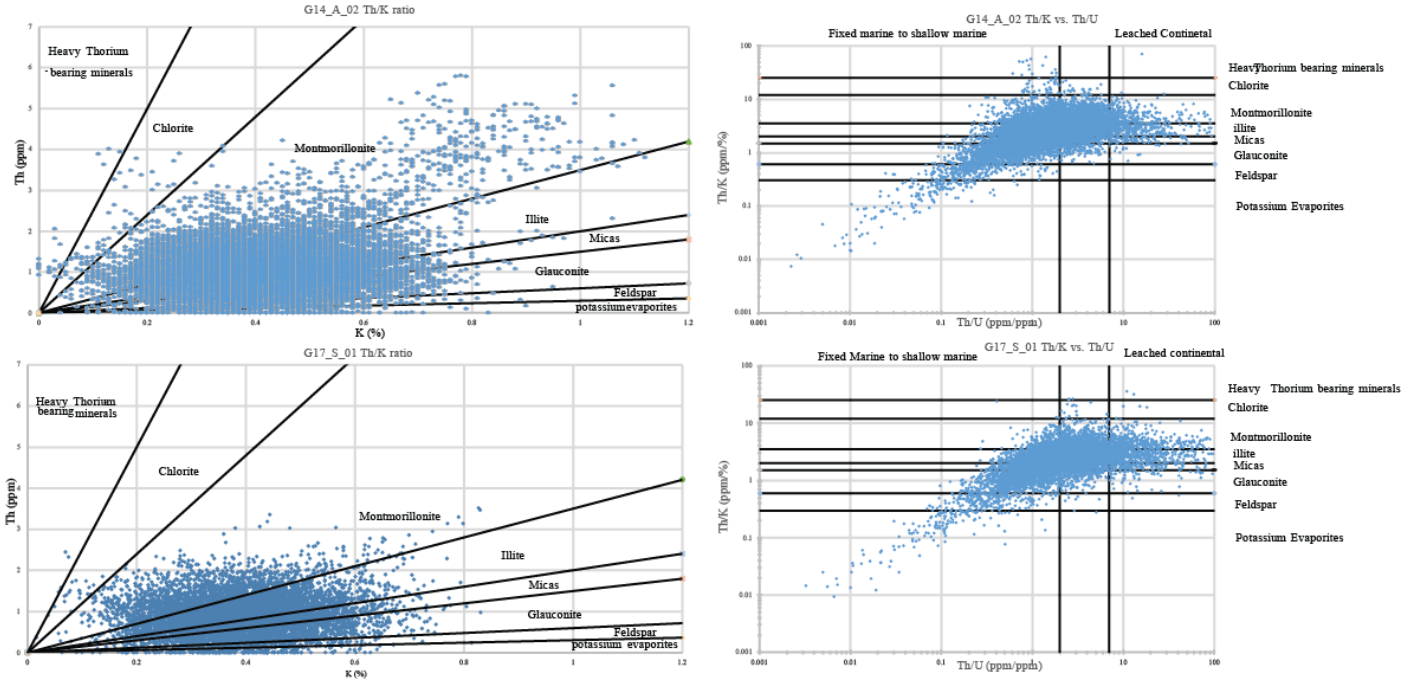

Figure 22. Left cross plot potassium (K) and thorium (Th). Right cross plots thorium/uranium (Th/U) to thorium/potassium (Th/K).

4.4 Seismic trace record

The seismic trace records were extracted from the seismic data using the Petrel seismic to well-tie option and converted from the time (seismic) to depth domain using sonic or checkshot data (for the instructions see S.I. 10.15). Figure 23 show sinusoidal fluctuations which are expected from a seismic trace record. The fluctuating patterns show multiple frequencies superimposed on top of each other.

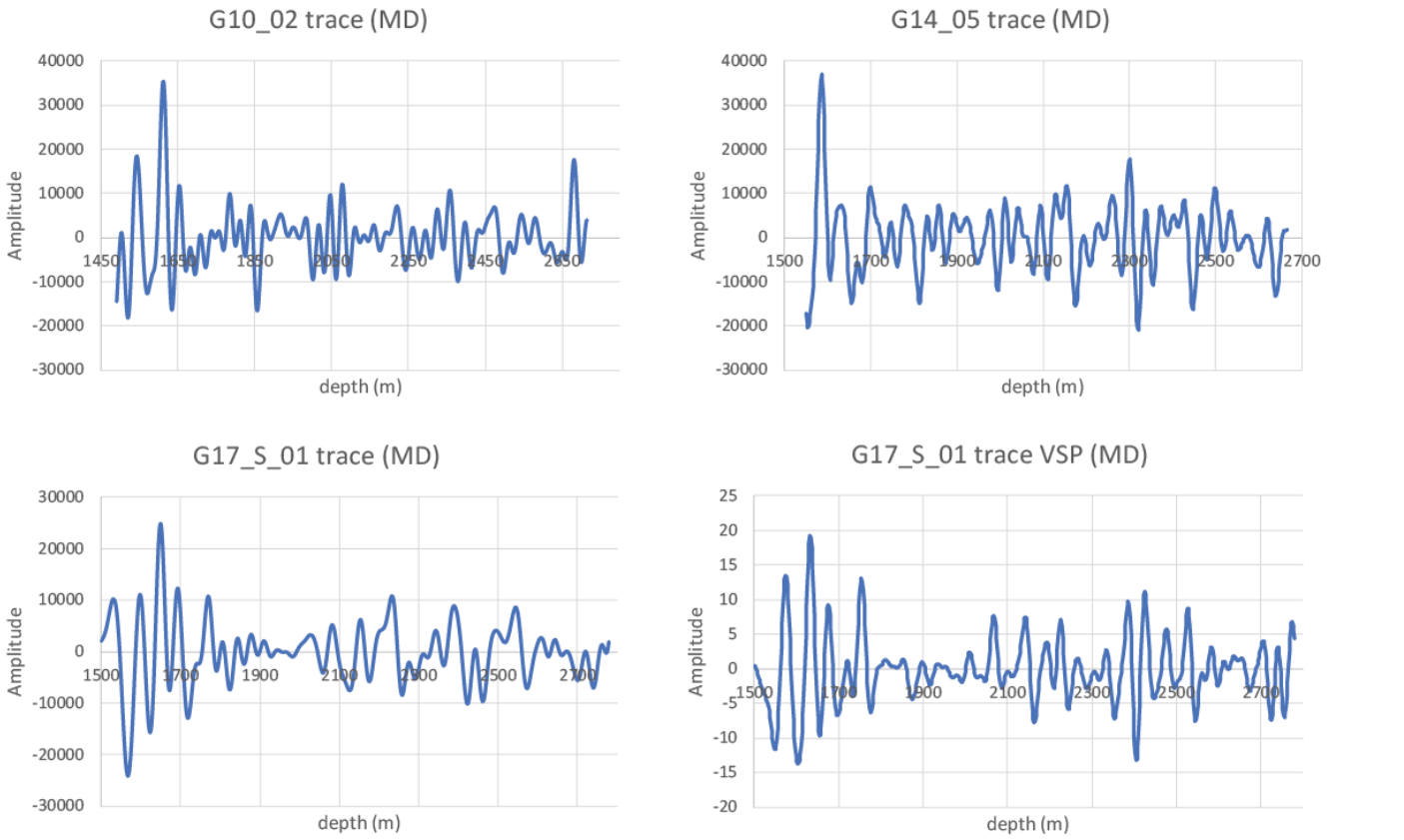

Figure 23. Seismic trace records of Chalk Group interval of well G10-02, G17-S-01 and G14-05. Trace G10_02 extracted from seismic survey F12_G10_Z3PET1991A. Trace G14-05 extracted from survey G13_G14_G17_Z3NAM1997A. Trace G17-S-01 from survey G17_Z3GDF2002A. Trace G17-S-01 trace VSP extracted from VSP NLOG_LIS_LAS_5023_g1705_20040714-4-01_G17-5-VSP_corzerophase

4.5 XRF and core plug data well A12-02

The interval of 2007.1 and 2052.5 MD of the core of well A12-02 was measured using a handheld XRF-scanner. Any data-point which were deemed too unreliable for an interpretation were excluded. Measurements with a marked iron-enrichment were excluded from the analyses because they probably reflect stylolite-rich intervals (Perdiou et al., 2015). The cross plots of As/S, S/Vshale, Rb/Vshale, S/Ca, Ca/Vshale, Rb/Sr vs Vshale, Ca/Mn, Mn/S, matrix density/Rb, Sonic derived density/NPHI, por.avg / Vshale, Por.avg/Rb and NPHI/Rb, RHOB/Rb, Ca/RHOB show a correlation (see Figures 24 and 25). For all the correlation coefficients between the measurements, see S.I. 10.2 Table 8.

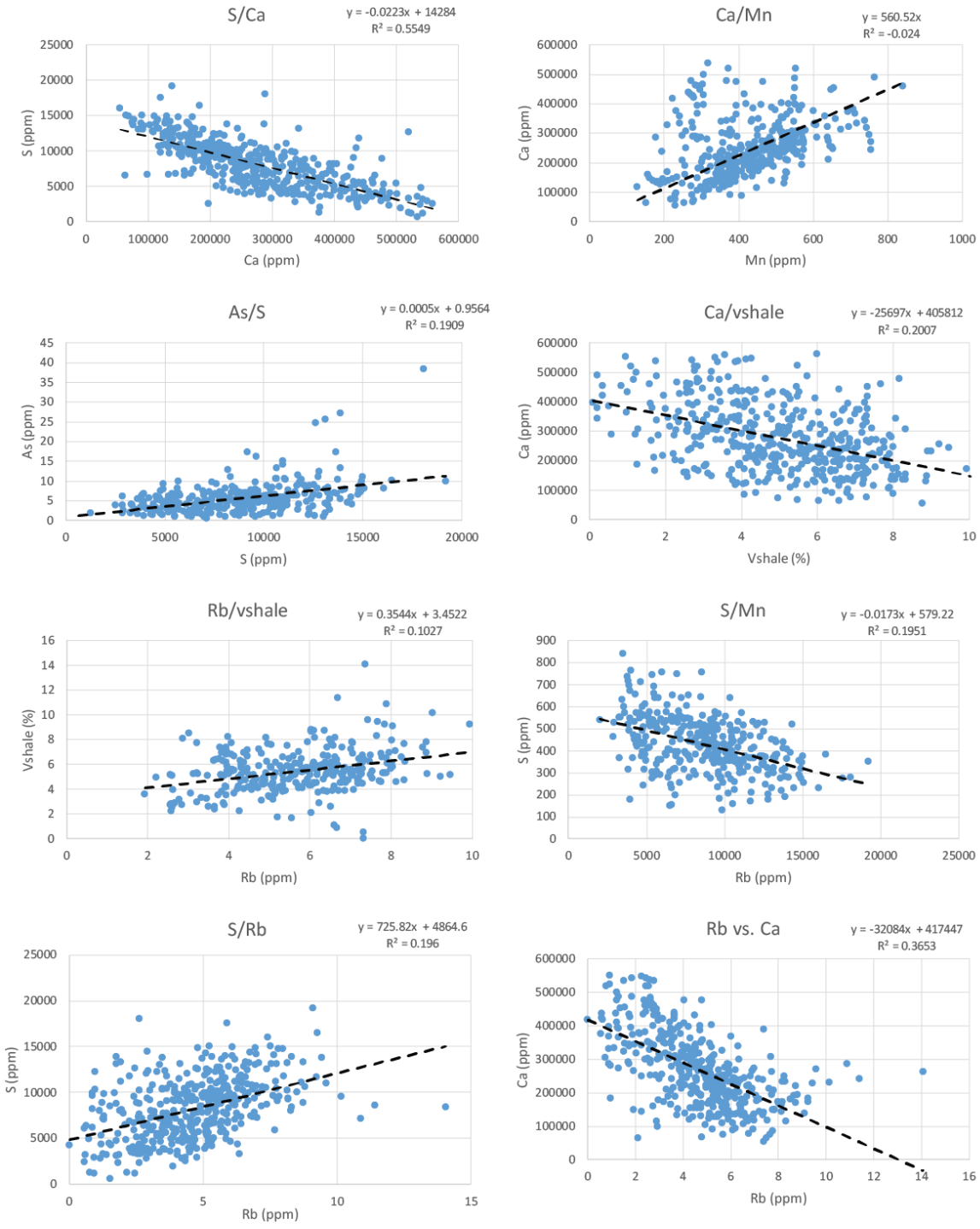

Figure 24. Cross plots XRF with trendline. From well A12-02 and depth interval 2007.1 and 2052.5 MD.

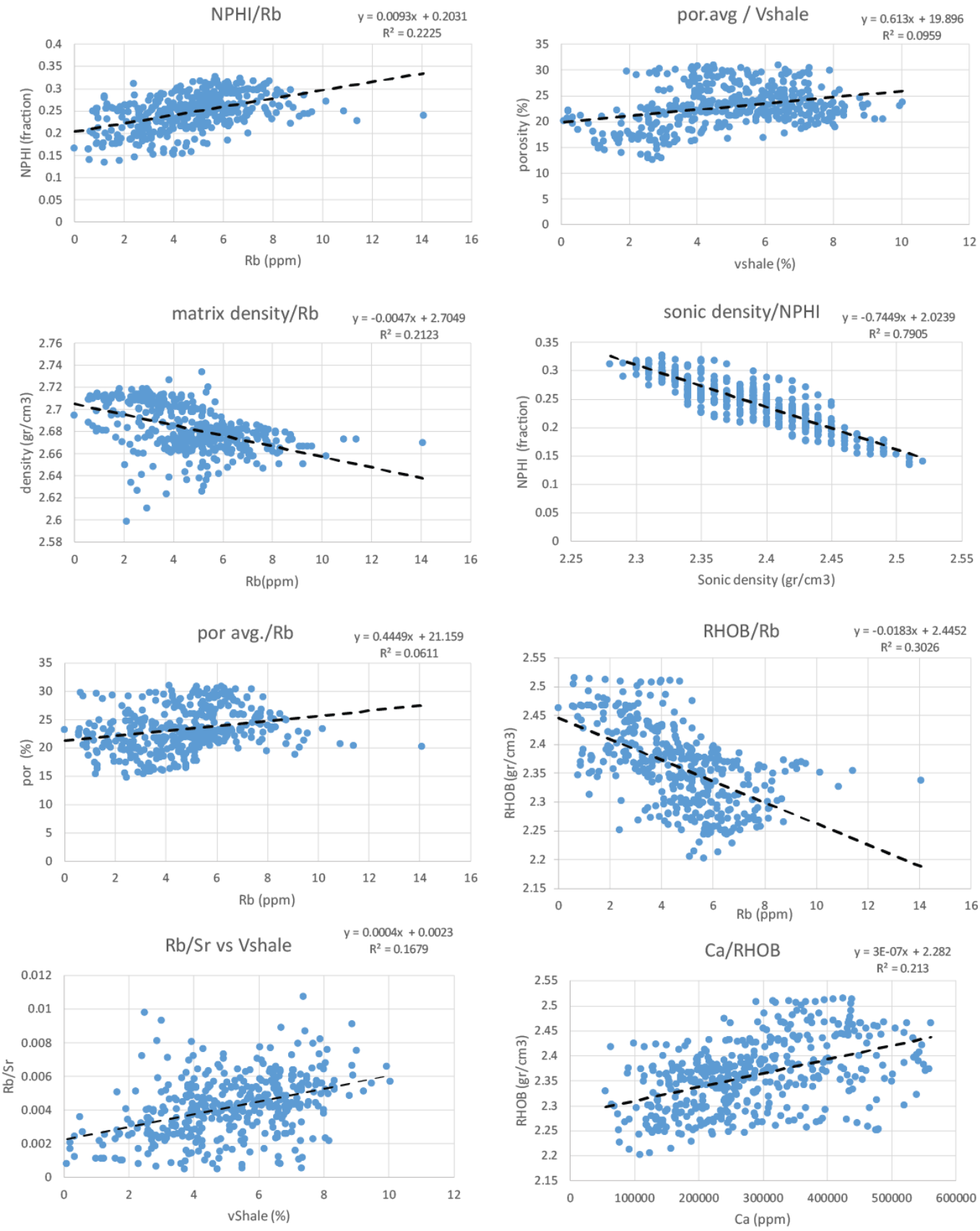

Figure 25. Cross plots XRF with trendline. From well A12-02 and depth interval 2007.1 and 2052.5 MD.

4.6 Sediment core of well A12-02

The core of well A12-02 shows a clear alternation between grey laminated chalks and white chalks (Figure 26). The alternation in colours most likely represents variations in the clay content. The grey layers are spaced at 50 to 90 cm. Figure 27 shows grey lines and blobs, which are interpreted as *Zoophycos* trace fossils (Zhang et al., 2015). Observations from the whole core indicates that the presence of *Zoophycos* is restricted to "clean" white chalk intervals. No distinct distribution pattern for the location of the flint layers was be observed (Figure 26 and 28). A pattern of jagged lines can be observed in Figure 29, which are interpreted as stylolites. The presence of stylolites is restricted to the "clean" white chalk intervals. The restricted occurrence of stylolites to the "clean" white chalks is also noted in the Chalk Group studies of Evans et al. (2003), Glennie (1998) and Maliva and Dickson (1992). Figure 30 shows a chalk clast within the grey chalk interval. The presence of such a clast indicates currents transporting the chalk. The observation of pyrite is restricted to the grey layers (see Figure 31,32 and 33). The perfect cube shape of the pyrite indicates that the pyrite was probably formed in-situ. Beside the presence of pyrite small nodules are also observed in the grey chalk intervals (see Figures 32 and 33). These nodules have a great resemblance to nodules found at the K/Pg boundary in Denmark which are identified as the outer walls of *Prasinophyte* green algae, which are covered in a pyrite crust (Hansen et al., 1986). In the paper of Hansen et al., (1986) the occurrence of the algae is restricted to the K/Pg boundary, but the nodules can be found in multiple grey layers within the core of well A12-02.

Figure 26. Shifts in colour between white and grey layers.

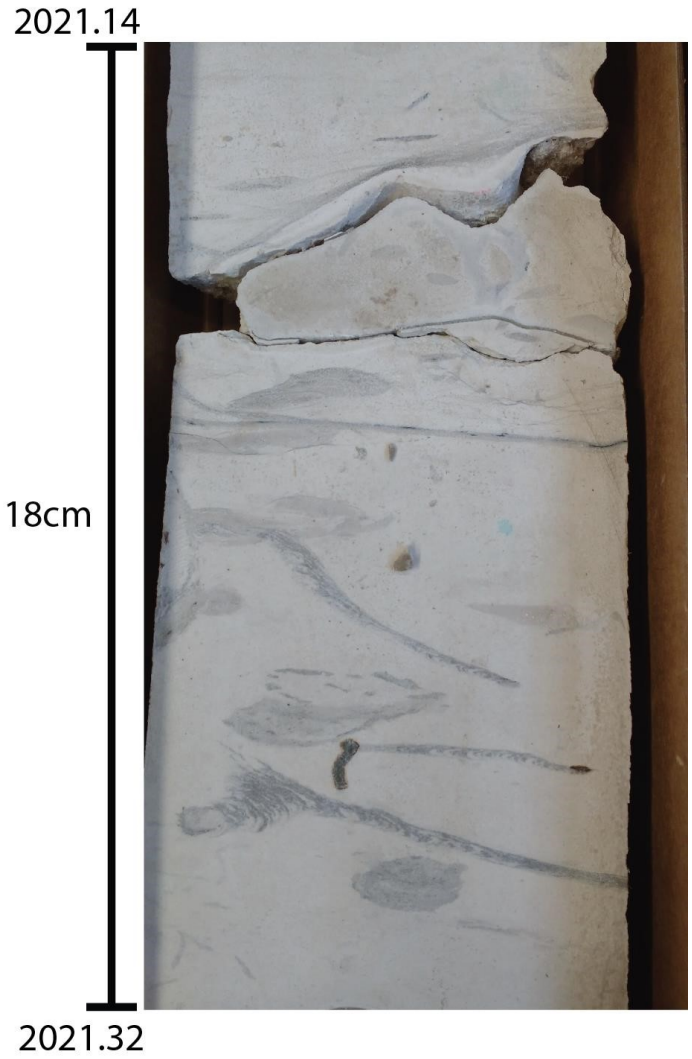

Figure 27. Zoophycos trace fossils. Left axis is depth in MD

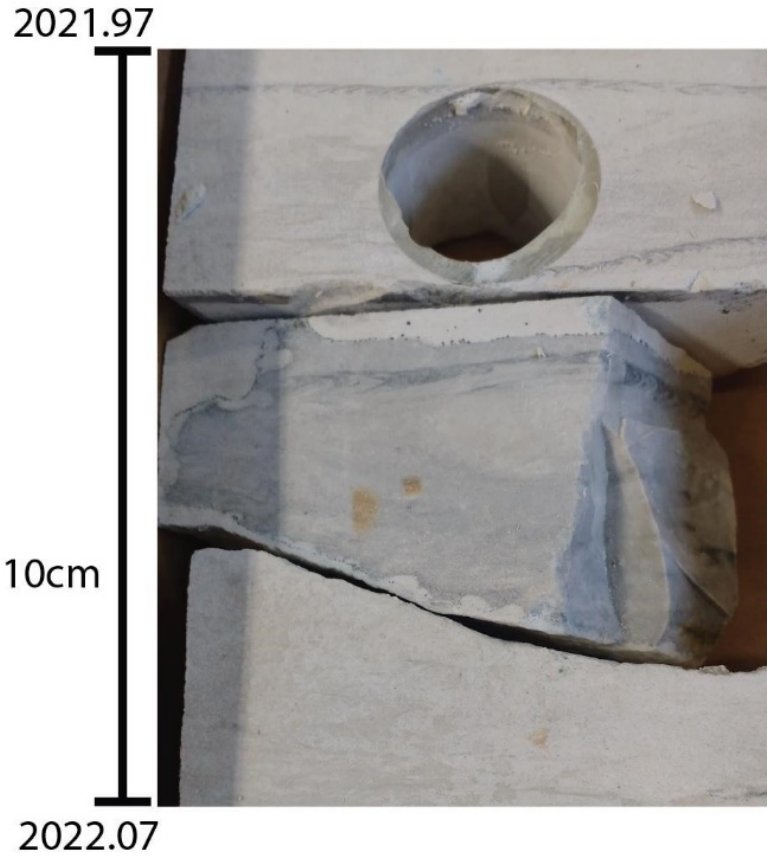

Figure 28. Flint layers within the chalk. Left axis is depth in MD

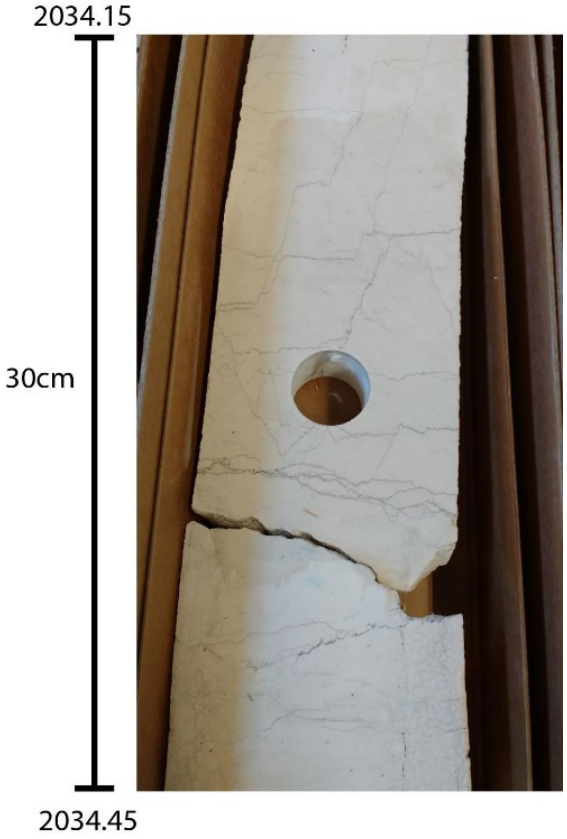

Figure 29. Stylolites in the "clean" white chalk facies. Left axis is depth in MD

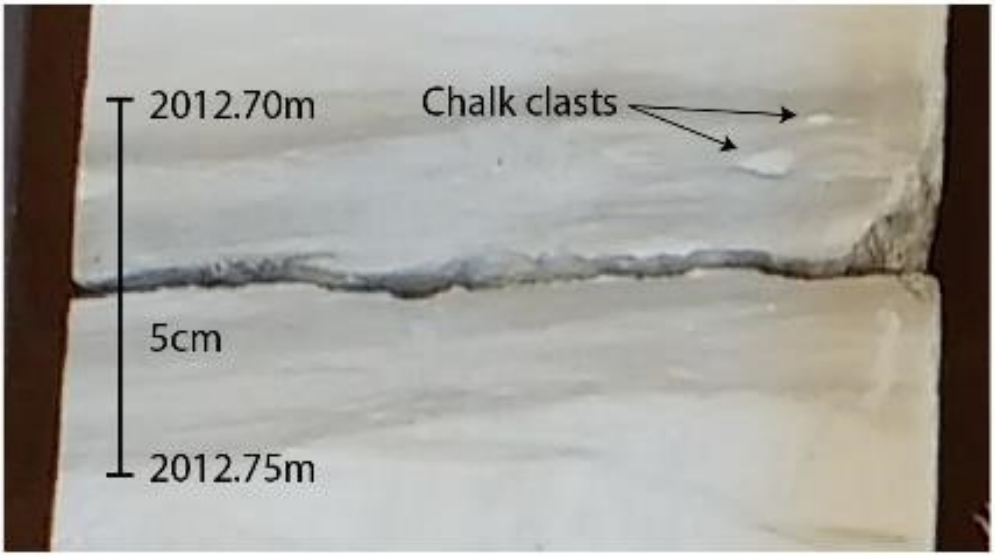

Figure 30. Chalk clasts inside the laminated grey interval. Left axis is depth in MD

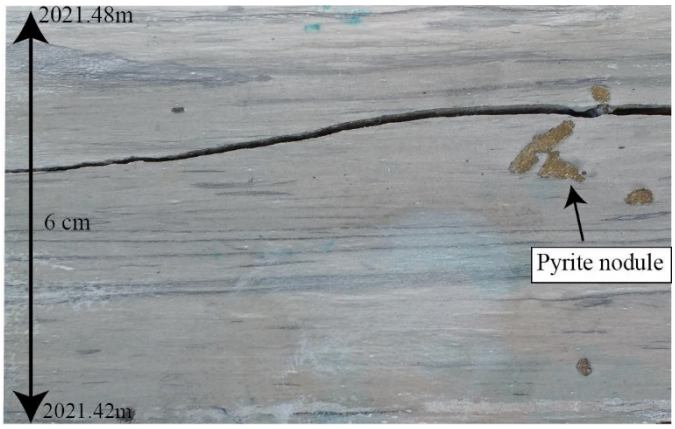

Figure 31. Pyrite nodule inside a laminated grey interval. Left axis is depth in MD

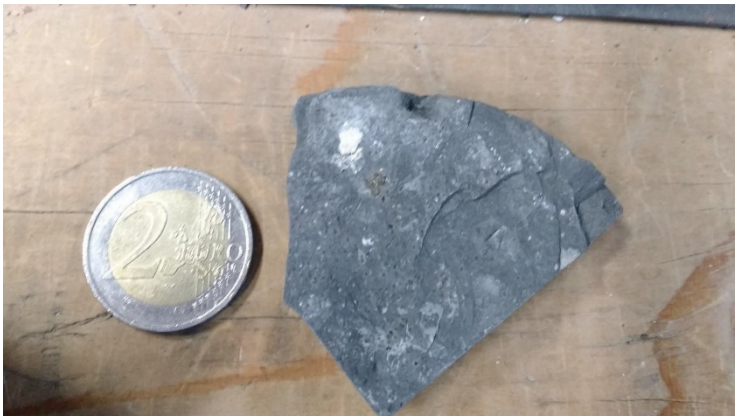

Figure 32. Sample from core A12-02 from 2051.82m MD. Note multiple black circular grains.

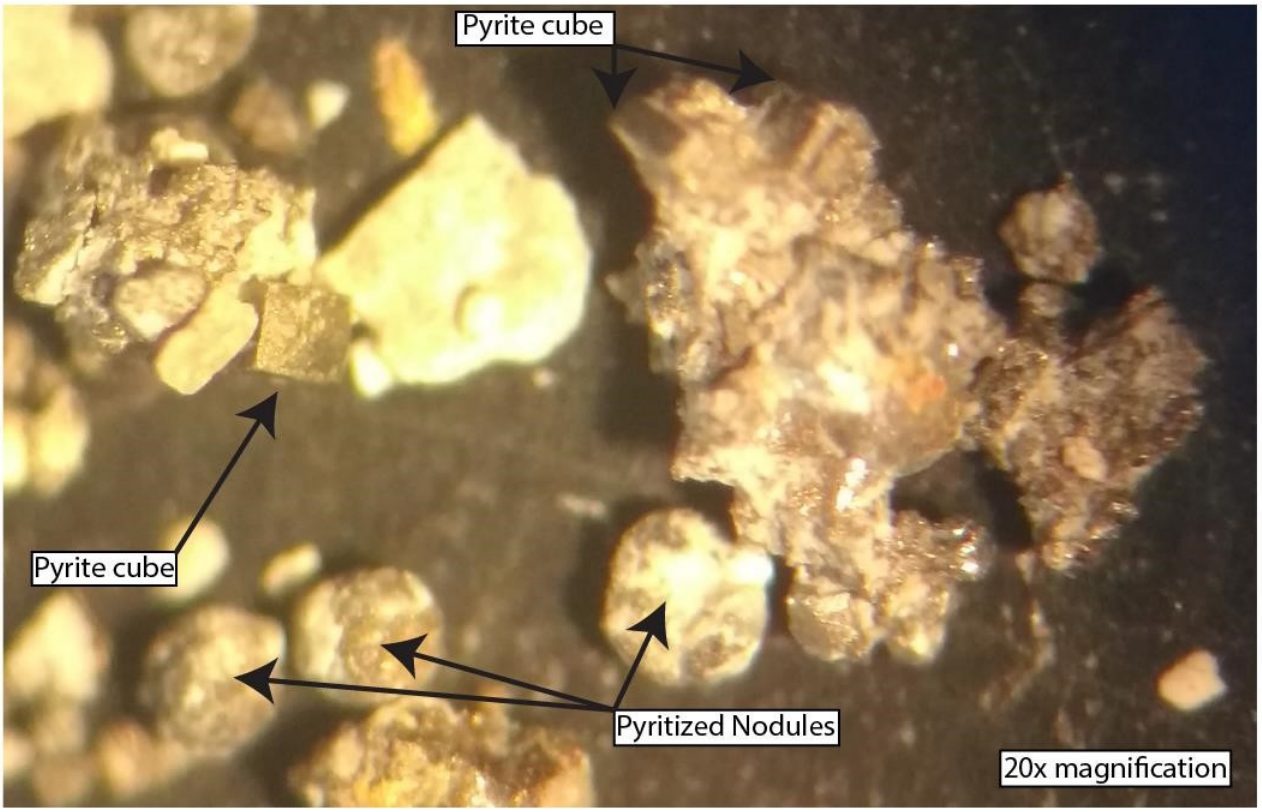

Figure 33. Sample extracted from the layer in figure 30. Note presence of pyrite cubes and the pyritized nodules.

4.7 Spectral analysis

4.7.1 Blackman Tuckey method

The Blackman-Tukey transformation was performed on gamma ray, sonic, thorium, uranium, potassium and seismic trace logs. The analysed logs span from the base to the top of the Chalk Group. Splitting the logs into multiple depth intervals and then analysing them did not significantly shift the spectral peaks so no further attention was paid to this approach.

4.7.1.1 Well-logs

The Blackman-Tukey transformation spectrograms of the gamma ray, sonic, thorium, uranium and potassium records can be observed in Figures 34, 35 and 36. According to the formulae of Worthington (1990) cycles smaller than 1.2 m are not statistically present in the GR log and cycles smaller then 2.4 m are not statistically present in the sonic log. Notable spectral power peaks can be seen for 4-6, 8, 15-22, 40-60, 105 and 120-160 m periods. See S.I. 10.6 Figures 76, 77 and 78 for additional Blackman-Tukey spectra of other wells.

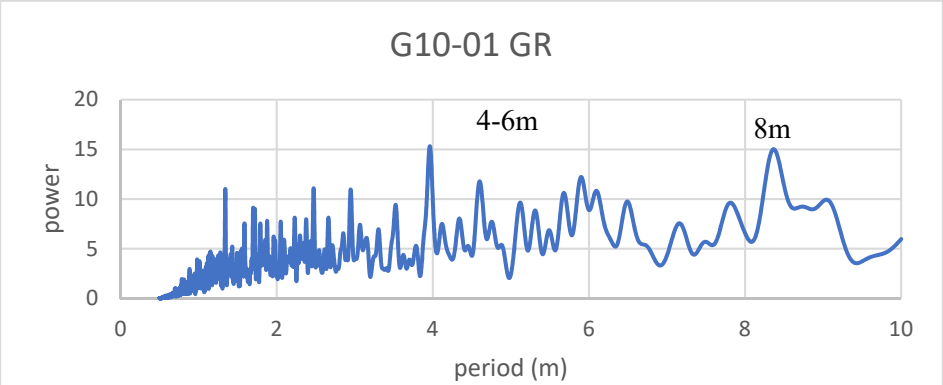

Figure 34. Redfit spectra with confidence intervals. Stretches 0-10m period interval. Notable peaks are indicated

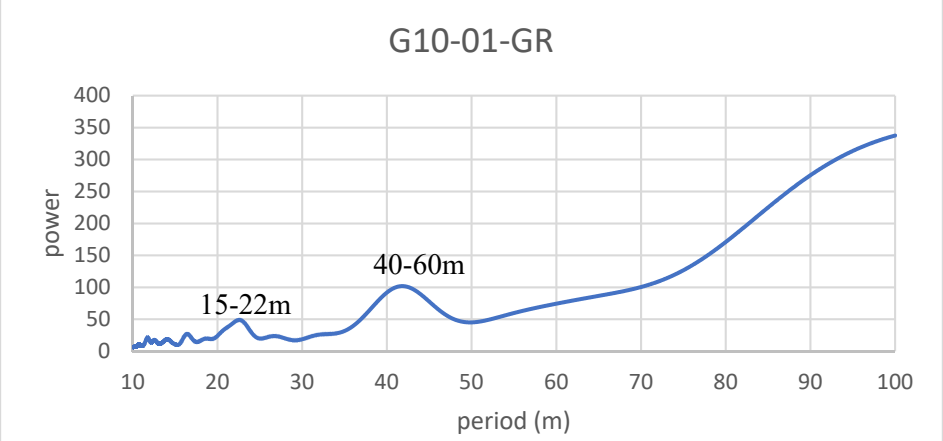

Figure 35. Redfit spectra with confidence intervals. Stretches 10-100m period interval. Notable peaks are indicated

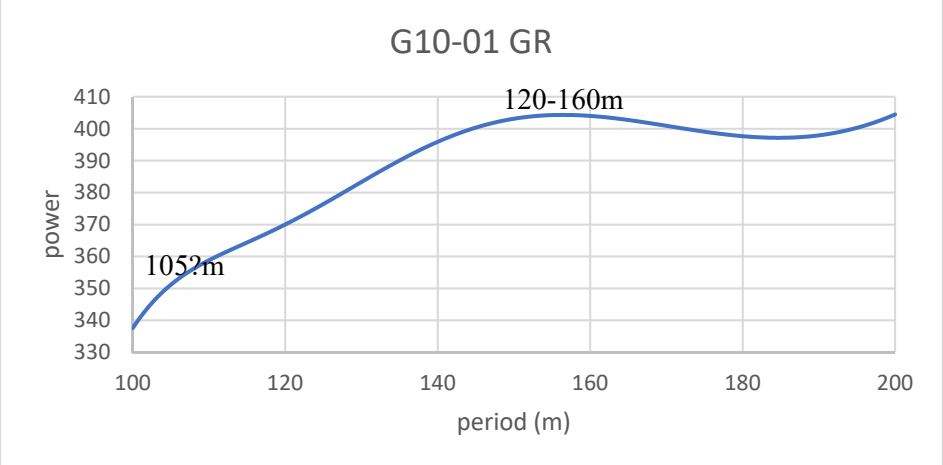

Figure 36. Redfit spectra with confidence intervals. Stretches 100-200m period interval. Notable peaks are indicated

4.7.1.2 Seismic trace

The Blackman-Tukey transformation of the trace signals, shows two significant peaks for the seismic trace (Figure 37). The first peak has a period of ~55 m and the second peak has a period of ~145 m. Two additional small peak can also be identified. The first peak has a period of 30-40 m and the second peak has a period of 80-105 m. The spectrum of G17-S-01 VSP zero phase only shows a broad peak at ~55 m.

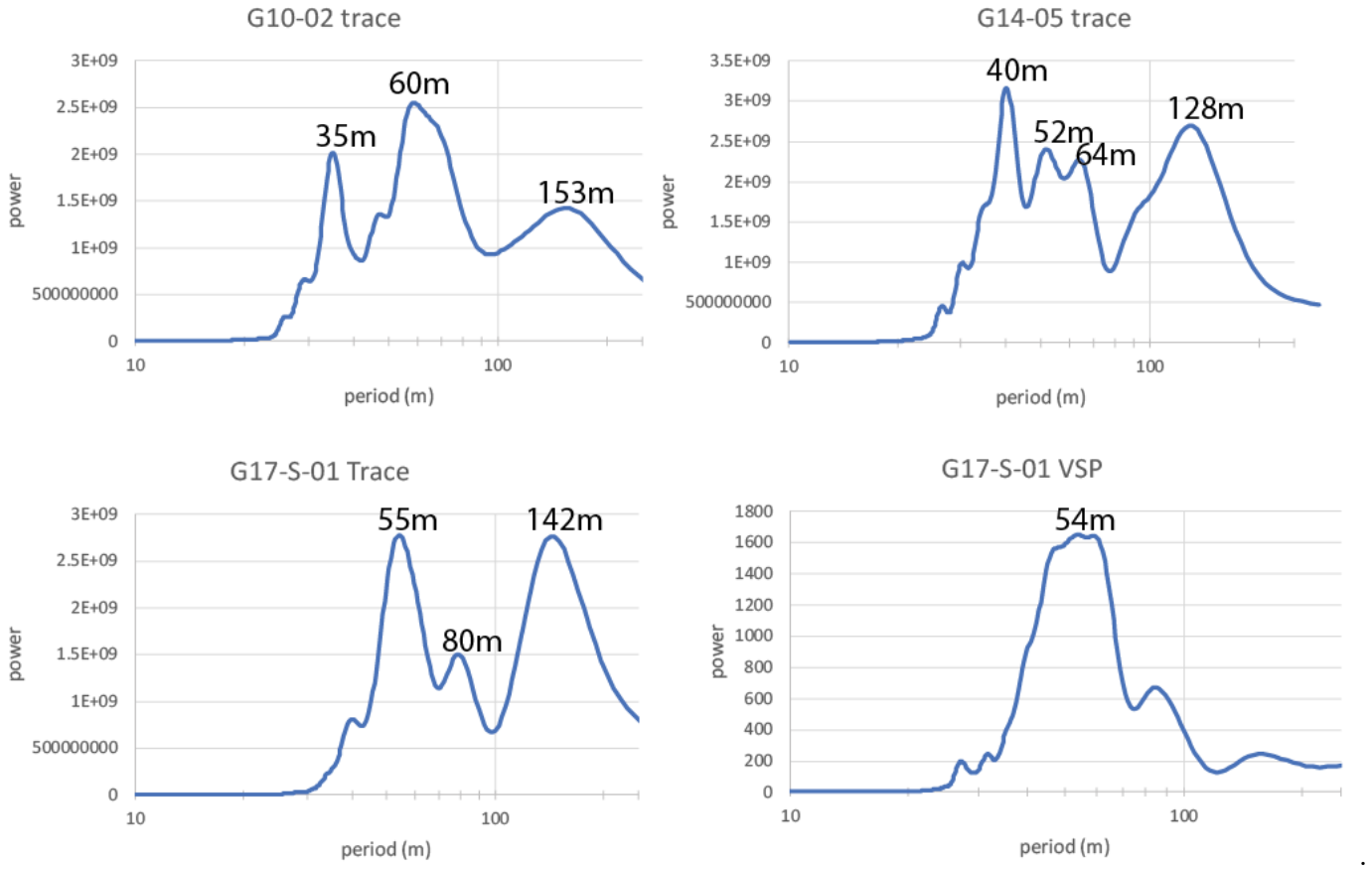

Figure 37. Blackman-Tukey spectrograms for the seismic trace records. Note that the x axis is logarithmic

4.7.2 Redfit spectra with confidence intervals

4.7.2.1 Well-logs

The Redfit spectra were constructed for the whole Chalk Group interval of each well. The chi-squared confidence intervals and the first-order autoregressive (AR1) were also created to indicate which statistical confidence the peaks carry. Seven different cycles have been identified in the Redfit spectra of the logs (Figure 38, 39 and 40). the identified cycles have periods of ~4, ~8, ~15-25, ~40-60, ~76, ~105 and ~120-160 m. See S.I. 10.7 for additional Redfit spectra of other wells see S.I. 10.7 Figures 79, 80 and 81.

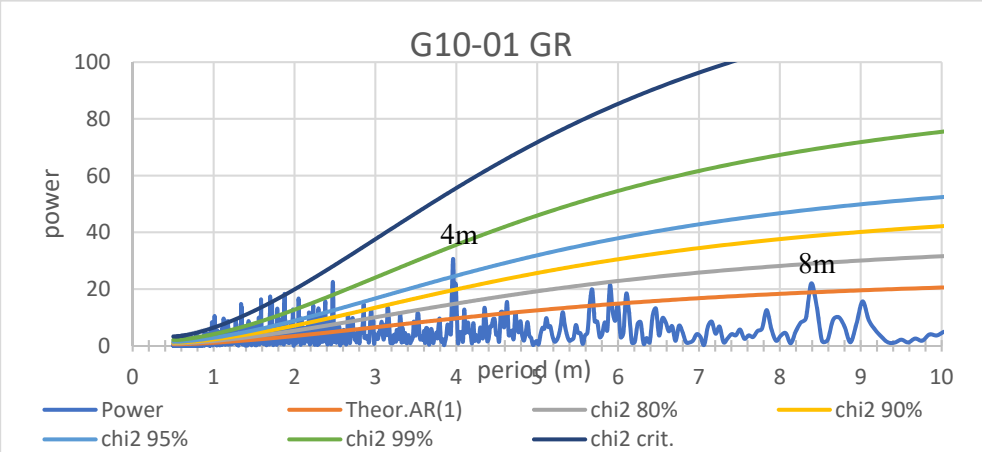

Figure 38. Redfit spectra with confidence intervals. Stretches 0.5-10m period interval. Notable peaks are indicated

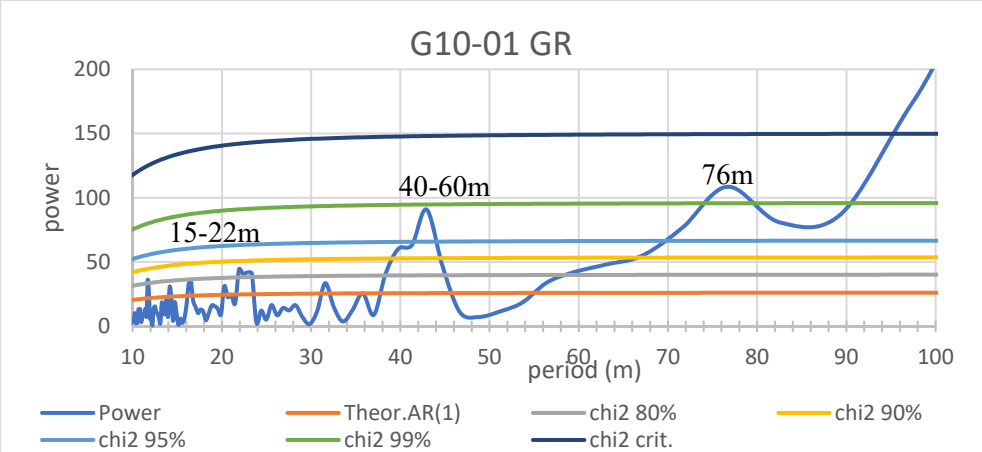

Figure 39. Redfit spectra with confidence intervals. Stretches 10-100m period interval. Notable peaks are indicated

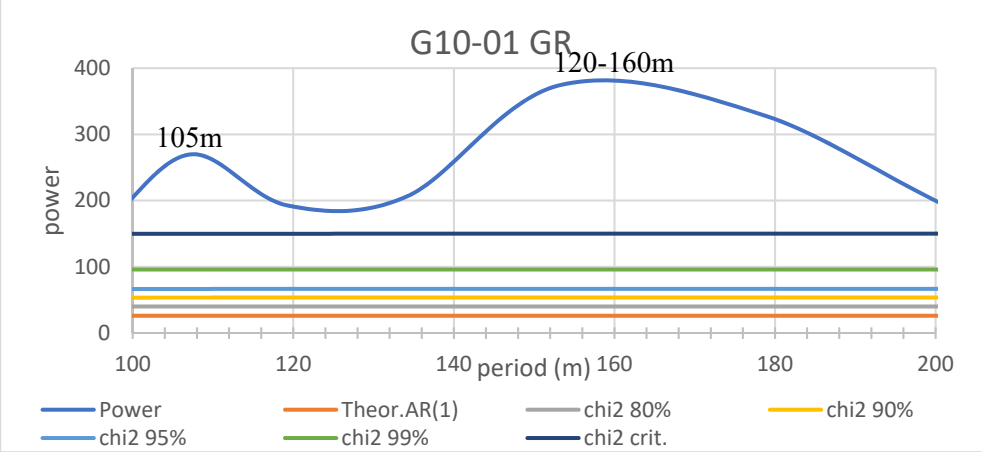

Figure 40. Redfit spectra with confidence intervals. Stretches 100-200m period interval. Notable peaks are indicated

4.7.2.2 Seismic trace

Three different cycles are identified in the Redfit spectra of the traces (Figure 41). The periods of the identified cycles are ~50, ~95 and ~142 m. It must be noted that in the Redfit spectra of G17-S-01 VSP zero phase there is only one single broad peak centred around the 50m period.

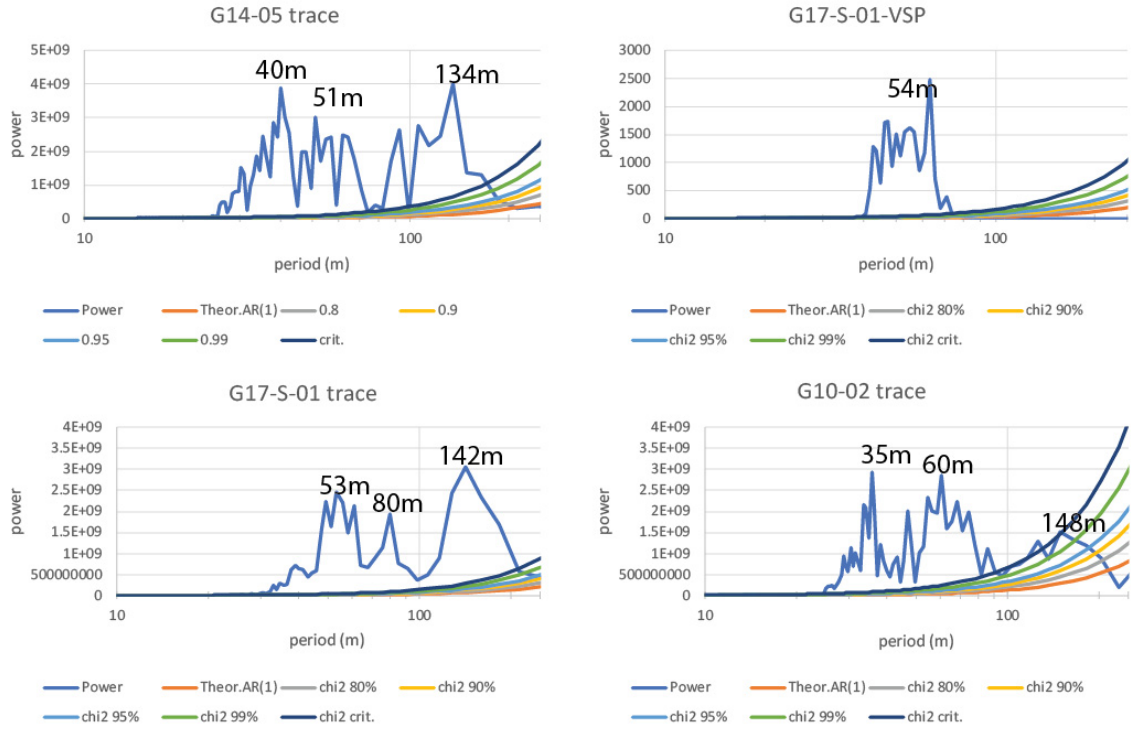

Figure 41. Redfit spectrograms of seismic trace data with confidence intervals. Note that some of axis scales are logarithmic. When the y-axis has a logarithmic scale then peaks are identified as positive deviations from the increasing baseline power. Note that the high significance of the peaks. The high significance is due to the sinusoidal shape of the trace data.

4.7.3 EHA spectra

4.7.3.1 Well-logs

The EHA spectra are grouped into 4 frequency ranges (Figure 42 and S.I. 10.6 Figures 82-102). The frequency ranges are: 0.001 to 0.01 with a long window (500 m), 0.001 to 0.01 with a short window (250 m), 0.01 to 0.1 (100m window) and 0.1 to 0.3 (50 m window). Larger or smaller frequencies have been analysed, but the EHA spectra of these frequencies did not contain significant peaks and are subsequently not considered for the remainder of this thesis. Consistent high spectral power peaks were identified in the EHA spectra, which have periods of 4-6, ~8, 15-22 40-60, ~105, 125-160 and 300-400 m (Figure 42 and S.I. 10.6 Figures 82-102).

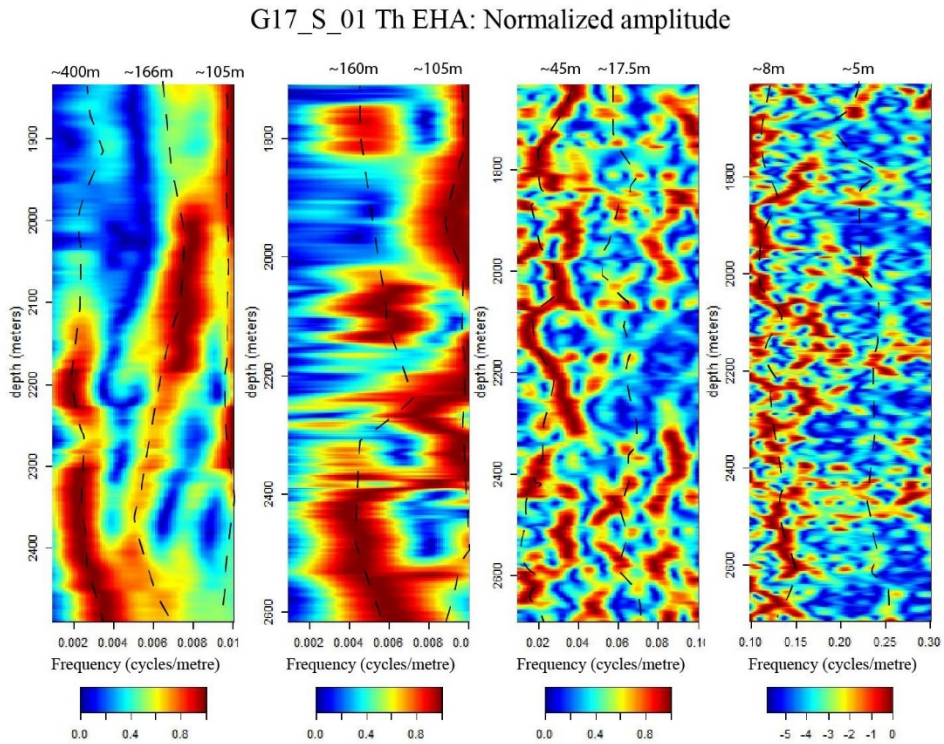

Figure 42. EHA spectra of well G17-S-01 Th. The left spectrum has the same frequency range as the one to the right of it but the sliding window on the left one is 500 m while one on the right is 200 m

4.7.3.2 Seismics traces

There are two main cycles that have been identified in the seismic trace EHA spectrum, which have periods of ~50 m and 110 m (Figure 43). Lower spectral power cycles of 80-100 m and 40-30 m are also present.

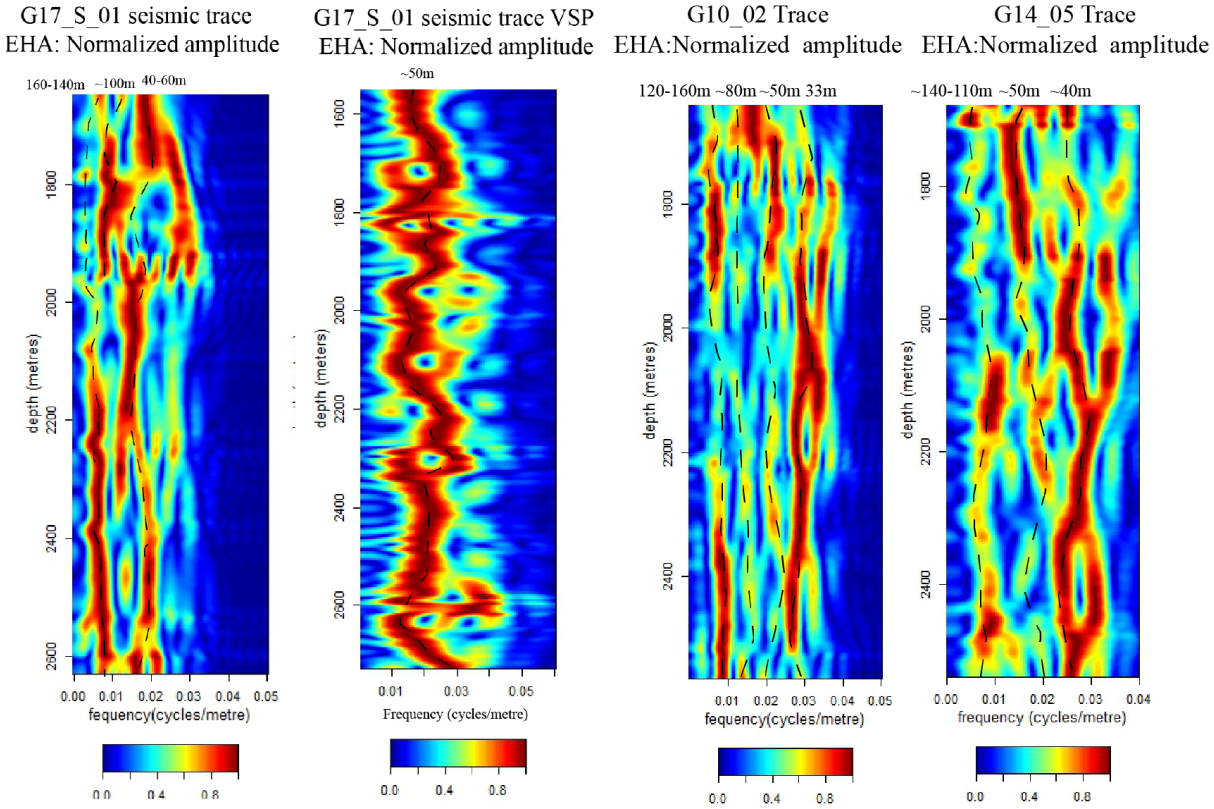

Figure 43. Seismic trace spectra of G17-S-01, G17-S-01 VSP, G10-02 and G14-05.

4.7.4 SSA-MTM

The SSA-MTM toolkit was used to create MTM spectra with confidence intervals. Initial spectra showed relatively low confidence and small spectral peaks in comparison to other spectral analysis techniques. The reason for this is unknown. It might be due to the technique itself, a poor understanding of the toolkit, the data-set itself is not compatible with this technique or the other techniques are simply wrong. The EHA spectra are also based on the Multitaper method and the EHA spectra do not show the same problems as the MTM analysis of the SSA-MTM toolkit. This might indicate that something went wrong while using the SSA-MTM toolkit. The poor results of the MTM spectral analysis in comparison to other spectral techniques has led to the decision not to include this technique in this research.

4.8 eASM

For the well-logs the 3463, 2373, 1200, 977, 812, 688, 486, 405, 346, 205, 187,174-kyr astronomical cycles (Hinnov, 2000; Laskar et al., 2004) were used for the eASM analysis. The multiple cycles making up the short eccentricity cycle (130 to 95-kyr) were also initially applied to the eASM analysis. These results indicate significantly lower or higher sedimentation rates then previously mentioned in literature (see chapter 2.2.5). The low sedimentation rates would indicate that there is too much time present in the Chalk Group. The high sedimentation rates would indicate a presence of one or more hiatuses. It is unlikely that almost double or the triple the time is present in the chalk, therefore the low sedimentation rate results are considered to be not realistic/reliable. No large hiatuses were observed in the seismic data and well-log data so the high sedimentation rates are thus most likely false. The calculated sedimentation rates fell within the sedimentation rate ranges stated literature when only a single 100-kyr cycle was used (see chapter 2.2.5). The null hypothesis values decreased even more when the 100-kyr cycle was left out (a lower null hypothesis value indicates a higher statistical significance for the optimal sedimentation rate). The 3463, 2373, 1200, 977, 812, 688-kyr astronomical cycle were used for the eASM analysis of the seismic trace data. Only the longer period cycles were used for the seismic trace data because the resolution of the trace data is much lower when compared to the well-log data (see chapters 3.2.1.1 and 3.2.2.2). The eASM results show comparable results for all the wells and seismic traces on the whole Schill Grund Platform (note that the significance level is much higher for the seismic trace data). The e-ASM results indicate that the optimal sedimentation rate varies between 30 and 70 mm/kyr (see Figure 44 and S.I. 10.7 Figures 103-106).

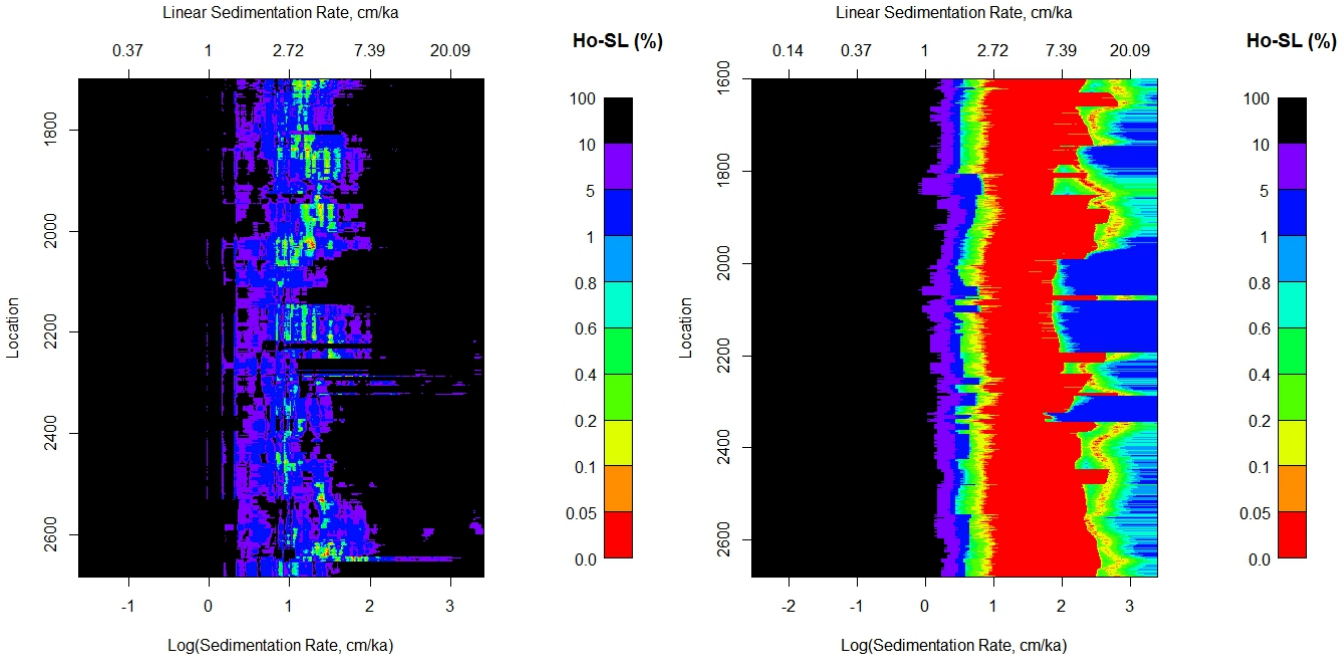

Figure 44. left: eASM plot G17-S-01 Th log. right: eASM plot G17-S-01-Trace. Ho-Sl (%) is null hypothesis. A lower null hypothesis indicates a better fit between the input cycle ratio and the EHA cycle ratio at a given sedimentation rate (a lower Ho-Sl indicates a higher statistical significance for a certain sedimentation rate).

5. Cyclostratigraphic interpretation and age model

5.1 Spectral peaks

The EHA, Blackman Tuckey and Redfit spectra of the well-logs indicated the presence of seven consistent clusters of cyclicity. The periods of the seven clusters are: 4-6, ~8, 15-22, 40-60, ~105, 125-160 and 300-400m. Other spectral peaks are also observed but they are not considered for this research because these peaks often have low spectral power or the peaks are only found by one spectral analysis technique. The EHA, Blackman Tuckey and Redfit spectra of the seismic trace indicated the presence of three consistent clusters of cyclicity with periods of 30-60, 80-100, 110-160m. The fewer spectral peaks of the seismic data when compared to the well-log data are due to the low(er) resolution range for the seismic data (see chapter 3.2.1.1).

5.2 405-kyr cycle theory

The 405 kyr eccentricity cycle is governed by the g2 − g5 fundamental frequency combination (Laskar et al., 2011a). Laskar et al. (2011) indicates that the 405-kyr eccentricity cycle was stable for at least the last 250 Myr. The 405-kyr cycle is the only stable cycle in the Cretaceous and should therefore be used as the main cycle to extrapolate ages for other cycles. Biostratigraphy in combination with the well and seismic data indicate that wells G17-01 and F15-01 contain an almost complete Maastrichtian to Cenomanian record. The biostratigraphy of wells G17-01 and F15-01 indicate sedimentation rates of around 40 mm/kyr, which means that the 405-kyr eccentricity cycle should be ~16 m. The eASM results indicated sedimentation rates between 30 and 70 mm/kyr which when extrapolated to the 405-kyr cycle leads to a thickness between 12.5 and 28.35 m. Spectral analysis shows spectral power around the 15-22 m period for the well-logs of the Schill Grund platform. The 15-22 m period is therefore interpreted as the 405-kyr long eccentricity cycle.

Extrapolation of the 15-22 m/405-kyr cycle to the other observed cycles is shown in table 5. There is a mismatch between the cycles in the seismic data and the cycles in the well-log data, but with some caution these cycles can be correlated. The 30-60m seismic cycle can be correlated to the 40-60m cycle in the well-logs. The 80-100 m seismic cycle can be correlated to the ~105 m cycle in the well-logs, but the correlation remains uncertain. The 110-160 m seismic cycle can be correlated to the 125-160 m well-log cycle.

Table 5		
Well log cycles in depth domain	Seismic cycles in the depth domain	Cycle in time domain
15-22 m	Not present	405-kyr eccentricity
4-6 m	Not present	100-kyr eccentricity
~8 m	Not present	200-kyr
40-60 m	30-60	1200-kyr (obliquity)
105 m	80-100	2400-kyr eccentricity
125-160 m	110-160	3500-kyr eccentricity
350-450 m	Not present	9500-kyr cycle

Table 5. Observed well-logs in depth extrapolated to cycles in the time domain

5.2.1 Obliquity and precession

If the 405-kyr cycle is indeed related to the 15-22 m cluster, then obliquity related cycles will have a thickness period of 1.4-2.2 m and precession related cycles will have a thickness period of 0.8-1.2 m. Table 3 indicates that the gamma ray tool has a detection limit of 1.2 m. Individual precession related cycles will therefore not be registered by the gamma ray logging tool, but the obliquity signal will be registered by the gamma ray logging tool. Without the ability to identify precession cycle the relative contribution of the obliquity and the precession cycles to the well-log measurements cannot be resolved. The expression of the obliquity and the precession cycles can therefore only be resolved with the help of core material. Well A12-02 has core material available was visually inspected and measured with a handheld XRF. The EHA spectra of the gamma ray log of the cored interval of well A12-02 contains spectral peaks with a 14 and 45 m period (Figure 82). If a similar sedimentation rate is assumed for the Step graben and Schill Grund Platform then the 14 m period would correspond to the 405-kyr eccentricity cycle and the 45 m period would correspond to the 1200-kyr cycle. A 14 m / 405-kyr cycle would indicate that the precession cycle is ~0.76 m thick and the obliquity cycle is ~1.40 m thick. Visual inspection of core A12-02 indicated decimetre scale alternations between “pure” white chalk and grey laminated chalks. The grey-white alternations are not equally spaced at either ~1.40 or ~0.76 m and therefore an interference pattern between the obliquity cycle and the precession cycle could be present. The resolution of the well-

logs and the XRF measurements is too low to resolve the issue of the contribution of obliquity and precession to the grey-white cycles. A higher resolution XRF or greyscale analysis may shed light on the contribution of the obliquity and the precession cycles to the grey-white alternations.

5.2.2 100-kyr cycle

The 100-kyr cycle found in this research most likely corresponds to the 100-kyr short eccentricity cycle and is therefore interpreted as the 100-kyr eccentricity cycle. The 100-kyr eccentricity cycle is part of the astronomical timescale for the Cenozoic (<50Ma). The 100-kyr eccentricity cycle cannot be accurately determined for ages older than 50 Ma the (Laskar et al., 2011a, 2011b). The 100-kyr cycle can therefore not be used for a tuning of the Chalk Group record. Higher frequencies in the EHA spectra contain proportionally more noise than the lower frequencies, which hampers an accurate tracking of a frequency "pathway" in the EHA spectra. The noisy signal does hamper an in-depth investigation of the 100-kyr cycle and thus the existence of the 100-kyr cycle can only be acknowledged

5.2.3 200-kyr cycle

The 200-kyr cycle is one of the cycles to which no orbital cycle could be readily assigned. There are three possible theories which might explain the existence of the 200-kyr cycle.

The first theory is that the cycle interpretation is simply wrong. It could well be possible that the 8 m / 200-kyr cycle is the 450-kyr long eccentricity or the 100-kyr short eccentricity cycle. If the 8m cycle is indeed the 100-kyr cycle then this would mean that there should be several hiatuses in the Chalk Group record. No perturbations in the well-logs nor in seismic data can be seen which would indicate hiatuses in the Chalk Group record. If the 8 m cycle is the 405-kyr cycle then there would be much more time present in the Chalk Group record then previously thought. This would change the ages of the biostratigraphy and the Plenus Marl significantly. Such a shift in the ages of the biostratigraphy and the Plenus Marl is highly unlikely.

The second theory is that the 200-kyr cycle is a harmonic cycle, which is the result of a half 405-kyr or a double 100-kyr cycle. To date no literature exists in which a half 405-kyr eccentricity cycle has been found in the geological record. A double 100-kyr eccentricity spectral peak has been found in an Albian marginal epicontinental sea record in the Lower Saxony Basin (Tyszka, 2009). The spectral analysis only consists of a simple periodogram and could therefore benefit from more advanced spectral analysis techniques, which could give a statistical significance level to the existence of the double eccentricity cycle. A more complete record of half and double cycles exists for the shorter period orbital cycles. A half precession modulation has already been postulated by Berger (1997). The half precession modulation is however restricted to intertropical latitudes. A double obliquity has been observed in the Mid Pleistocene age eastern Mediterranean sediments (Dols, 2015), middle Miocene Maltese marine carbonates (Mourik et al., 2011) and an early Campanian deep marine low palaeolatitude succession in the South Atlantic (De Winter et al., 2014).

The third theory is that the 200-kyr cycle is related to an amplitude modulation effect of the obliquity cycle. Amplitude modulation and frequency modulation spectra of the orbital obliquity solution of the past 10 Ma showed three peaks around the 200-kyr period (Hinnov, 2000). The three peaks have durations of 205.5, 187.8 and 174.7-kyr. The 174.7-kyr period is explained by the s3-s6 the fundamental frequency combination (Hinnov, 2000). The 187.8-kyr period is explained by the s3-g4+g3-s6 fundamental frequency combination (Hinnov, 2000). No fundamental frequency combination was assigned to the 205.5-kyr cycle by Hinnov (2000). A 194-kyr cycle in the cherts and pelagic limestone alternations of Cenomanian Scaglia Bianca formation was interpreted as having an obliquity origin (Mitchell et al., 2008). This interpretation was based on the work of Hinnov (2000). In the southern Indian Ocean a Miocene record shows a record in which the 200-kyr cycle is attributed to modulation of a 184-kyr obliquity signal (Beaufort, 1994). The 184 kyr cycle interpretation was based on the work of Liu (1992), which attributed the 184-kyr cycle to an asymmetry within the obliquity cycle. A 170-kyr cycle was found in de $\delta^{13}C$ record of Bohemia-Saxony Basin, which is attributed to a modulating effect of the obliquity cycle (Laurin et al., 2015).

5.2.4 1200 and 2400-kyr cycle

The strong expression of the 1200-kyr cycle in the depth domain is a distinctive feature of the Chalk Group record on the Schill Grund Platform. The Earth obliquity reveals a long-term 1200-kyr modulation related to precession of the ascending nodes of Mars and Earth (s4–s3) and thus the 1200-kyr cycle could be interpreted as the 1200-kyr obliquity cycle. Earth's eccentricity has a 2400-kyr modulation related to precession of the orbital perihelia of Mars and Earth (g4−g3) and thus the 2400-kyr cycle is interpreted as the 2400-kyr eccentricity cycle. The 1200-kyr could also be an eccentricity cycle. Between 50 and 100 Ma the secular resonance is proposed to have changed from the 2(g4−g3)=(s4−s3) fundamental frequency combination to the (g4−g3)=(s4−s3) fundamental frequency combination (Laskar, 1999; Laskar et al., 2011a, 2004), which transformed the 2400-kyr eccentricity cycle into a 1200-kyr eccentricity cycle.

5.2.5 3500-kyr cycle

The 120-160m spectral power cluster is interpreted as the 3500-kyr long eccentricity cycle. The 3500-kyr cycle is explained by the g2 +g4 −g3 −g5= 3463.318-kyr fundamental frequency combination (Berger, 1976; Laskar et al., 2004). A noticeable decrease in the power of the 3500-kyr cycle towards the top the EHA spectra is observed (best example Figure 42). The noticeable decrease in spectral power complicates the interpretation of this cycle. None of the existing astronomical solutions does specifically mention the expression and stability of the 3500-kyr. The decrease of the spectral power and the unknown stability of the 3500-kyr cycle makes the 3500-kyr cycle unsuitable for defining a cyclostratigraphic framework.

5.2.6 9500-kyr cycle

The presence of the 9500-kyr cycle is picked up by the EHA and Redfit spectra. The Redfit technique does show a peak around the 400 m interval, but the exact frequency of the peak cannot be determined due to a frequency scaling issues with the Redfit technique. Even though the exact frequency of the 9500-kyr peak is unknown the spectral peak is still statistically significant.

The origin of the 9500-kyr cycle has been attributed to an amplitude modulation effect by most authors (Boulila et al., 2012; Ikeda and Tada, 2014; Martinez and Dera, 2015; Sprovieri et al., 2013). Martinez and Dera (2015) proposed a high latitude quasi-stable organic matter reservoir as the cause for the strong expression of the 9500-kyr cycle during the Jurassic and early Cretaceous. Martinez and Dera (2015) based this quasi-stable reservoir modulation of the 9500-kyr cycle on Laurin et al. (2015). Laurin et al. (2015) however, indicated that organic matter burial in high latitude reservoirs was governed by obliquity. The Astronomical solution of Laskar et al. (2004) does contain an obliquity cycle with an 9500-kyr duration. The obliquity term is expressed as the P+s6+g5-g6=9582.151-kyr fundamental frequency combination (Laskar et al., 2004). If Laurin et al. (2015) is right and the burial of organic matter is governed by the obliquity cycle then the 9500-kyr obliquity cycle could be a viable explanation for the observed 9500-kyr cycle

5.3 Filtering in the depth domain

5.3.1 Log filtering

The logs of wells G10-02 Gr, G14-05 GR and G17-S-01 were filtered in the depth domain using R statistics. The filtered periods are: the 4-6 m (100-kyr), ~8 m (200-kyr), 15-22 m (405-kyr), 40-60 m (1200-kyr), ~105 m (2400-kyr), 125-160 (3500-kyr) and 300-400 m (9500-kyr) cycles (Figure 45). The width of each filter was adjusted to fit the entire main spectral peak of each cycle in the periodogram, which is created in simultaneously with the filtering bandpass filter option of R statistics.

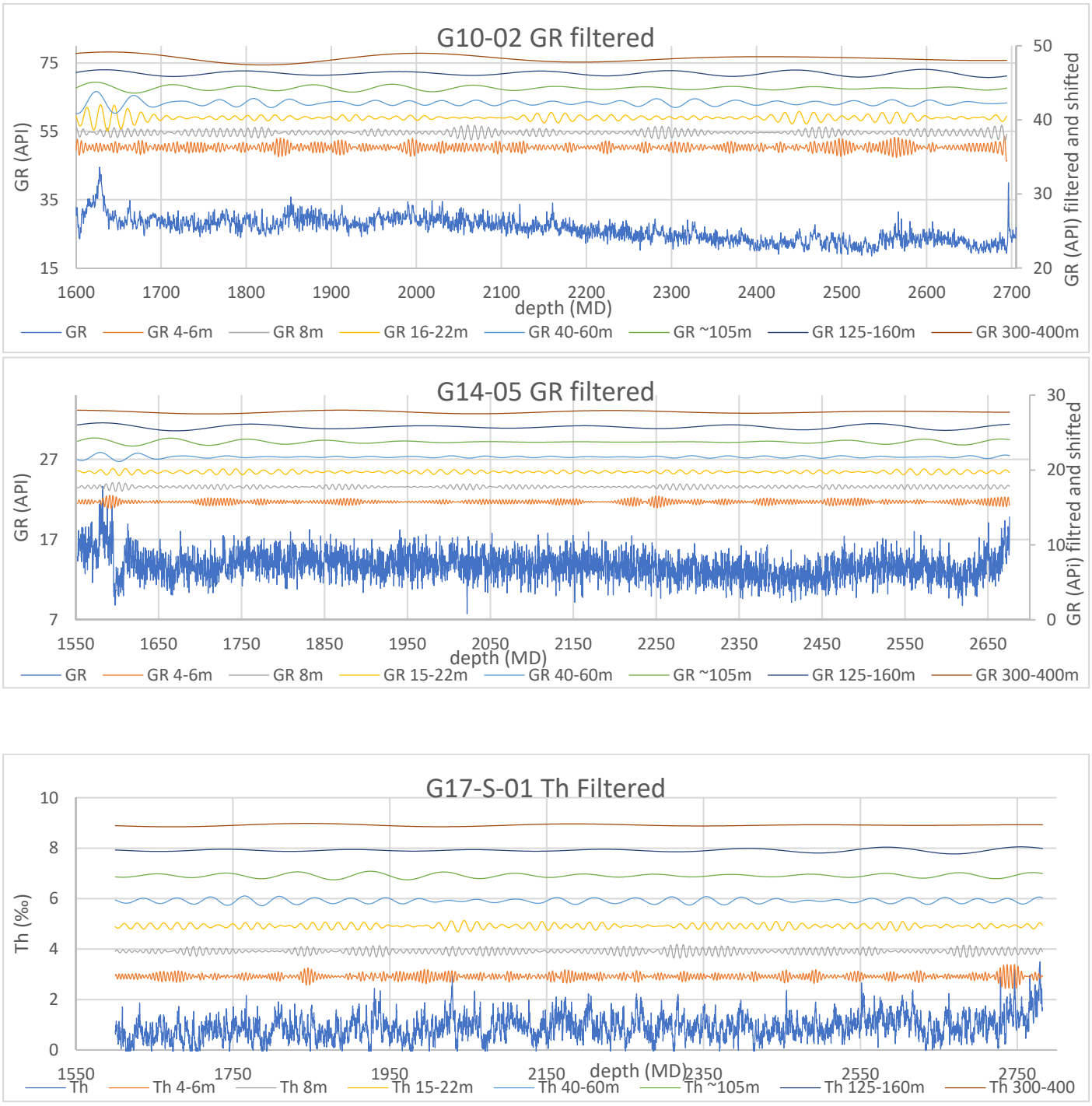

Figure 45. bandpassed records of wells G10-02 Gr, G14-05 GR and G17-S-0 Th

5.3.2 Trace filtering

The extracted seismic trace data of wells G14-05 G10-02, G17-S-01 and G17-S-01 VSP were depth filtered using R statistics. The filtered periods are the 30-60 m (1200-kyr), 80-100 m (2400-kyr) and 110-160 m (3500-kyr) cycles (Figure 46). The filtered 30-60 m cycle has the highest amplitude, while the filtered records of the 80-100 m and 110-160 m cycles have a significantly lower amplitude.

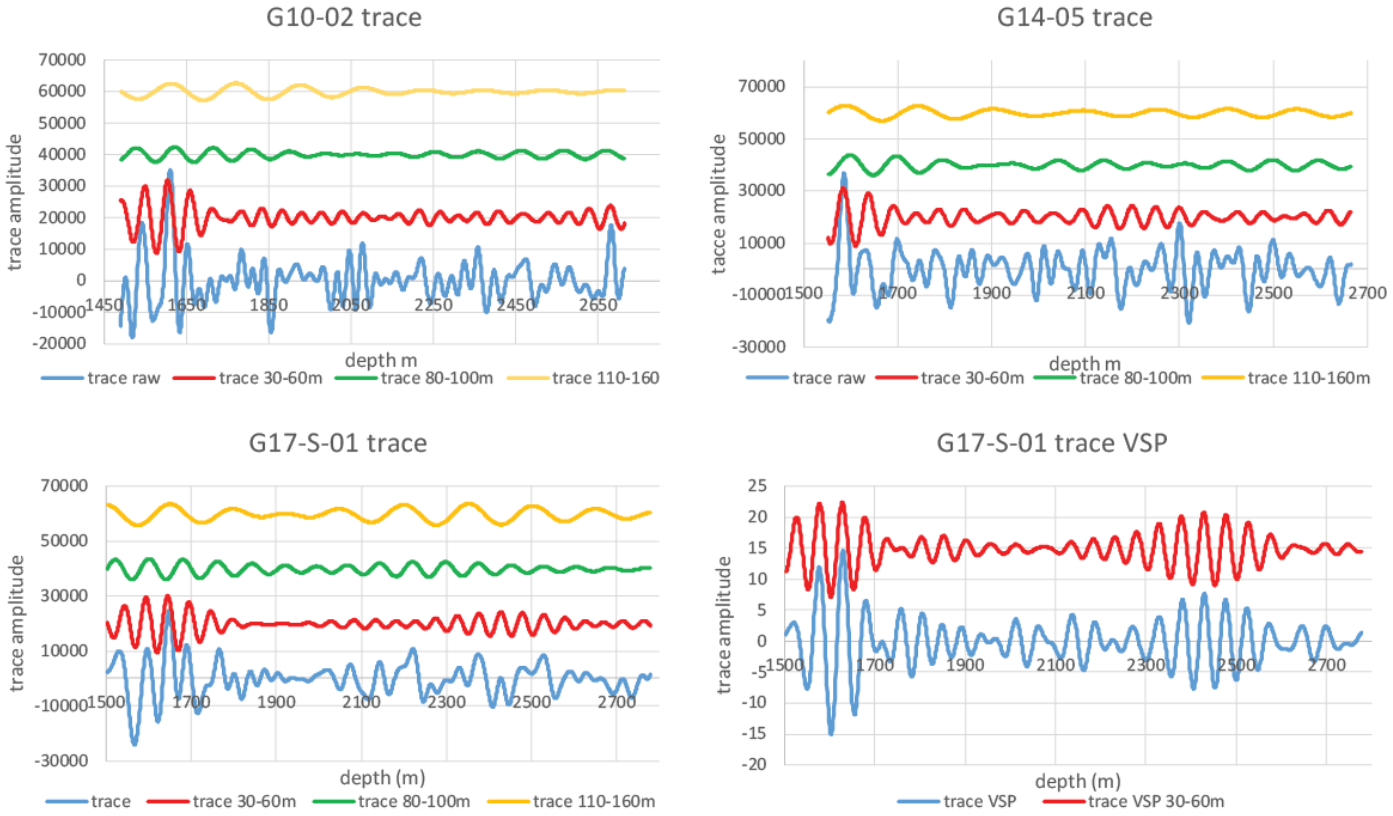

Figure 46. Filtered trace with original trace. Note: the 80-100 and 110-160m cycle were not filtered for well G17-S-01 VSP because no spectral peaks were present for these periods.

5.3.3 Seismic data filtering

To filter out different frequencies in the seismic depth domain the seismic volume attribute frequency filtering with Butterworth filter was used in Petrel. The Butterworth filter was used because it enables one to change the size of the filtering window and the influence of the frequencies outside of the window. The 50 m (1200-kyr), 105 m (2400-kyr) and 125-160 m (3500-kyr) periods which were detected in both the well-logs and the seismic trace data were filtered from the seismic data in the depth domain. Only the 50m (1200-kyr) cycle showed a result with a sufficiently high amplitude to be used and to be compared with the filtered trace and well-log data. Frequency filtering of the seismic data in the time (TWT) domain was also tried by converting the cycle thickness into hertz with the help of the internal velocity. The significant difference in the internal velocity between the top and the bottom of the Chalk Group created a range in the frequency in Hertz which is too large for the Butterworth filtering to enable accurate filtering of the seismic data. The result is that no filtering in time (TWT) was possible. The 40-60 m (1200-kyr), ~105 m (2400-kyr) and 125-160 m (3500-kyr) cycles were bandpass filtered from the logs (GR, DT, Th and Trace) and compared to the 40-60 m Butterworth filtered seismic data and raw seismic data (in TVD and TWT domain) (Figures 47, 48 and S.I. 10.8 107-123). The 40-60m filtered records could be visually correlated to seismic reflectors of the time-depth converted and TWT seismic data. Positive seismic amplitude peaks are coupled to the maximum positive slope of the filtered GR and DT records and filtered maxima in the filtered trace records. The ~105 m filtered well-log and trace records did not match the raw of filtered seismic data and therefore no correlation lines were drawn. The 125-160m filtered records could be correlated to seismic reflectors to the time-depth converted and TWT seismic data. The bright high amplitude sections are coupled to the minima of the filtered GR and DT records and filtered minima in the filtered trace records.

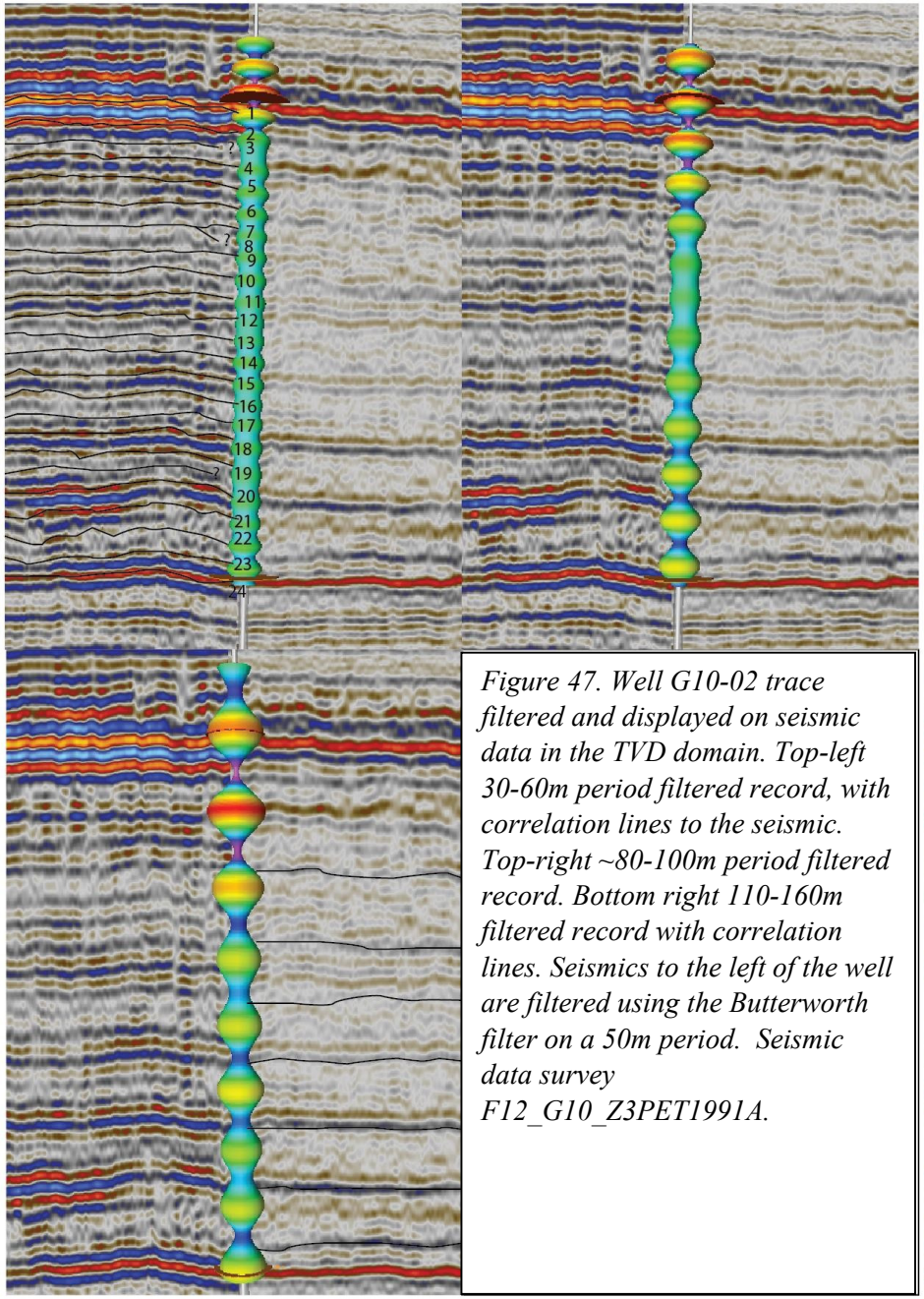

Figure 47. Well G10-02 trace filtered and displayed on seismic data in the TVD domain. Top-left 30-60m period filtered record, with correlation lines to the seismic. Top-right ~80-100m period filtered record. Bottom right 110-160m filtered record with correlation lines. Seismics to the left of the well are filtered using the Butterworth filter on a 50m period. Seismic data survey F12_G10_Z3PET1991A.

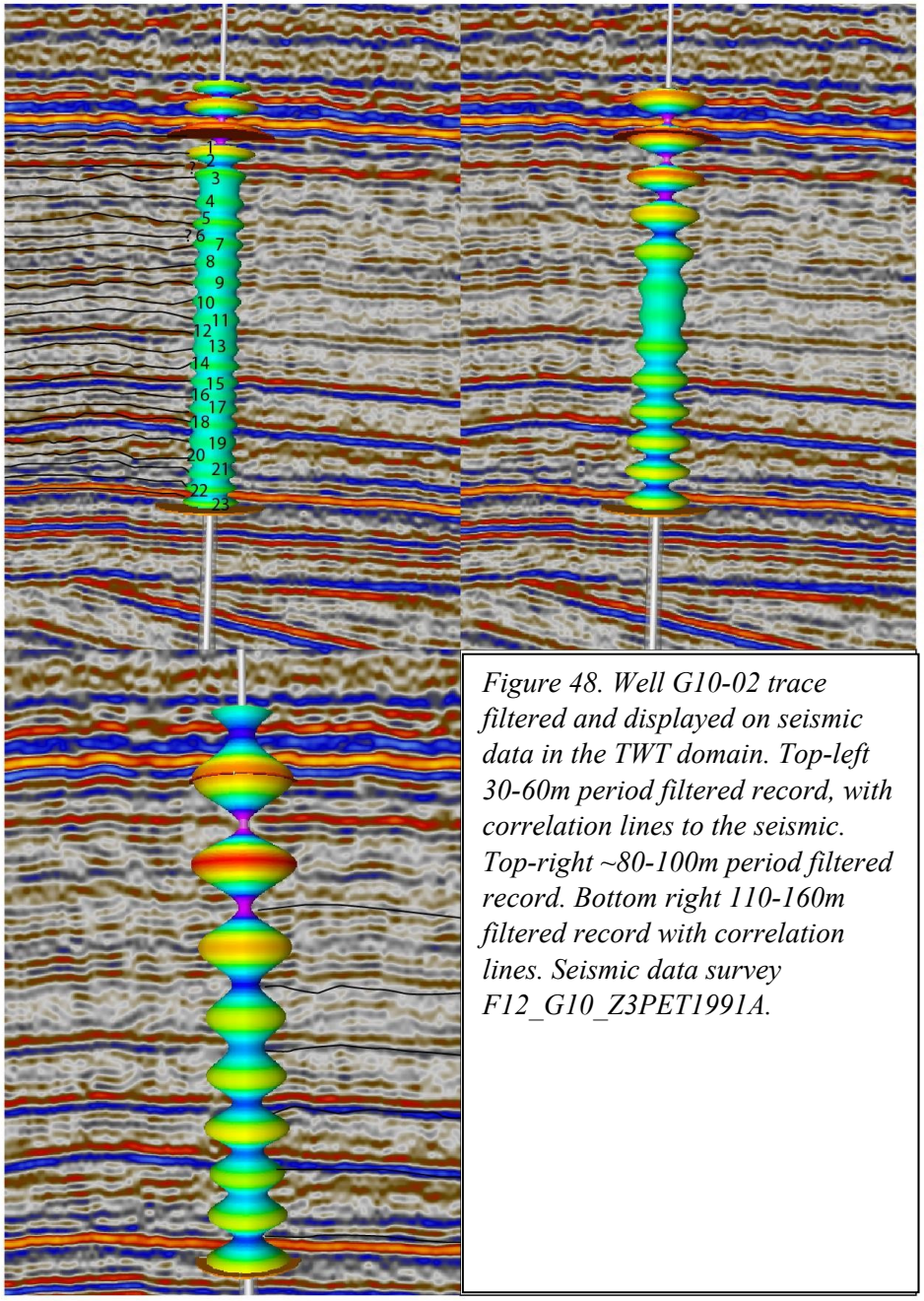

Figure 48. Well G10-02 trace filtered and displayed on seismic data in the TWT domain. Top-left 30-60m period filtered record, with correlation lines to the seismic. Top-right ~80-100m period filtered record. Bottom right 110-160m filtered record with correlation lines. Seismic data survey F12_G10_Z3PET1991A.

5.4 Depth time conversion

The main goal of a depth time conversion is to eliminate changes in the orbital frequencies caused by changes in the sedimentation rate (time in years and depth in metres). A depth time converted dataset will enable a more accurate filtering and a more accurate identification of the different orbital cycles. The gamma ray record of well G14-05 and thorium record of well G17-S-01 were time-depth converted (figure 49). They were used because the EHA spectra of well G14-05 GR and G17-S-01 Th showed high spectral amplitudes for the 15-22m / 405-kyr cycle and the seismic data and well-logs did not indicate any hiatuses making a tuning down to the Plenus Marl possible (OAEII).

To convert the logs of wells G14-05 GR and well G17-S-01 Th from the depth domain to time domain the Astrochron package for R statistics was used. The frequency identified as the 405-kyr cycle in the EHA spectra was selected/traced within a graphic user interface of R statistics. The tracking points were picked from the line indicated as the 15-22m / 405-kyr cycle in the EHA plots (Figure 42 and 86.). The traced 405-kyr cycles were converted to sedimentation rate (Figure 49). The sedimentation rate varies between ~26 and ~51 mm/kyr. The sedimentation rate was used to create a time depth relationship which was used to convert the well-logs from the depth domain to time domain (Figure 49). The well-logs in the time domain were then bandpass filtered for the 405-kyr cycle. The fit of the 405-kyr bandpassed record to the wells logs was evaluated. If the fit between the 405-kyr bandpass and the well-logs was deemed unsatisfactory, then the location of the traced points was changed to create a better fit. The process of depth-time conversion was repeated until the fit between the 405-kyr filtered record and the time converted well-log record was satisfactory (Figure 49).

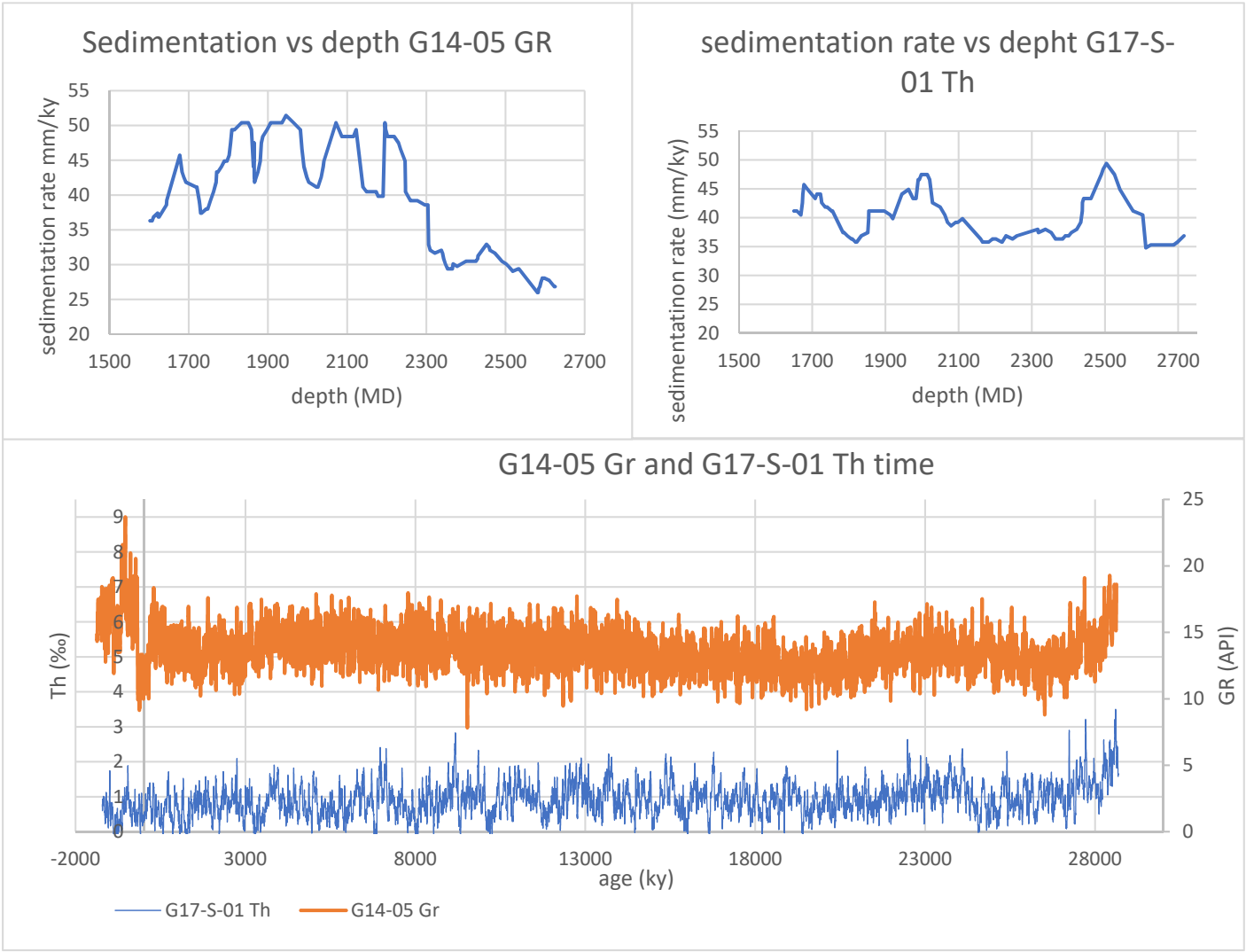

Figure 49. EHA derived sedimentation rates for wells G14-05 GR and G17-S-01 Th and the corresponding depth-time converted well-logs. Note that the timescale s floating

5.5 *Spectral analysis in the time domain*

To validate the depth time conversion a spectral analysis in the time domain was subsequently performed. The EHA and Redfit spectral analysis techniques were performed on the depth-time converted records of well G17-S-01 Th and well G14-05 GR (Figures 50-52). The Redfit spectral analysis technique indicates peaks with periods of 115, 200, 300, 405, 700-1000, 1200-1600, 2400 and 3500-kyr. The EHA spectra has continuous high spectral power traces for the periods of 2400, 1200, 100-700 and 405-kyr. Only scattered power can be observed for the 200 and 100-kyr cycles. A Hilbert transformation (performed in R) was followed by an EHA and Redfit spectral analysis of the depth-time converted records. The Hilbert transformation was performed to account for the modulating astronomical cycles, which often has problems being registered by spectral analysis. The Redfit spectral analysis technique registered spectral peaks with periods of 200-250, ~ 405, ~1200, ~2100, ~3100 and 3600ky. The EHA spectral analysis technique indicated continuous high spectral power traces with periods of 2400, 1200 and 405kyr. Scattered power can be observed for the cycles with a 1000-700, 200 and 100-kyr period. The 100-ky cycle in the time domain can be matched with the 4-6m cycle 100-kyr eccentricity cycle in the depth domain. The 200-250ky cycle in the time domain can be matched with the ~8 m 200-kyr cycle in the depth domain. The 405-kyr cycle in the time domain can be matched to the 22-15 m / 405-kyr eccentricity cycle in the depth domain. The 2100-2400-kyr cycle can be matched to the ~105 m / 2400-kyr eccentricity cycle in the time domain. The 3100-3600ky in the time domain can be matched with the 125-160 m / 3500-kyr eccentricity cycle in the depth domain. The 1200 and 1200-1600-kyr cycles can be matched to the 1200-kyr cycle but this correlation is ambiguous. The 300 and 700-100-kyr cycle were previously not identified in the depth domain.

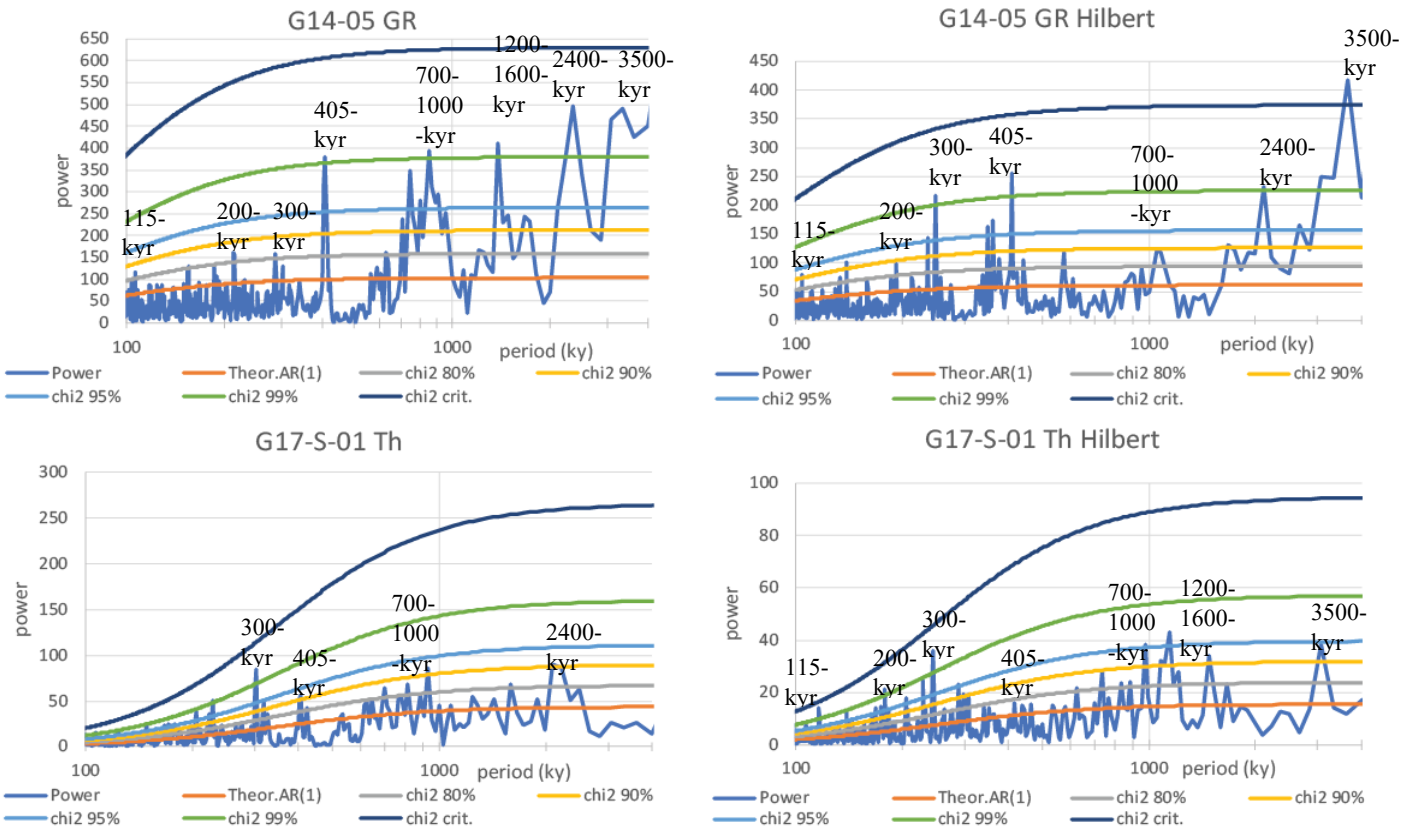

Figure 50. Redfit spectra of G14-05 GR and G17-S-01 Th in the time domain

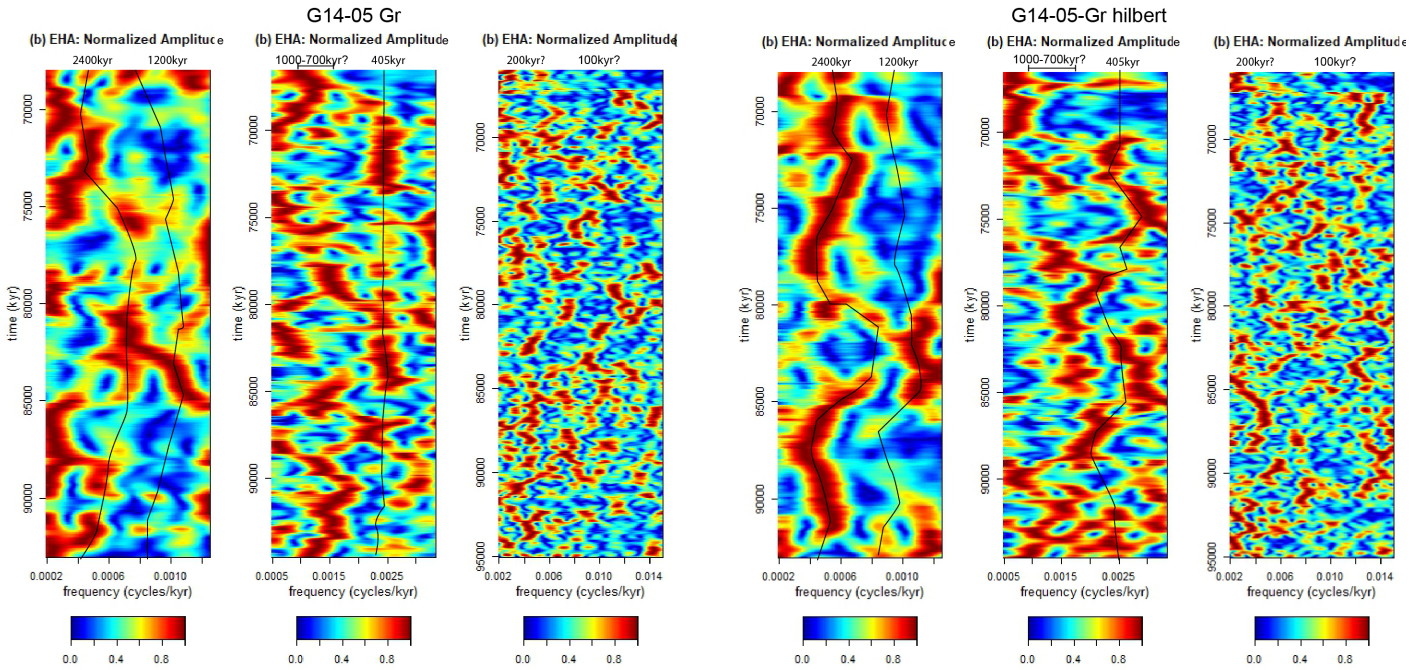

Figure 51. EHA spectra of G14-05 GR in the time domain. Note the time in (kyr) is based on the relationship between the biostratigraphy and the seismic data and thus still contains a large uncertainty in the absolute age (e.g. floating age model).

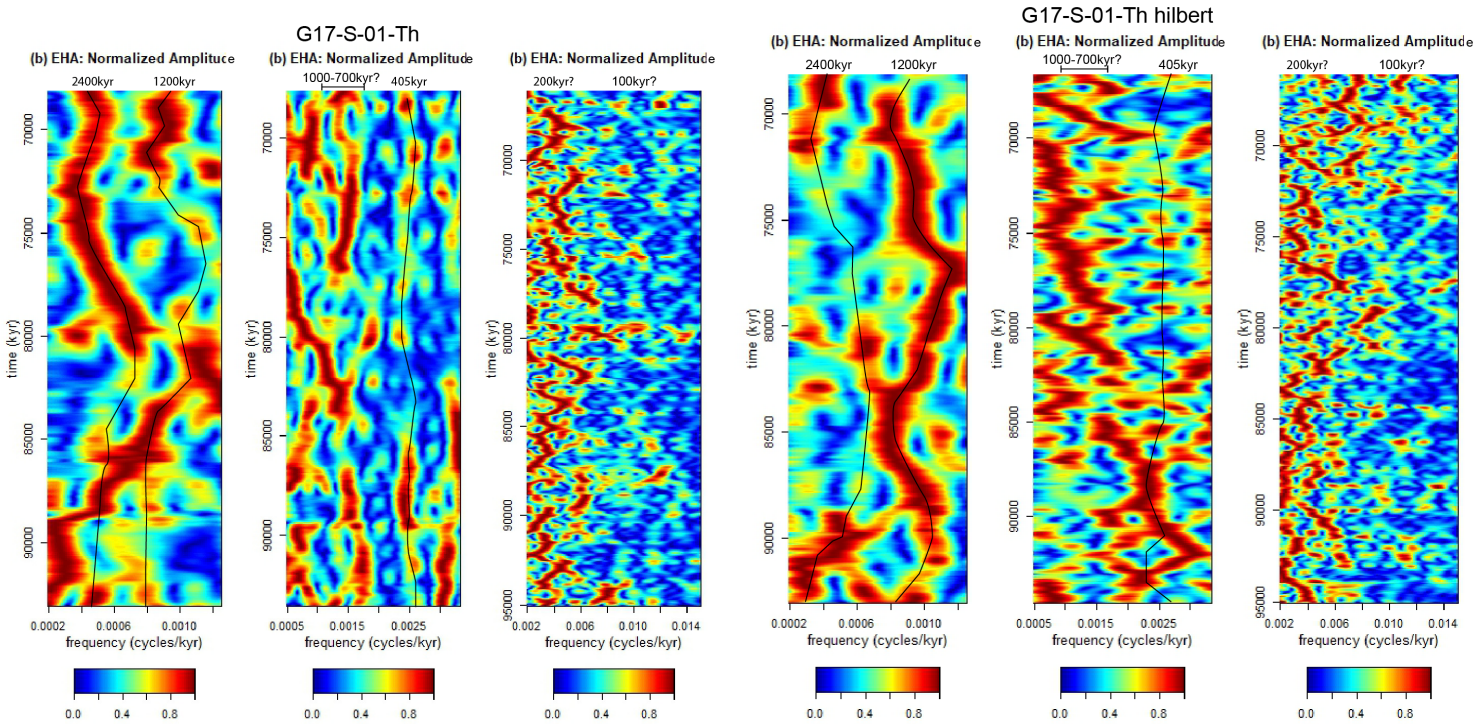

Figure 52. EHA spectra of G17-S-01 Th in the time domain. Note the time in (kyr) is based on the relationship between the biostratigraphy and the seismic data and thus still contains a large uncertainty in the absolute age (e.g. floating age model).

5.5.1 300-kyr cycle

The 300-kyr cycle cannot be readily assigned to an astronomical cycle nor to a cyclic modulating component of an astronomical solution. There are four possible theories which might explain the existence of the 300-kyr cycle.

The first theory is that the 300-kyr is related to the g2 + g4 − g3 − g5 =346.318-kyr cycle (Laskar et al., 2004). The Hilbert transformation Redfit spectra of the la2010a 65-97 Ma and la2010d 65-97 Ma solution did in fact show spectral peaks around for the 346-kyr cycle (Figures 53), but the spectral power is very low in comparison to the 405-kyr eccentricity cycle. In the spectra of G14-05 GR and G17-S-01 Th the opposite is true were the 405-kyr cycle has a comparable spectral power to the 346-kyr cycle (see Figure 53).

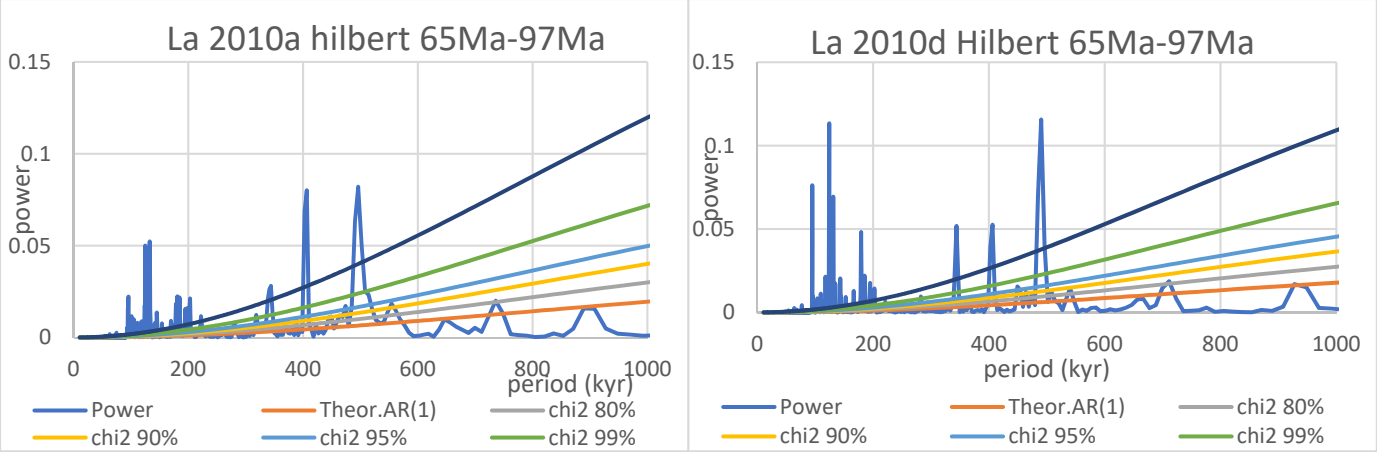

Figure 53. La2010a and La2010d astronomical solutions on which a Hilbert transformation was performed followed by a Redfit spectra analysis (including confidence intervals).

The second theory is that of erosion. It is assumed that the Chalk Group record is complete on the Schill Grund Platform, but there are many processes which could create an incomplete record. Beside large features such as slumping and channel formation, the Chalk Group is also influenced by winnowing and bottom currents. Re-sedimentation features smaller than the seismic resolution are hard to distinguish in the Chalk Group record. It could well be possible that part of a 405-kyr cycle was eroded and a relatively thin 405-kyr cycle was formed. During the depth-time conversion this thinner cycle would have been recognized as a 300ky cycle.

The third theory is that the EHA tracking "pathway" was wrong. During the selection of the frequency points some wrong points might have been selected. The wrong track points would have assigned the wrong frequency to the 405-kyr cycle, which changes the duration of all the other spectral peaks and as a result a ~300-kyr cycle might show up in the depth-time converted spectral record.

The fourth theory is that the interpretation of the different cycles is wrong. This option has already been elaborated upon in chapter 5.2.3.

5.5.2 405-kyr cycle

The Redfit spectrum of well G14-05 GR in the time domain show a high spectral power peak for the 405-kyr cycle. This is in line with the spectra in the depth domain which showed high spectral power for the 15-22 m cycle which is interpreted as the 405-kyr eccentricity cycle. The spectral peak of the 405-kyr cycle in well G14-05 GR also has a small width. The small width gives a higher confidence to the hypothesis that the 15-22m cycle is indeed the 405-kyr eccentricity cycle in well G14-05 GR. The EHA spectra of G14-05 GR contains high power peaks for the 405-kyr cycle, but the 405-kyr cycle is less well defined in the Hilbert transformed spectrum. The Redfit spectra of well G17-S01 Th in the time domain shows low spectral peaks for the 405-kyr cycle. The power of the spectral peak of the 405-kyr cycle is low, but the 405-kyr cycle peak still has as significance of 90%. The Redfit spectra of well G17-S-01 Th do also have low spectral power in the depth domain. The low power spectral peak for the 405-kyr cycle calls into question the

accuracy of the (eventual) tuning of well G17-S-01 Th. The EHA spectra of G17-S-01 Th do show an almost straight line with spectral power for the 405-kyr cycle, which increases the confidence in such a tuning.

5.5.3 700-1000-kyr cycle

A broad spectral peak of 700-1000-kyr was identified from the spectral analysis in the time domain. This spectral peak was not identified in the depth domain. The reason this cycle was overlooked was because the 700-1000-kyr cycle is only intermittently present with depth in the EHA spectra. Spectral power of the 700-1000-kyr cycle is concentrated in intervals were the power of the 1200-kyr cycle decreased. A connection between the 1200 and 700-1000-kyr cycle is possible because both the 1200 and 700-100-kyr cycles modulate the obliquity signal (Hinnov, 2000; Lourens and Hilgen, 1997). The 812-kyr cycle is represented by the s4-s3+g4-g3 fundamental frequency combination but is complicated by the presence of the g1-g5 977-kyr eccentricity cycle (Hinnov, 2000; Laskar et al., 2004). Because of the broad peak it is hard to asses, which part of the peak can be attributed to the 812 cycle and which part can be attributed to the 977ky cycle.

5.5.4 1200 and 2400-kyr cycle

Spectral analysis using the Redfit technique in the time domain does not show the strong 1200-kyr signal and weak 2400-kyr observed in the spectral analysis in the depth domain. In the regular spectra, the 1200-kyr cycle has 2 distinct peaks at 1100 and 1200-1600ky. The 1200ky cycle can be observed in the Hilbert amplitude demodulated spectra. Spectral analysis using the EHA technique in the time domain shows low spectral power for the 1200-kyr peak, while there is a strong (continuous) presence of the 1200-kyr cycle in the Hilbert amplitude demodulated spectra. The fact that the 1200ky cycle can best be observed in the Hilbert transformed spectra might indicate that the contribution of 1200ky cycle to signal is mainly restricted to as a modulating effect. The Redfit and EHA spectra of the 2400-kyr cycle contain high spectral power peaks in both the normal spectra and in the Hilbert transformed spectra. The EHA spectra of G14-05 GR Hilbert transformed and G17-S-01 Th both show a notable decrease in the power and a shift towards a shorted period for the 2400ky cycle.

5.6 Bandpass filtering in the time domain

A bandpass filtering in the time domain of was performed on the gamma ray record of well G14-05 and the thorium record of well G17-S-01 (see Figures 54 and 55). The records were filtered on the 100, 200, 405, 1200, 2400, 3500 and 9500-kyr periods to highlight the overall contribution of the different cycles to the general record and to highlight the possibility of modulation between the different cycles.

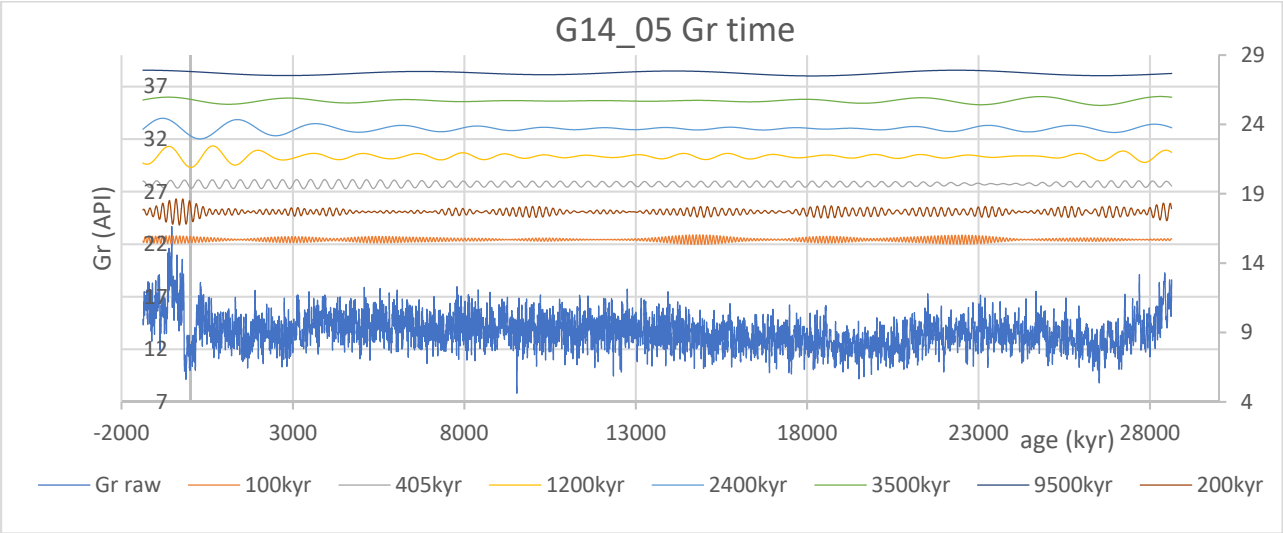

Figure 54. G14-05 GR in time and with bandpassed periods. Note that the timescale is floating.

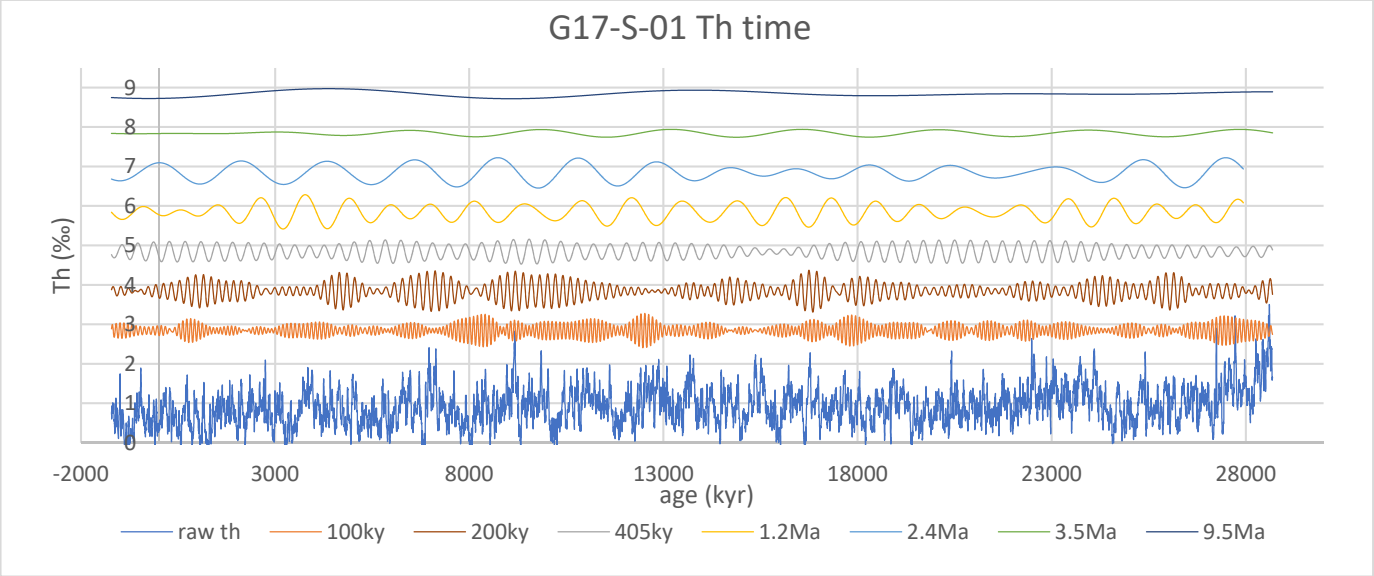

Figure 55. G17-S-01 Th in time and with bandpassed periods. Note that the timescale is floating.

5.7 Tuning options

No definite orbital phase relationship exists for the Chalk of the North Sea area and therefore two tuning options are possible; an eccentricity minimum and an eccentricity maximum tuning option (Figure 56 and 57). In the eccentricity minimum option the peaks in the GR or Th records are coupled to the 405-kyr eccentricity minima of a 405-kyr bandpass filtered signal of the La2010a solution. In the eccentricity maxima option the peaks in the GR or Th records are coupled to 405 eccentricity maxima of a 405-kyr bandpass filtered signal of the la2010a solution. With the help of biostratigraphy, the location of the K/Pg boundary has been identified as being at or near the S-crossing above the third peak beneath the top Chalk reflector. The seismic reflector based K/Pg boundary narrows down the location to a single 405-kyr cycle which still gives and uncertainty of 15-22m. According to the tuning option 2 of Husson et al. (2011) the K/Pg boundary is located just above an eccentricity minimum at 66Ma years. Peaks in the GR and Th records can correspond to either an eccentricity maxima or a minima, which results in two positions for the K/Pg boundary and subsequently in two tuning options. The K/Pg boundary is just past a peak in the 405-kyr bandpassed filtered record in the tuning option where peaks in the GR and Th records correspond to an eccentricity minima or the K/Pg boundary is just past a through in in the 405-kyr bandpassed filtered record in the tuning option where peaks in the GR and Th records correspond to an eccentricity maxima. It should be noted that there is an uncertainty with the pick for the location of the K/Pg boundary. There is about a 5m interval in the depth domain at which the K/Pg in boundary can be placed. At the top of the Chalk Group the EHA spectra indicate that the 405-kyr cycle has a period of ~20m and thus the ~5m an uncertainty results in a time uncertainty range of ±55 kyr for the K/Pg boundary. The uncertainty range of ±55 kyr should also be accounted for when inferring any ages for the tuning options.

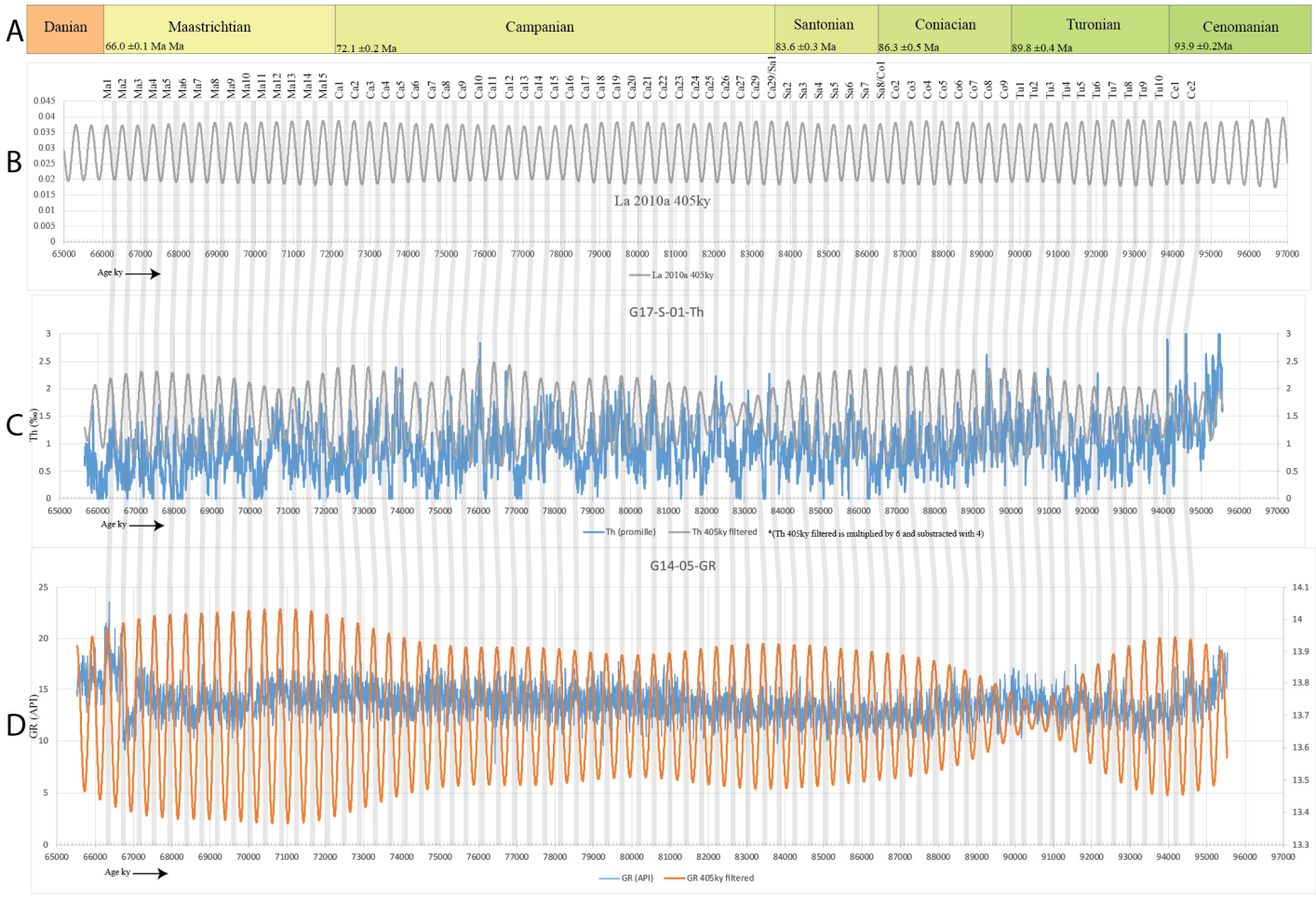

figure 56. Eccentricity minimum tuning option. Ages and uncertainties for the stage boundaries are from (Ogg et al., 2012). A. The colour scheme is from the International chronostratigraphic chart 2016/12 (Cohen et al., 2013). B. 405-kyr La2010a peaks are extracted with help of a bandpass filter of the La2010a solution (Laskar et al., 2011a). The naming scheme of the eccentricity maxima consists of two first letters of the stage and a number for the position of the peak (numbers increase from young to old). If a peak could be within either stage a double name is given to the peaks. The naming scheme is a continuation of the scheme of Husson et al. (2011). C. (405-kyr bandpassed) record of G17-S-01 Th. D. (405-kyr bandpassed) record of G14-05-GR

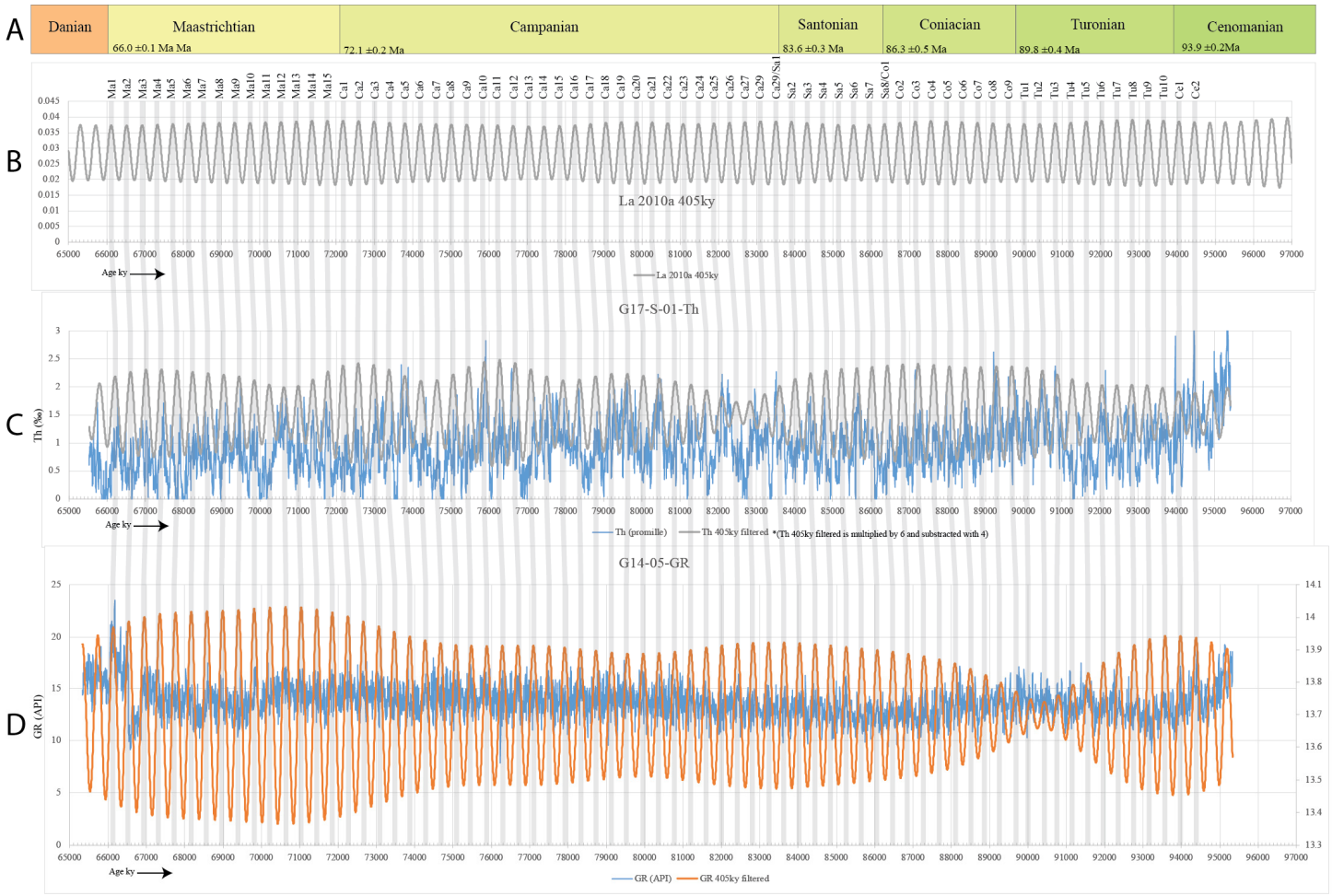

figure 57. Eccentricity maximum tuning option. Ages and uncertainties for the stage boundaries are from (Ogg et al., 2012). A. The colour scheme is from the International chronostratigraphic chart 2016/12 (Cohen et al., 2013). B. 405-kyr La2010a peaks are extracted with help of a bandpass filter of the La2010a solution (Laskar et al., 2011a). The naming scheme of the eccentricity maxima consists of two first letters of the stage and a number for the position of the peak (numbers increase from young to old). If a peak could be within either stage a double name is given to the peaks. The naming scheme is a continuation of the scheme of Husson et al. (2011). C. (405-kyr bandpassed) record of G17-S-01 Th. D. (405-kyr bandpassed) record of G14-05-GR.

6. Discussion

6.1 Astronomical cycles and age model

6.1.1 Gaps, tie-points and the sedimentation rate

Currently only the K/Pg boundary and the Plenus Marl are used as tie-points for the tuning options. The biostratigraphic data yielded a reliable interpretation of the K/Pg boundary but the definition of other stage or biozone boundaries is harder. Especially so if these stage boundaries need to be correlated to other wells. The Plenus Marl (OAEII) is the mayor tie point besides the K/Pg boundary. The tie-point of the Plenus Marl was based on the log response of the gamma ray and sonic logs. The Plenus Marl coincides with OAEII, which has an age of ~94 Ma and is situated just below the Cenomanian-Turonian boundary (Eldrett et al., 2015; Meyers et al., 2012; Ogg et al., 2012; Schlanger et al., 1987a). The K/Pg boundary and OAEII tie-points are ~28 Myrs apart. Large shifts in the sedimentation rate could have occurred within these 28 myrs or even hiatuses could be present in the record. The EHA spectra were interpreted with an age of 94 Ma in mind for the Plenus Marl. The absence of additional tie points between the K/Pg boundary has biased the tuning results towards a tuning without hiatuses and an age of ~94 Ma for the Plenus Marl. The EHA based sedimentation rate curve was picked/modified to create the best available bandpassed fit with the 405-kyr cycle and still have a resulting age for the Plenus Marl of ~94 Ma. Basing the age of the Plenus Marl on literature and subsequently tuning to that age does carry a component of circular reasoning. The best argument against circular reasoning are the eASM results and seismic data. The eASM results independently indicated a sedimentation rate between 3 and 7cm/kyr and the seismic data did not indicate any major hiatuses on the Schill Grund Platform, suggesting a complete succession. Additional tie points are required to put extra constraints on possible hiatuses, changes in the sedimentation rate and to increase the confidence in the hypothesis that the 15-22 m cycle represents the 405-kyr eccentricity cycle.

The best hint for perturbations in the well-log records is the smearing effect in the EHA spectra (Figure 58). The smearing effect manifests itself as a horizontal line in the EHA spectra. At a smearing interval, the power and/or the frequency of the cycles promptly change and a stretched or smeared effect is observed. The main reasons behind the smearing effect are rapid changes in the sedimentation rate, the presence of hiatuses or changes in the duration of a cycle. It is virtually impossible to distinguish between sedimentation rate change or hiatus induced smearing by purely looking at the EHA spectra. Smearing features should therefore be approached with caution when an EHA spectra is used to construct a cyclostratigraphic framework.

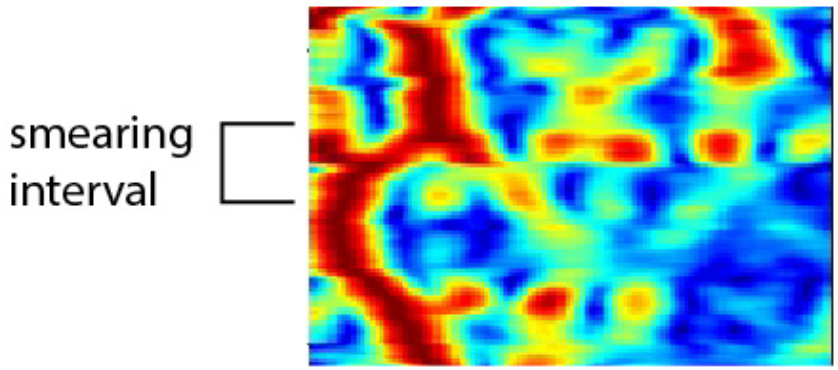

Figure 58. G17-S-01 Th smearing example from the 0.01 to 0.1 frequency

The eASM and the EHA based depth-time conversion techniques generated sedimentation rate graphs. The EHA derived sedimentation rate already includes a manual selection/interpretation step, while the eASM technique is based on the relationships between different depth frequencies and orbital frequencies. The eASM and EHA derived sedimentation rates are similar, which increases the confidence in the 15-22 m / 405-kyr hypothesis. The eASM derived and EHA derived sedimentation rates are in the range of most of the literature, which furthermore increases the confidence in the 15-22 m / 405-kyr hypothesis (see chapter *2.2.5*).

The eASM technique can only give an estimation of the sedimentation rate because the optimal sedimentation rate scenario is based on the relationship between multiple orbital cycles. The eASM derived sedimentation rates does not

show a single line as an optimal high power sedimentation rate but rather shows multiple parallel yet discontinuous high significance streaks. The discontinuity of these streaks might indicate the presence of hiatuses. Only the 405-kyr cycle is stable during the Late Cretaceous which means that the ratios between the different cycles is not constant. The eASM technique requires orbital cycles to be constant and have an uncertainty. The exact periods and variation/uncertainty of the orbital cycles are less well known for the late Cretaceous and the eASM results therefore carry a large degree of uncertainty. The uncertainty regarding the chaotic behaviour of the 2.4 Myr cycle impairs the reliability of the eASM results even more.

The EHA derived sedimentation rate carries a degree of error in interpretation does creates uncertainty. The EHA derived sedimentation rate is based on the depth frequency relationship with the 405-kyr cycle, which is manually defined in a graphical user interface. It is up to the user to select the correct data-points and to quality check the results. Which data point is the correct data-point depends on the goal of the user which could be: to have the least variance in the sedimentation rate, the best fit between the filtering of a specific cycle and the raw data, the best fit without hiatuses or only having the data-points with highest spectral power. Different goals result in different sedimentation rates, which subsequently impact a depth-time conversion using the EHA derived sedimentation rate

Both the eASM and EHA derived sedimentation rates indicate an increase in the sedimentation rate towards the top of the Chalk Group. This observation is confirmed by the EHA spectra which indicate an increase in the length of the period of the 15-22 m 405-kyr cycle towards the top of the Chalk Group. An example is well G10-02, where the 15-22 m / 405-kyr cycle increases from a ~16 m period at the bottom of the Chalk Group to a ~20 m period at the top of the Chalk Group (Figure 85). The shift in the period can be explained by an increase in the sedimentation rate and a lower compaction rate towards the top of the Chalk Group. The increase in the cycle thickness from 16 to 20 m can be explained by using the already calculated 12% increase in sedimentation rate (chapter 4.3.1) and the 15% compaction factor (chapter 4.3.3). The increase in the sedimentation rate and the compaction factor together explains the increase in the period. A similar shift in the period can be observed in the in the 40-60 m / 1200-kyr cycle. The 1200-kyr cycle increases from a 50 m period at the bottom of the Chalk Group to a of 60 m period at the top of the Chalk Group (Figure 86). The periods of both cycles increase but their ratio remains the same (1:3). The stability of the ratio gives additional proof of a possible 1200 and 405-kyr cycle relationship and provides an additional confirmation for the 15-22 m / 405-kyr cycle hypothesis.

6.1.2 Cycles in seismics data?

The repetitive pattern observed in the seismic data of the Chalk Group is a feature, which could be caused by climatic and non-climatic perturbations.

The repetitive cycles in the seismic data could be caused by multiples, which are a seismic artefact. Multiples are caused by internal reflections of the seismic wave within the subsurface, which causes a single layer to produce multiple equally spaced reflectors beneath it. Multiples often crosscut other seismic reflectors and can therefore be distinguished from the true seismic signal. No multiples appear to be present in the Chalk Group, although the conformable nature of the Chalk Group might induce internal multiples within the Chalk Group. This option is not likely because the seismic data does not show any features which might be related to the occurrence of multiples.

The cyclic pattern could also be an inherent feature of the seismic signal. One could argue that when a seismic wave is sent, a wave and thus a period always comes out. It is indeed correct that the seismic trace has a sinusoidal shape but the sinusoidal shape is due to the change in sonic travel time. The seismic velocity of the wave creates the seismic amplitude signal and not the sinusoid of the seismic wave itself. The change in the seismic velocity is inherently linked to the velocity of the formation which is linked to lithology. The seismic to well tie did in fact show a clear relationship between the sonic and gamma-ray logs and the seismic signal, thus proving that the lithology is the main source of the seismic reflector pattern. If changes in the lithology are caused by astronomical cycles and these lithological variations are recorded in the seismic signal then a modulation of the seismic signal by astronomical cycles is possible.

The primary signal of seismic data appears to be modulated by a 40-60 m / 1200-kyr cycle. The seismic to well tie indicated that an increase in the sonic or gamma ray readings corresponds to a positive reflector. A maximum positive slope in the 50 m / 1200-kyr filtered well-log cycle is therefore coupled to a positive seismic reflector. The spectral analysis of the extracted traces further proved the existence of the 1200-kyr cycle with a spectral power peak around 50

m. The filtered sonic log, (un)filtered seismic data and filtered traces indicate that there are ~23/24 1200-kyr cycles in between the K/Pg boundary and the Plenus Marl (Figures 47,48 and 101-117). This results in a 27.6-28.8 Myr duration of the Maastrichtian-Turonian interval and an age estimate between 93.6 and 94.8 Ma for the Plenus Marl layer. The base of the CIE-A event corresponds to the middle of the Plenus Marl (Jarvis et al., 2006) and is dated at 94.68 ± 0.16 Ma (Eldrett et al., 2015). The age of Eldrett et al. (2015) overlaps with the ages indicated by the 1200-kyr seismic cycles, which further strengthens the arguments for the existence of the 1200-kyr cycle and a modulation of the seismic signal by the 1200-kyr cycle.

Besides the 1200-kyr, 2400 and 3500-kyr cycles are also present in the spectra of the seismic traces. The 3500-kyr cycle shows an especially strong modulation of the seismic signal in the bottom part of the Chalk Group near well G10-02 (Figures 47 and 48). The low modulating effect of the 2400-kyr cycle and the strong modulating effect of 3500-kyr cycle is in line with the spectral analysis of the seismic trace data, which shows a high spectral power for the 3500-kyr peak but a low spectral power for 2400-kyr peak. The strong parallel continuous reflectors (CK3, CK4, CK5, CK6?) used by van der Molen (2004) as seismic stratigraphic boundaries for the Dutch Chalk Group coincide with 3500-kyr maxima of the filtered trace record and maximum positive slope values for the 3500-kyr cycle filtered from the well-logs. Van der Molen (2004) already indicated that a non-tectonic origin for these strong parallel continuous reflectors could be possible. If the origin of the CK3, CK4, CK5 and CK6? seismic sequence boundaries are indeed of a non-tectonic origin then the boundaries are most likely created by a modulation of the sedimentary system by the 3500-kyr eccentricity cycle.

6.1.3 Proof of chaos or just the data?

Before 50 Ma, the 1200-kyr obliquity and 2400-kyr eccentricity cycles had a 2:1 secular resonance expressed as the 2(g4−g3)=(s4−s3) principal frequency terms (Laskar, 1999; Laskar et al., 2011a, 2004). Between 50 and 100 Ma the secular resonance is proposed to have changed from the 2(g4−g3)=(s4−s3) fundamental frequency combination to the (g4−g3)=(s4−s3) fundamental frequency combination (Laskar, 1999; Laskar et al., 2011a, 2004). The change in the resonance between the fundamental frequency combinations changes the 2400-kyr eccentricity cycle to a 1200-kyr cycle eccentricity cycle. The relatively low spectral power of the 2400-kyr cycle and the high spectral power of the 1200-kyr cycle in the depth domain could be indicative of the chaotic behaviour between the orbits of Mars and Earth between 50 and 100 Ma ago (Figures 42, 51, 52 and 83).

The strong expression of the 1200-kyr cycle and the weak expression of the 2400-kyr cycle is also observed in the spectral analysis of the seismic trace data (Figures 47, 48 and 101-107). The filtered well-logs and filtered trace data of the 1200-kyr cycle seems to have a relatively strong modulation effect on the seismic signal while the 2400-kyr cycle does not show any modulation of the seismic signal at all. The 2400-kyr cycle is only represented by a vague spectral peak, while the 1200-kyr cycle has a strong spectral peak. The 2400-kyr also has a period mismatch between the trace and well-log data. The 2400-kyr period has a cycle period of ~105m in the well-logs, while the period is 80-100 m in the seismic data. This cycle period mismatch does impair a proper assessment of the of chaos in the solar system.

The EHA spectra of the seismic and well-log data in the depth domain show an increase in the spectral power of the 3500-kyr cycle towards the bottom of the Chalk Group (Figures 42, 51, 52 and 83). To date no clear expression of the 3500-kyr cycle has been observed in the Cenozoic. The absence of the 3500-kyr cycle in the Cenozoic is peculiar ,especially because the 3500-kyr cycle is distinctly present in the Mesozoic and Palaeozoic (Ikeda et al., n.d.; Ikeda and Tada, 2014, 2013; Olsen and Kent, 1999; Sprovieri et al., 2013; Tassell, 1988). The 3500kyr cycle is explained by the g2 +g4 −g3 −g5= 3463.318-kyr fundamental frequency combination, which contains the g4 −g3 fundamental frequencies which also governs the 2400kyr cycle. A coupling between the behaviours of the 2400kyr cycle and 3500kyr is therefore likely. The increase in the power of the 3500-kyr cycle and the chaotic behaviour of the 1200 and 2400-kyr cycles might well be indicative for the chaotic behaviour of the solar system during the Late Cretaceous.

The Redfit spectral analysis in the time domain does not show the strong 1200-kyr signal and weak 2400-kyr observed in the spectral analysis in the depth domain. The 1200-kyr cycle in the Redfit spectra in the time domain is split into a 1100 and 1200-1600-kyr cycle. The spectral expression of the 1200-kyr cycle in a post depth-time conversion setting is problematic and calls into question the quality of the data, the quality of the time-depth conversion and the chaos interpretation for the data in the depth domain. A single spectral peak for the 1200-kyr cycle is present but only in the Hilbert transformation transformed Redfit spectra. The EHA spectra of G14-05 GR and G17-S-01 Th in the time domain

shows a more mixed picture. The G17-S-01 Th Hilbert EHA spectrum shows a continuous high spectral power trace for the 1200-kyr cycle, while the 1200-kyr cycle is less clearly observed in the other spectra. Between 75 and 80 Ma the EHA spectrum of G17-S-01 Th shows gradual drop in the period of the 2400-kyr cycle. The period of the 2400-kyr cycle in the EHA spectrum of G17-S-01 Th returns to a 2400-kyr duration at 85 Ma. Between 80 Ma and 85 Ma the period of the 2400-kyr cycle is reduced in the EHA spectrum of G14-05-GR-Hilbert. The 2400-kyr signal is discontinuous and the spectral power is low in the spectra of G17-S-01 Th Hilbert and G14-05-GR. The low spectral power in the time domain and the splitting into multiple spectral peaks hinders an exact interpretation for the duration of the 1200-kyr cycle. A better constrained 405-kyr based timescale could enable a more complete assessment of dynamics behind the 1200-kyr cycle in the depth domain.

Modulation of different cycles is one of the best pieces of evidence for an astronomical connection between different the cycles. The clearest modulation between the different cycles can be observed in the bandpassed filtered records in the depth domain (Figure 45). A reason for the poorer phase relationship between the different filtered records in the time domain could be due to the smaller frequency windows used in the time domain when compared to the frequency window in the depth domain. Two clear phase relationships can be observed. The first is the relationship between the 40-60m / 1200-kyr cycle and the 4-6m / 100-kyr short eccentricity cycle. The 1200-kyr cycle observed in this research might have an eccentricity component which is explained in the shift in the secular resonance between 50 and 100 Ma changing the 2400-kyr eccentricity cycle to a 1200-kyr eccentricity cycle. If the 1200-kyr cycle is indeed an eccentricity cycle then the modulation of 100-kyr eccentricity cycle by the 1200-kyr cycle is within the realm of expectations and it could prove the chaotic behaviour of the solar system during the Late Cretaceous. The presence of chaos does complicate the modulation between different cycles. The fundamental frequency combination which make up the short eccentricity cycles and the 2.4 Myr cycle is governed by the fundamental frequency combinations (g4 −g5) – (g3 −g5) = 1/95-1/99 = 2.4 myrs and (g4 −g2) - (g3 −g2) = 1/124-1/131 = 2.4 Myr. All short eccentricity cycles contain either the g4 or g3 term, which will change the period of the short eccentricity cycle when the resonance change when the 2.4 Myr eccentricity cycle to a 1.2myr eccentricity cycle. The 1200-kyr cycle could be an obliquity cycles, which in turn modulates a 100-kyr of obliquity origin. The 100-kyr short eccentricity is usually modulated by the 405-kyr long eccentricity, but in this study the modulation of the small eccentricity cycle by the large eccentricity cycle is virtually non-existent, which might hint to an obliquity origin for the 100-kyr cycle. The modulation effect of the 1200-kyr cycle is supported by the Hilbert transformed spectra in the time domain. The 100-kyr cycle can be explained as an amplitude-frequency resonance effect of the obliquity cycle (Liu, 2001, 1992). If the 100-kyr cycle has an origin in the obliquity cycle then a modulation by the 1200-kyr obliquity cycle is possible. The second phase relationship is between the 300-400m 3500-kyr cycle and the 15-22m 405-kyr cycle. A modulation of the of the 405-kyr eccentricity signal by the 3500-kyr eccentricity signal is logical because both cycles are eccentricity cycles. The modulation between the 405-kyr eccentricity and the 3500-kyr cycle does indicate that eccentricity is the main orbital parameter influencing the lithology. It therefore makes sense that both the 100-kyr and the 1200-kyr cycles have an origin in the eccentricity parameter.

The presence of a strong 1200-kyr cycle and a weak 2400-kyr cycle has been documented for multiple late Cretaceous records (Batenburg, 2013; Batenburg et al., 2014, 2012; Laurin et al., 2015; Ma et al., 2017; Mitchell et al., 2008). A $\delta^{13}C$ composite record of section consisting of the English chalk, the Apennine carbonate chert alternations and a core from the Saxony basin all contain a 1 Myr obliquity cycle (Laurin et al., 2015). Laurin et al. (2015) correlates the strong 1 Myr obliquity cycle to variations in storage and release organic carbon or methane quasi-stable high latitude reservoirs. The quasi-stable reservoirs in which organic carbon or methane can be stored and released are wetlands, soils, marginal zones of marine euxinic strata, or permafrost. Models indicated that a nonlinear response of the quasi-stable reservoirs by means of changes in the high-latitude obliquity insolation signal are required to produce a 1Myr perturbation of the carbon cycle. The burial, storage and release organic carbon of or methane is either controlled via direct changes in the insolation or controlled by an interconnected system which is mediated by different oceanographic and climatic mechanism. According to Laurin et al. (2015) a non-linear response of the quasi-stable reservoirs is most likely the result of the chain mechanism influencing the burial, storage and release organic carbon of or methane.

Batenburg (2013) and Batenburg et al. (2014, 2012) did find a 1.2 Myr cycle between 70-66 Ma in the Zumaya and Sopelana sections in northern Spain. Batenburg (2013) and Batenburg et al. (2014, 2012) gave four explanations for the existence of the 1.2 Myr cycle. The first is explanation is that the 1.2 Myr periodicity is present as an obliquity cycle, however no strong imprint of the short obliquity cycle was found in the data. The second explanation is that the 1.2 Myr cycle is the result of a chaotic resonance period of the 2.4 Myr eccentricity cycle. The third explanation is that the 1.2

Myr cycle is the result of an underlying climatic or tectonic trend. The fourth explanation is that the 1.2 Myr cycle is the result of tectonic pulses. These pulses would been of regular occurrence and tectonic pulses do not explain the intervals of reduced amplitude of the 100-kyr cycle. Ma et al. (2017) documented a chaotic resonance period for the 2.4 Myr and 1.2 Myr cycles during the late Cretaceous in the Western Interior Basin. The 2.4 Myr cycle transitioned to a 1.2 Myr cycle between 85 and 87 Ma. The transition indicated by Ma et al. (2017) is in contrast to the transition found in this thesis. The transition to a dominant 1.2 Myr cycle already starts at 80 Ma in this study and seems to continue past the Plenus Marl (see Figure 51 ,52 and 59). The main interval during which the 2400-kyr cycle is reduced is in-between 80 and 85 Ma (see Figures 51,52). The timing of the transition from the 2(g4−g3)=(s4−s3) fundamental frequency combination to the (g4−g3)=(s4−s3) fundamental frequency combination should occur at the same time everywhere. The transition to a dominant 1200-kyr cycle at 80 Ma in this study, at 66-70 Ma in Batenburg (2013) and Batenburg et al. (2014, 2012) and at 85 Ma in Ma et al. (2017) indicates that there is still a problem regarding the timing for onset of the chaos in the solar system.

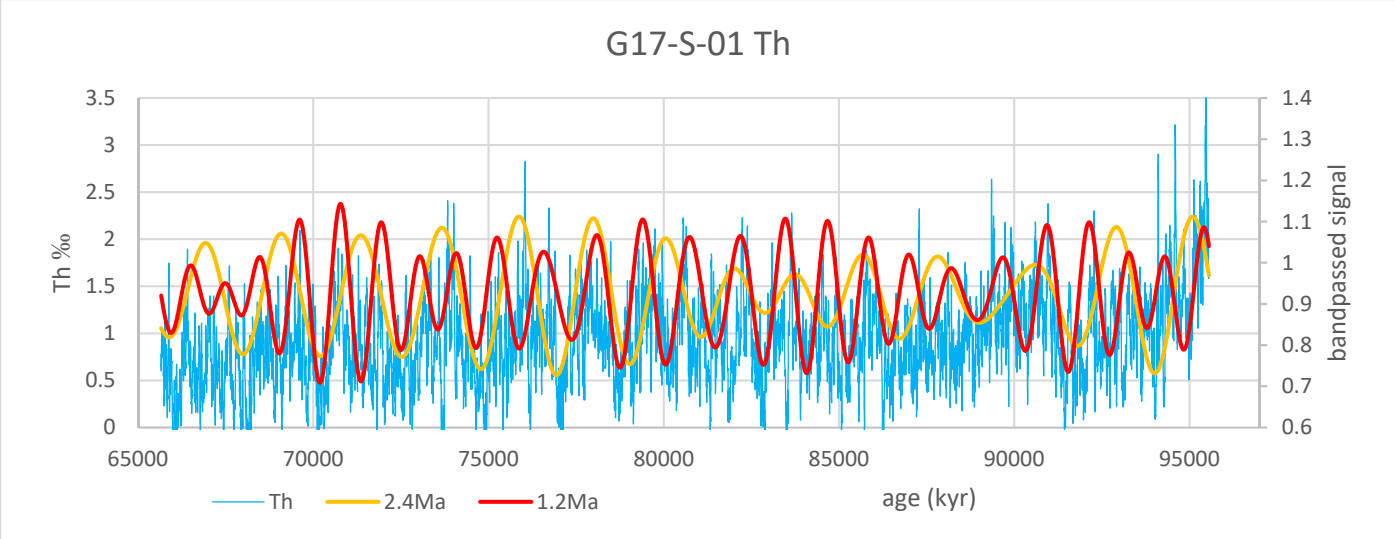

Figure 59. G17-S-01 Th with bandpassed record of the 2400-kyr and 1200-kyr period

6.1.4 Tuning the late Cretaceous record

The tuning of G14-05 GR and G17-S-01 Th to the La2010a solution is still preliminary and could still benefit from more refinement. The current tuning already highlights some notable features. Both the G14-05 GR and G17-S-01 Th tuning options contain the same amount of 405-kyr cycles, which further increases the confidence in the tuning. The exact ages of the peaks of the tuned records and the ages for the peaks of 405-kyr bandpassed La2010a solution do differ, but difference is never more than half an eccentricity cycle. A final tuning by assigning the ages of filtered peaks of the 405-kyr period bandpass filtered record of the La2010a solution to the 405-kyr period filtered peaks of the G14-05 GR and G17-S-01 Th records should be possible. For a definite tuning it is also important to check the fit with all the astronomical solutions (La2010a-d and La2011) (Laskar et al., 2011a, 2011b). The fit with the La2010a solution is quite good but another astronomical solution might even have a better fit. The 405-kyr filtered records of G14-05 GR and G17-S-01 Th do have sections with reduced amplitude for the bandpassed 405-kyr cycle. The reduced amplitude indicates a problem with the filtering, which could be due to a wrong pick in the EHA time-depth conversion process, hiatuses, rapid changes in the sedimentation rate, astronomical perturbations and climatic event perturbations in the record.

The presence of the 300 and 700-100-kyr cycle is still problematic and reduces the overall confidence in the interpretation of the cycles. A similar problem with the presence of the 300 and 700-100-kyr cycle has been observed in the Cenomanian Scaglia Bianca in Italian Apennines (Mitchell et al., 2008). Mitchell et al. (2008) found a 355, 675 and 810-kyr cycle. The 355-kyr cycle was interpreted as being part of the 405-kyr eccentricity cycle. The 675-kyr cycle was interpreted as a 700-kyr eccentricity cycle. Mitchell et al. (2008) does note that the 675-kyr has a much higher

spectral power then the 405-kyr cycle, for which Mitchell et al. (2008) does not have an explanation. No explanation was given for the 810-kyr cycle even though it was result from a Hilbert transformation of the precession signal.

The K/Pg boundary is located just past to an eccentricity minima (Husson et al., 2011). The combination of the filtering of the gamma ray on 15-22m 405-kyr cycle and the dinoflagellate biostratigraphy of well A12-02 indicates that K/Pg boundary is located just below a minimum in the filtered gamma ray (Figure 60). The location of the K/Pg boundary agrees with the eccentricity maximum tuning. The location of the K/Pg boundary can only be laterally extrapolated using the seismic data and thus the uncertainty of the K/Pg boundary is the thickness of one reflector.

The preferred tuning results in an age of 93.840 ± 0.11 Myr* for the Cenomanian Turonian boundary. This is in line with Meyers et al. (2012b) which has a radiometrically and cyclostratigraphically constrained age of 93.90 +0.07/-0.09 (± 0.15Ma) for the Cenomanian-Turonian boundary in the Western Interior Basin (USA). There is a slight age difference with radiometrically and cyclostratigraphically constrained age of Eldrett et al. (2015) which arrived at an age of 94.10 ± 0.33 Ma or 94.19 ± 0.35 Ma for the Cenomanian-Turonian boundary in the Southern Western Interior Basin. Although there is a difference with Eldrett et al. (2015), the age of the Cenomanian-Turonian boundary of this study and that of Eldrett et al. (2015) still overlaps when considering the uncertainty ranges.

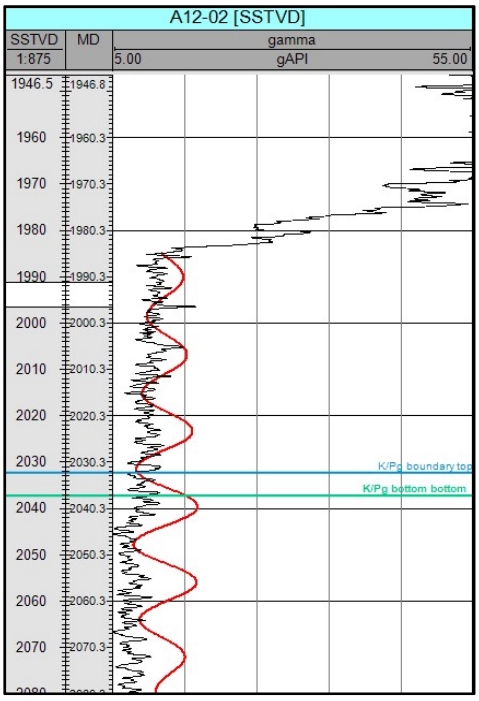

Figure 60. K/Pg boundary in Well A12-02 top and bottom K/Pg are based on the dinoflagellate study in this study.

6.1.4.1 Other cyclostratigraphic studies of the Chalk

Perdiou et al. (2015) conducted a cyclostratigraphic analysis on the Adda core from the Danish part of the Danish-Norwegian Central Graben. $\delta^{13}C$, Fe concentration and gamma ray measurement were analysed using the MTM spectral analysis method. Perdiou et al. (2015) identified spectral peaks with of periods ~4 m, ~1 m and ~25 cm (for interpretation by author see table 6). Perdiou et al. (2015) did not investigate cycles longer than the ~4 m eccentricity cycle, which might have given more confidence to the identification of the ~4 m 405-kyr cycle. The resulting sedimentation rate is ~10mm/kyr, which is relatively low in comparison to other literature (see chapter 2.2.5). An $\delta^{13}C$ excursion within the core was identified as the late Campanian isotope excursion (LCE). If the sedimentation remains constant between the LCE and the Plenus Marl (OAEII) then there will be a hiatus of ~19 Myr within this 85 m interval. No hiatus was mentioned in the article of Perdiou et al.

Table 6.				
Cycle	This study (period m)	Perdiou et al., 2015 (period m)	Voigt and Schönfeld, 2010 (period m)	Thibault et al., 2016 (period m)
Precession 23-kyr	0.8-1.2 m (predicted, not observed)	25 cm		0.75-0.56 m
Obliquity 40-kyr	1.4-2.2 m (predicted, not observed)			1.18 m
Short eccentricity 100-kyr	4-6 m	1 m	2.5 m	4.2 m
Long Eccentricity 405-kyr	15-22 m	4 m	9.6 m	16 m

Table 6. Comparison between this study and 3 other cyclostratigraphic studies of the Chalk Group in the North Sea. Indicated are periods metres of the different astronomical cycles identified in their respective studies. For the prediction of the period of the precession and obliquity cycle of this study see chapter 5.2.1.

* Because there is a 5m pick uncertainty with the K/Pg boundary and a similar pick uncertainty with the Cenomanian-Turonian boundary the total pick uncertainty is 10m. Using the 15-20m 405-kyr cycle hypothesis this results in an uncertainty of ±110kyr.

(2015), but it was mentioned that previous research inferred a Cenomanian to Santonian age for the Adda core. When taking the Plenus Marl age into account a negative excursion event such as the Haven brow event near the Coniacian-Santonian boundary (Jarvis et al., 2006) might be a better fit with observed $\delta^{18}O$ and $\delta^{13}C$ excursion.

Voigt and Schönfeld (2010) created a Campanian–early Maastrichtian floating timescale for the Lägerdorf–Kronsmoor section. The floating timescale was linked to spontaneous-potential logs for a basin wide correlation. The record consists of chalk with varying amounts of detrital clay. The Blackman-Tukey power spectra of the carbonate record showed spectral peaks with periods of 9.6 and 2.5 m (for interpretation by author see table 6). The 9.6 m / 405-kyr cycle is significantly thinner than the 15-22 m cycle found in this research. A thinner cycle would indicate significantly lower sedimentation rates. The Lägerdorf–Kronsmoor section is located more proximal setting which might explain the lower sedimentation rate.

Thibault et al. (2016b) studied the upper Coniacian to lower Campanian succession at the Seaford Head section in south eastern England. Bulk $\delta^{18}O$ and $\delta^{13}C$ measurements were performed on the samples and spectral analysis using the MTM method was performed on the $\delta^{13}C$ $\delta^{18}O$ record, which indicated spectral peaks with periods of 16, 4.2, 1.18 and 0.75-0.56 m (for interpretation by author see table 6). In the MTM spectra the obliquity peak for the $\delta^{18}O$ peak was much larger than the of $\delta^{13}C$ peak. Thibault et al. (2016b) explained the larger expression of obliquity for the oxygen isotope by the fact that organic carbon has a long residence time of more than 200-kyr. The average spectral misfit method was used to check the interpretation, which confirmed the MTM spectral data. Thibault et al. (2016) proposed two phase relationships between $\delta^{13}C$ and eccentricity. In the first relationship, the $\delta^{13}C$ maxima correspond to eccentricity maxima. Thibault et al. (2016) linked carbonate poor intervals in the Western Interior Basin to eccentricity maxima. The continental weathering rate increases during eccentricity maxima, which leads to a higher nutrient flux. An increase in the nutrient flux results in an increase of marine productivity and thus a higher organic burial rate. $\Delta^{13}C$ increases due to preferential fractionation of 12C during photosynthesis. A $\delta^{13}C$ minima corresponds to an eccentricity maximum in the second relationship. During an eccentricity maxima weathering rates increase and the continental flux of lighter $\delta^{13}C$ HCO3-, increases, which leads to a decrease in $\delta^{13}C$. During eccentricity minima $\delta^{13}C$ increases by higher removal as $\delta^{13}C$ in form of carbonate. The eccentricity minima option is favoured by Thibault et al. (2016b). Thibault et al. (2016b) did not make a correlation between the $\delta^{18}O$, $\delta^{13}C$ and the lithological records. The $\delta^{13}C$-lithology-orbital phase relationship was extrapolated from the Western Interior Basin (Locklair and Sageman, 2008). The Anglo-Paris Basin and the western interior can have different lithological responses to orbital forcing and it is therefore problematic to extrapolate the $\delta^{13}C$-lithology-orbital phase relationship. The 16m / 405-kyr cycle identified by Thibault et al. (2016b) is similar to the 15-22m / 405-kyr cycle proposed in this research.

6.2 Palaeoclimatological interpretation

6.2.1 Data interpretation

6.2.1.1 Spectral gamma ray

Th/Vshale and K/Vshale cross-plots of wells G14-A-02 and G17-S-01 show a positive correlation (R^2=0.255 to 0.55). The positive correlation indicates that a higher shale content corresponds to higher thorium and potassium content. because thorium and potassium are mainly of a detrital origin the Vshale signal can be interpreted as being primarily a detrital signal. The spread around the trend is larger in the K/Vshale compared to the Th/Vshale. The larger spread could be due to the fact that potassium bearing minerals such as montmorillonite can also precipitate from the porewater, which has previously been observed in other chalk sediments (Jeans, 1968).

The U/Vshale correlation shows an ambiguous signal (well G17-S-01 R^2=0.034 and well G14-05 R^2=0.26) In well G17-S-01 there is a non-correlation while in well G14-A-02 there is a small positive relationship. The ambiguous relationship could be due to fact that uranium can adsorb to coccolith and clay platelets, be fixed to uranyl-tricarbonate in carbonates or precipitate under anoxic conditions. This means that under oxic conditions uranium can be deposited by adsorbing to coccoliths or from uranyl-tricarbonate in carbonate, while under anoxic conditions carbonate dissolves and uranium precipitates directly from seawater. The fact that uranium can adsorb to clay platelets further complicates an interpretation. Because uranium has such an ambiguous signal no interpretation can be given to the uranium signal.

The positive correlation between the Vshale values and potassium and thorium indicates that the Vshale signal is mainly of detrital origin. Because the Vshale is a recalculation of the gamma ray signal it can be concluded that the gamma ray signal is primarily an indicator for the detrital fraction. Even though Vshale is interpreted as a proxy for the detrital fraction, it can still not be determined if the higher detrital fraction corresponds to higher sediment fluxes, lower carbonate productivity or carbonate dissolution.

6.2.1.1.1 Clay mineralogy/uranium origin

Illite, montmorillonite, micas and glauconite are the main constituents of the clay fraction of the Chalk Group sediments (Figure 22). This composition is in line with work of Håkansson et al. (1974), Jeans (1968) and Sumbler (1999) which indicated illite and montmorillonite as the main non-carbonate constituents in chalks of the Chalk Group. The presence of glauconite in the Chalk Group has been noted by Ball (1985), Herngreen and Wong (2007), Jeans (1968), Lauridsen et al. (2009) and Schürch and Buckley (2002). The mica fraction represents all the mica minerals except the montmorillonite and illite mica minerals. The mica fraction only constitutes a relatively small fraction of the mineralogical content. When comparing the clay mineralogy plots of wells G14-A-01 and G17-S-01 there are more data points and a larger degree of scattering of the data points within the montmorillonite segment in the clay mineralogy plot of well G14-A-01. The scattering of the data within the montmorillonite segment of well G14-A-02 is interpreted as the effect of clay mineral precipitation from porewaters (Jeans, 1968). Figure 22 indicates that uranium is mainly of a marine origin with only a minor continental contribution. The Th/U ratio is highest in montmorillonite and progressively lower in illite, micas and glauconite. The difference in uranium content in the different minerals might well be indicative of the ability to adsorb uranium to the platelet surfaces of individual mineral. It is certain that the uranium has a marine origin, but there is still uncertainty regarding the process under which the uranium accumulated. The inconsistent correlation between U and Vshale prevents the discrimination between the accumulation mechanisms in the marine setting.

6.2.1.2 XRF data

The correlation coefficient (R^2) for the different cross plots is low (see Figures 24, 25, Table 7 and S.I. 10.2 Table 8). This can be attributed to the relatively short measuring time per sample leading to a larger measuring error. A shorter measurement time was chosen due to time constraints. The interpretation of the absolute values is unreliable, because of the larger measuring errors due to the short measuring time.

Table 7.

measurement	Proxy for	Reference/explanation
Arsenic	Pyrite	(Thomson et al., 2006)
Sulphur	Anoxic conditions and sulphides formation	(März, 2007; Rothwell and Croudace, 2015)
Rubidium	Detrital content	(Da Silva et al., 2013; Niebuhr, 2005; Rothwell and Croudace, 2015; Tribovillard et al., 2006)
Calcium	Carbonate content	(Rothwell and Croudace, 2015)
Manganese	Oxic conditions	conditions (Algeo and Maynard, 2004; März, 2007; Rothwell and Croudace, 2015)
Rb/Sr	Chemical weathering	(Rothwell and Croudace, 2015)
Vshale	Shale/Detrital fraction	Spectral gamma chapter
Gamma ray	Shale content	Gamma ray and spectral gamma ray chapter
Sonic	Shale content	Sonic chapter
Matrix, RHOB and Sonic derived density	Carbonate/shale content	Shale has a lower density then carbonate thus lower densities can be interpreted a higher shale content, while higher density can be interpreted as higher carbonate content (see chapter 3.2.3).
Core plug measured average porosity and NPHI	Shale content	In the Chalk Group porosity increases in shale rich layers (see porosity chapter)

The interpretation of the XRF data and petrophysical measurements has been performed according to Table 7. The correlation between the elements indicates that the Chalk Group has two settings; an oxic carbonate setting and an anoxic shale enriched detrital setting. In the oxic setting the carbonate content is high (Ca), the oxic element concentration is high (Mn), the porosity is low, the density is high and the anoxic (S), sulphidic (S and As), detrital (Rb and Vshale) and chemical weathering (Rb/Sr) proxies are low. In the anoxic/detrital setting, carbonate content is low, the oxic proxy concentration is low, the porosity is high, the density is low and the concentrations of anoxic, sulphides, detrital proxies are high. For the anoxic/detrital model it still remains unclear whether the increase in

the detrital fraction is due to a higher sediment flux, lower carbonate productivity or carbonate dissolution. The two models also explain the ambiguous signal of the uranium values in the spectral gamma ray data. During the oxic setting uranium can be adsorbed to coccolith platelets and form as uranyl-tricarbonate in carbonates. In the anoxic/detrital setting uranium directly precipitates from the sea-water or uranium is adsorbed to the clay platelets. During both settings uranium can accumulate which explains the ambiguous uranium signal.

6.2.1.3 Core observations

The core observations (chapter 4.6) conforms with the two depositional settings models. At places where the oxic setting is inferred, white chalk is observed, while at places where the anoxic/detrital setting is inferred the grey clay rich chalk facies is present. Pyrite can be observed within the grey chalk (Figures 31,32 and 33). Pyrite is an indicator for anoxic condition, which confirms the inferred anoxic setting for the grey chalks.

Multiple laminae can be observed within the grey chalk interval (Figure 31). In the Danish Central Graben similar laminae are interpreted as low-density turbidity currents (Damholt and Surlyk, 2004). If the laminae observed in well A12-02 have the same origin, then laminae can be linked to periods of increased turbidity derived detrital input. It could be possible that the turbidity frequency was stable and that due to pervasive bioturbation (Figure 27) the laminae were reworked in the white chalk intervals. In the Danish Central graben the preservation of the laminae is thought to be related to episodes of bottom-water anoxia (Damholt and Surlyk, 2004). This bottom water anoxia prevented bioturbation of newly formed layers. The current data does not enable a discrimination between the increased detrital flux or anoxic preservation scenarios.

The nodules in the grey chalk (Figure 33) are interpreted as *Prasinophyte* algae remains. The *Prasinophyte* algae interpretation is still preliminary and should be double-checked. Dodsworth (2004) studied the Cenomanian-Turonian shale-chalk alternation of Crimea and linked the presence of *Prasinophyte* algae in high TOC rich shales to oxygen-deficient bottom waters. Dodsworth (2015) linked the presence of *Prasinophyte* algae in the Cenomanian lower Eagle Ford in the Western Interior Basin in Texas to upwelling or a vertical expansion of the oxygen minimum zone. Both upwelling and the vertical expansion of the oxygen minimum zone increase the availability of the limiting nutrient nitrogen, which leads to an *Prasinophyte* bloom. Prauss (2007) studied the Cenomanian to Turonian laminated black shales, dark organic-rich marls and marly limestones of the Wunstorf section in North Germany. The highest *Prasinophyte* abundances were found in the shales. The shales and *Prasinophyte* algae are linked to a vertical expansion of the oxygen minimum zone. Prauss (2007) also linked the presence of *Prasinophyte* algae to cooler water conditions. The origin of this cooler waters is linked to the flooding of the Greenland-Fennoscandia seaway during the Cenomanian to Turonian, enabling a connection with the proto-Artic Ocean and thus leading to the establishment of a cool-water current. Cooler water increases the stability of biochemical ammonium and thus increased the availability of nitrogen thus leading to an increase in the *Prasinophyte* algae. The presence of *Prasinophyte* algae in the core sediments can thus be linked to cooler water conditions with anoxic/sub-oxic bottom waters. The presence of anoxic bottom waters is in line with the two settings model.

6.2.2 Synthesis

The literature indicates two depositional settings for the western Europe Chalk Group record (for summary of articles on chalk palaeoclimatology see S.I. 10.11): a cool water detrital/anoxic conditions with marl deposition and a warm water chalk deposition. These two depositional settings correspond to the two depositional settings inferred from the XRF data and core observations. The two setting model is only valid for the deeper water depositional environment and no for shallower settings where these two setting are not observed. (Jarvis et al., 2015; Pearce et al., 2003; Van Helmond et al., 2015)**.** Only in the deeper parts of the basin anoxic conditions were observed. (Damholt and Surlyk, 2004; Ineson et al., 2006; Rasmussen and Sheldon, 2015). There is still uncertainty regarding the detrital flux. It could be that changes in the detrital flux created the marl layers or that the marls were formed due to a decrease in the carbonate productivity (Ditchfield and Marshall, 1989; Leary et al., 1989; Niebuhr, 2005; Stage, 2001b, 1999). The cool water interpretation is based on the link between more marly layer and less negative $\delta^{18}O$ values (Pearce et al., 2003; Surlyk et al., 2010). The interpretation of the $\delta^{18}O$ record is problematic due to diagenetic overprints, which are often observed in the Chalk Group (Jorgenson, 1987; Schönfeld et al., 1991; Surlyk et al., 2010). The generally higher $\delta^{13}C$ values in the marl

indicate a higher organic carbon burial rate (Pearce et al., 2003; Surlyk et al., 2010). This burial could be due to a higher productivity or a better preservation.

6.2.3 Palaeoclimatological models

The spectral gamma ray records in combination with XRF measurements and literature points towards two possible palaeo-climatological models which can explain the observed cyclicity. These models are an upwelling model and a stagnation model (Figures 61 and 62). The upwelling model is coupled to the eccentricity maximum tuning option while the stagnation model is coupled to the eccentricity minimum tuning option.

6.2.3.1 Stagnation model

Seasonal contrasts are reduced during insolation minima, which leads to a less efficient mixing between the top and bottom waters. This stagnation leads to the formation of anoxic bottom waters. In these anoxic bottom waters carbonate dissolves, anoxic elements are absolutely enriched and detrital elements get relatively enriched. The lower efficiency of nutrient recycling in stagnant waters also creates a drop-in productivity leading to a relative enrichment of non-carbonate elements. The anoxic bottom waters also promote the preservation of carbon leading to higher $\delta^{13}C$ values. The reduced seasonality could have led to lower overall water temperatures and thus higher $\delta^{18}O$ values. A sea-level fall (glacially induced) might emerge landmasses around the North Sea Basin during an insolation minimum. Emergence of landmasses could lead to an increase in the sediment flux. There is still an uncertainty regarding the glacial induced sea-level fall and the presence and/or extent of Antarctic ice-sheets during the Late Cretaceous (Miller, 2009; Miller et al., 2008).

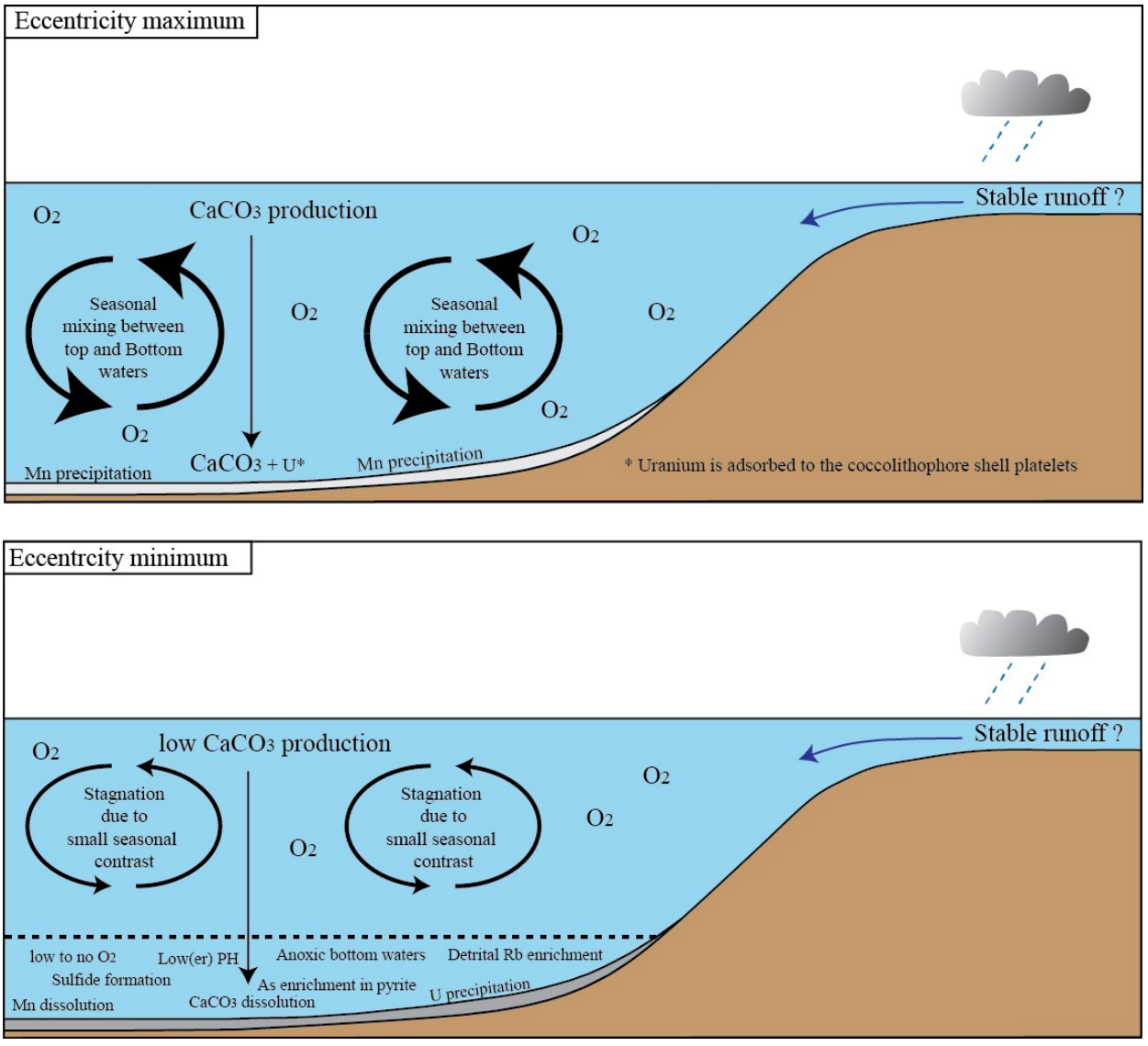

Figure 61. Stagnation model

6.2.3.2 Upwelling model

The upwelling model explains the cyclicity via changes in upwelling intensity. The seasonal contrast gets enhanced during an eccentricity maximum, which leads to an increase in current and wind strength and thus an increase in the upwelling intensity. Upwelling brings cool $\delta^{18}O$ and nutrient rich water to the surface. The cool $\delta^{18}O$ and nutrient rich water most likely originates from the proto-Artic Ocean and was transported through the Greenland-Fennoscandia seaway. Upwelling leads to an increase in nutrients, which leads to a higher productivity, which in term leads to higher oxygen consumption, which leads to an intensifying/shallowing of the oxygen minimum zone. The shallowing of the oxygen minimum leads to an enrichment of anoxic elements and enhanced organic matter preservation (higher $\delta^{13}C$ values). High productivity could also lead to an increase in the CO2 concentration at depth and thus a lower pH which leads to carbonate dissolution. A similar process is observed in the Arabian sea where coccolithophores show dissolution features (Mergulhao et al., 2006). An increase in the input of detrital material due to increased weathering rates and/or higher runoff during insolation maxima could also contribute in the enrichment of the detrital fraction.

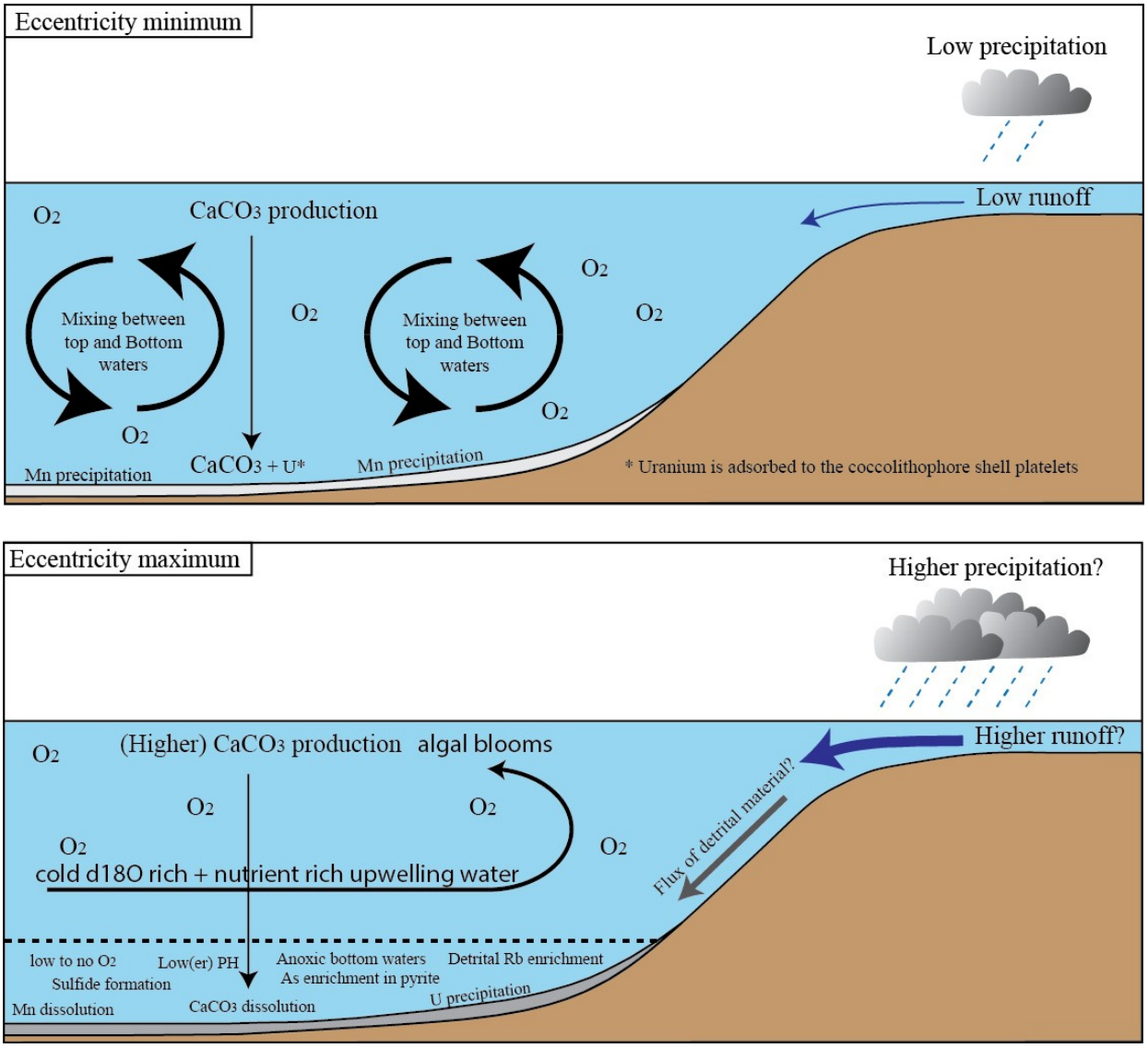

Figure 62. Upwelling model

6.2.4 Basin setting

There is still uncertainty regarding the palaeography/palaeo-water depth of north-western Europe during the late Cretaceous (chapter 2.2.3). The palaeogeography heavily influences the validity of the palaeoclimatological models. If the North Sea Basin was an open basin with connections to the palaeo-Arctic, Atlantic and Tethys Oceans then the upwelling model is most likely, but if the flow of water in the North Sea Basin was restricted by features such the London-Brabant high then the stagnation model would be more plausible.

The palaeocurrent interpretation of Remin et al. (2016) (Figure 63) shows a large current system with a flow of cool water from the artic. This current system is in-line with the observations of Gennaro and Wonham (2014) which combined the observations of Esmerode et al. (2008, 2007), Esmerode and Surlyk (2009), Hart (2007), Jarvis (1980), Lykke-Andersen and Surlyk (2004), Surlyk et al. (2008) and Surlyk and Lykke-Andersen (2007) and proposed a large current system in the central North Sea which created multiple subaqueous channel systems. A channel feature was also observed in this study (see SI) and the study of van der Molen (2004). A wind direction model for June, July and August in the Cenomanian indicates a W to NW wind direction (Fluteau et al., 2007). This wind direction could have created Ekman motion induced coastal upwelling along the Fennoscandian coastline or shoaling induced upwelling over topographic highs in the central North Sea Basin. Modelling of upwelling by Kruiys and Barron (1990) and (Trabucho Alexandre et al. (2010) and figure 64 indicates that upwelling was possible along the Fennoscandian coastline during the early late Cretaceous. The presence of *Prasinophyte* algae indicates a connection between cool nutrient rich waters and upwelling. Pearce et al. (2009) indicates that upwelling occurred in the Anglo-Paris Basin during and before the Cenomanian-Turonian boundary but during the late Turonian hyperstratification ensued, which indicates a change from the upwelling model to the stagnation model.

For a stratified water column, a restricted basin is required. The connections across the London-Brabant High and the Polish Trough are relatively shallow and a poor connectivity through these straits could have caused a restricted circulation in the North Sea Basin. The Mid-Polish through was inverted during the Turonian to Palaeocene times, which could have reduced the flow through the Polish through and thus restricted flow in the North Sea Basin (Krzywiec, 2001; Krzywiec and Stachowska, 2016). The connection across the London-Brabant High was gradually flooded during the Cenomanian to Turonian (Dusar and Lagrou, 2007). The Cenomanian to Turonian chalks are glauconite-bearing indicating a transgressive nature and deposition above the storm wave base (Lasseur et al., 2009; Mcrae, 1972). Fully pelagic chalk facies deposition only started in the late Santonian and maximum flooding occurred during the Late Campanian. A major relative sea-level fall occurred during the Latest Campanian, which caused the pelagic chalk facies to be replaced by a shallow calcarenite facies. The relatively shallow depth across the London-Brabant might hinder an effective flow between the Anglo-Paris Basin and the North Sea Basin and thus favours the stagnation model.

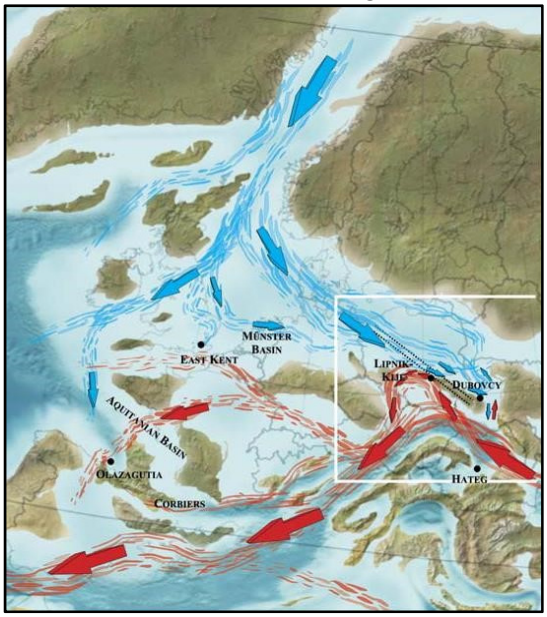

Figure 63. Palaeo circulation of western-Europe during the Coniacian-Santonian. modified after Remin et al. (2016)

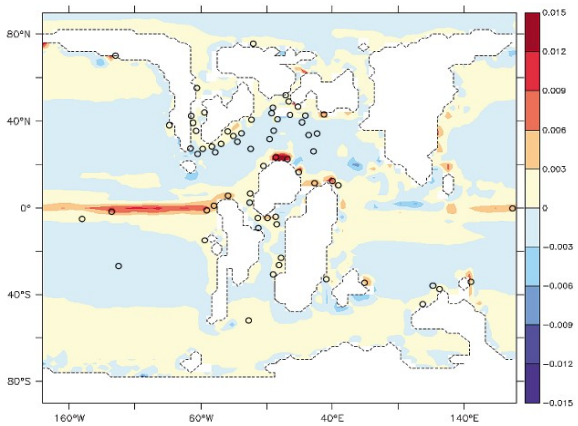

Modeled annual mean vertical velocity (in mm s^{-1}) at 50 m depth. Positive velocities denote upwelling. Strong upwelling is shown in orange/red colors. Besides a large equatorial upwelling zone in the Pacific (divergence zone), our model shows the existence of an upwelling zone along the southern margins of the North Atlantic. Black shale localities are shown with black circles and show that our results are in agreement with geologic data.

Figure 64. Upwelling intensity during the middle Cretaceous. From Trabucho Alexandre et al. (2010).

6.2.5 Preferred palaeoclimatological model

The stagnation and upwelling models cannot be discarded nor confirmed due the quality issues with the XRF data and little literature providing confident arguments. The upwelling model is preferred over the stagnation model due to significantly more evidence in literature for upwelling and the presence of *Prasinophyte* algae in the clay rich layers of core A12-02. The stagnation model also has one caveat namely the $\delta^{18}O$ chalk records (Pearce et al., 2003; Surlyk et al., 2010). The $\delta^{18}O$ records indicated cooler conditions for the deposition of the marls. It is hard to explain a significant cooling during eccentricity minima where stagnation occurred. Extra explanations such as Antarctic glacial cover or seasonal productivity cycles are needed to explain higher $\delta^{18}O$ values. The upwelling model has a more elegant solution and is therefore favoured over the stagnation model. The biostratigraphy filtered well-log connection of well A12-02 also favours the upwelling hypothesis.

6.3 Towards an improved chronostratigraphic framework of the Chalk Group

6.3.1 Long distance correlation

The tuning options of wells G17-S-01 Th and G14-05 enabled a long-distance correlation (Figures 121). The tuned record enabled the assigning of stage boundaries to individual seismic reflectors. Even though there are 2 tuning records the tuning options do not differ enough to change the assigning of a stage boundary to a seismic reflector. The long-distance correlation does show three notable aspects. the first aspect is that the reflectors are continuous and easily traceable and enable a precise correlation of stage boundaries across the Schill Grund Platform. The second aspect is the south west-ward tilting Turonian tilting observed by van der Voet (2015). On the Schill Grund Platform no tilting is observed but on the Terschelling Basin the Turonian is absent. The absence of the Turonian on the Terschelling Basin indicates a period of non-deposition or even uplift related erosion during the Turonian tilting phase. The Campanian inversion is the third aspect. A thinning of the Campanian-Maastrichtian strata can be observed between wells F15-01 and F09-02 at the edge of the Dutch Central graben. This thinning is in line with van der Molen (2004) and van der Voet (2015), which proposed an inversion phase of the eastern Central graben during the Campanian to Maastrichtian.

6.3.2 CK sequence subdivision

The ages of the CK seismic sequence boundaries of Van der Molen (2004) have been reassessed using the tuning of well G14-05-GR (Figure 65 left column Netherlands Schill Grund Platform.). The tuning from well G14-05-GR was used because the seismic sequences of van der Molen (2004) can be identified with much greater ease in well G14-05 then in well G17-S-01. Because there is a 5m pick uncertainty with the K/Pg boundary and a similar pick uncertainty with the sequence boundaries the total pick uncertainty is 10m. Using the 15-20m / 405-kyr cycle hypothesis this results in an uncertainty of ±110 kyr. The G14-05-GR eccentricity maximum tuning option was used because the eccentricity maximum tuning option is the preferred option at moment (see chapter 6.1.5.2 and 6.2.5). A 3500-kyr eccentricity cycle origin for the CK boundaries of CK3, CK4 CK5 and CK6? has been proposed in this research. Sequences CK4, CK5 and CK6 have durations of 3680, 3620 and 3320-kyr and, which provides further evidence for an astronomical forcing for some of the CK cycles by the 3500-kyr astronomical cycle.

6.3.3 Formation boundaries

The Ekofisk Formation is generally defined as the Danian part of the Chalk Group. the Ekofisk Formation in the Dutch offshore is characterised by a high amplitude reflector pattern and an associated chaotic resedimented facies (e.g. large shifts in both the DT and GR records). In some instances, the Ekofisk consists of purely autochthonous facies and only towards the top of the Ekofisk formation there is gradual increase in the GR and DT values. The start of chaotic pattern in the GR and DT records associated with the Ekofisk Formation cannot be tied to any specific reflector. The current biostratigraphy defines the K/Pg boundary as being an S-crossing above the third peak beneath the top Chalk reflector. The onset of the deposition of the Ekofisk Formation type facies depends on the location and can be either late Maastrichtian or early Danian (above or below the K/Pg boundary reflector). The onset of the deposition of chaotic Ekofisk Formation facies is thus of an diachronous nature. The new definition of the K/Pg boundary could be used as a new chronostratigraphic boundary within the Chalk Group. When viewed from a cyclostratigraphic point of view, the diachronous nature and onset of the chaotic lithology associated Ekofisk Formation could be better defined as individual

diachronous lithological member within the Ommelanden Formation (Figure 65 right column Netherlands Schill Grund Platform).

Currently the Plenus Marl is used as the definition for the top of the Texel Formation. No exact age has been assigned for the deposition of the Plenus Marl in the North Sea Basin. The Plenus marl has a clear expression in the gamma-ray and sonic logs. If the preferred eccentricity maximum tuning option is correct and the La2010a solution is used then the upper marl can be assigned to 405-kyr cycle Ce1 with an age of 94.0435 ± 0.055* Ma and the lower marl can be assigned to Ce2 with an age of 94.45 ± 0.055* Ma (Figure 65 right column Netherlands Schill Grund Platform).

* There is a 5m pick uncertainty with the K/Pg boundary. Using the 15-20m 405-kyr cycle hypothesis this results in an uncertainty of ±55 kyr.

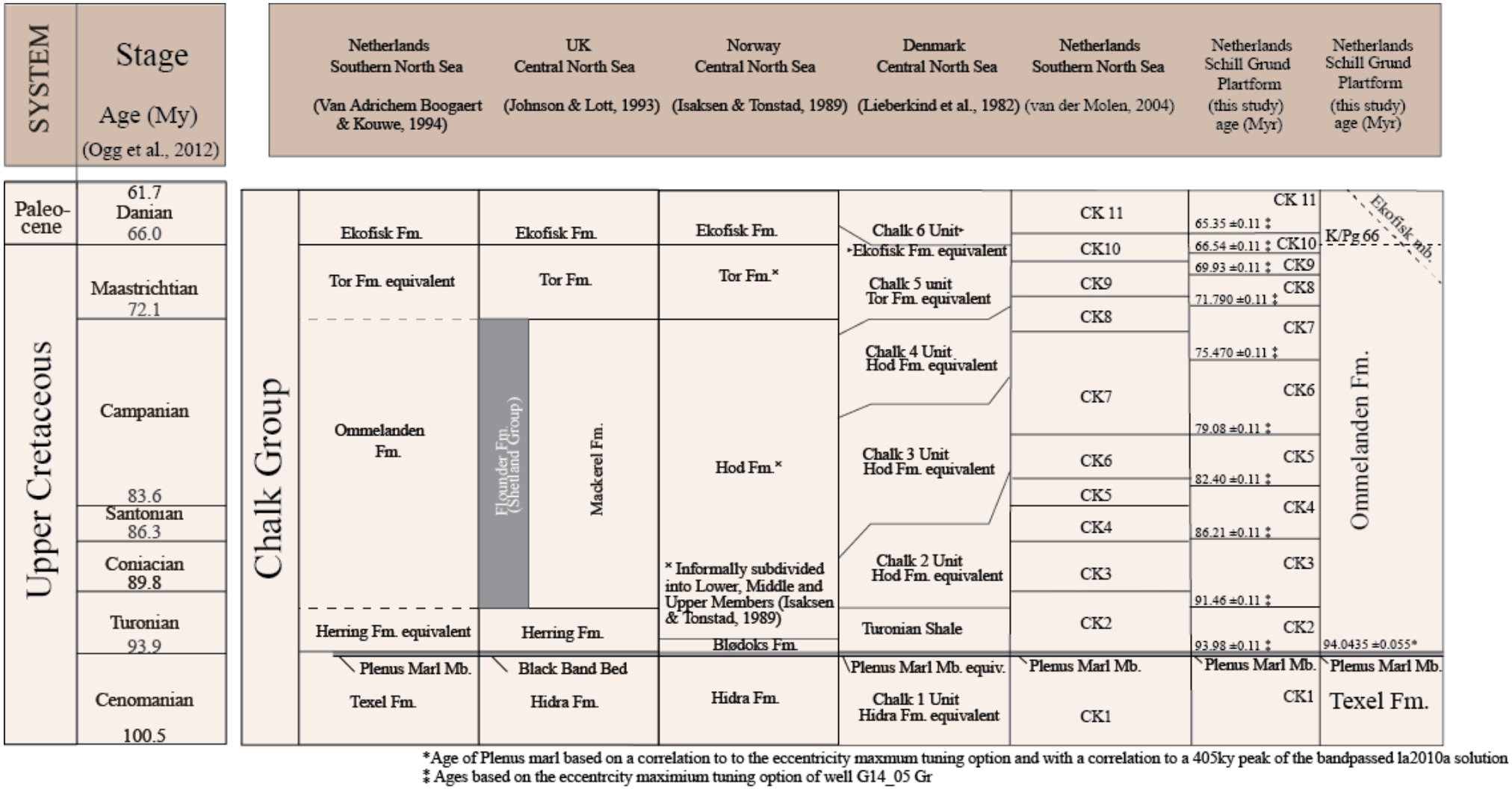

Figure 65 modified after van der Molen and Wong (2007). With stratigraphic division of the Chalk Group (Johnson and Lott, 1993; Lieberkind et al., 1982; van Adrichem Boogaert and Kauwe, 1997; Van der Molen, 2004). *Left Netherlands Schill Grund Platform stratigraphic division is based on the work of van der Molen (2004) and assigned ages based on the tuning of G14-05 of this study. The right Netherlands Schill Grund Platform stratigraphic division is a re-evaluation of the Ekofisk Formation and the age of the Top Texel Formation boundary.*

7. Conclusion

This study provides the basis for the establishment of a Late Cretaceous cyclostratigraphic framework for the Chalk Group on the Schill Grund Platform. The influence of Milankovitch cycles is observed from core to seismic scale. A 15-22m cycle in the well-log records is interpreted as the 405-kyr eccentricity cycle. This interpretation is supported by the biostratigraphy and eASM results. Two preliminary 405-kyr tuning options are put forward; an eccentricity minimum and an eccentricity maximum tuning option. Cycles with periods of 100, 200, 300, 405, 700-1000,1200, 2400, 3500 and 9500-kyr are registered by different spectral techniques in the depth and time domain. The 100,405, 1200, 2400, 3500-kyr periods could be assigned to orbital cycles. The assignment of an orbital cycle to 200,300, 700-1000 and 9500-kyr cycles is more problematic and multiple interpretations are possible.

The presence of a high power ~50m / 1200-kyr cycle in the EHA spectra is linked to chaotic behaviour due to the breakdown off the resonance between the orbital motions of Mars and Earth. The post depth-time conversion spectral peak of the 1200-kyr cycle splits into two separate peaks and/or the spectral power decreases. The split and decrease in spectral power is problematic and hinders an accurate interpretation for the duration of the 1200-kyr cycle.

The 1200-kyr cycle is thick (>15m) enough to be identified in the EHA spectra of the seismic traces. Well-log data filtered on the ~50m cycle shows a good correlation with the (un)filtered trace and (un)filtered seismic record. A modulating effect of 1200-kyr cycle on the seismic data is therefore assessed as being likely. A 3500-kyr eccentricity cycle is also identified in the seismic data. The CK3, CK4, CK5 and CK6? seismic sequence boundaries of van der Molen (2004) do coincide with the filtered 3500-kyr cycle. An astronomical origin for the CK3, CK4, CK5 and CK6? seismic sequence boundaries is therefore likely.

A palaeoclimatological evaluation of the well-logs, XRF measurements and literature points towards two possible climatological models which could explain the observed cyclicity; an upwelling model and a stagnation model. Both models cannot be discarded nor be confirmed due to the low resolution of the XRF data and no literature providing definite arguments discarding or confirming either model. The upwelling model is preferred over the stagnation model because there is significant more evidence in literature supporting the upwelling model, the presence of *Prasinophyte* algae in core A12-02 and the biostratigraphy bandpass filtered gamma ray relationship of core A12-02.

The presented cyclostratigraphic framework for the Chalk Group enabled a refinement of the CK cycle stratigraphic subdivision of van der Molen (2004) and enabled a long-distance correlation of stage boundaries between the different wells on the Schill Grund Platform. The current cyclostratigraphic framework also provides a basis for future high(er)resolution (land based section) studies which can provide insights into the dynamics the 1200-kyr cycle, the expression of higher frequency cycles and the orbital phase relationship with the lithology. Further insights into the behaviour of 1200-kyr cycle during the late Cretaceous could help to better understand the chaotic behaviour of the solar system and help refine future astronomical solutions.

8. Acknowledgements

I would like to thank Dr. Frits Hilgen (UU) and Dr. Geert-Jan Vis (TNO) for being my supervisors. I would like to thank Dr. Dirk Munsterman (TNO) for conducting biostratigraphic research on the core of well A12-02 and providing me with that data. The biostratigraphic research of Dr. Dirk Munsterman TNO would not have been possible without the funding which TNO arranged for the biostratigraphic research. I am grateful for the help of Dr. Geert de Bruin (TNO) in recognising the polarity of seismic data. The instructions on seismic to well ties by Dr. Johan ten Veen (TNO) is also appreciated. I would like to thank Dr. Anne-Christine da Silva Rangel de Almeida (University of Liège/UU) for her instructions on the Astrochron package of R statistics. I am grateful that I could borrow the XRF analyser from The Palaeomagnetic lab Fort Hoofddijk on such a short notice. The Geo-ICT group of the UU is thanked for enabling a Petrel VPN connection on my laptop. Family and friends are thanked for their support and care during my thesis.

9. References

Adams, D.D., Hurtgen, M.T., Sageman, B.B., 2010. Volcanic triggering of a biogeochemical cascade during Oceanic Anoxic Event 2. Nat. Geosci. 3, 201–204. doi:10.1038/ngeo743

Adams, J.A.S., Weaver, C.E., Adams, John A. S.; Weaver, C.E., 1958. Thorium-to-uranium ratios as indicators of sedimentary processes: Examples of concept of geochemical facies. Am. Assoc. Pet. Geol. Bull. 42, 387–430. doi:10.1306/0BDA5A89-16BD-11D7-8645000102C1865D

Algeo, T.J., Maynard, J.B., 2004. Trace-element behavior and redox facies in core shales of Upper Pennsylvanian Kansas-type cyclothems. Chem. Geol. 206, 289–318.

Anderskouv, K., Surlyk, F., 2011. Upper Cretaceous chalk facies and depositional history recorded in the Mona-1 core, Mona Ridge, Danish North Sea. Geol. Surv. Denmark Greenl. Bull. 25, 60.

Arfai, J., Lutz, R., Franke, D., Gaedicke, C., Kley, J., 2016. Mass-transport deposits and reservoir quality of Upper Cretaceous Chalk within the German Central Graben, North Sea. Int. J. Earth Sci. 105, 797–818. doi:10.1007/s00531-015-1194-y

Arthur, M.A., Bottjer, D.J., Dean, W.E., Fischer, A.G., Hattin, D.E., Kauffman, E.G., Pratt, L.M., Scholle, P.A., 1986. Rhythmic bedding in Upper Cretaceous pelagic carbonate sequences: Varying sedimentary response to climatic forcing. Geology 14, 153–156. doi:10.1130/0091-7613(1986)14<153:RBIUCP>2.0.CO;2

Bachmann, G.H., Geluk, M.C., Warrington, G., Beutler, G.B.-R.A., Hagdorn, H., Hounslow, M.W., Nitsch, E., Röhling, H.-G., Simon, T., Szulc, A., 2010. Triassic, in: Petroleum Geological Atlas of the Southern Permian Basin Area. pp. 140–173.

Back, S., Van Gent, H., Reuning, L., Grotsch, J., Niederau, J., Kukla, P., 2011. 3D seismic geomorphology and sedimentology of the Chalk Group, southern Danish North Sea. J. Geol. Soc. London 168, 393–405. doi:10.1144/0016-76492010-047.

Baker, G.S., 1994. An examination of triassic cyclostratigraphy in the Newark Basin from shallow seismic profiles and geophysical logs. Theses Diss. paper 260, 155.

Ball, K.C., 1985. A foraminiferal biostratigraohy of the upper cretaceous of the Southern North Sea Basin (UK Sector). doi:10.1017/CBO9781107415324.004

Batenburg, S.J., 2013. Cyclostratigraphy and astronomical tuning of the Maastrichtian limestone-marl alternations at Zumaia and Sopelana, Basque country, N-Spain. Dr. Thesis Univ. Portsmouth 203.

Batenburg, S.J., De Vleeschouwer, D., Sprovieri, M., Hilgen, F.J., Gale, A.S., Singer, B.S., Koeberl, C., Coccioni, R., Claeys, P., Montanari, A., Vleeschouwer, D. De, Sprovieri, M., Hilgen, F.J., Gale, A.S., Singer, B.S., Koeberl, C., Coccioni, R., Claeys, P., Montanari, A., 2016. Orbital control on the timing of oceanic anoxia in the Late Cretaceous. Clim. Past 12, 2009–2016. doi:10.5194/cp-12-1995-2016

Batenburg, S.J., Gale, A.S., Sprovieri, M., Hilgen, F.J., Thibault, N., Boussaha, M., Orue-Etxebaria, X., 2014. An astronomical time scale for the Maastrichtian based on the Zumaia and Sopelana sections (Basque country, northern Spain). J. Geol. Soc. London. 171, 165–180. doi:10.1144/jgs2013-015

Batenburg, S.J., Sprovieri, M., Gale, A.S., Hilgen, F.J., Hüsing, S.K., Laskar, J., Liebrand, D., Lirer, F., Orue-Etxebarria, X., Pelosi, N., Smit, J., 2012. Cyclostratigraphy and astronomical tuning of the Late Maastrichtian at Zumaia (Basque country, Northern Spain). Earth Planet. Sci. Lett. 359–360, 264–278.

Bathurst, R.G.C., 1975. Carbonate sediments and their diagenesis, Geoforum. doi:10.1016/0016-7185(73)90072-9

Beaufort, L., 1994. Climatic importance of the modulation of the 100 kyr cycle inferred from 16 m.y. long Miocene records. Paleoceanography 9, 821–834. doi:10.1029/94PA02115

Bełka, Z., Devleeschouwer, X., Narkiewicz, M., Piecha, M., Reijers, T.J.A., Ribbert, K.-H., Smith, N.J.., 2010. Devonian, in: Petroleum Geological Atlas of the Southern Permian Basin Area. pp. 71–79.

Bergen, J.A., Sikora, P.J., 1999. Microfossil diachronism in southern Norwegian North Sea chalks: Valhall and Hod fields. Geol. Soc. London, Spec. Publ. 152, 85–111. doi:10.1144/GSL.SP.1999.152.01.06

Berger, A., 1997. Intertropical Latitudes and Precessional and Half-Precessional Cycles. Science (80-.). 278, 1476–1478. doi:10.1126/science.278.5342.1476

Berger, A.L., 1976. Obliquity and precession for last 5000000 years. Astron. Astrophys. 51, 127–135.

Black, M., Barnes, B., 1959. The Structure of Coccoliths from the English Chalk. Geol. Mag. 96, 321. doi:10.1017/S0016756800062294

Bolli, H.M., Saunders, J.B., Perch-Nielson, K., Caron, M., Toumarkine, M., Luterbacher, H., Jenkins, D.G., Laccarino, S., Rogl, F., Remane, J., 1989. Volume 1. Planktic Foraminifera, Calcareous Nannofossils and Calpionellids.

Boulila, S., Galbrun, B., Laskar, J., Pälike, H., 2012. A ~9myr cycle in Cenozoic ?? 13C record and long-term orbital eccentricity modulation: Is there a link? Earth Planet. Sci. Lett. 317–318, 273–281. doi:10.1016/j.epsl.2011.11.017

Boussaha, M., Thibault, N., Stemmerik, L., 2016. Integrated stratigraphy of the late Campanian – Maastrichtian in the Danish Basin: revision of the Boreal calcareous nannofossil zonation. Newsletters Stratigr. 49, 337–360. doi:10.1127/nos/2016/0075

Brand, L.E., 1994. Physiological ecology of marine coccolithophores, in: Coccolithophores (Ed. A. Winter and W. G. Sieser). pp. 39–50.

Brasher, J.E., Vagle, K.R., 1996. 1996 - Brasher and Vagle - Influence of lithofacies on diagenesis on Norwegian North Sea Chalk Reservoirs.pdf. Am. Assoc. Pet. Geol. Bull. 80, 746–769.

Chenet, A.L., Courtillot, V., Fluteau, F., Gérard, M., Quidelleur, X., Khadri, S.F.R., Subbarao, K. V., Thordarson, T., 2009. Determination of rapid Deccan eruptions across the Cretaceous-Tertiary boundary using paleomagnetic secular variation: 2. Constraints from analysis of eight new sections and synthesis for a 3500-m-thick composite section. J. Geophys. Res. Solid Earth 114. doi:10.1029/2008JB005644

Cohen, A.S., Scholz, C.A., Johnson, T.C., 2000. The International Decade of East African Lakes (IDEAL) drilling initiative for the African Great Lakes. J. Paleolimnol. 24, 231–235. doi:10.1023/A:1008158902422

Cohen, K.M., Finney, S.C., Gibbard, P.L., Fan, J.-X., 2013. The ICS International Chronostratifraphic Chart. Episodes 36, 199–204.

Cottle, R.A., 1989. Orbitally mediated cycles from the Turonian of southern England: their potential for high-resolution stratigraphic correlation. Terra Nov. 1, 426–431. doi:10.1111/j.1365-3121.1989.tb00404.x

Da Silva, A.C., De Vleeschouwer, D., Boulvain, F., Claeys, P., Fagel, N., Humblet, M., Mabille, C., Michel, J., Sardar Abadi, M., Pas, D., Dekkers, M.J., 2013. Magnetic susceptibility as a high-resolution correlation tool and as a climatic proxy in Paleozoic rocks – Merits and pitfalls: Examples from the Devonian in Belgium. Mar. Pet. Geol. 46, 173–189.

Damholt, T., Surlyk, F., 2004. Laminated-bioturbated cycles in Maastrichtian chalk of the North Sea: Oxygenation fluctuations within the Milankovitch frequency band. Sedimentology 51, 1323–1342. doi:10.1111/j.1365-3091.2004.00672.x

Darling, T., 2005. Well Logging and Formation Evaluation, Well Logging and Formation Evaluation. doi:10.1016/B978-075067883-4/50005-X

de Jager, J., 2007. Geological development, in: Geology of the Netherlands Edited by Th.E.Wong, D.A.J. Batjes & J. de Jager Royal Netherlands Academy of Arts and Sciences, 2007. pp. 5–26.

De Vos, W., Feldrappe, H., Pharaoh, T.C., Smith, N.J.P., Vejbæk, O.V., Verniers, J., Nawrocki, J., Poprawa, P., Bełka, Z., 2010. Pre-Devonian, in: Petroleum Geological Atlas of the Southern Permian Basin Area. pp. 59–69.

De Winter, N.J., Zeeden, C., Hilgen, F.J., 2014. Low-latitude climate variability in the Heinrich frequency band of the Late Cretaceous greenhouse world. Clim. Past 10, 1001–1015. doi:10.5194/cp-10-1001-2014

Deconinck, J.-F., Chamley, H., 1995. Diversity of smectite origins in late creataceous sediments: example of chalks from northern France. Clay Miner. 30, 365–379.

Ditchfield, P., Marshall, J.D., 1989. Isotopic variation in rhythmically bedded chalks: paleotemperature variation in the Upper Cretaceous. Geology 17, 842–845. doi:10.1130/0091-7613(1989)017<0842:IVIRBC>2.3.CO

Dodsworth, P., 2015. Palynostratigraphy and palaeoenvironments of the Eagle Ford Group (Upper Cretaceous) at the Lozier Canyon outcrop reference section, west Texas, USA. Palynology 6122, 22pp. doi:10.1080/01916122.2015.1073188

Dodsworth, P., 2004. The palynology of the Cenomanian-Turonian (Cretaceous) boundary succession at Aksudere in Crimea, Ukraine. Palynology 28, 129–141. doi:10.1080/01916122.2004.9989594

Dols, A., 2015. The mid-Pleistocene transition : An Eastern Mediterranean perspective. Master thesis Utr. Univ. Fac. Geosci. Dep. Earth Sci. 1–55.

Doornenbal, H., Stevenson, A., 2010. Petroleum Geological Atlas of the Southern Permian Basin Area. EAGE Publ. b.v. 354.

Dusar, M., Lagrou, D., 2007. Cretaceous flooding of the Brabant Massif and the lithostratigraphic characteristics of its chalk cover in northern Belgium. Geol. Belgica 10, 27–38.

Eberli, G., Swart, P., Malone, M., 1996. Ocean Drilling program leg 166 Preliminary Report The Bahamas Transect.

Eberli, G.P., Anselmetti, F.S., Kroon, D., Sato, T., Wright, J.D., 2002. The chronostratigraphic significance of seismic refleections along the Bahamas Transect. Mar. Geol. 185, 1–17.

Eldrett, J.S., Ma, C., Bergman, S.C., Lutz, B., Gregory, F.J., Dodsworth, P., Phipps, M., Hardas, P., Minisini, D., Ozkan, A., Ramezani, J., Bowring, S. a., Kamo, S.L., Ferguson, K., Macaulay, C., Kelly, A.E., 2015. An astronomically calibrated stratigraphy of the Cenomanian, Turonian and earliest Coniacian from the Cretaceous Western Interior Seaway, USA: Implications for global chronostratigraphy. Cretac. Res. 56, 316–344. doi:10.1016/j.cretres.2015.04.010

Ellis, D. V, Singer, J.M., 2007. Well Logging for Earth Scientists. doi:10.1007/978-1-4020-4602-5

Esmerode, E.V., Lykke-Andersen, H., Surlyk, F., 2008. Interaction between bottom currents and slope failure in the Late Cretaceous of the southern Danish Central Graben, North Sea. J. Geol. Soc. London. 165, 55–72. doi:10.1144/0016-76492006-138

Esmerode, E. V., Lykke-Andersen, H., Surlyk, F., 2007. Ridge and valley systems in the Upper Cretaceous chalk of the Danish Basin: contourites in an epeiric sea. Geol. Soc. London, Spec. Publ. 276, 265–282. doi:10.1144/GSL.SP.2007.276.01.13

Esmerode, E. V., Surlyk, F., 2009. Origin of channel systems in the Upper Cretaceous Chalk Group of the Paris Basin. Mar. Pet. Geol. 26, 1338–1349. doi:10.1016/j.marpetgeo.2009.05.001

Fabricius, I.., Rogen, B., Gommesen, L., 2007. How depositional texture and diagenesis control petrophysical and elastic properties of samples from five North Sea chalk fields. Pet. Geosci. 13, 81–95. doi:10.1144/1354-079306-707

Fabricius, I.L., 2007. Chalk: Composition, diagenesis and physical properties. Bull. Geol. Soc. Denmark 55, 97–128.

Fluteau, F., Ramstein, G., Besse, J., Guiraud, R., Masse, J.P., 2007. Impacts of palaeogeography and sea level changes on Mid-Cretaceous climate. Palaeogeogr. Palaeoclimatol. Palaeoecol. 247, 357–381. doi:10.1016/j.palaeo.2006.11.016

Friedrich, O., Herrle, J.O., Hemleben, C., 2005. Climatic changes in the Late Campanian - Early Maastrichtian: micropaleontological and stable isotopic evidence from an epicontinental sea. 1. J. Foraminifer. Res. 35, 228–247. doi:10.2113/35.3.228

Gale, A.S., Kennedy, W.J., Voigt, S., Walaszczyk, I., 2005. Stratigraphy of the Upper Cenomanian-Lower Turonian Chalk succession at Eastbourne, Sussex, UK: Ammonites, inoceramid bivalves and stable carbon isotopes. Cretac. Res. 26, 460–487. doi:10.1016/j.cretres.2005.01.006

Gale, A.S., Young, J.., Shackleton, N.., Crowhurst, S.., Wray, D.., 1999. Orbital tuning of Cenomanian marly chalk successions: towards a Milankovitch time-scale for the Late Cretaceous. Phil. Trans. R. Soc. Lond. A 357, 1815–1829. doi:10.1098/rsta.1999.0402

Gardener, G.H.F., Gardener, L.W., Gregory, A.R., 1974. Formation velocity and Density- the Diagnostic basic for stratigraphyic traps. Geophysics 39, 770–780. doi:10.1007/s10910-012-0115-6

Gast, R.E., Dusar, M., Breitkreuz, C., Gaupp, R., Stemmerik, L.S.J.W., Geluk, M.C., Geißler, M., Kiersnowski, H., Glennie, K.W., Kabel, S., Jones, N.S., 2010. Rotliegend, in: Petroleum Geological Atlas of the Southern Permian Basin Area. pp. 101–121.

Geluk, M.C., 2007a. Permian, in: Geology of the Netherlands Edited by Th.E.Wong, D.A.J. Batjes & J. de Jager Royal Netherlands Academy of Arts and Sciences, 2007. pp. 63–83.

Geluk, M.C., 2007b. Triassic, in: Geology of the Netherlands Edited by Th.E.Wong, D.A.J. Batjes & J. de Jager Royal Netherlands Academy of Arts and Sciences, 2007. pp. 85–106.

Geluk, M.C., Dusar, M., De Vos, W., 2007. Pre-Silesian, in: Geology of the Netherlands Edited by Th.E.Wong, D.A.J. Batjes & J. de Jager Royal Netherlands Academy of Arts and Sciences, 2007. pp. 27–42.

Gennaro, M., 2011. 3D seismic stratigraphy and reservoir characterization of the Chalk Group in the Norwegian Central Graben, North Sea. Diss. degree Philos. Dr. Dep. Earth Sciene Univ. Bergen 17–46.

Gennaro, M., Wonham, J.P., 2014. Channel development in the chalk of the Tor Formation, North Sea: Evidence of bottom current activity, in: From Depositional Systems to Sedimentary Successions on the Norwegian Continental Margin. pp. 551–586. doi:10.1002/9781118920435.ch19

Gennaro, M., Wonham, J.P., Gawthorpe, R., Sælen, G., S??len, G., Sælen, G., 2013. Seismic stratigraphy of the Chalk Group in the Norwegian Central Graben, North Sea. Mar. Pet. Geol. 45, 236–266. doi:10.1016/j.marpetgeo.2013.04.010

Ghil, M., Allen, M.R., Dettinger, M.D., Ide, K., Kondrashov, D., Mann, M.E., Robertson, a W., Saunders, a, Tian, Y., Varadi, F., Yiou, P., 2002. Advanced spectral methods for climate time series. Rev. Geophys. 40, 3.1-3.41. doi:10.1029/2001RG000092

Glennie, K., 1998. Petroleum Geology of the North Sea: Basic Concepts and Recent Advances, Blackwell Scientific Publications, Oxford.

Gradstein, F.M., Waters, C.N., 2016. Stratigraphic Guide to the Cromer Knoll, Shetland and Chalk Groups, North Sea and Norwegian Sea. Newsletters Stratigr. 49, 71–280. doi:10.1127/nos/2016/0071

Guterch, A., Wybraniec, S., Grad, M., Chadwick, R.A., Krawczyk, C.M., Ziegler, P.A., Thybo, H., De Vos, W., 2010. Crustal structure and structural framework, in: Petroleum Geological Atlas of the Southern Permian Basin Area. pp. 11–23.

Håkansson, E., Broomley, R., Perch-Nielsen, K., 1974. Maastrichtian chalk of north-west Europe - a pelagic shelf sediment. Spec. Publs int. Ass. Sediment 1, 211–233. doi:10.2475/ajs.276.5.670

Hansen, H.R., Gwozdz, R., Bromley, R.G., Rasmussen, K.L., Vogesen, E.W., Pedersen, K.R., 1986. Cretaceous/Tertiary spherules from Denmark, New Zeland and Spain. Geol. Soc. Denmark Bull. 35, 75–82.

Haq, B.U., 2014. Cretaceous eustasy revisited. Glob. Planet. Change 113, 44–58. doi:10.1016/j.gloplacha.2013.12.007

Hardenbol, J., Thierry, J., Farley, M.B., Jacquin, T., De Graciansky, P.-C., Vail, P.R., 1998. Mesozoic and Cenozoic Sequence Stratigraphy of European Basins. SEPM Spec. Publ. 60, 3–13. doi:10.2110/pec.98.02.0003

Harrington, P.K., 1985. Formation of Pockmarks by Pore-Water Escape. Geo-marine Lett. 5, 193–197.

Hart, M.B., 2007. Late Cretaceous climates and foraminiferid distributions, in: Time Perspectives on Climate Change: Marrying the Signal from Computer Models and Biological Proxies. Special Publications of the Micropalaeontological Society. pp. 235–250.

Hart, M.B., 1987. Orbitally induced cycles in the chalk facies of the United Kingdom. Cretac. Res. 8, 335–348. doi:10.1016/0195-6671(87)90003-6

Heim, S., Lutz, R., Nelskamp, S., Verweij, H., Kaufmann, D., Reinhardt, L., 2013. Geological Evolution of the North Sea: Cross-border Basin modeling study on the Schillground high. Energy Procedia 40, 222–231. doi:10.1016/j.egypro.2013.08.026

Hernandez-Molina, F.J., Sierro, F.J., Llave, E., Roque, C., Stow, D.A. V, Williams, T., Lofi, J., Van der Schee, M., Arn??iz, A., Ledesma, S., Rosales, C., Rodr??guez-Tovar, F.J., Pardo-Ig??zquiza, E., Brackenridge, R.E., 2015. Evolution of the gulf of Cadiz margin and southwest Portugal contourite depositional system: Tectonic, sedimentary and paleoceanographic implications from IODP expedition 339. Mar. Geol. 377, 7–39. doi:10.1016/j.margeo.2015.09.013

Herngreen, G.F.W., Wong, T.E., 2007. Cretaceous, in: Geology of the Netherlands Edited by Th.E.Wong, D.A.J. Batjes & J. de Jager Royal Netherlands Academy of Arts and Sciences, 2007. pp. 127–150.

Hinnov, L.A., 2000. New Perspectives on Orbitally Forced Stratigraphy. Annu. Rev. Earth Planet. Sci. 28, 419–475. doi:10.1177/0741713604268894

Hinnov, L., Hilgen, F.J., 2012. Cyclostratigraphy and astrochronology. Geol. time scale 2012, 63–83.

Hudson, J.D., 1967. Speculations on the depth relations of calcium carbonate solution in recent and ancient seas. Mar. Geol. 5, 473–480.

Husson, D., Galbrun, B., Laskar, J., Hinnov, L.A., Thibault, N., Gardin, S., Locklair, R.E., 2011. Astronomical calibration of the Maastrichtian (Late Cretaceous). Earth Planet. Sci. Lett. 305, 328–340. doi:10.1016/j.epsl.2011.03.008

Ikeda, M., Tada, R., 2014. A 70 million year astronomical time scale for the deep-sea bedded chert sequence (Inuyama, Japan): Implications for Triassic-Jurassic geochronology. Earth Planet. Sci. Lett. 399, 30–43. doi:10.1016/j.epsl.2014.04.031

Ikeda, M., Tada, R., 2013. Long period astronomical cycles from the triassic to jurassic bedded chert sequence (Inuyama, Japan); Geologic evidences for the chaotic behavior of solar planets. Earth, Planets Sp. 65, 351–360. doi:10.5047/eps.2012.09.004

Ikeda, M., Tada, R., Hasegawa, H., n.d. Long periodicity (3.5 m.y.) Milankovitch cycles and its potential impacts on the Earth system dynamics. doi:10.1017/CBO9781107415324.004

Ineson, J., Buchardt, B., Lassen, S., Rasmussen, J.., Schiøler, P., Schovsbo, N.., Sheldon, E., Surlyk, F., 2006. Stratigraphy and palaeoceanography of upper Maastrichtian chalks, southern Danish Central Graben. Geus 9–12.

Japsen, P., 1998. Regional velocity-depth anomalies, North Sea Chalk: A record of overpressure and Neogene uplift and erosion. Am. Assoc. Pet. Geol. Bull. 82, 2031–2074. doi:10.1306/00AA7BDA-1730-11D7-8645000102C1865D

Jarvis, I., 1980. the Initiation of Phosphatic Chalk Sedimentation the Senonian Cretaceous of the Anglo Paris Basin. SEPM Spec. Publ. 167–192.

Jarvis, I., Gale, A.S., Jenkyns, H.C., Pearce, M.A., 2006. Secular variation in Late Cretaceous carbon isotopes: a new delta C-13 carbonate reference curve for the Cenomanian-Campanian (99.6-70.6 Ma). Geol. Mag. 143, 561–608. doi:10.1017/S0016756806002421

Jarvis, I., Joao Trabucho-Alexandre, J., Grocke, D.R., Uličný, D., Laurin, J., 2015. Intercontinental correlation of organic carbon and carbonate stable isotope records: evidence of climate and sea-level change during the Turonian (Cretaceous). Depos. Rec. 1, 53–90. doi:10.1002/dep2.6

Jarvis, I., Lignum, J.S., Grcke, D.R., Jenkyns, H.C., Pearce, M.A., 2011. Black shale deposition, atmospheric CO 2 drawdown, and cooling during the Cenomanian-Turonian Oceanic Anoxic Event. Paleoceanography 26, 1–17. doi:10.1029/2010PA002081

Jeans, C. V., 1968. The origin of montmorillonite of European chalk with special reference to the Lower Chalk of England. Clay Miner. 7, 311.

Jeans, C. V, Mitchell, J.G., Fisher, M.J., Wray, D.S., Hall, I.R., 2001. Age, origin and climatic signal of English Mesozoic clays based on K/ Ar signatures. Clay Miner. 36, 515–539. doi:10.1180/0009855013640006

Jenkyns, H.C., Gale, A.S., Corfield, R.M., 1994. Carbon- and oxygen-isotope stratigraphy of the English Chalk and Italian Scaglia and its palaeoclimatic significance. Geol. Mag. 131, 1. doi:10.1017/S0016756800010451

Johnson, H., Lott, G.K., 1993. Cretaceous of the Central and Northern North Sea, in: Lithostratigraphic Nomenclature of the UK North Sea. pp. 1–206.

Jones, E., Jones, R., Ebdon, C., Ewen, D., Milner, P., Plunkett, J., Hudson, G., Slater, P., 2003. The Millennium Atlas: petroleum geology of the central and northern North Sea, Geological Society of London.

Jorgenson, N.O., 1987. Oxygen and carbon isotope composition of Upper Cretaceous chalk from the Danish sub-basin and the North Sea Central Graben. Sedimentology 34, 559–570.

Juignet, P., Breton, G., 1992. Mid-cretaceous sequence stratigraphy and sedimentary cyclicity in the western Paris Basin. Palaeogeogr. Palaeoclimatol. Palaeoecol. 91, 197–218. doi:10.1016/0031-0182(92)90067-F

Keller, G., Han, Q., Adatte, T., Burns, S.J., 2001. Palaeoenvironment of the Cenomanian–Turonian transition at Eastbourne, England. Cretac. Res. 22, 391–422. doi:10.1006/cres.2001.0264

Kennedy, W.., 1987. Sedimentology of Late Cretaceous-Palaeocene chalk reservoirs, North Sea Central Graben. Pet. Geol. north west Eur. 469–481. doi:-

Knox, R.W.O.B., Bosch, J.H.A., Rasmussen, E.S., Heilmann-Clausen, C., Hiss, M., De Lugt, I.R., Kasińksi, J., King, C., Köthe, A., Słodkowska, B., Standke, G. Vandenberghe, N., 2010. Cenozoic, in: Petroleum Geological Atlas of the Southern Permian Basin Area. pp. 211–223.

Kombrink, H., Besly, B.M., Collinson, J.D., Den Hartog Jager, D.G., Drozdzewski, G., Dusar, M., Hoth, P., Pagnier, H.J.M., Stemmerik, L. Waksmundzka, M.I. Wrede, V., 2010. Carboniferous, in: Petroleum Geological Atlas of the Southern Permian Basin Area. pp. 81–99.

Kombrink, H., Doornenbal, J.C., Duin, E.J.T.J.T., Den Dulk, M., Ten Veen, J.H.H., Witmans, N., Doornebal, J.C., Duin, E.J.T.J.T., Den Dulk, M., Van Gessel, S.F., Ten Veen, J.H.H., Witmans, N., Doornenbal, J.C., Duin, E.J.T.J.T., Den Dulk, M., Ten Veen, J.H.H., Witmans, N., 2012. New insights into the geological structure of the

Netherlands: results of a detailed mapping project. Netherlands J. Geosci. Geol. en Mijnb. 91, 419–446. doi:10.1017/S0016774600000329

Köthe, A., 2007. Cenozoic biostratigraphy from the German North Sea sector (G-11-1 borehole, dinoflagellate cysts, calcareous nannoplankton). Zeitschrift der Dtsch. Gesellschaft für Geowissenschaften 158, 287–327. doi:10.1127/1860-1804/2007/0158-0287

Kruiys, E., Barron, E., 1990. Climate model prediction of paleoproductivity and potential source- rock distribution, in: Deposition of Organic Facies. pp. 195–216.

Krzywiec, P., 2001. Mid-Polish Trough inversion - seismic examples, main mechanisms, and its relationship to the Alpine-Carpathian collision. Stephan Mueller Spec. Publ. Ser. 1, 151–165. doi:10.5194/smsps-1-151-2002

Krzywiec, P., Stachowska, A., 2016. Late Cretaceous inversion of the NW segment of the Mid-Polish Trough--how marginal troughs were formed, and does it matter at all? Zeitschrift der Dtsch. Gesellschaft für Geowissenschaften 167, 107–119. doi:10.1127/zdgg/2016/0068

Lanci, L., Muttoni, G., Erba, E., 2010. Astronomical tuning of the Cenomanian Scaglia Bianca Formation at Furlo, Italy. Earth Planet. Sci. Lett. 292, 231–237. doi:10.1016/j.epsl.2010.01.041

Larionov, V. V., 1969. Radiometrija skwaschin. Nedra verlag. Moscow 329.

Laskar, J., 1999. The limits of Earth orbital calculations for geological time-scale use. Philos. Trans. R. Soc. A Math. Phys. Eng. Sci. 357, 1735–1759. doi:10.1098/rsta.1999.0399

Laskar, J., Fienga, A., Gastineau, M., Manche, H., 2011a. La2010: A new orbital solution for the long term motion of the Earth. Astron. Astrophys. 4, 17. doi:10.1051/0004-6361/201116836

Laskar, J., Gastineau, M., Delisle, J.-B., Farrés, A., Fienga, A., 2011b. Strong chaos induced by close encounters with Ceres and Vesta. Astron. Astrophys. 532, L4. doi:10.1051/0004-6361/201117504

Laskar, J., Robutel, P., Joutel, F., Gastineau, M., Correia, a. C.M., Levrard, B., 2004. A long-term numerical solution for the insolation quantities of the Earth. Astron. Astrophys. 428, 261–285. doi:10.1051/0004-6361:20041335

Lasseur, E., Guillocheau, F., Robin, C., Hanot, F., Vaslet, D., Coueffe, R., Neraudeau, D., 2009. A relative water-depth model for the Normandy Chalk (Cenomanian-Middle Coniacian, Paris Basin, France) based on facies patterns of metre-scale cycles. Sediment. Geol. 213, 1–26. doi:10.1016/j.sedgeo.2008.10.007

Lauridsen, B.W., Gale, A.S., Surlyk, F., 2009. Benthic macrofauna variations and community structure in Cenomanian cyclic chalk-marl from Southerham Grey Pit, SE England. J. Geol. Soc. London. 166, 115–127. doi:10.1144/0016-76492007-164

Lauridsen, B.W., Surlyk, F., 2008. Benthic faunal response to late Maastrichtian chalk-marl cyclicity at Rordal, Denmark. Palaeogeogr. Palaeoclimatol. Palaeoecol. 269, 38–53. doi:10.1016/j.palaeo.2008.07.001

Lauridsen, B.W., Surlyk, F., Bromley, R.G., 2011. Trace fossils of a cyclic chalk-marl succession; the upper Maastrichtian Rordal Member, Denmark. Cretac. Res. 32, 194–202. doi:10.1016/j.cretres.2010.12.002

Laurin, J., Cech, S., Uličný, D., Staffen, Z., Svobodova, M., 2014. Astrochronology of the Late Turonian: Implications for the behavior of the carbon cycle at the demise of peak greenhouse. Earth Planet. Sci. Lett. 394, 254–269. doi:10.1016/j.epsl.2014.03.023

Laurin, J., Meyers, S.R., Galeotti, S., Lanci, L., 2016. Frequency modulation reveals the phasing of orbital eccentricity during Cretaceous Oceanic Anoxic Event II and the Eocene hyperthermals. Earth Planet. Sci. Lett. 442, 143–156. doi:10.1016/j.epsl.2016.02.047

Laurin, J., Meyers, S.R., Uličný, D., Jarvis, I., Sageman, B.B., 2015. Axial obliquity control on the greenhouse carbon budget through middle- to high-latitude reservoirs. Paleoceanography 30, 133–149. doi:10.1002/2014PA002736

Leary, P.N., Cottle, R.A., Ditchfield, P., 1989. Milankovitch control of foraminiferal assemblages from the Cenomanian of southern England. Terra Nov. 1, 416–419. doi:10.1111/j.1365-3121.1989.tb00402.x

Levin, L.A., Hönisch, B., Frieder, C.A., 2015. geochemical proxies for estimating faunal exposure to ocean Acidification. Oceanography 1, 1–18. doi:10.1017/CBO9781107415324.004

Lieberkind, K., Bang, I., Mikkelsen, N., Nygaard, E., 1982. Late Cretaceous and Danian limestone, in: Geology of the Danish Central Graben. Series B. No. 8. pp. 49–62.

Lindgreen, H., Drits, V.A., Jakobsen, F.C., Sakharov, B.A., 2008. Clay mineralogy of the central North Sea upper cretaceous tertiary chalk and the formation of clay-rich layers. Clays Clay Miner. 56, 693–710. doi:10.1346/CCMN.2008.0560610

Lindgreen, H., Drits, V. a., Sakharov, B. a., Jakobsen, H.J., Salyn, a. L., Dainyak, L.G., Krøyer, H., 2002. The structure and diagenetic transformation of illite-smectite and chlorite-smectite from North Sea Cretaceous-Tertiary chalk. Clay Miner. 37, 429–450. doi:10.1180/0009855023730055

Liu, H., 2001. Obliquity modulation of the incoming solar radiation. Recent Res. Devel. Atmos. Sci 1, 15–37.

Liu, H.-S., 1992. Frequency variations of the Earths obliquity and the 100-kyr ice-age Cycles. Nature 358, 397–399. doi:10.1038/358397a0

Lobo, F.J., Ridente, y D., 2013. Milankovitch cyclicity in modern continental margins : stratigraphic cycles in terrigenous shelf settings. boletín geológico y Min. 124, 169–185.

Locklair, R.E., Sageman, B.B., 2008. Cyclostratigraphy of the Upper Cretaceous Niobrara Formation, Western Interior, U.S.A.: A Coniacian-Santonian orbital timescale. Earth Planet. Sci. Lett. 269, 539–552. doi:10.1016/j.epsl.2008.03.021

Lott, G.K., Wong, T.E., Dusar, M., Andsbjerg, J., Mönnig, E., Feldman-Olszewska, A., Verreussel, R.M.C.H., 2010. Jurassic, in: Petroleum Geological Atlas of the Southern Permian Basin Area. pp. 175–193.

Lourens, L.J., Hilgen, F.J., 1997. Long-periodic variations in the earth's obliquity and their relation to third-order eustatic cycles and late Neogene glaciations. Quat. Int. 40, 43–52. doi:10.1016/S1040-6182(96)00060-2

Lykke-Andersen, H., Surlyk, F., 2004. The Cretaceous-Palaeogene boundary at Stevns Klint, Denmark: inversion tectonics or sea-floor topography? J. Geol. Soc. London. 161, 343–352. doi:10.1144/0016-764903-021

Ma, C., Meyers, S.R., Sageman, B.B., 2017. Theory of chaotic orbital variations confirmed by Cretaceous geological evidence. Lett. to Nat. 542, 468–470. doi:10.1038/nature21402

Ma, C., Meyers, S.R., Sageman, B.B., Singer, B.S., Jicha, B.R., 2014. Testing the astronomical time scale for oceanic anoxic event 2, and its extension into Cenomanian strata of the Western Interior Basin (USA). Bull. Geol. Soc. Am. 126, 974–989. doi:10.1130/B30922.1

Maliva, R.G., Dickson, J.A.D., 1992. Microfacies and diagenetic controls of porosity in Cretaceous/Tertiary chalks, Eldfisk field, Norwegian North Sea. Am. Assoc. Pet. Geol. Bull.

Martinez, M., Dera, G., 2015. Orbital pacing of carbon fluxes by a ~9-My eccentricity cycle during the Mesozoic. Proc. Natl. Acad. Sci. 112, 12604–12609. doi:10.1073/pnas.1419946112

März, C., 2007. Inorganic geochemical redox proxies - Indicators for rapid paleoenvironmental changes and related diagenetic processes in recent and ancient marine sediments. Diss. Rev. Dr. Degree Nat. Sci. (Dr. rer. nat.) Fac. Geosci. Bremen Univ. Ger. 1–127.

Masoumi, S., Reuning, L., Back, S., Sandrin, A., Kukla, P.A., 2014. Buried pockmarks on the Top Chalk surface of the Danish North Sea and their potential significance for interpreting palaeocirculation patterns. Int. J. Earth Sci. 103, 563–578. doi:10.1007/s00531-013-0977-2

Mavko, G., 2005. Conceptual Overview of Rock and Fluid Factors that Impact Seismic Velocity and Impedance. Stanford Rock Phys. Lab. 40.

Mazaheri, A., Memarian, H., Tokhmechi, B., Araabi, B.N., 2015. Developing fracture measure as an index of fracture impact on well-logs. Energy, Explor. Exploit. 33, 555–574. doi:10.1260/0144-5987.33.4.555

Mcrae, S.G.G., 1972. Glauconite. Earth-Science Rev. 8, 397–440.

Mergulhao, L.P., Mohan, R., Murthy, V.S.N., Guptha, M.V.S., Sinha, D.K., 2006. Coccolithophores from the central Arabian Sea: Sediment trap results. J. Earth Syst. Sci. 115, 415–428. doi:10.1007/BF02702870

Meyers, S.R., 2014. Astrochron: An R package for astrochronology [WWW Document]. https://cran.r-project.org/web/packages/astrochron/index.html. URL https://cran.r-project.org/package=astrochron

Meyers, S.R., Siewert, S.E., Singer, B.S., Sageman, B.B., Condon, D.J., Obradovich, J.D., Jicha, B.R., Sawyer, D.A., 2012. Intercalibration of radioisotopic and astrochronologic time scales for the Cenomanian-Turonian boundary interval, western interior Basin, USA. Geology 40, 7–10. doi:10.1130/G32261.1

Miller, K.G., 2009. Palaeoceanography: Broken greenhouse windows. Nat. Geosci. 2, 465–466. doi:10.1038/ngeo563

Miller, K.G., Wright, J.D., Katz, M.E., Browning, J. V., Cramer, B.S., Wade, B.S., Mizintseva, S.F., 2008. A View of Antarctic Ice-Sheet Evolution from Sea-Level and Deep-Sea Isotope Changes During the Late Cretaceous-Cenozoic, in: Antarctica: A Keystone in a Changing World. pp. 55–70. doi:10.3133/of2007-1047.kp06

Mitchell, A.J., Uličný, D., Hampson, G.J., Allison, P.A., Gorman, G.J., Piggott, M.D., WELLS, M.R., Pain, C.C., 2010. Modelling tidal current-induced bed shear stress and palaeocirculation in an epicontinental seaway: The Bohemian Cretaceous basin, Central Europe. Sedimentology 57, 359–388. doi:10.1111/j.1365-3091.2009.01082.x

Mitchell, R.N., Bice, D.M., Montanari, A., Cleaveland, L.C., Christianson, K.T., Coccioni, R., Hinnov, L. a., 2008. Oceanic anoxic cycles? Orbital prelude to the Bonarelli Level (OAE 2). Earth Planet. Sci. Lett. 267, 1–16. doi:10.1016/j.epsl.2007.11.026

Molenaar, N., Zijlstra, J.J.P., 1997. Differential early diagenetic low-Mg calcite cementation and rhythmic hardground development in Campanian-Maastrichtian chalk. Sediment. Geol. 109, 261–281. doi:10.1016/S0037-0738(96)00064-4

Mourik, A.A., Abels, H.A., Hilgen, F.J., Di Stefano, A., Zachariasse, W.J., 2011. Improved astronomical age constraints for the middle Miocene climate transition based on high-resolution stable isotope records from the central Mediterranean Maltese Islands. Paleoceanography 26, 1–14. doi:10.1029/2010PA001981

Nanda, N.C., 2016. Seismic Data Interpretation and Evaluation for Hydrocarbon Exploration and Production. doi:10.1007/978-3-319-26491-2

Niebuhr, B., 2005. Geochemistry and time-series analyses of orbitally forced Upper Cretaceous marl–limestone rhythmites (Lehrte West Syncline, northern Germany). Geol. Mag. 142, 31–55. doi:10.1017/S0016756804009999

Niebuhr, B., Prokoph, a., 1997. Periodic-cyclic and chaotic successions of Upper Cretaceous (Cenomanian to Campanian) pelagic sediments in the North German Basin. Cretac. Res. 18, 731–750. doi:10.1006/cres.1997.0083

Niebuhr, B., Wiese, F., Wilmsen, M., 2001. The cored konrad 101 borehole (Cenomanian-Lower coniacian, lower saxony): Calibration of surface and subsurface log data for the lower upper cretaceous of northern Germany. Cretac. Res. 22, 643–674. doi:10.1006/cres.2001.0283

Ogg, J.G., Hinnov, L.A., Huang, C., 2012. Cretaceous, The Geologic Time Scale. Elsevier. doi:10.1016/B978-0-444-59425-9.00027-5

Olsen, P.E., Kent, D. V., 1999. Long-period Milankovitch cycles from the Late Triassic and Early Jurassic of eastern North America and their implications for the calibration of the Early Mesozoic time-scale and the long-term behaviour of the planets. Philos. Trans. R. Soc. A Math. Phys. Eng. Sci. 357, 1761–1786. doi:10.1098/rsta.1999.0400

Paillard, D., Labeyrie, L., Yiou, P., 1996. AnalySeries 1.0: a Macintosh software for the analysis of geophysical time-series. Eos (Washington. DC). 77, 379.

Pearce, M.A., Jarvis, I., Swan, A.R.H., Murphy, A.M., Tocher, B.A., Edmunds, W.M., 2003. Integrating palynological and geochemical data in a new approach to palaeoecological studies: Upper Cretaceous of the Banterwick Barn Chalk borehole, Berkshire, UK. Mar. Micropaleontol. 47, 271–306. doi:10.1016/S0377-8398(02)00132-9

Pearce, M.A., Jarvis, I., Tocher, B.A., 2009. The Cenomanian-Turonian boundary event, OAE2 and palaeoenvironmental change in epicontinental seas: New insights from the dinocyst and geochemical records. Palaeogeogr. Palaeoclimatol. Palaeoecol. 280, 207–234. doi:10.1016/j.palaeo.2009.06.012

Perch Nielsen, K., 1968. Der Feinbau und die Klassifikation der Coccolithen aus dem Maastrichtien von Dänemark. Biol. Skr. Copenhaguen 16, 96 p., 32 .

Perdiou, A., Thibault, N., Anderskouv, K., van Buchem, F., Arie Buijs, G.J., Bjerrum, C.J., 2015. Orbital calibration of the late Campanian carbon isotope event in the North Sea. J. Geol. Soc. London. 173, 2015–120. doi:10.1144/jgs2015-120

Peryt, T.M., Geluk, M.C., Mathiesen, A., Paul, J., Smith, K., 2010. Zechstein, in: Petroleum Geological Atlas of the Southern Permian Basin Area. pp. 123–147.

Petersen, N.W., Toft, J., Hansen, P.M., 2003. Appraisal of an Extensive Thin Chalk Reservoir with Long Horizontal Wells: Cyclostratigraphy as Complementary Steering Tool 183–190.

Pharaoh, T.C., Dusar, M., Geluk, M.C., Kockel, F., Krawczyk, C.M., Krzywiec, P., Scheck-Wenderoth, M., Thybo, H., Vejbæk, O. V, Wees, J.D. Van, 2010. Tectonic evolution, in: Petroleum Geological Atlas of the Southern Permian Basin Area. pp. 25–57.

Pienaar, R.N., 1994. Ultrastructure and calcification of coccolithophores, in: Coccolithophores (Ed. A. Winter and W. G. Sieser). p. 252.

Prauss, M.L., 2007. Availability of Reduced Nitrogen Chemospecies in Photic-Zone Waters As the Ultimate Cause for Fossil Prasinophyte Prosperity. Palaios 22, 489–499. doi:10.2110/palo.2005.p05-095r

Rasmussen, J.A., Sheldon, E., 2015. Late Maastrichtian foraminiferal response to sea-level change and organic flux, Central Graben area, Danish North Sea. 2. Mesozoic Biotas Scand. its Arct. Territ. - 1. Geol. Soc. London Spec. Publ. 434, SP434.13-. doi:10.1144/SP434.13

Remin, Z., Gruszczyński, M., Marshall, J.D., Gruszczy??ski, M., Marshall, J.D., 2016. Changes in paleo-circulation and the distribution of ammonite faunas at the Coniacian–Santonian transition in central Poland and western Ukraine. Acta Geol. Pol. 66, 107–124. doi:10.1515/agp-2016-0006

Ridente, D., Trincardi, F., Piva, A., Asioli, A., 2009. The combined effect of sea level and supply during Milankovitch cyclicity: Evidence from shallow-marine ??18O records and sequence architecture (Adriatic margin). Geology 37, 1003–1006. doi:10.1130/G25730A.1

Rothwell, R.G., Croudace, I.W., 2015. Micro-XRF Studies of Sediment Cores: Applications of a non-destructive tool for the environmental

sciences (Developments in Paleoenvironmental Research), Tracking Environmental Change Using Lake Sediments. Volume 2: Physical and Geochemical Methods. doi:10.1007/978-94-017-9849-5

Ruddiman, W.F., 2014. Earth's climate: Past and Future. W.H. Free. Co. 352.

Sageman, B.B., Meyers, S.R., Arthur, M.A., 2006. Orbital time scale and new C-isotope record for Cenomanian-Turonian boundary stratotype. Geology 34, 125–128. doi:10.1130/G22074.1

Salminen, R., Batista, M.J., Bidovec, M.D., Demetriades, A., De Vivo, B., De Vos, W., Duris, M., Gilucis, A., Gregorauskiene, V., Halamic, J., Heitzmann, P., Lima, A., Jordan, G., Klaver, G., Klein, P., Lis, J., Locutura, J., Marsina, K., Mazreku, A., O'Connor, P.J., Olsson, S.Å., Ottesen, R.-T., Petersell, V., Plant, J.A., Reeder, S., Salpeteur, I., Sandström, H., Siewers, U., Steenfelt, A., Tarvainen, T., 2005. Th – Thorium. Geochemical atlas Eur. Part 1- Backgr. information, Methodol. maps. A Contrib. to IUGS/IAGC Glob. Geochemical Baselines, Eur. GTK. Foregs. 367–371.

Schlanger, S.O., Arthur, M.., Jenkyns, H.C., Scholle, P.A., 1987a. The Cenomanian Turonian oceanic anoxic event I . Stratigraphy and distribution of organic carbon rich beds and the C13 excursion. Mar. Pet. Source Rocks Geol. Soc. Spec. Publ. 26, 371–399. doi:10.1144/GSL.SP.1987.026.01.24

Schlanger, S.O., Arthur, M.A., Jenkyns, H.C., Scholle, P.A., 1987b. The Cenomanian-Turonian Oceanic Anoxic Event, I. Stratigraphy and distribution of organic carbon-rich beds and the marine δ 13 C excursion. Geol. Soc. London, Spec. Publ. 26, 371–399. doi:10.1144/GSL.SP.1987.026.01.24

Schlumberger, 20013. Log Interpretation Charts. Schlumberger 310.

Scholle, P.A., Albrechtsen, T., Tirsgaard, H., 1998. Formation and diagenesis of bedding cycles in uppermost Cretaceous chalks of the Dan Field, Danish North Sea. Sedimentology 45, 223–243. doi:10.1046/j.1365-3091.1998.0148e.x

Scholle, P.A., Arthur, M.A., 1980. Carbon isotope fluctuations in Cretaceous pelagic limestones: potential stratigraphic and petroleum exploration tool. Am. Assoc. Pet. Geol. Bull. 64, 67–87. doi:10.1306/2F91892D-16CE-11D7-8645000102C1865D

Scholz, C.A., 1995. Deltas of the Lake Malawi Rift, East Africa: seismic expression and exploration implications. Am. Assoc. Pet. Geol. Bull. 79, 1679–1697. doi:10.1306/7834DE54-1721-11D7-8645000102C1865D

Schönfeld, J., Sirocko, F., Jørgensen, N.O., 1991. Oxygen isotope composition of Upper Cretaceous chalk at Lagerdorf (NW Germany): its original environmental signal and palaeotemperature interpretation. Cretac. Res. 12, 27–46. doi:10.1016/0195-6671(91)90025-8

Schovsbo, N.H., Lauridsen, B.W., Knudsen, C., Stemmerik, L., 2006. Palaeoceanographic changes across the Lower / Upper Maastrichtian boundary in Denmark. Geophys. Res. Abstr. 8, 2.

Schulz, M., Mudelsee, M., 2002. REDFIT: Estimating red-noise spectra directly from unevenly spaced paleoclimatic time series. Comput. Geosci. 28, 421–426. doi:10.1016/S0098-3004(01)00044-9

Schürch, M., Buckley, D., 2002. Integrating geophysical and hydrochemical borehole-log measurements to characterize the Chalk aquifer, Berkshire, United Kingdom. Hydrogeol. J. 10, 610–627. doi:10.1007/s10040-002-0220-x

Serra, O., 1984. Fundamentals of Well-Log Interpretation, Science. doi:10.1126/science.143.3606.560-a

Sheriff, R., Geldart, 1995. Exploration Seismology. Cambridge Univ. Press 2, 1–592.

Siesser, W.G., Winter, A., 1994. Composition and morphology of coccolithophore skeletons, in: Coccolithophores (Ed. A. Winter and W. G. Sieser). pp. 51–62.

Sprovieri, M., Sabatino, N., Pelosi, N., Batenburg, S.J., Coccioni, R., Iavarone, M., Mazzola, S., 2013. Late cretaceous orbitally-paced carbon isotope stratigraphy from the bottaccione gorge (Italy). Palaeogeogr. Palaeoclimatol. Palaeoecol. 379–380, 81–94. doi:10.1016/j.palaeo.2013.04.006

Stage, M., 2001a. Magnetic susceptibility as carrier of a climatic signal in chalk. Earth Planet. Sci. Lett. 188, 17–27. doi:10.1016/S0012-821X(01)00304-1

Stage, M., 2001b. Recognition of cyclicity in the petrophysical properties of a Maastrichtian pelagic chalk oil field reservoir from the Danish North Sea. Am. Assoc. Pet. Geol. Bull. 85, 2003–2015.

Stage, M., 1999. Signal analysis of cyclicity in Maastrichtian pelagic chalks from the Danish North Sea. Earth Planet. Sci. Lett. 173, 75–90. doi:10.1016/S0012-821X(99)00213-7

Steinmetz, J.C., 1994a. Sedimentation of Coccolithophores, in: Coccolithophores (Ed. A. Winter and W. G. Sieser). pp. 179–199.

Steinmetz, J.C., 1994b. Stable isotopes in modern coccolithophores, in: Coccolithophores (Ed. A. Winter and W. G. Sieser). pp. 219–230.

Stephen, E.C., Pedersen, T.F., Calvert, S.E., Pedersen, T.F., 2007. Elemental Proxies for Palaeoclimatic and Palaeoceanographic Variability in Marine Sediments : Interpretation and Application. Dev. Mar. Geol. 1, 567–644. doi:10.1016/S1572-5480(07)01019-6

Sumbler, M.G., 1999. The stratigraphy of the Chalk Group in Yorkshire and Lincolnshire Geographical index. Br. Geol. Surv. Tech. Rep. WN99f02 40.

Surlyk, F., Jensen, S.K., Engkilde, M., 2008. Deep channels in the Cenomanian-Danian chalk group of the German North sea sector: Evidence of strong constructural and erosional bottom currents and effect on reservoir quality distribution. Am. Assoc. Pet. Geol. Bull. 92, 1565–1586. doi:10.1306/07100808035

Surlyk, F., Lykke-Andersen, H., 2007. Contourite drifts, moats and channels in the Upper Cretaceous chalk of the Danish Basin. Sedimentology 54, 405–422. doi:10.1111/j.1365-3091.2006.00842.x

Surlyk, F., Stemmerik, L., Ahlborn, M., Harlou, R., Lauridsen, B.W., Rasmussen, S.., Schovsbo, N., Sheldon, E., Thibault, N., 2010. The cyclic Rørdal Member – a new lithostratigraphic unit of chronostratigraphic and palaeoclimatic importance in the upper Maastrichtian of Denmark. Bull. Geol. Soc. Denmark 58, 89–98.

Takashima, R., Nishi, H., Hayashi, K., Okada, H., Kawahata, H., Yamanaka, T., Fernando, A.G., Mampuku, M., 2009. Litho-, bio- and chemostratigraphy across the Cenomanian/Turonian boundary (OAE 2) in the Vocontian Basin of southeastern France. Palaeogeogr. Palaeoclimatol. Palaeoecol. 273, 61–74. doi:10.1016/j.palaeo.2008.12.001

Tassell, J. Van, 1988. upper devonian catskill delta milankovitch cycles. Geol. F. Guid. - Devonian delta East-Central West Virignia Adjac. Virginia 77–84.

Ten Veen, J.H., Van Gessel, S.F., Den Dulk, M., 2012. Thin- and thick-skinned salt tectonics in the Netherlands; a quantitative approach. Netherlands J. Geosci. Geol. en Mijnb. 91, 447–464. doi:10.1017/S0016774600000330

Thibault, N., Anderskouv, K., Bjerager, M., Boldreel, L.O., Jelby, M.E., Stemmerik, L., Surlyk, F., 2015. Upper Campanian-Maastrichtian chronostratigraphy of the Skaelskor-1 core, Denmark: Correlation at the basinal and global scale and implications for changes in sea-surface temperatures. Lethaia 48, 549–560. doi:10.1111/let.12128

Thibault, N., Husson, D., 2016. Climatic fluctuations and sea-surface water circulation patterns at the end of the Cretaceous era: Calcareous nannofossil evidence. Palaeogeogr. Palaeoclimatol. Palaeoecol. 441, 152–164. doi:10.1016/j.palaeo.2015.07.049

Thibault, N., Jarvis, I., Voigt, S., Gale, A.S., Attree, K., Jenkyns, H.C., 2016. Astronomical calibration and global correlation of the Santonian (Cretaceous) based on the marine carbon isotope record. AGU Publ. 1–19. doi:10.1002/2016PA002941.Received

Thomson, J., Croudace, I.W., Rothwell, R.G., 2006. A geochemical application of the ITRAX scanner to a sediment core containing eastern Mediterranean sapropel units. Geol. Soc. London, Spec. Publ. 267, 65–77. doi:10.1144/gsl.sp.2006.267.01.05

TNO, 2011. Tectono-stratigraphic charts of the Netherlands Continental Shelf. TNO 9.

Torsvik, T.H., Rehnström, E.F., 2003. The Tornquist Sea and Baltica-Avalonia docking. Tectonophysics 362, 67–82. doi:10.1016/S0040-1951(02)00631-5

Townsend, R., 2016. K/Pg dinoflagellate stratigraphy UK, Stratablog,Stratdata [WWW Document]. URL http://www.stratadata.co.uk/blog/

Trabucho Alexandre, J., Tuenter, E., Henstra, G.A., Van Der Zwan, K.J., Van De Wal, R.S.W., Dijkstra, H.A., De Boer, P.L., 2010. The mid-Cretaceous North Atlantic nutrient trap: Black shales and OAEs. Paleoceanography 25, 1–14. doi:10.1029/2010PA001925

Tribovillard, N., Algeo, T.J., Lyons, T., Riboulleau, A., 2006. Trace metals as paleoredox and paleoproductivity proxies: An update. Chem. Geol. 232, 12–32.

Tucker, M.E., Wright, V.P., 1990. Carbonate Sedimentology. Blackwell Sci. Publ. Oxford 482.

Tyszka, J., 2009. Foraminiferal response to seasonality modulated by orbital cycles in the Cretaceous mid-latitudes: The Albian record from the Lower Saxony Basin. Palaeogeogr. Palaeoclimatol. Palaeoecol. 276, 148–159. doi:10.1016/j.palaeo.2009.03.006

van Adrichem Boogaert, H.A., Kauwe, W.F.P., 1997. Chalk group in: Stratigraphic Nomenclature of the Netherland, Retrieved (April 2017), from (https://www.dinoloket.nl/chalk-group-ck).

Van Buchem, F.S.P., Smit, F.W.H., Buijs, G., Trudgil, B., Larsen, P.H., 2017. Tectono-stratigraphic framework and depositional history of the Cretaceous–Danian succession of the Danish Central Graben (North Sea) – new light on a mature area. Proc. Pet. Conf. Ser.

van Buggenum, J.M., Den Hartog Jager, D.G., 2007. Silesian, in: Geology of the Netherlands Edited by Th.E.Wong, D.A.J. Batjes & J. de Jager Royal Netherlands Academy of Arts and Sciences, 2007. pp. 43–62.

van Dalfsen, W., Van Gessel, S.F., Doornenbal, J.C., 2007. TNO report 2007-U-R1272C Velmod-2.

Van der Molen, A.. S., 2004. Sedimentary development, seismic stratigraphy and burial compaction of the Chalk Group in the Netherlands North Sea area. Geol. ULTRAIECTINA.

Van der Molen, A.S., Wong, T.E., 2007. Towards an improved lithostratigraphic subdivision of the chalk group in the Netherlands North Sea area - A seismic stratigraphic approach. Geol. en Mijnbouw/Netherlands J. Geosci. 86, 131–143.

Van der Voet, E., 2015. Geological evolution of the Chalk Group in the northern Dutch North Sea. MSc. thesis VU Amsterdam 104.

Van Helmond, N.A.G.M., Sluijs, A., Sinninghe Damsté, J.S., Reichart, G.J., Voigt, S., Erbacher, J., Pross, J., Brinkhuis, H., 2015. Freshwater discharge controlled deposition of Cenomanian-Turonian black shales on the NW European epicontinental shelf (Wunstorf, northern Germany). Clim. Past 11, 495–508. doi:10.5194/cp-11-495-2015

Vejbæk, O.V., Andersen, C., Dusar, M., Herngreen, G.F.W., Krabbe, H., Leszczyński, K., Lott, G.K., Mutterlose, J., Van der Molen, A.., 2010. Cretaceous, in: Petroleum Geological Atlas of the Southern Permian Basin Area. pp. 195–209.

Voigt, S., Aurag, A., Leis, F., Kaplan, U., 2007. Late Cenomanian to Middle Turonian high-resolution carbon isotope stratigraphy: New data from the Münsterland Cretaceous Basin, Germany. Earth Planet. Sci. Lett. 253, 196–210. doi:10.1016/j.epsl.2006.10.026

Voigt, S., Erbacher, J., Mutterlose, J., Weiss, W., Westerhold, T., Wiese, F., Wilmsen, M., Wonik, T., 2008. The Cenomanian – Turonian of the Wunstorf section – (North Germany): global stratigraphic reference section and new orbital time scale for Oceanic Anoxic Event 2. Newsletters Stratigr. 43, 65–89. doi:10.1127/0078-0421/2008/0043-0065

Voigt, S., Hilbrecht, H., 1997. Late Cretaceous carbon isotope stratigraphy in Europe: Correlation and relations with sea level and sediment stability. Palaeogeogr. Palaeoclimatol. Palaeoecol. 134, 39–59. doi:10.1016/S0031-0182(96)00156-3

Voigt, S., Schönfeld, J., 2010. Cyclostratigraphy of the reference section for the Cretaceous white chalk of northern Germany, Lägerdorf-Kronsmoor: A late Campanian-early Maastrichtian orbital time scale. Palaeogeogr. Palaeoclimatol. Palaeoecol. 287, 67–80. doi:10.1016/j.palaeo.2010.01.017

Weigelt, E., Uenzelmann-Neben, G., 2007. Orbital forced cyclicity of reflector strength in the seismic records of the Cape basin. Geophys. Res. Lett. 34, 1–4. doi:10.1029/2006GL028376

Wong, T.E., 2007. Jurassic, in: Geology of the Netherlands Edited by Th.E.Wong, D.A.J. Batjes & J. de Jager Royal Netherlands Academy of Arts and Sciences, 2007. pp. 107–125. doi:10.1016/S0197-2510(10)70023-1

Wong, T.E., Batjes, D.A.J., De Jager, J., 2007a. Geology of the Netherlands. Netherlands Acad. Arts Sci. 356.

Wong, T.E., de Lugt, I.R., Kuhlmann, G., Overeem, I., 2007b. Tertiary, in: Geology of the Netherlands Edited by Th.E.Wong, D.A.J. Batjes & J. de Jager Royal Netherlands Academy of Arts and Sciences, 2007. pp. 151–171.

Worthington, P.F., 1990. Sediment cyclicity from well logs. Geol. Soc. London, Spec. Publ. 48, 123–132. doi:10.1144/GSL.SP.1990.048.01.11

Wray, D.., 1999. Identification and long-range correlation of bentonites in Turonian–Coniacian (Upper Cretaceous) chalks of northwest Europe. Geol. Mag. 136, 361–371. doi:10.1017/S0016756899002836

Wray, D.S., 1995. Origin of clay-rich beds in Turonian chalks from Lower Saxony, Germany - A rare-earth element study. Chem. Geol. 119, 161–173. doi:10.1016/0009-2541(94)00089-Q

Wray, D.S., Gale, A.S., 2006. The palaeoenvironment and stratigraphy of Late Cretaceous Chalks. Proc. Geol. Assoc. 117, 145–162. doi:10.1016/S0016-7878(06)80006-4

Wray, D.S., Wood, C.J., 1998. Distinction between detrital and volcanogenic clay-rich beds in Turonian-Coniacian chalks of eastern England. Proc. Yorksh. Geol. Soc. 52, 95–105. doi:10.1144/pygs.52.1.95

Wray, D.S., Wood, C.J., Ernst, G., Kaplan, U., 1996. Geochemical subdivision and correlation of clay-rich beds in Turonian sediments of northern Germany. Terra Nov. 8, 603–610. doi:10.1111/j.1365-3121.1996.tb00790.x

Wu, H., Zhang, S., Jiang, G., Hinnov, L., Yang, T., Li, H., Wan, X., Wang, C., 2013. Astrochronology of the Early Turonian-Early Campanian terrestrial succession in the Songliao Basin, northeastern China and its implication for long-period behavior of the Solar System. Palaeogeogr. Palaeoclimatol. Palaeoecol. 385, 55–70. doi:10.1016/j.palaeo.2012.09.004

Young, J., 1984. Function of coccoliths, in: Coccolithophores (Ed. A. Winter and W. G. Sieser). pp. 63–82.

Zhang, L.-J., Fan, R.-Y., Gong, Y.-M., 2015. Zoophycos macroevolution since 541 Ma. Sci. Rep. 5, 14954. doi:10.1038/srep14954

Ziegler, P.., 1990. Geological Atlas of Western and Central Europe (2nd Edition), Geological Society Publishing House.

Zijlstra, J.J.P., 1995. The sedimentology of chalk. Lect. Notes Earth Sci. 54, 194 pp. doi:10.1007/BFb0028303

Zijlstra, J.J.P., 1994. Sedimentology of the Late Cretaceous and Early Tertiary (Tuffaceous) Chalk of the Northwest Europe. Meded. van Fac. Aardwetenschappen Univ. Utr. 119, 1–192.

10. Supplementary information

10.1 Geological setting

10.1.1 Plate tectonic evolution

Based on the works of De Jager (2007) and Pharaoh et al. (2010) the plate tectonic evolution of the Netherlands can be subdivided into 4 phases (Figure 66). Phase 1 was the Caledonian orogenic event leading to creation of Laurussia. During the late Ordovician- early Silurian Avalonia and Baltica amalgamated (Torsvik and Rehnström, 2003). In the middle Silurian and early Devonian, Avalonia-Baltica and Laurentia collided creating Laurussia and the associated Caledonian orogen. During phase 1 the Netherlands moved from 60S to 30S. Phase 2 was the Variscan orogenic phase. During the Carboniferous Gondwana and Laurussia collided and formed the Variscan orogen. The Netherlands was located near the equator within the foreland of Variscan orogeny. Phase 3 occurred From the Late Triassic to Early Cretaceous. The Netherlands experienced multiple rifting events associated with the breakup of Pangea. In-between these rifting events thermal subsidence occurred. The Netherlands was located at ~35N. Phase 4 occurred from the early Cretaceous to present. The rifting ceased and a thermal sag phase ensued. The thermal sag was interrupted by multiple inversion phases related to the Alpine orogeny. The Netherlands moved north from 35N to its present latitude.

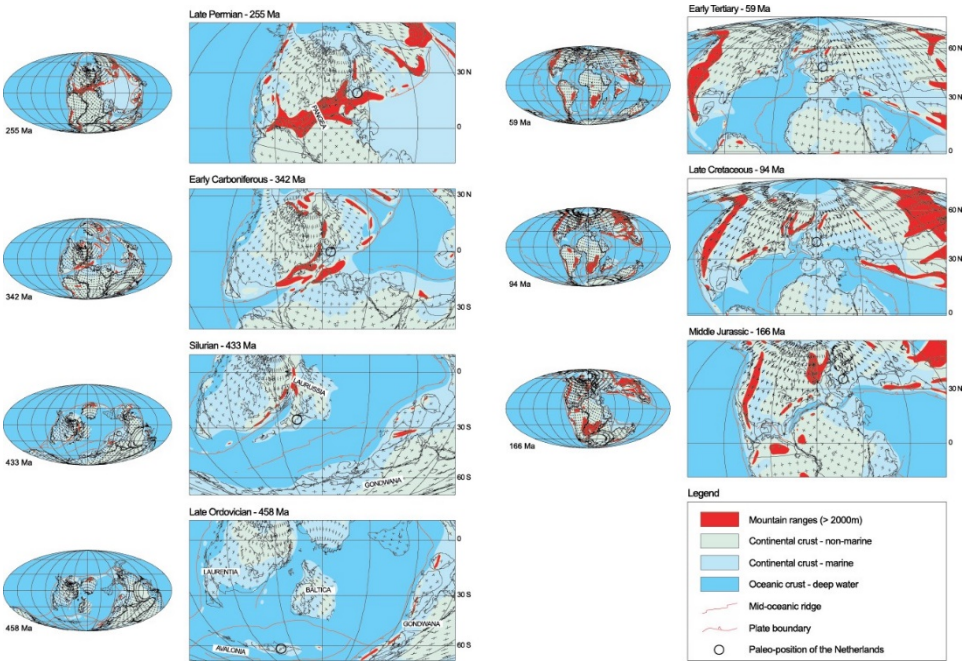

Figure 66. plate tectonic evolution of the Netherlands (De Jager, 2007)

10.1.2 Crustal structure

The main fault framework was formed during the Caledonian and Variscan Orogenic phases (de Jager, 2007; Guterch et al., 2010). There are two main fault trends; the N-S and NW-SE fault trends (Figure 67). The N-S fault trend is most prevalent in the north-western Dutch offshore. The N-S trends runs parallel to the Avalonia-Baltica suture trend. Towards the south of the Netherlands the NW-SE fault trend becomes more dominant. The NW-SE oriented fault trend is parallel to both Variscan orogenic and the Avalonia-Baltica trends.

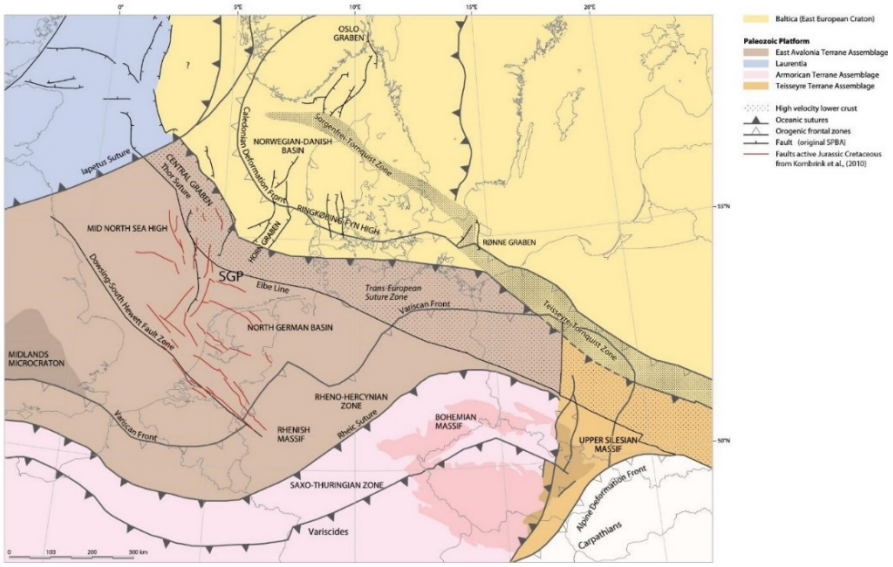

Figure 67. modified from Guterch et al. (2010). Map of the different terranes forming the basement of the Southern Permian Basin. Note the change in orientation for the Baltica Avalonia suture trend from N-S to EW

.

10.1.3 Tectonostratigraphic framework

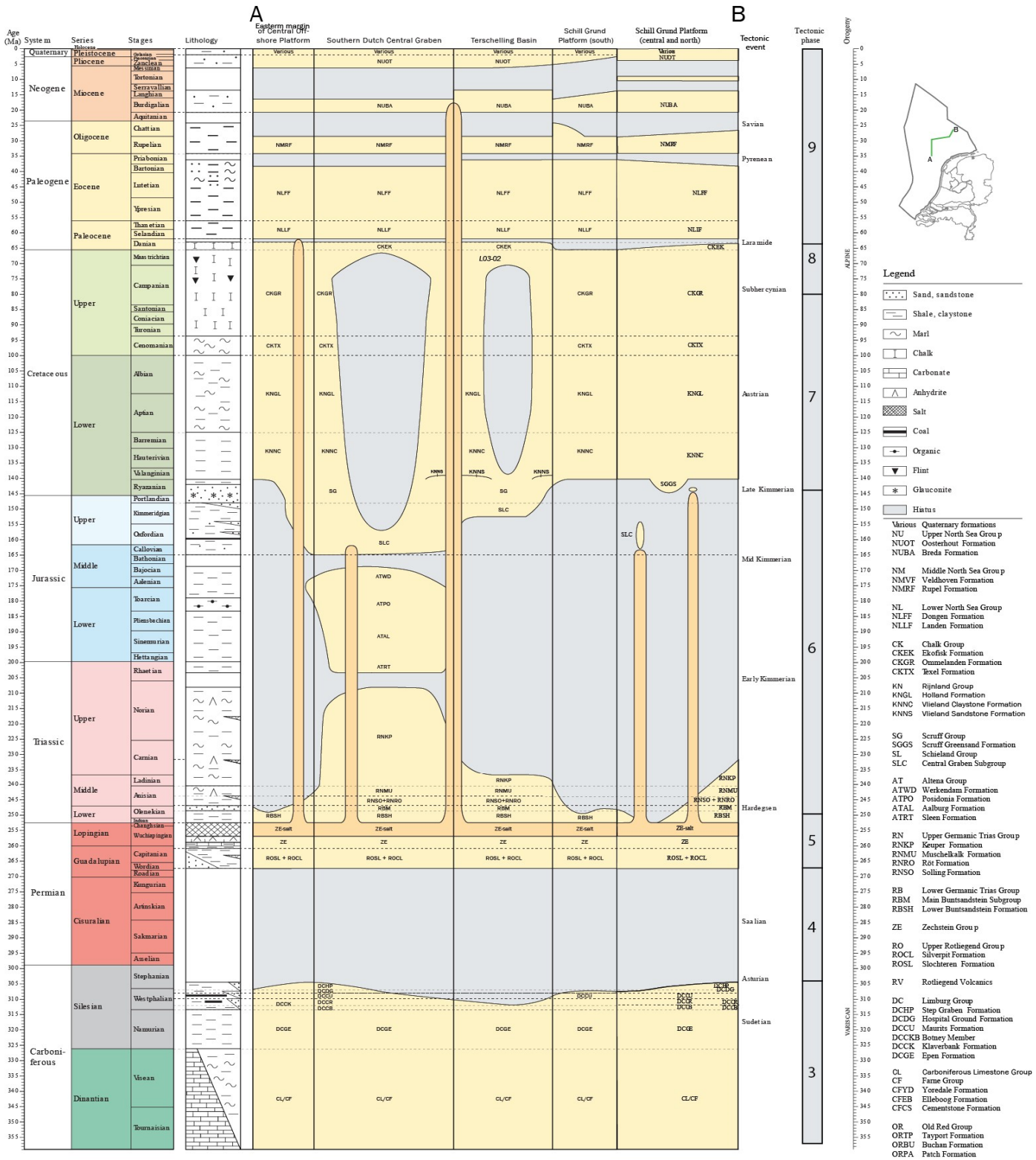

Figure 68. tectonostratigraphic cross-section modified after (TNO, 2011)

10.1.4 Sedimentary succession structural elements

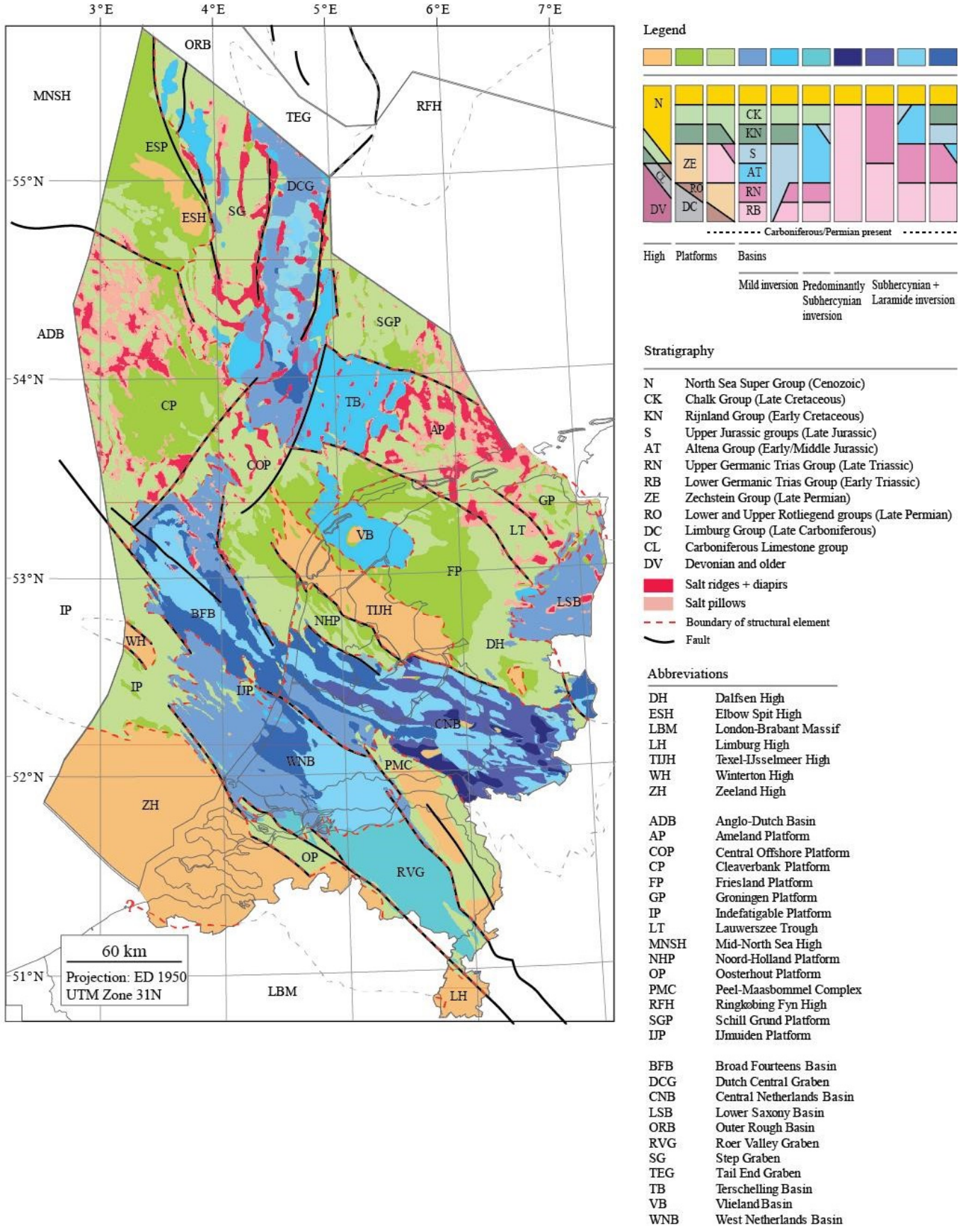

Figure 69. Modified after (Kombrink et al., 2012) *Structural elements in the Netherlands with a generalised sedimentary succession.*

10.1.5 Locations wells with biostratigraphy

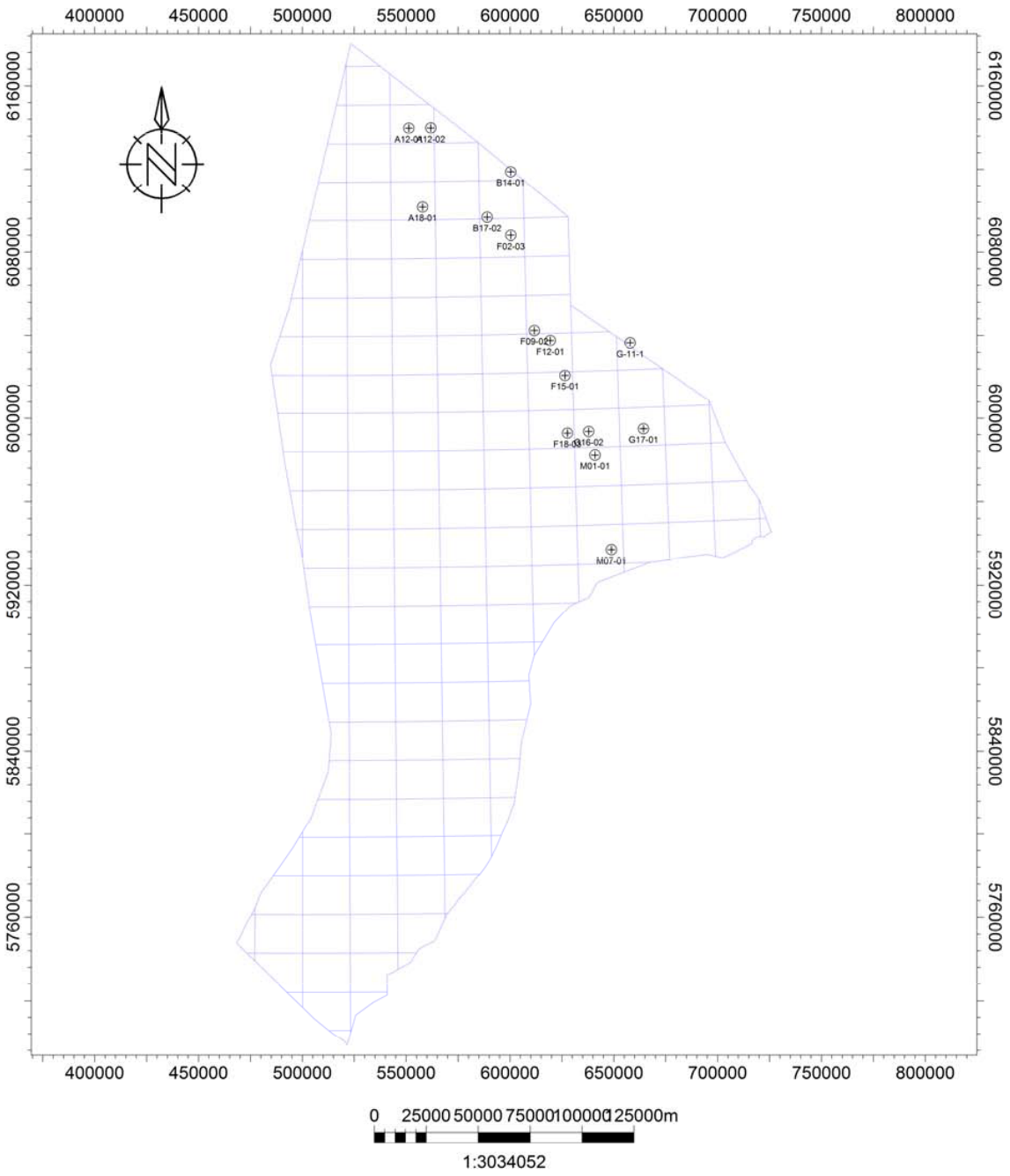

Figure 70. Location wells with biostratigraphy

10.1.6 Biostratigraphy complete

For Table 2. See file table-2-biostrat-complete.pdf

10.1.7 Coccolithophores (extended)

Coccolithophore remains are the main constituent of chalk (Figure 4). The coccolithophore is a unicellular, eukaryotic phytoplankton (algae) (Figure 4). Coccolithophores consist of a Protoplasm and a Periplasm cell covering made of scales (coccoliths) which can be made from organic and non-organic (carbonate) material (Pienaar, 1994). The coccolith disks are formed on an organic baseplate or an organic matrix. Calcite Coccoliths consist of Low-mg calcite. Motile species additionally possess flagella.

The coccoliths can be grouped into two categories: the Holococcoliths and Heterococcoliths (Siesser and Winter, 1994). Holococcoliths consist of hexagonal prisms and/or rhombohedral crystals. The crystal faces and angles of Holococcoliths can be easily observed. Heterococcoliths consist of rhombohedral and hexagonal crystals. The crystal faces and angles of Heterococcoliths are suppressed, which results in disc shaped coccoliths. The most common coccolith morphology is the placolith shape in which a gap in between the distal and proximal shield enables the interlocking of the coccolith plates. Non-interlocking plates are held together by an organic membrane.

Multiple functions have been ascribed to coccoliths (Young, 1984). One function of the coccolith could be protection related. The coccolith can protect itself from predation by increasing its size making the coccolithophore harder and less efficient to digest. The coccolith covering also protects the delicate cell membrane. The coccolith covering might also help with environmental buffering and nutrient uptake. The arrangement of coccoliths might help with the passage of nutrients waste products, carbon dioxide and other dissolved gasses. The coccolith covering might also act as a transition layer in between the cell and the seawater. The water in between the coccolith and the cell membrane might act as a buffer which protects the cell from sudden shifts or unfavourable conditions outside the cell. The larger surface area and volume due to presence of the coccoliths might enhance nutrient uptake and provide additional storage for nutrients. Coccoliths could also have a biochemical function. Calcification creates CO_2 which in term can be used in photosynthesis. Calcite precipitation could therefore be favoured over the creation of organic scales. Calcite coccoliths could also act as sink for hydroxyl ions during photosynthesis and thus make photosynthesis more efficient. Another function might be flotation-related. Forced convection enhances nutrient uptake and therefore moving through the water column is a competitive advantage. Calcite increases the density and thus the sinking rate increasing the nutrient uptake. Turbulent mixing will make the cell remain in the photic zone and a higher sinking rates will enhance the movement of the cell through the water column increasing the nutrient uptake. Temperature affects the viscosity and therefore changing the density by calcification can mitigate viscosity differences and thus maintain a favoured sinking rate. Calcification might also enable variable sinking rates enabling nutrient uptake from deeper waters while the cell is growing. A different shape may reduce sinking rates in non-turbulent areas were slow sinking rates are favourable. Although coccoliths do not have a direct influence on the motility of the cell a reduced size of coccoliths will make cells have a neutral density enabling easier motility. Possible differences in morphology of the coccolith might also impact its motility. Coccoliths might also play a role in regulating the light entering the cell. A coccolith can reflect ultraviolet-light enabling species to live near the sea surface or focus light to enable species to live in the deeper parts of the photic zone.

Different Coccolithophore species are adapted to different salinities temperatures and nutrient availability and therefore the presence of coccoliths in general does not imply any specific environment (Brand, 1994). Coccolithophore species can be grouped into 4 distinct ecological distributions: Placolith bearing, umbelliform, Floriform and miscellaneous (Young, 1984). Placolith bearing coccolithophores are found in upwelling regions. Placolith coccolithophores are the important bloom forming type of coccolithophore. Placolith coccolithophores also dominate in seasonally stratified higher latitude waters and coastal and shallow sea areas. Umbelliform coccolithophores mainly occur in subtropical latitudes in oligotrophic waters. Floriform coccolithophores occur in the deep photic zone. Floriform coccolithophore have flagellar openings indicating that they are most likely motile. Miscellaneous coccolithophores consist of 80% of the species but often no more than 20% of the individuals in a sample (Young, 1984) . The miscellaneous coccolithophores have highly variable morphologies and are often associated with a specific environmental setting.

Coccolithophores are transported to the sea bottom in the form of faecal pellets or marine snow (Kennedy, 1987; Steinmetz, 1994a). Faecal pellets are made by zooplankton. Coccoliths often pass through alimentary canals of zooplankton without being mechanically or chemically impacted by the process. Marine snow is an amorphous particulate made of different components (organic, non-organic and detrital) and is bounded by intermolecular,

intramolecular, atomic forces, surface tension, organic cohesion or electrostatic force. On the seabed, the marine snow and faecal pellets are reworked and disintegrate into clay to silt sized mud ((Fabricius et al., 2007) and Figure 5).

Coccolith dominated sediments can be good recorders $\delta^{13}C$ and $\delta^{18}O$ at the sea surface (Steinmetz, 1994b). Coccolithophores live in the in top 100 to 50m of the water column and will therefore record the isotopic ratio at the sea surface. Coccolithophores do not actively migrate to varying depths during their lifespan so the isotope ratio within a specimen does not vary during its lifetime. No stages of calcification are present in coccolithophores so the isotope ratio within a specimen remains the constant. The pure low Mg-calcite skeleton has a higher resistance to dissolution and recrystallization during sedimentation when compared to other types of calcite. Foraminifera and coccolithophores do follow the same $\delta^{13}C$ and $\delta^{18}O$ trend but there is often a difference in the absolute values (Steinmetz, 1994b).

10.2 Correlation coefficient XRF

	vshale	vshale larionov old corrected	Zr	Zn	Sr	Sc	S	Rb	Ni	Mn	K	Fe	Cu	Co	Ca	Au	As	por.calc	por_1_2_1 (por avg.)	matrix density	NPHI	RHOB	Sonicdensity
vshale	1																						
vshale larionov old corrected	1	1																					
Zr	0.056959665	0.056959665	1																				
Zn	-0.101317418	-0.101317418	4.22E-05	1																			
Sr	0.113895571	0.113895571	-0.06317	0.032203	1																		
Sc	-0.195363343	-0.195363343	0.040266	0.339556	0.173034	1																	
S	0.272539038	0.272539038	0.013727	0.070517	0.206068	0.175366	1																
Rb	0.443012324	0.443012324	0.268706	-0.08797	0.280869	-0.1228	0.442707	1															
Ni	0.094003185	0.094003185	0.253396	0.036189	-0.08993	-0.07884	0.14122	0.119775	1														
Mn	0.049784368	0.049784368	0.173952	0.238993	0.126641	0.102163	-0.33351	-0.00992	0.198025	1													
K	0.109585774	0.109585774	0.396316	0.336731	-0.14325	-0.21457	-0.36401	0.15853	0.267844	0.289121	1												
Fe	-0.097528531	-0.097528531	0.018637	0.210375	-0.1166	-0.02883	0.17931	0.058665	0.30686	0.329243	0.233834	1											
Cu	0.317779718	0.317779718	0.181918	0.020032	0.513628	-0.12419	0.368181	0.331762	0.177736	-0.2225	-0.13468	-0.05871	1										
Co	0.027612094	0.027612094	0.337809	0.139392	0.074454	0.101578	0.22427	0.111391	0.447243	0.030624	0.250844	0.43897	0.267912	1									
Ca	-0.448021478	-0.448021478	0.020835	0.024083	-0.03092	-0.0059	-0.74495	-0.60444	0.053124	0.263694	0.361323	-0.10639	-0.34507	-0.05472	1								
Au	-0.139618328	-0.139618328	0.314336	-0.08614	0.218951	0.255949	0.18655	-0.08818	0.044762	-0.00098	-0.00895	-0.26578	0.229896	0.000478	0.163756	1							
As	0.045474916	0.045474916	0.1745	0.079433	0.170106	-0.02831	0.436893	0.144024	0.345803	-0.22399	-0.06999	0.606583	0.15797	0.428404	-0.25939	0.144005	1						
por.calc	0.237240654	0.237240654	-0.19598	-0.11855	0.143827	-0.08664	0.164806	0.172733	-0.13559	-0.19794	-0.2468	-0.20333	0.059498	-0.08515	-0.23701	0.029175	0.109342	1					
por_1_2_1 (por avg.)	0.309649451	0.309649451	-0.12531	-0.15674	0.094912	-0.17581	0.174412	0.247169	-0.17643	-0.32175	-0.22795	-0.17045	0.059231	-0.12933	-0.28787	-0.07264	0.080247	0.942361	1				
matrix density	-0.316200541	-0.316200541	-0.04526	-0.042	0.19293	0.205085	-0.18356	-0.46074	-0.09076	-0.06815	-0.13549	-0.28936	-0.11279	-0.04975	0.534626	0.308351	-0.06752	0.029209	-0.070010365	1			
NPHI	-0.099742127	-0.099742127	0.115757	-0.0079	0.164421	0.009281	0.318139	0.471682	-0.00429	-0.05556	-0.37828	0.098893	0.26896	0.040703	-0.35139	-0.05173	0.224412	0.170264	0.153508155	-0.22597053	1		
RHOB	0.020452332	0.020452332	-0.0711	0.037603	-0.09891	0.00947	-0.37271	-0.5501	0.035698	0.07105	0.384432	-0.09615	-0.10802	-0.01461	0.461551	0.062021	-0.20701	-0.24789	-0.236051484	0.338955647	-0.91932	1	
Sonicdensity	-0.135231615	-0.135231615	-0.2015	0.101225	-0.1734	0.090249	-0.34815	-0.58508	-0.00954	-0.00808	0.273061	-0.15318	-0.32805	-0.0582	0.470959	0.079801	-0.26631	-0.28241	-0.304678409	0.412929559	-0.88908	0.901347	1

Table 8. Correlation coefficient between measurements well and core A12-02.

10.3 Seismic anomalies

10.3.1 Channel system

As mentioned by van der Molen et al., (2004) there is a channel system on the east side of the Schill Grund Platform. In the 3D survey G13-G14-G17-Z3NAM1997A the channel systems can be identified (Figure 71). A More extensive 3D study has been done on the German part of the channel system by (Surlyk et al., 2008). The channel in the German sector connects to the channel found in the Dutch sector indicating that there was a single large channel complex active present on the eastern part of the Schill Grund Platform during the Late Cretaceous. Another smaller channel feature has been identified in well F18-03 (Figure 72)

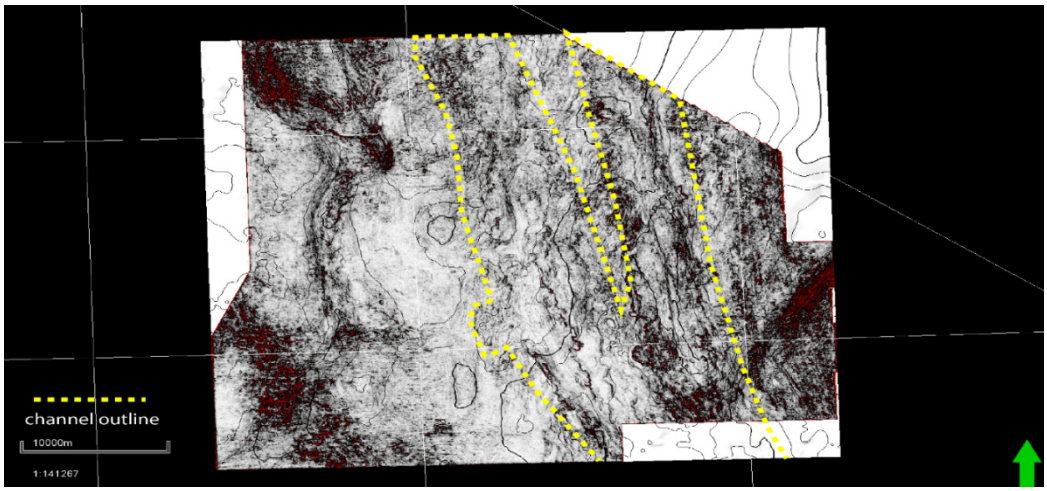

Figure 71. Variance cube attribute extracted from seismic cube G13-G14-G17-Z3NAM1997A on the top CK surface which is in term shifted down by 200m. note that within the channel there are elongated wavy lines running lengthwise in the channel. These lines are interpreted as being an erosional feature. (note this is a top view of the channel)

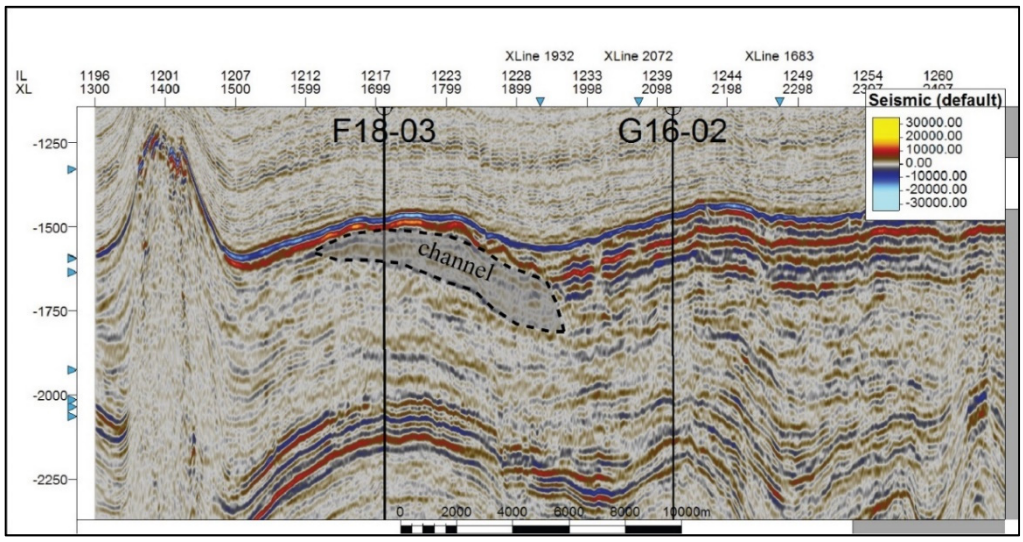

Figure 72. Channel feature around well F18-03.

10.3.2 Pockmarks

In the 3D survey G13-G14-G17-Z3NAM1997A many spherical shapes can be identified (Figure 73). These spherical shapes have a similar appearance to the pockmarks found in the Danish central graben (Arfai et al., 2016; Masoumi et al., 2014). The upper Carboniferous coals in the area reached a maximum maturity during the early Triassic to Late Jurassic (Heim et al., 2013). Leakage of hydrocarbons into the Chalk Group is a possible mechanism for the creation of these pockmarks. Pockmarks can also form as the result of porewater escaping (Harrington, 1985). No hydrocarbon accumulations have been found in the Chalk Group on the Schill Grund Platform, which makes the pore-water escape option the most likely process.

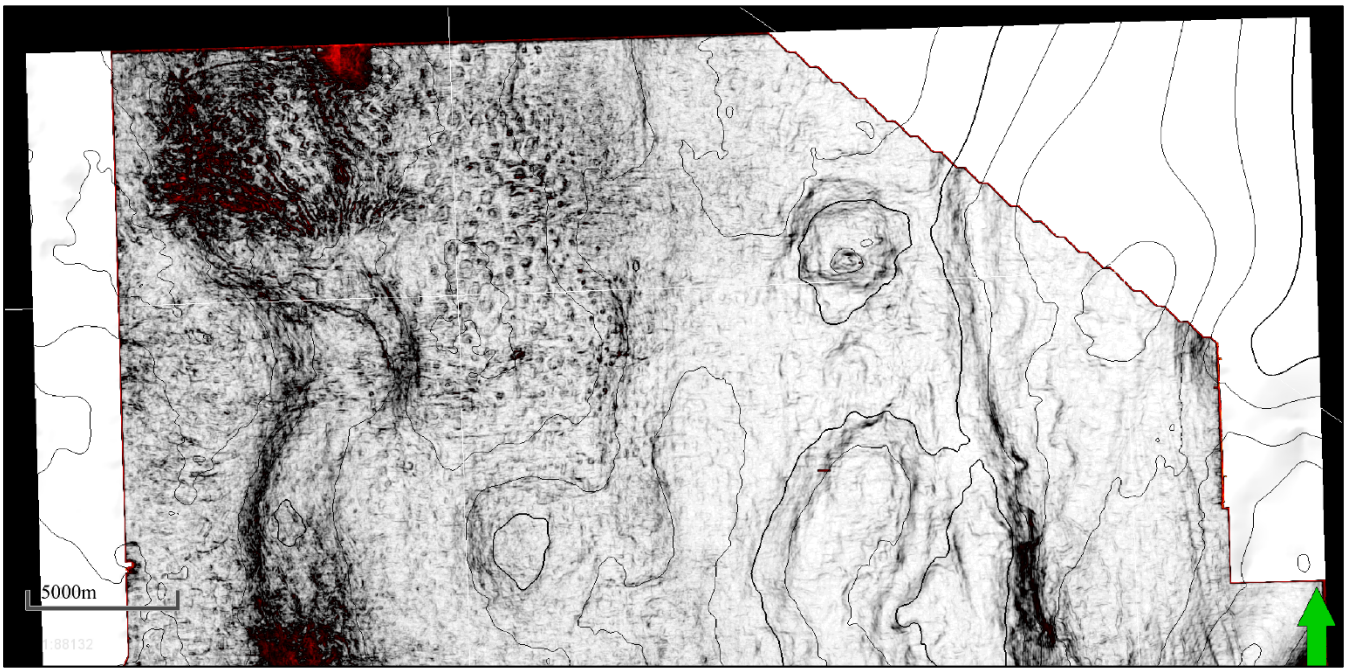

Figure 73. Variance cube attribute extracted from seismic cube G13-G14-G17-Z3NAM1997A on the top CK surface which is in term shifted down by 80m. in the upper left corner of the seismic there are many spherical features present.

10.4 Porosity trend

A breakdown of the Vshale-porosity correlation is seen in Figures 19 and 20. The Lower North Sea Group covers the Chalk Group. The Lower North Sea Group consist of mainly shaly/clayey deposits and acts as a seal trapping porewater. The trapping of the porewater has led to overpressures in the Chalk Group (Japsen, 1998; Van der Molen, 2004). This overpressure leads to undercompaction and thus results in higher porosities (Figure 74). The overpressure effect on porosity is largest towards the top of the Chalk Group where it overrules the gamma-ray porosity relationship (Figure 19 and 20). In the bottom part of the Chalk Group the porosity-Vshale correlation can correlated to shale rich laminae (Damholt and Surlyk, 2004; Scholle et al., 1998). The shale rich are linked to low density turbidity currents (Damholt and Surlyk, 2004). local reworking and redeposition might have also occurred during the deposition of turbidity currents. The reworking and redeposition can be deducted from the presence of chalk clasts in the laminated layers (Figure 30).

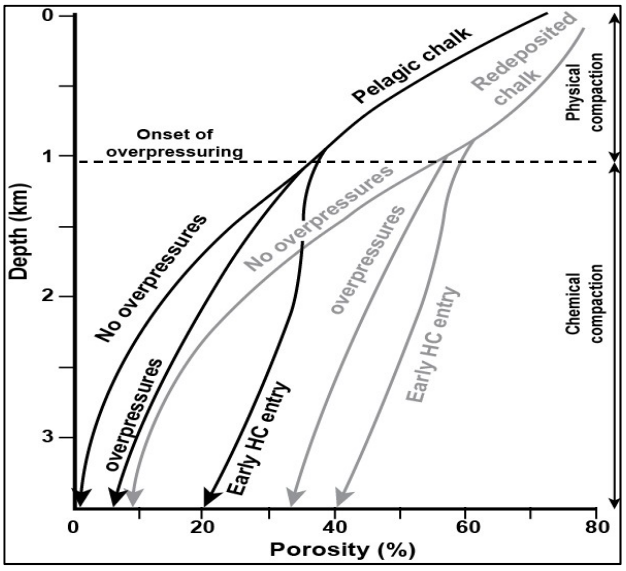

Figure 74. Porosity compaction from (Gennaro, 2011) which is in term modified from (Brasher and Vagle, 1996)

10.5 Trace data in TWT domain

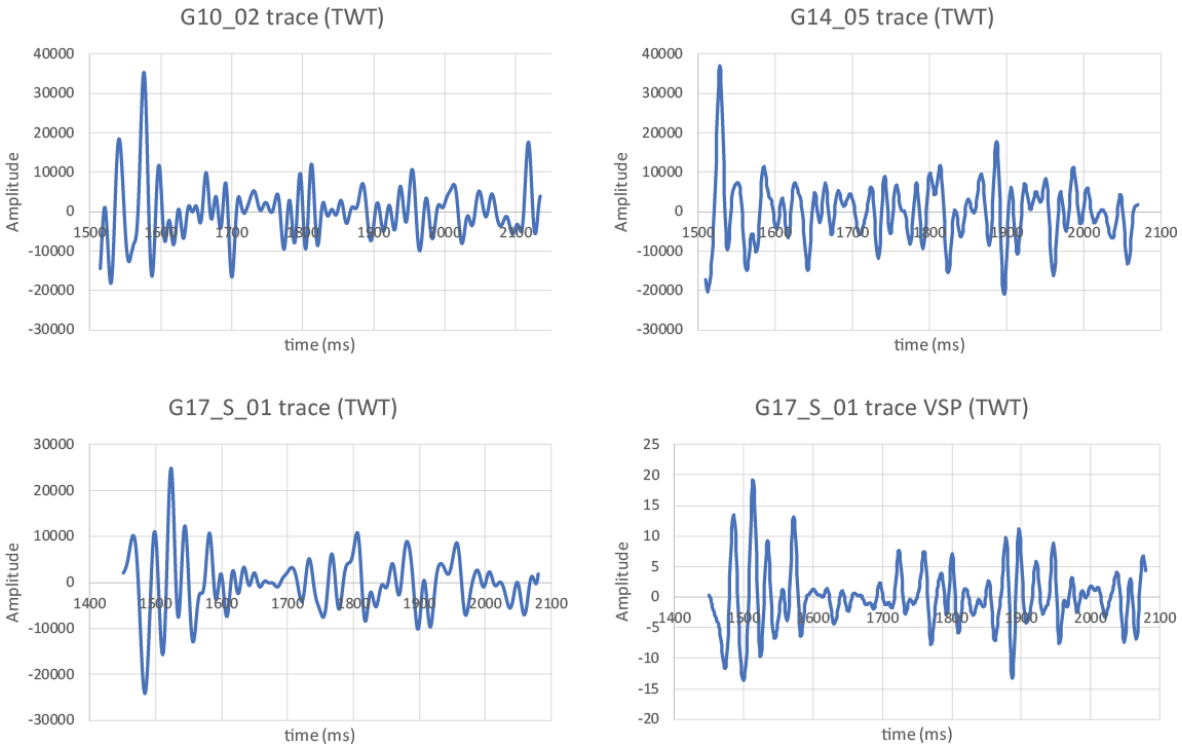

Figure 75. Trace data in seismic time domain

10.6 B-T spectra

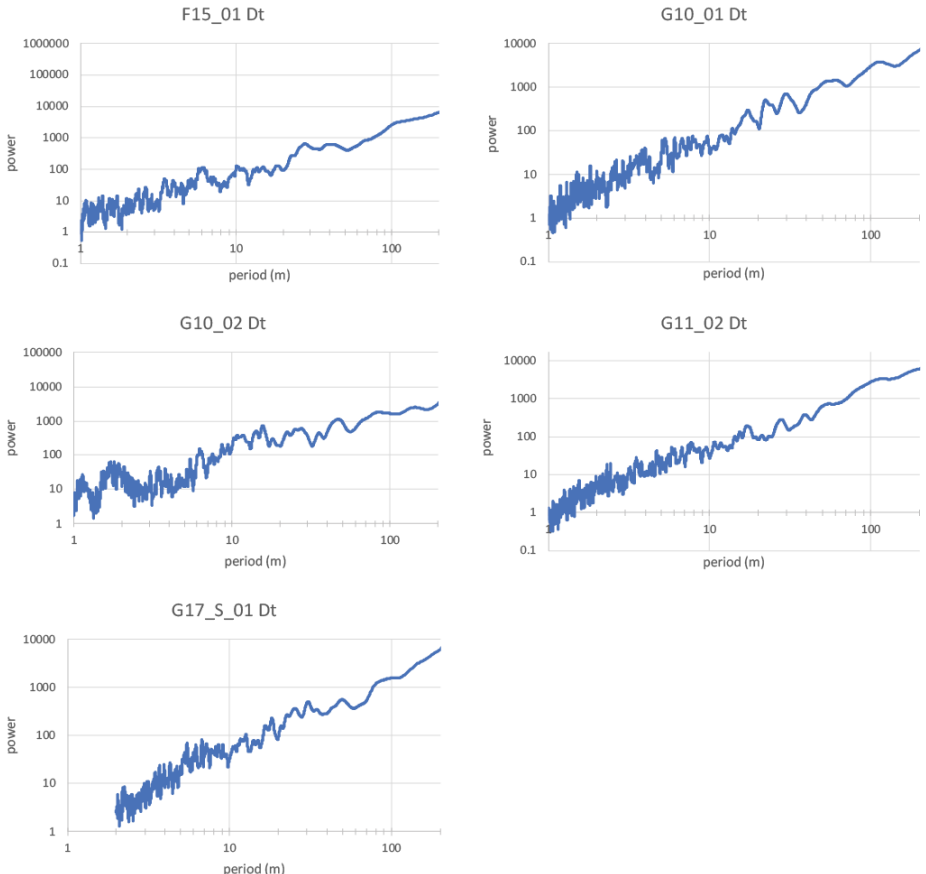

Figure 76. Note Blackman-Tukey spectrograms for the DT records. Note that the scales are logarithmic. Peaks are identified as being positive deviations from the increasing baseline power

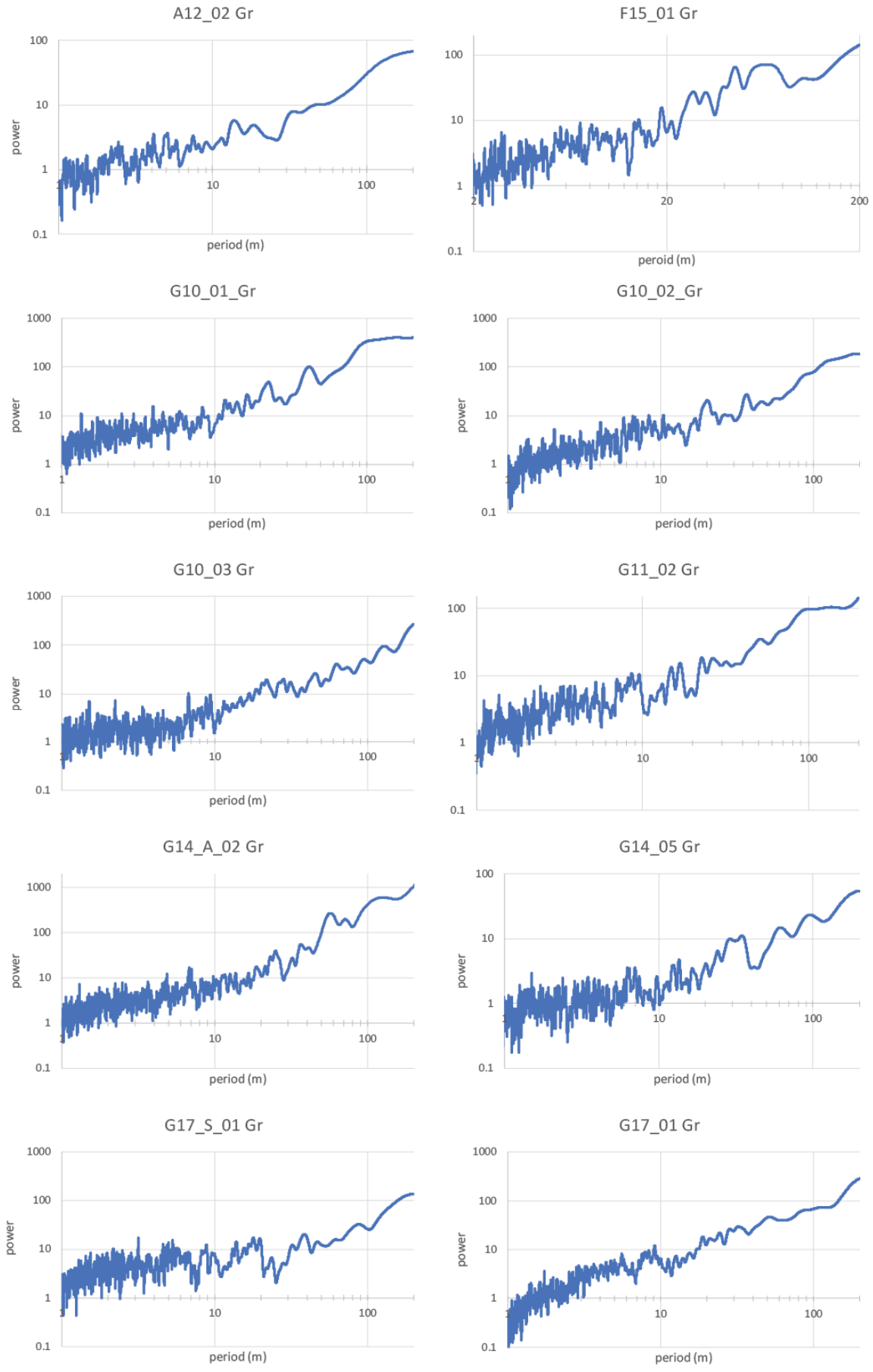

Figure 77. Note Blackman-Tukey spectrograms for the Dr records. Note that the scales are logarithmic. Peaks are identified as being positive deviations from the increasing baseline power.

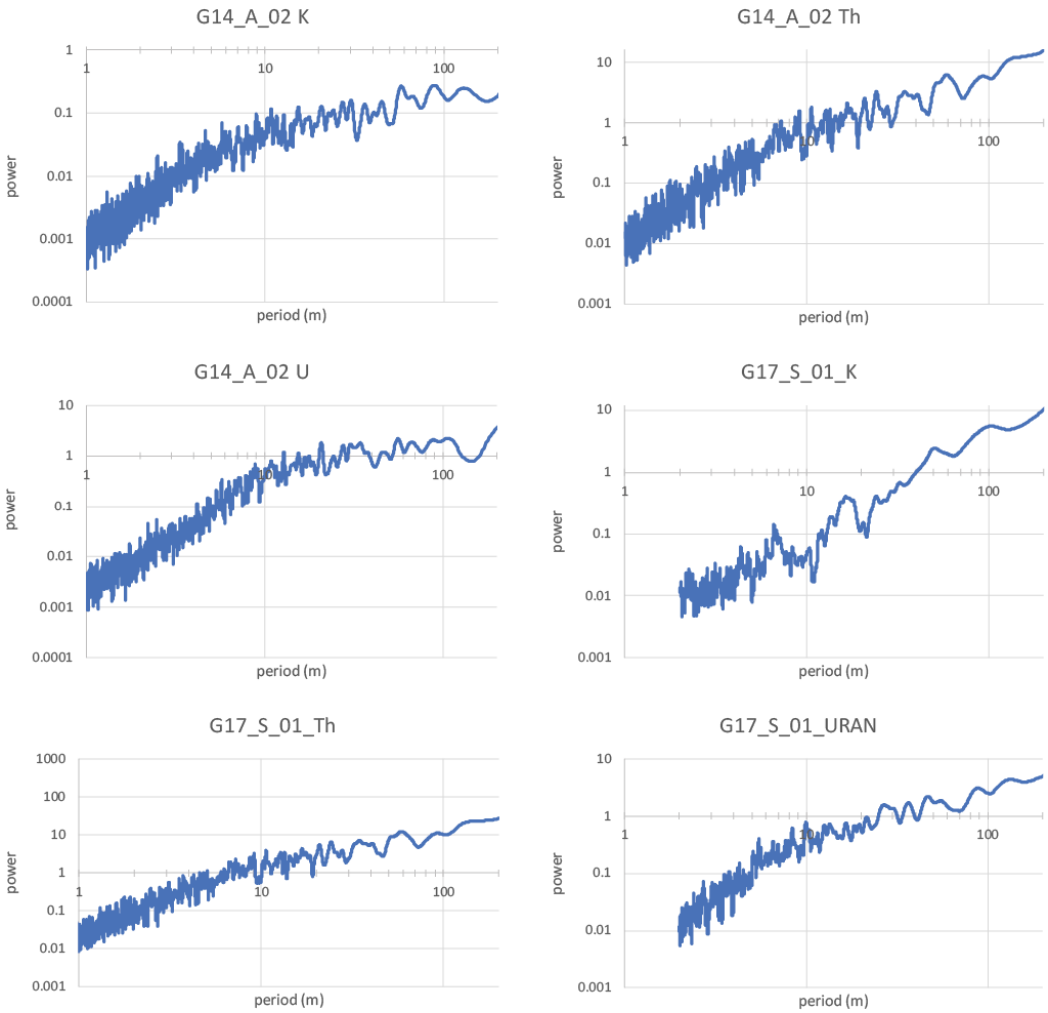

Figure 78. Note Blackman-Tukey spectrograms for the spectral gamma ray records. Note that the scales are logarithmic. Peaks are identified as being positive deviations from the increasing baseline power.

10.7 Redfit spectra

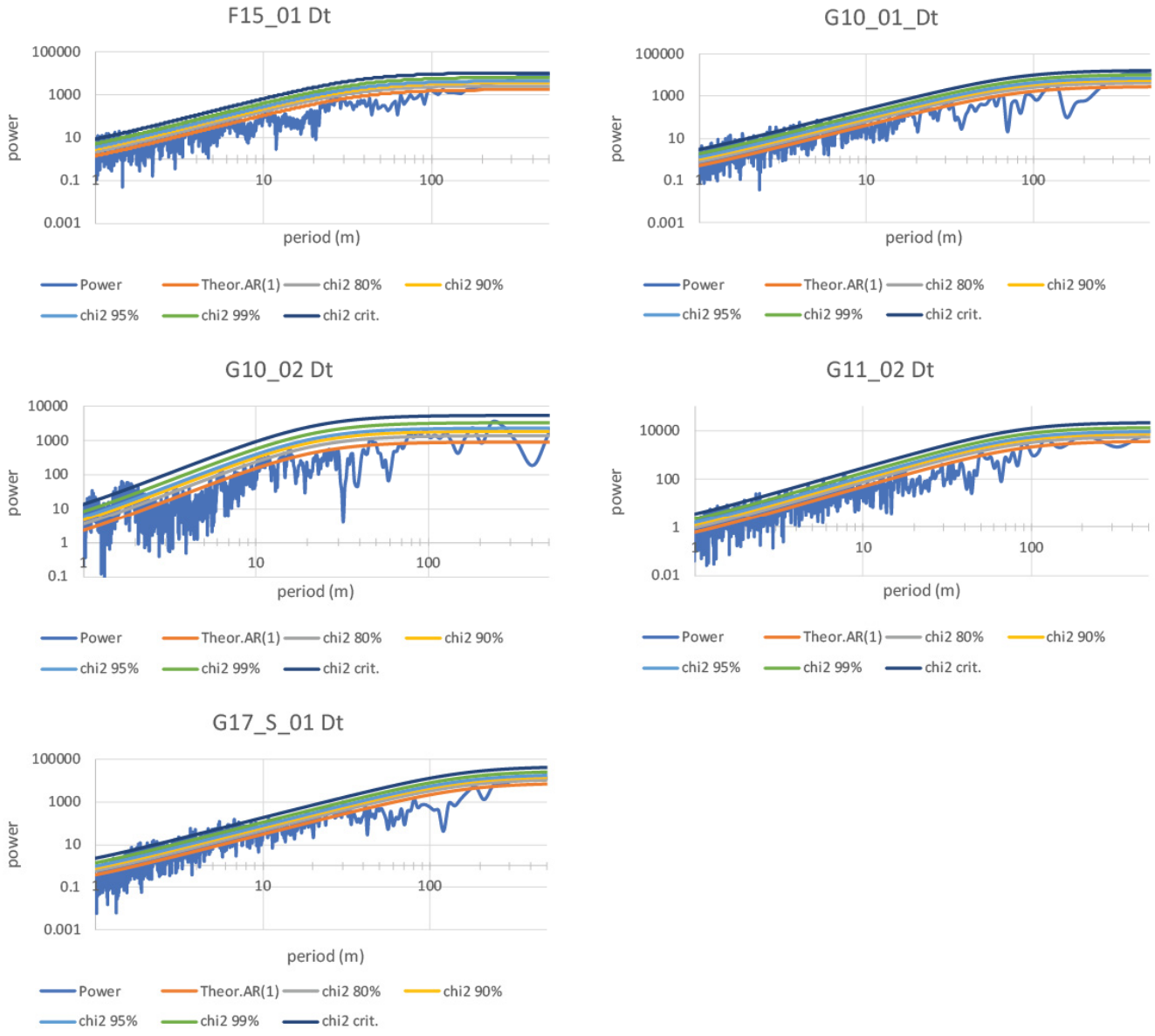

Figure 79. Redfit spectrograms with confidence intervals. Note that some of axis scales are logarithmic. When the y-axis has a logarithmic scale them peaks are identified as positive deviations from the increasing baseline power.

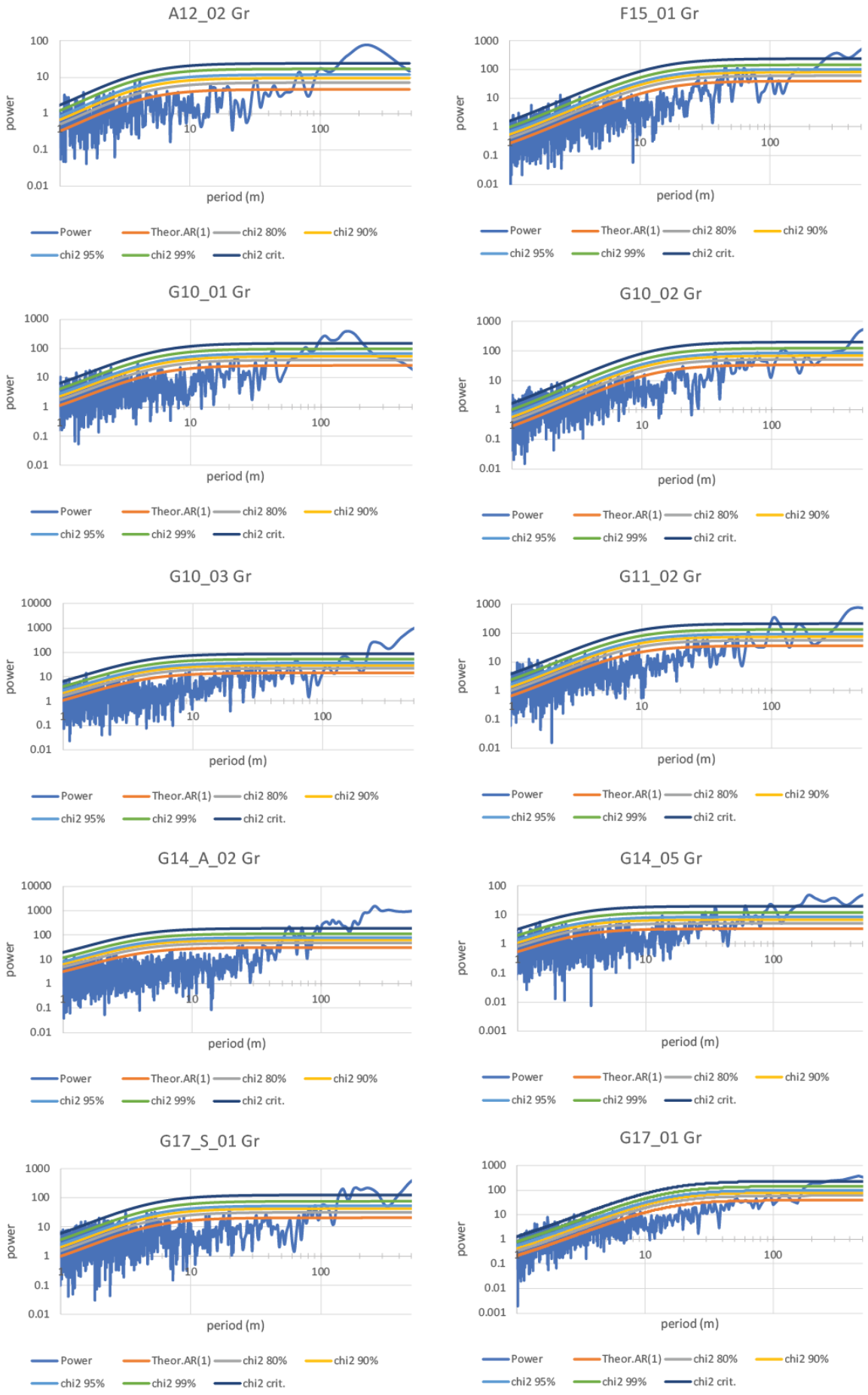

Figure 80. Redfit spectrograms with confidence intervals. Note that some of axis scales are logarithmic. When the y-axis has a logarithmic scale them peaks are identified as positive deviations from the increasing baseline power.

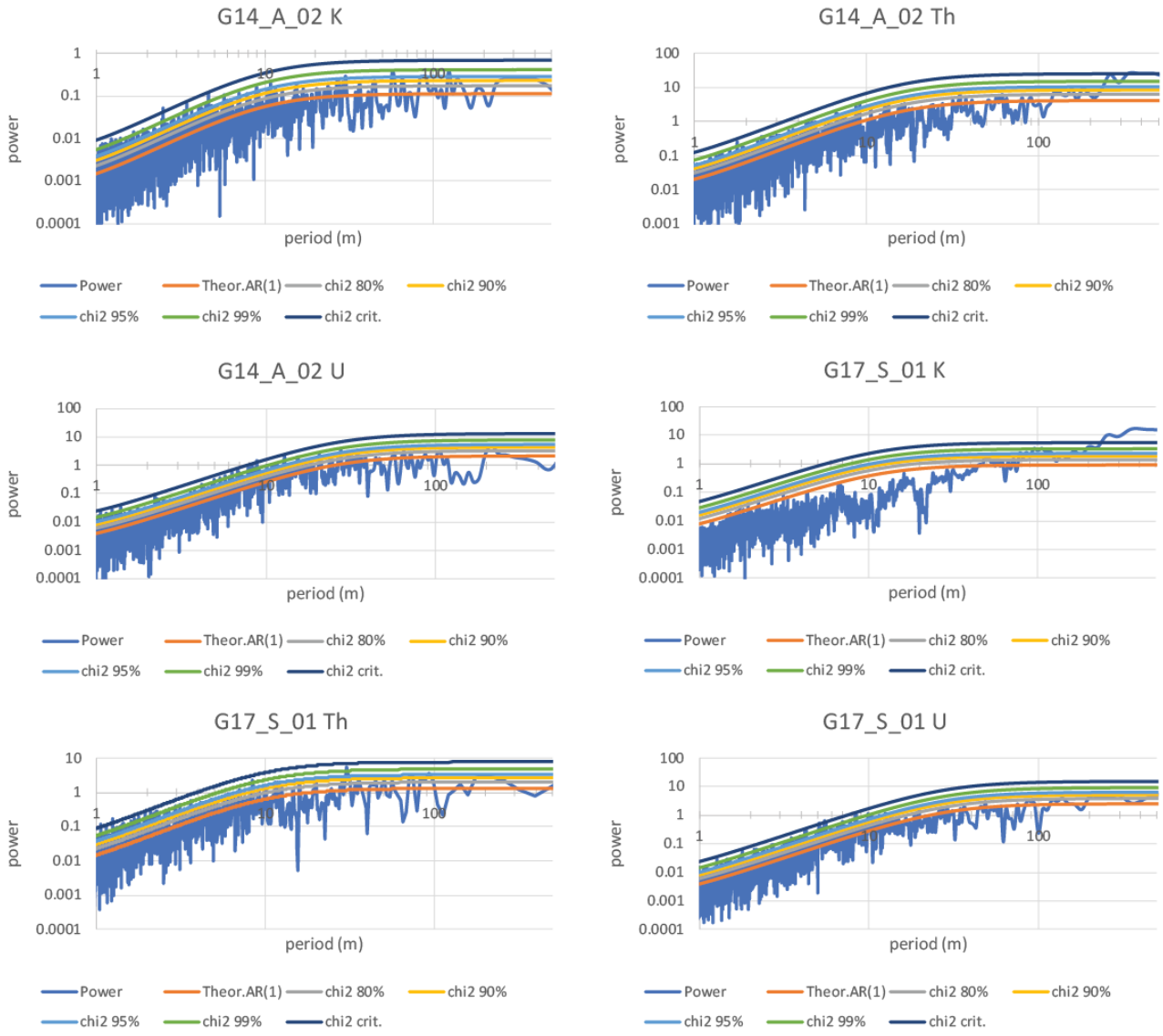

Figure 81. Redfit spectrograms with confidence intervals. Note that some of axis scales are logarithmic. When the y-axis has a logarithmic scale them peaks are identified as positive deviations from the increasing baseline power.

10.8 EHA spectra

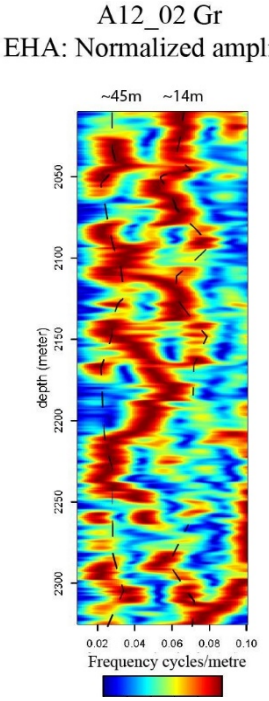

Figure 82. Spectrum of GR record of well A12-02.

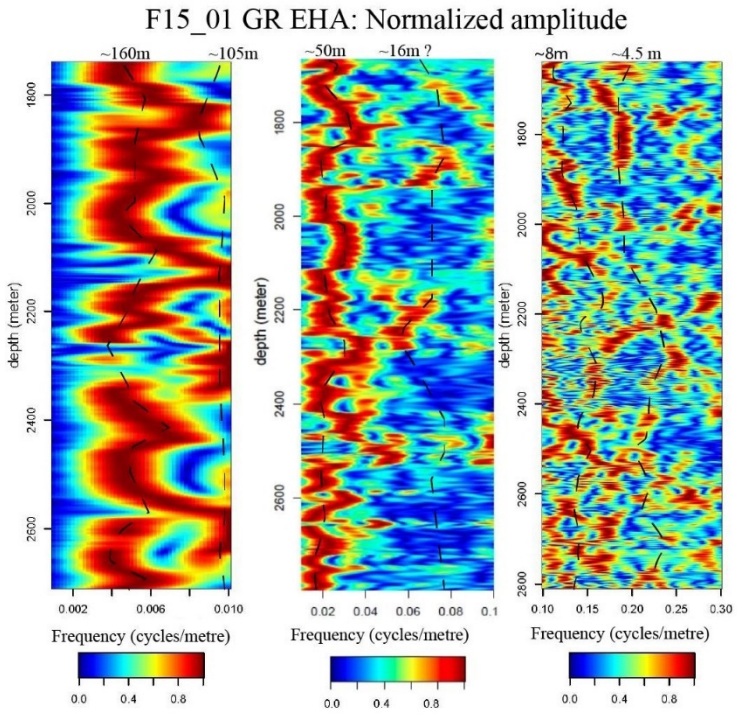

Figure 83. Spectra of GR record of well F15-01.

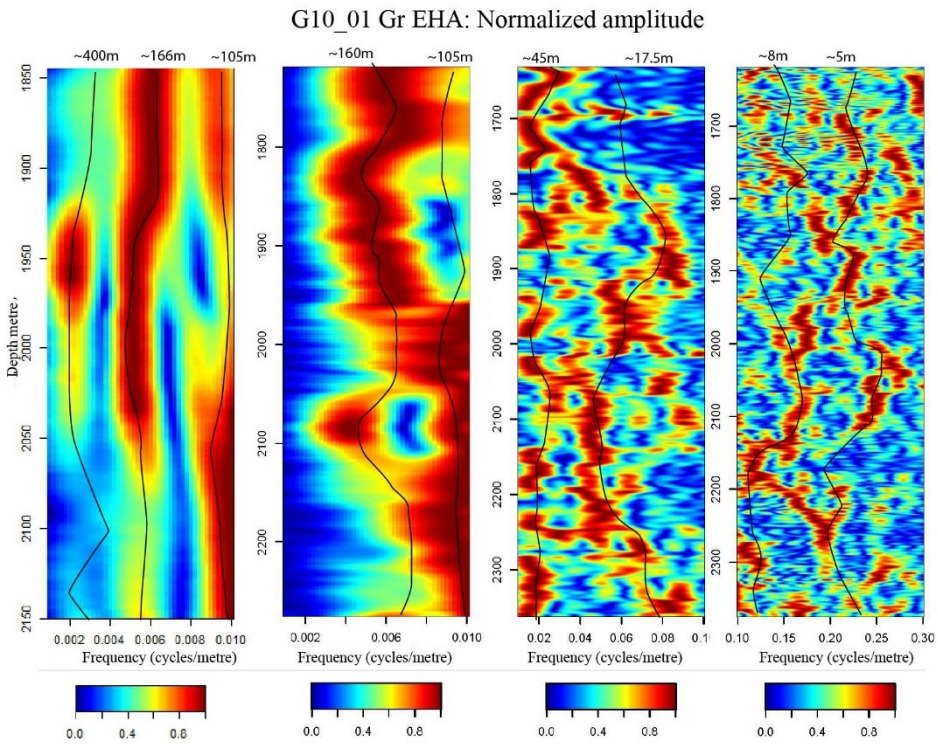

Figure 84. Spectra of GR record of well G10-01. The left spectrum has the same frequency range as the one to the right of it but the sliding window on the left one is 500 while one on the right is 500m.

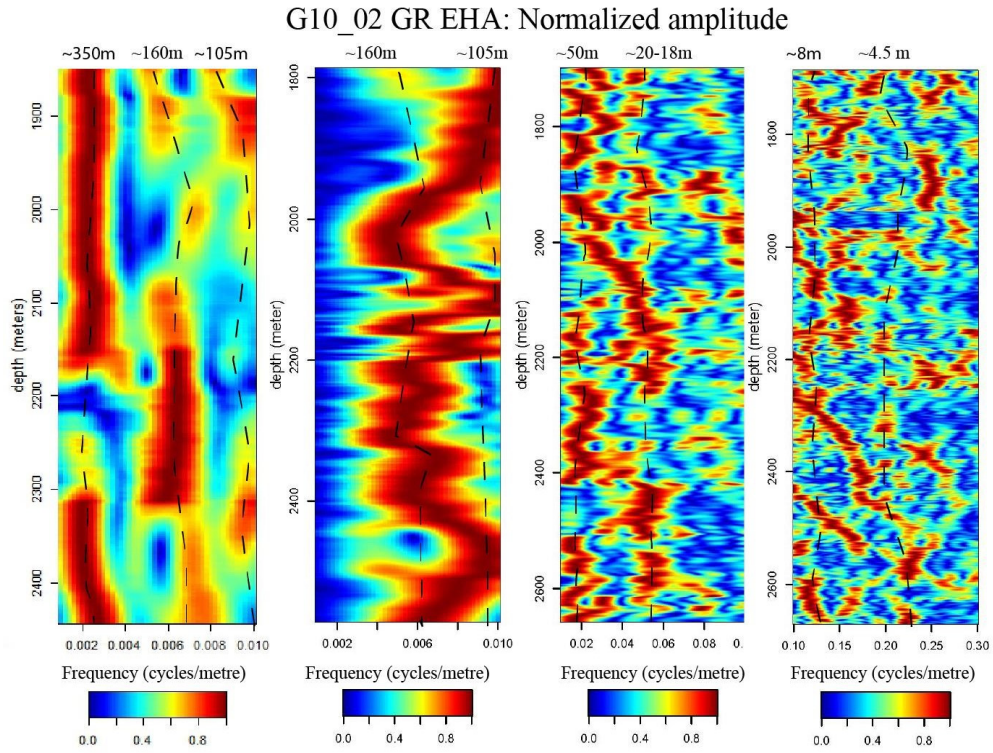

Figure 85. Spectra of GR record of well G10-02. The left spectrum has the same frequency range as the one to the right of it but the sliding window on the left one is 500 while one on the right is

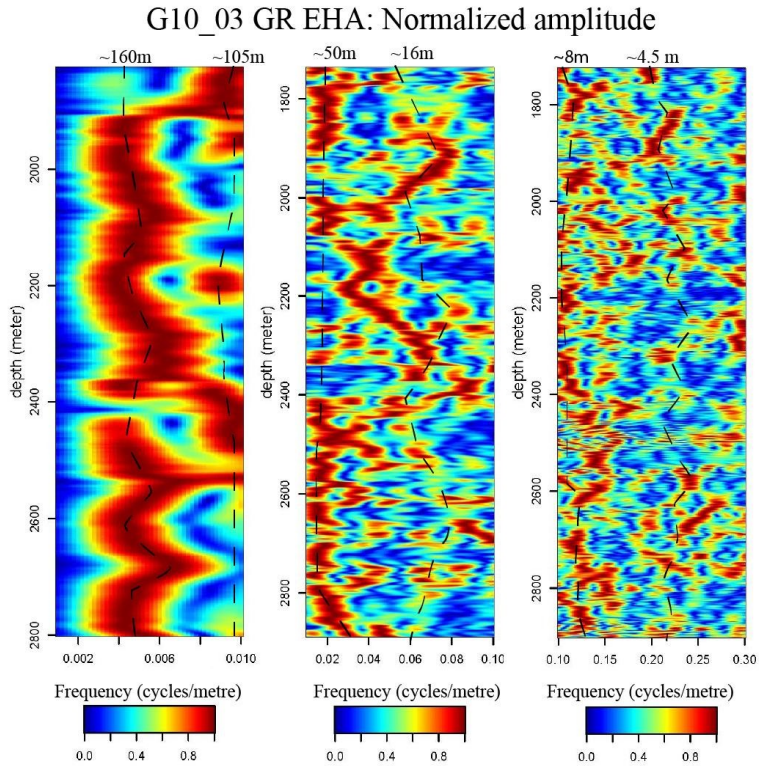

Figure 86. Spectra of GR record of well G10-03. The left spectrum has the same frequency range as the one to the right of it but the sliding window on the left one is 500 while one on the right is 500m.

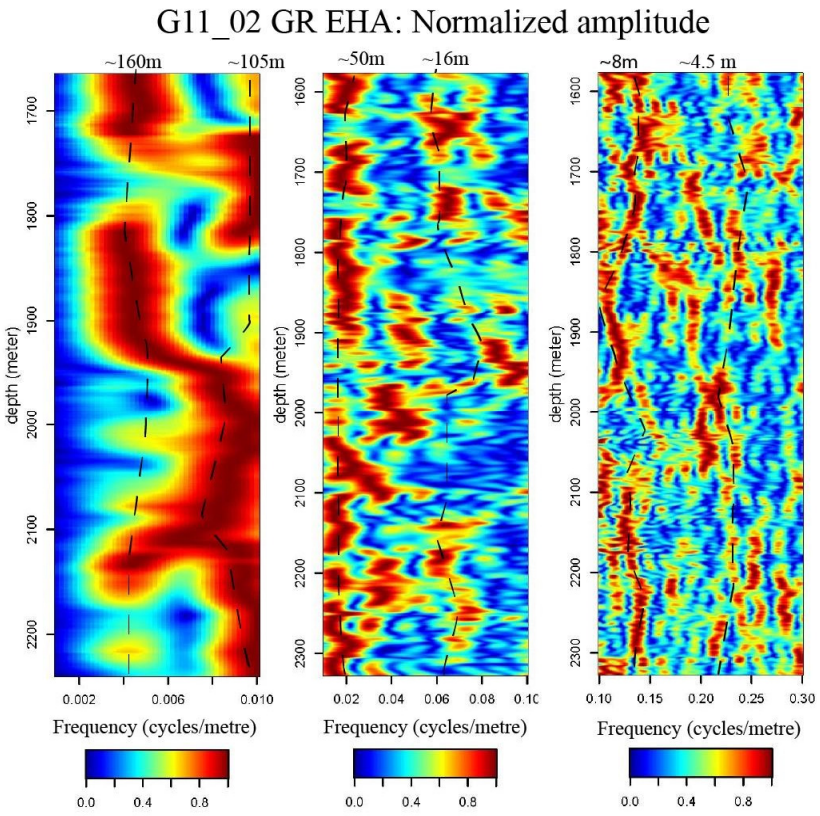

Figure 87. Spectra of GR record of well G11-02.

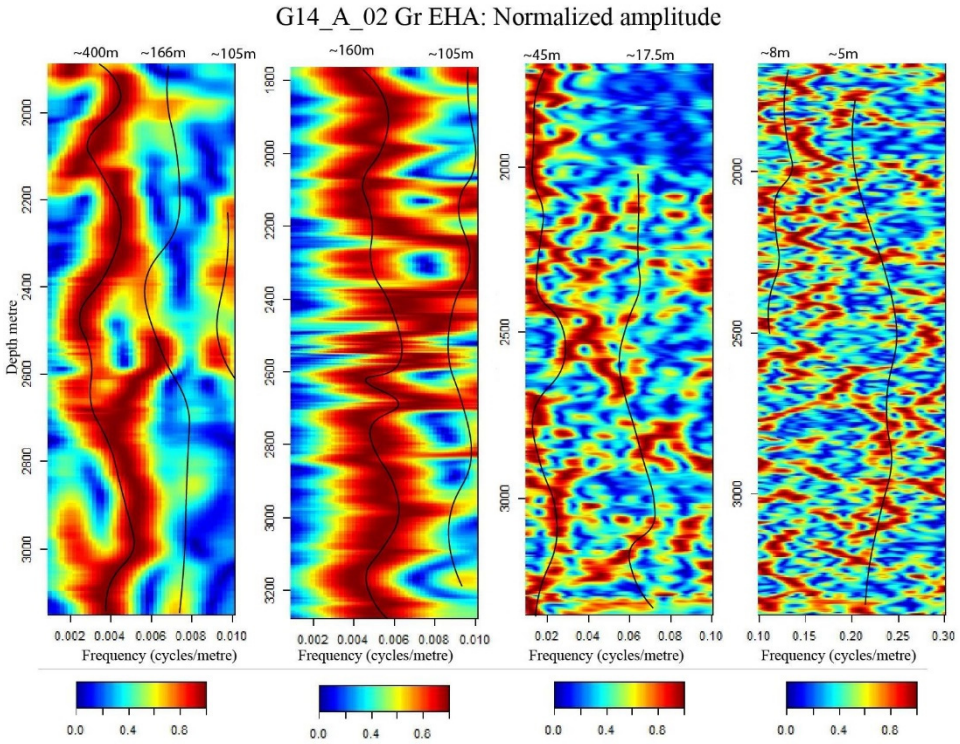

Figure 88. Spectra of GR record of well G14-A-02 Gr. The left spectrum has the same frequency range as the one to the right of it but the sliding window on the left one is 500 while one on the right is 500m.

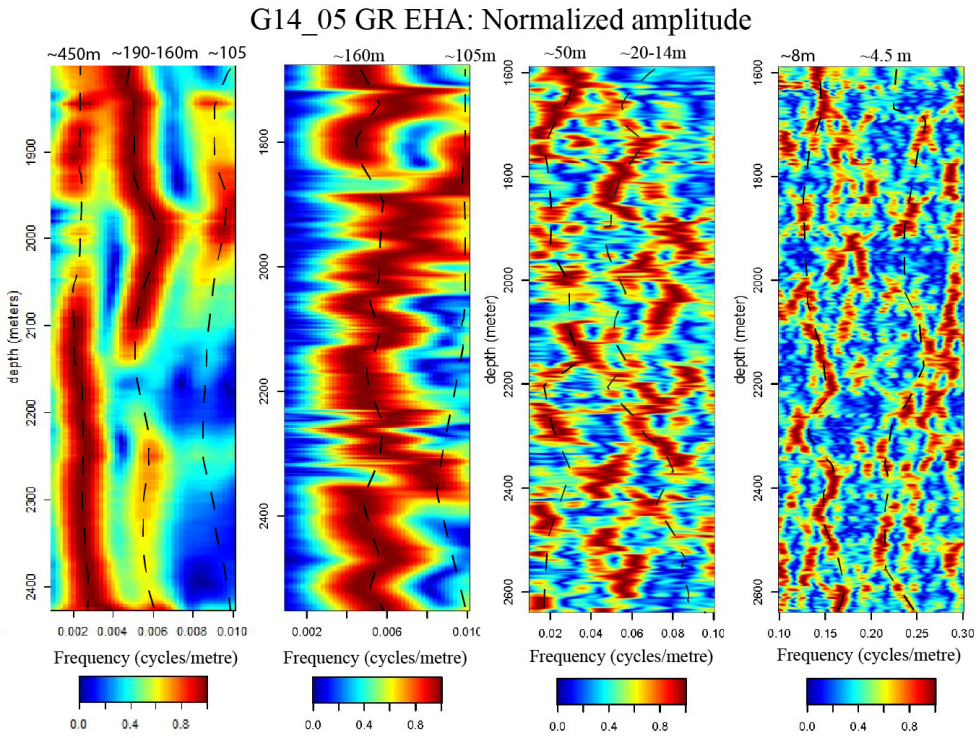

Figure 89. Spectra of GR record of well G14-05. The left spectrum has the same frequency range as the one to the right of it but the sliding window on the left one is 500 while one on the right is

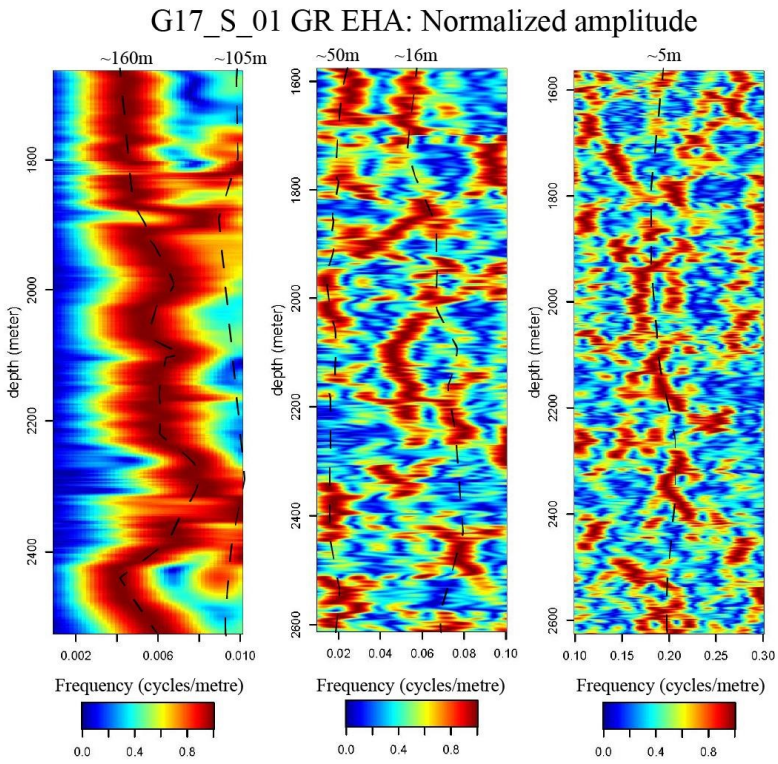

Figure 90. Spectra of GR record of well G17-S-01.

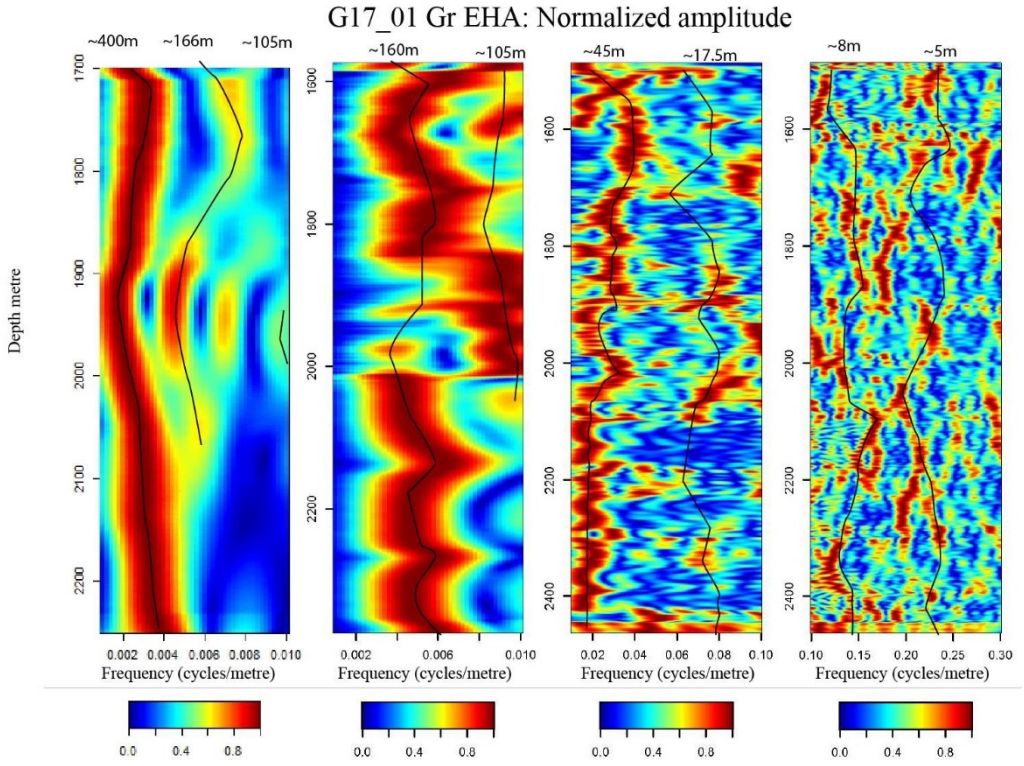

Figure 91. Spectra of GR record of well G17-01. The left spectrum has the same frequency range as the one to the right of it but the sliding window on the left one is 500 while one on the right is

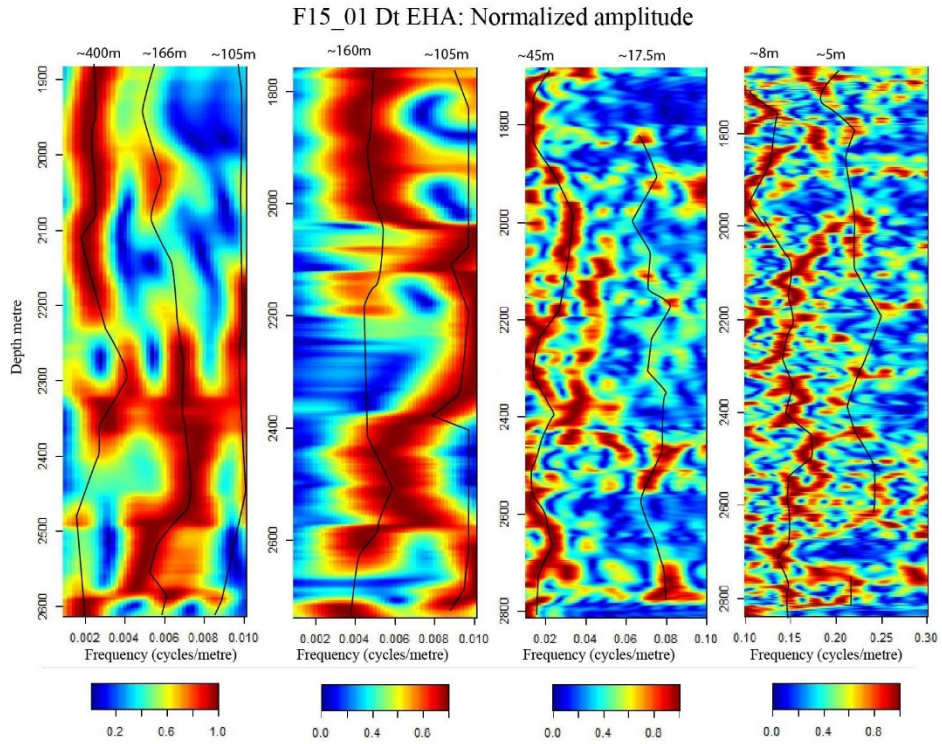

Figure 92. Spectra of DT record of well F15-01. The left spectrum has the same frequency range as the one to the right of it but the sliding window on the left one is 500 while one on the right is

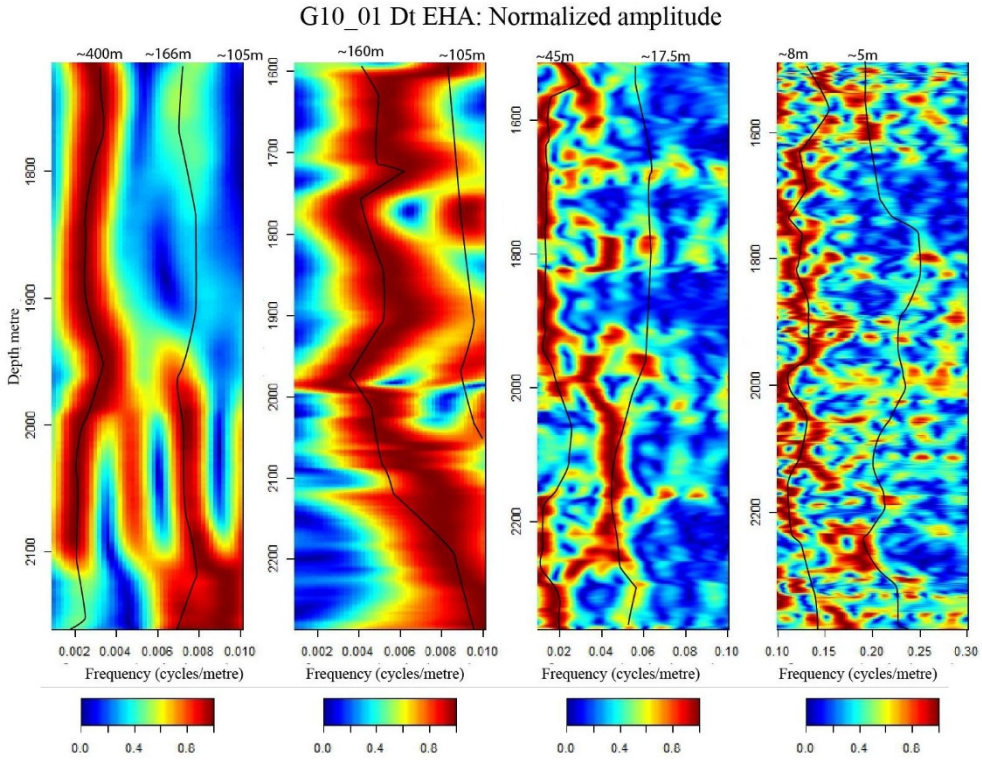

Figure 93. Spectra of DT record of well G10-01. The left spectrum has the same frequency range as the one to the right of it but the sliding window on the left one is 500 while one on the right is 500m.

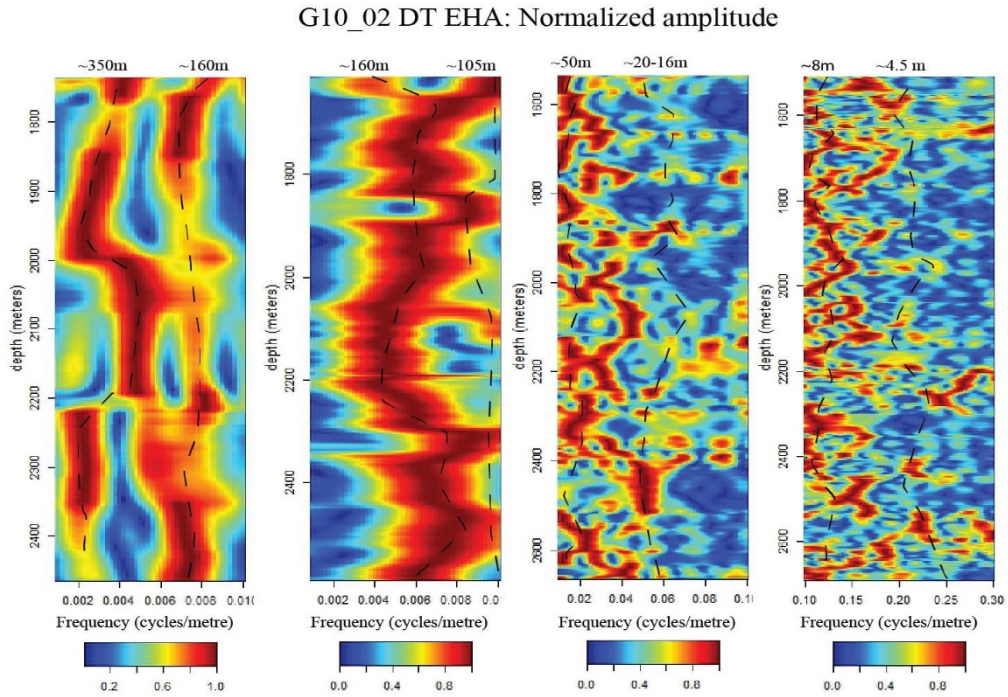

Figure 94. Spectra of DT record of well G10-02. The left spectrum has the same frequency range as the one to the right of it but the sliding window on the left one is 500 while one on the right is 500m.

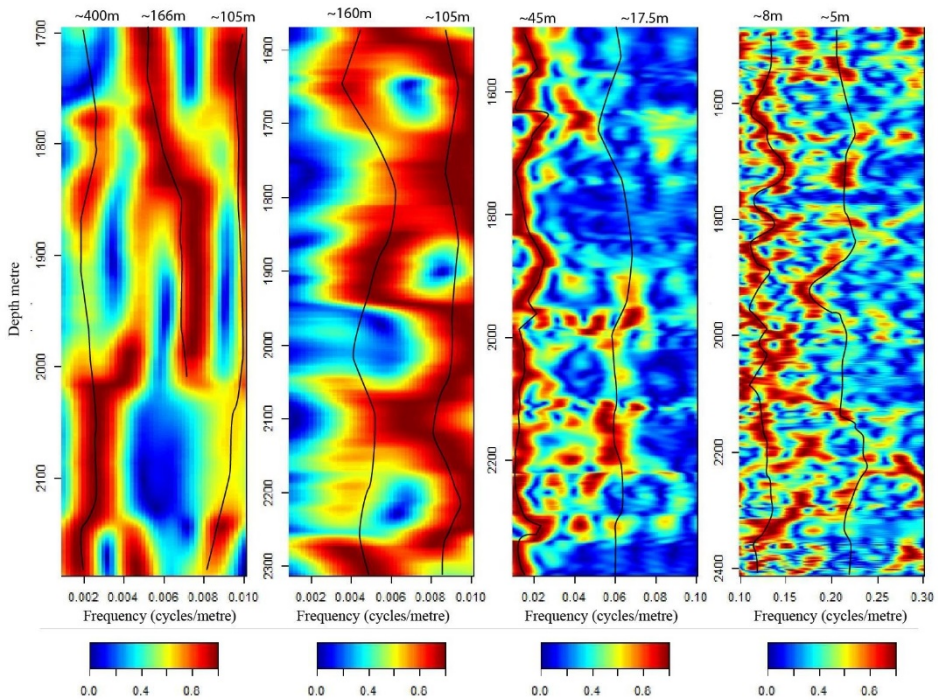

Figure 95. Spectra of DT record of well G11-02. The left spectrum has the same frequency range as the one to the right of it but the sliding window on the left one is 500 while one on the right is 500m.

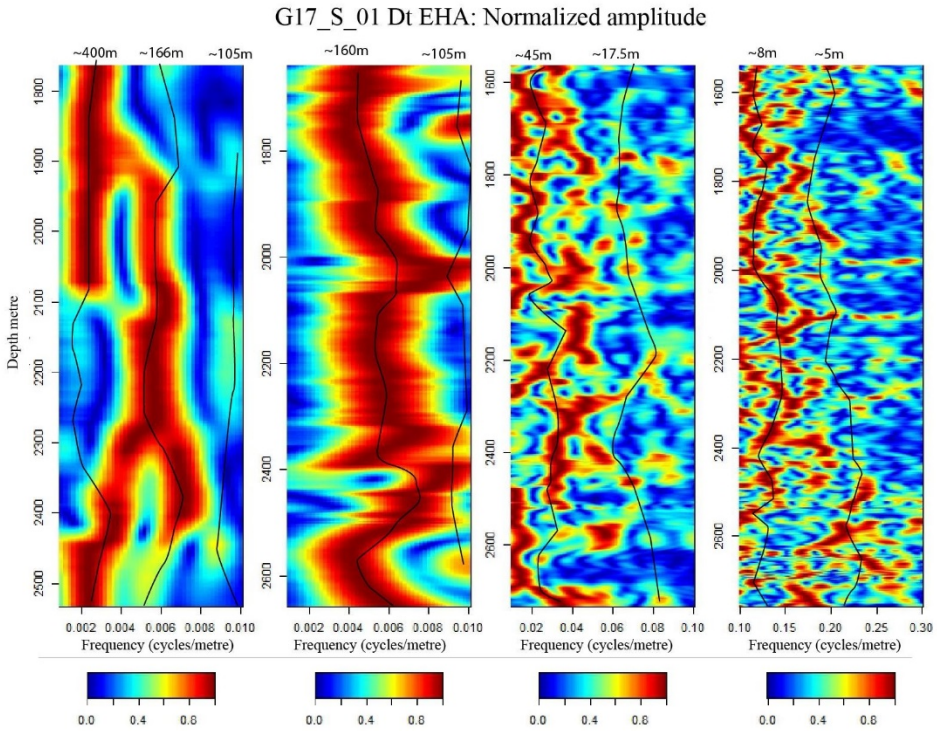

Figure 96. Spectra of DT record of well G17-S-01. The left spectrum has the same frequency range as the one to the right of it but the sliding window on the left one is 500 while one on the right is

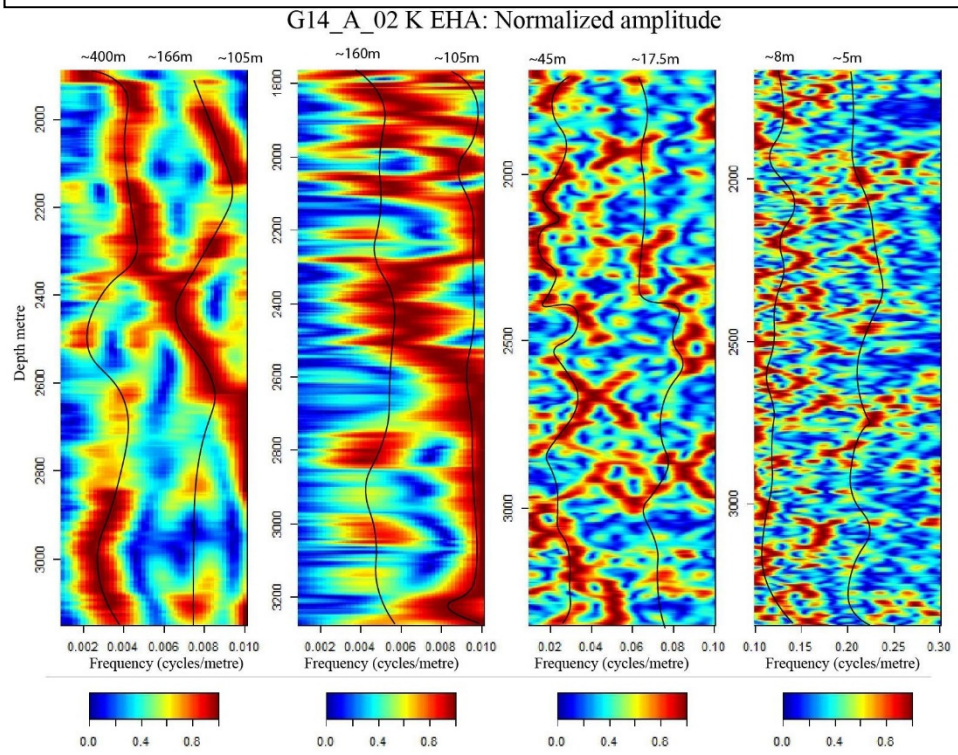

Figure 97. Spectra of K record of well G14-A-02. The left spectrum has the same frequency range as the one to the right of it but the sliding window on the left one is 500 while one on the right is 500m.

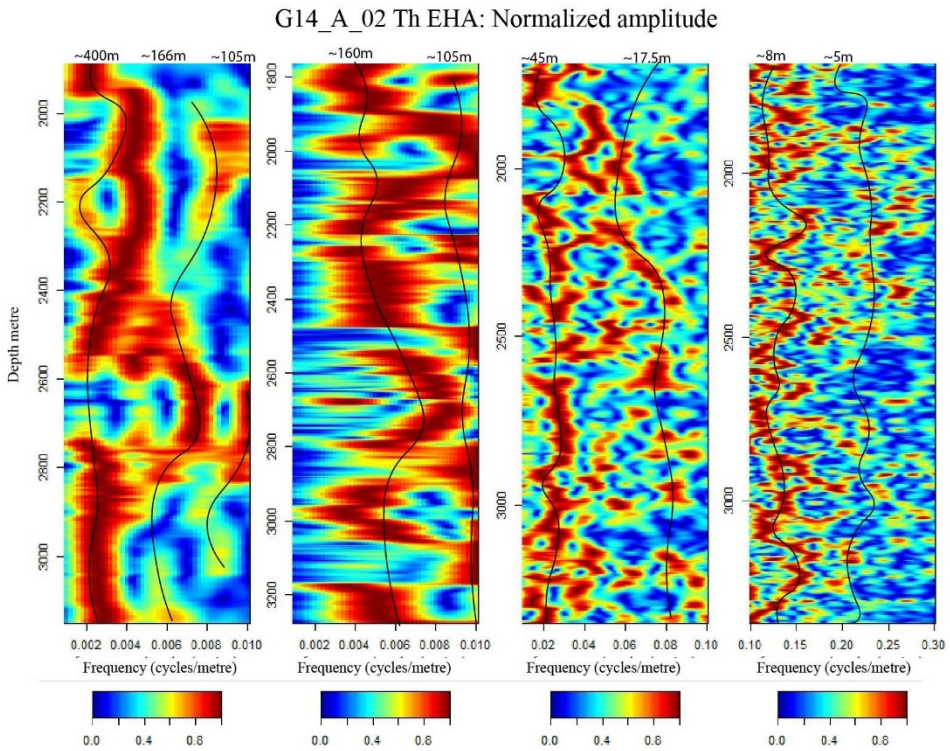

Figure 98. Spectra of Th record of well G14-A-02. The left spectrum has the same frequency range as the one to the right of it but the sliding window on the left one is 500 while one on the right is 500m.

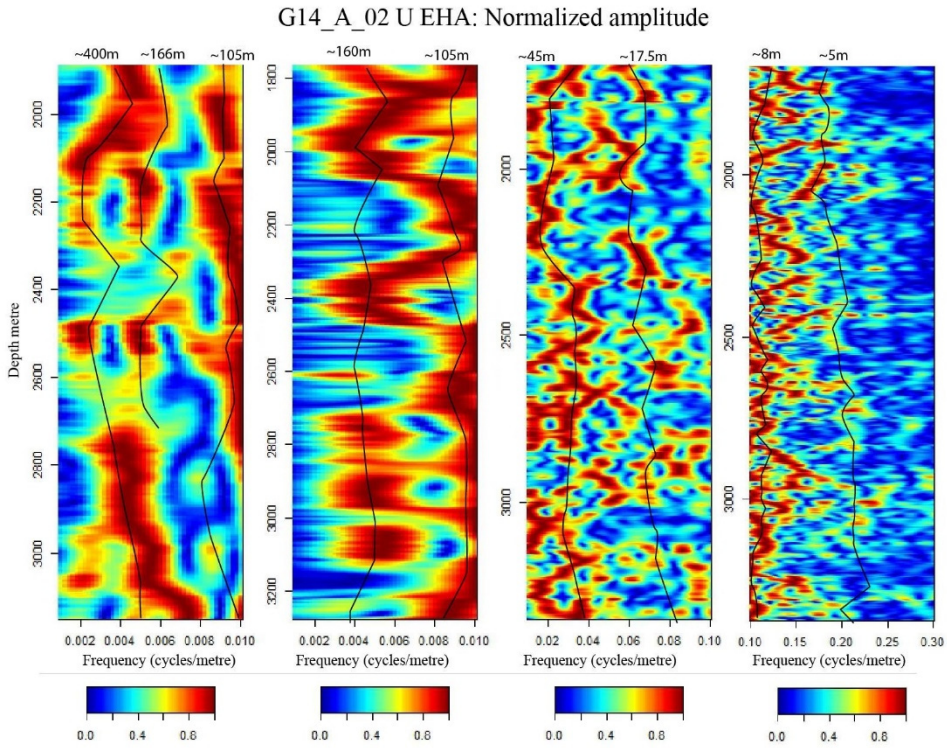

Figure 99. Spectra of U record of well G14-A-02. The left spectrum has the same frequency range as the one to the right of it but the sliding window on the left one is 500 while one on the right is 500m.

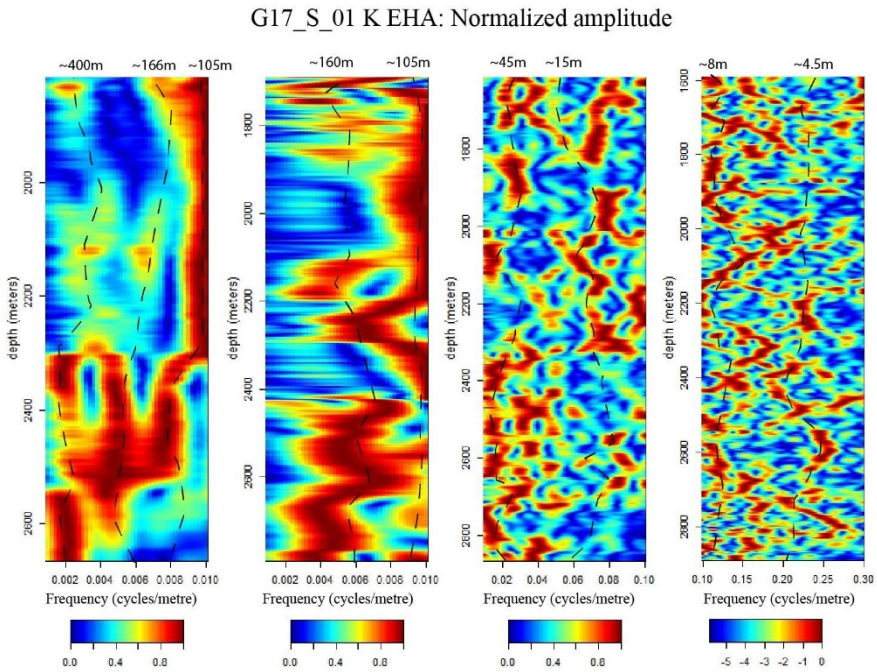

Figure 100. Spectra of K record of well G17-S-01. The left spectrum has the same frequency range as the one to the right of it but the sliding window on the left one is 500 while one on the right is 500m.

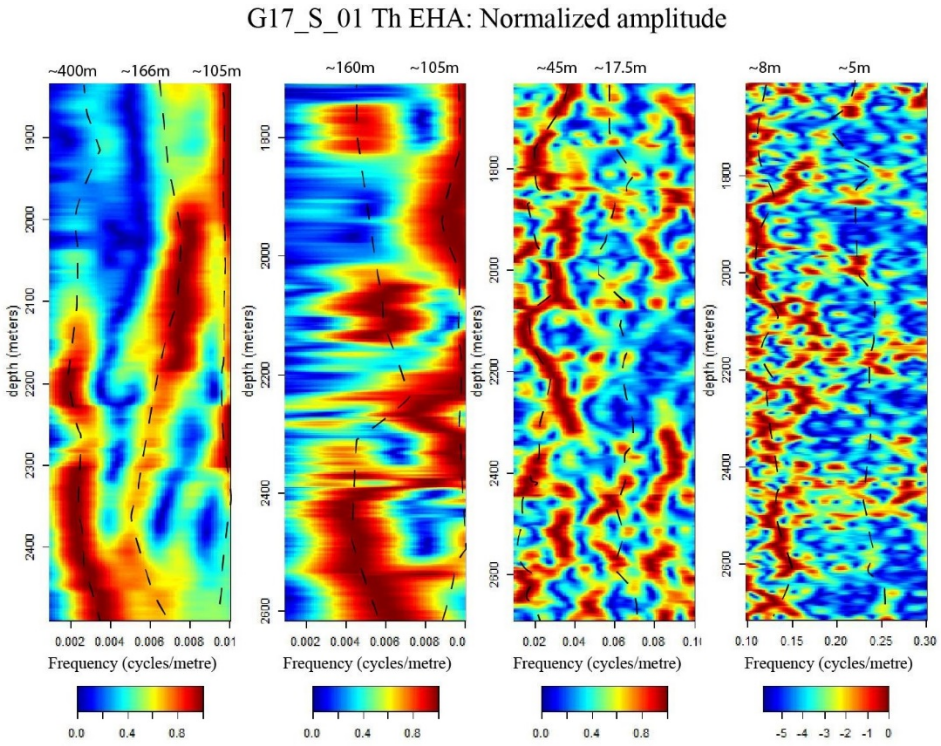

Figure 101. Spectra of Th record of well G17-S-01. The left spectrum has the same frequency range as the one to the right of it but the sliding window on the left one is 500 while one on the right is 500m.

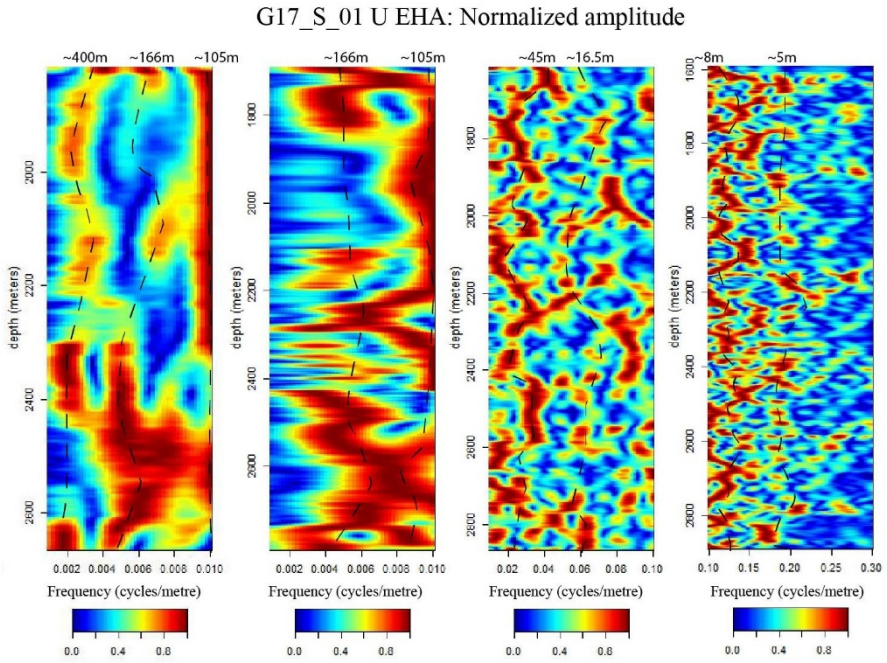

Figure 102. Spectra of U record of well G17-S-01. The left spectrum has the same frequency range as the one to the right of it but the sliding window on the left one is 500 while one on the right is 500m.

10.9 eASM Figures

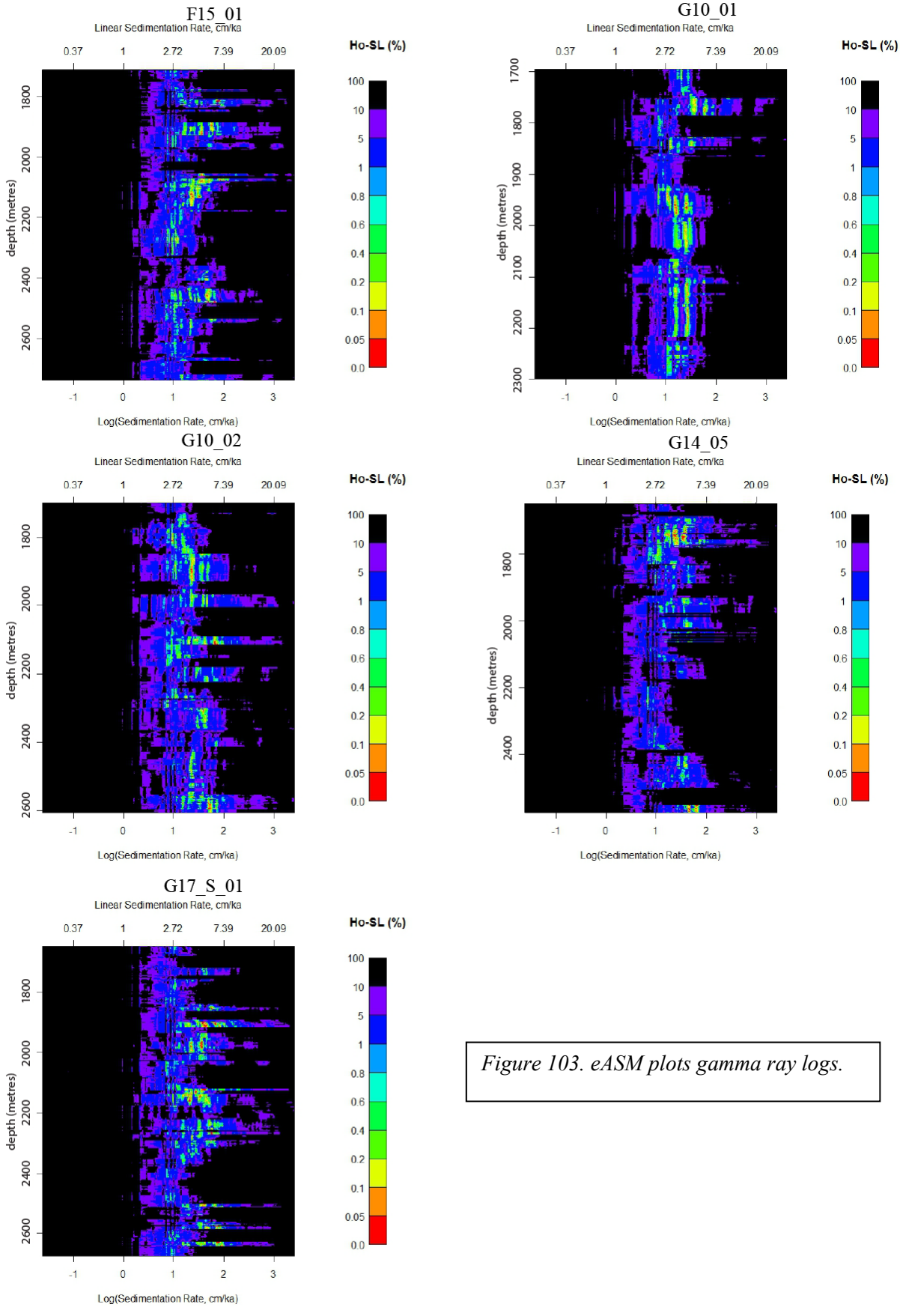

Figure 103. eASM plots gamma ray logs.

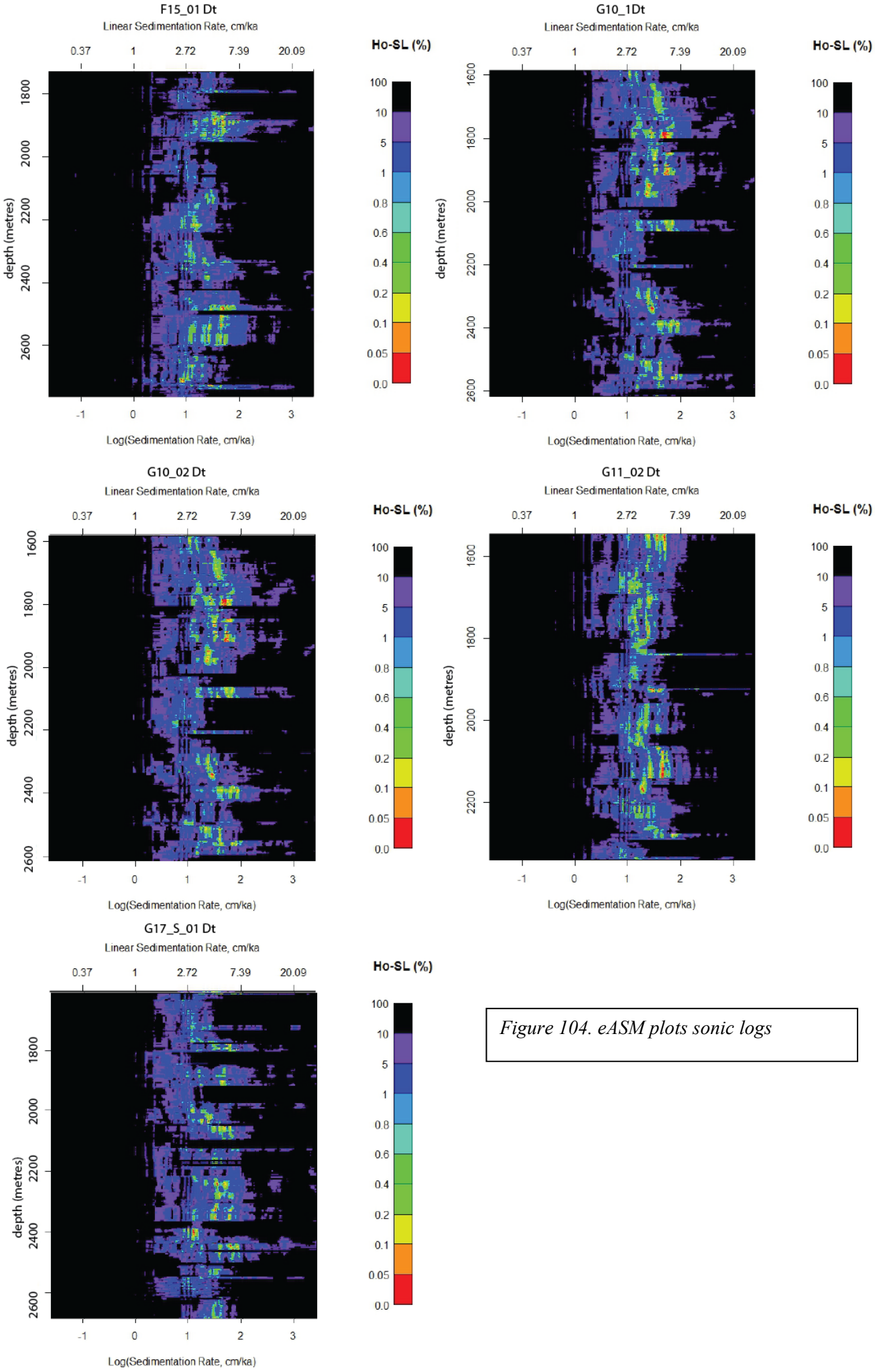

Figure 104. eASM plots sonic logs

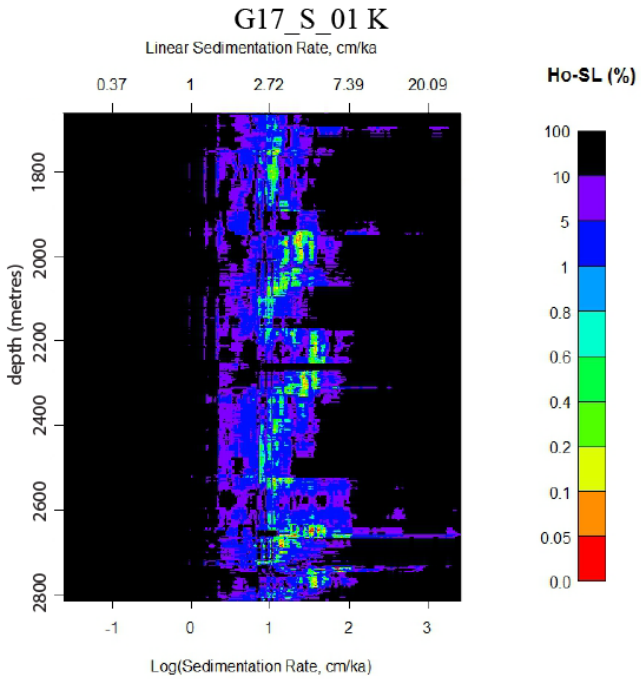

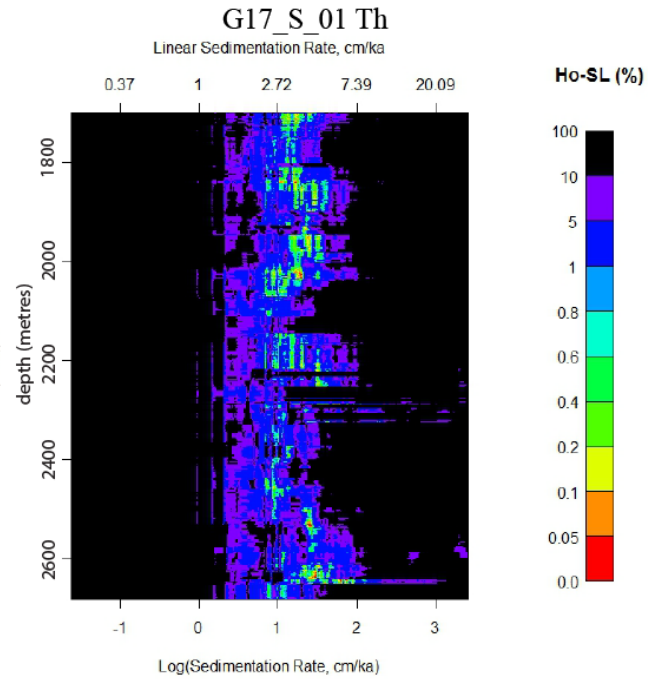

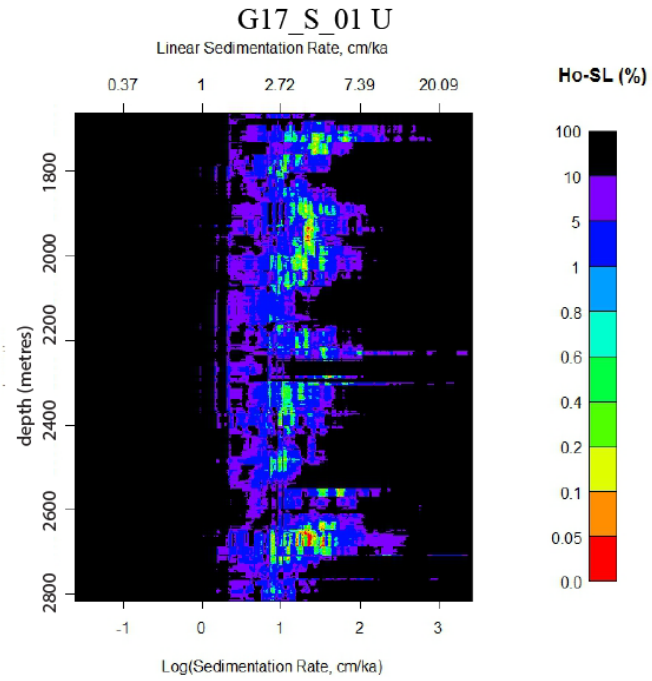

Figure 105. eASM plots G17-S-01-K, Th and U

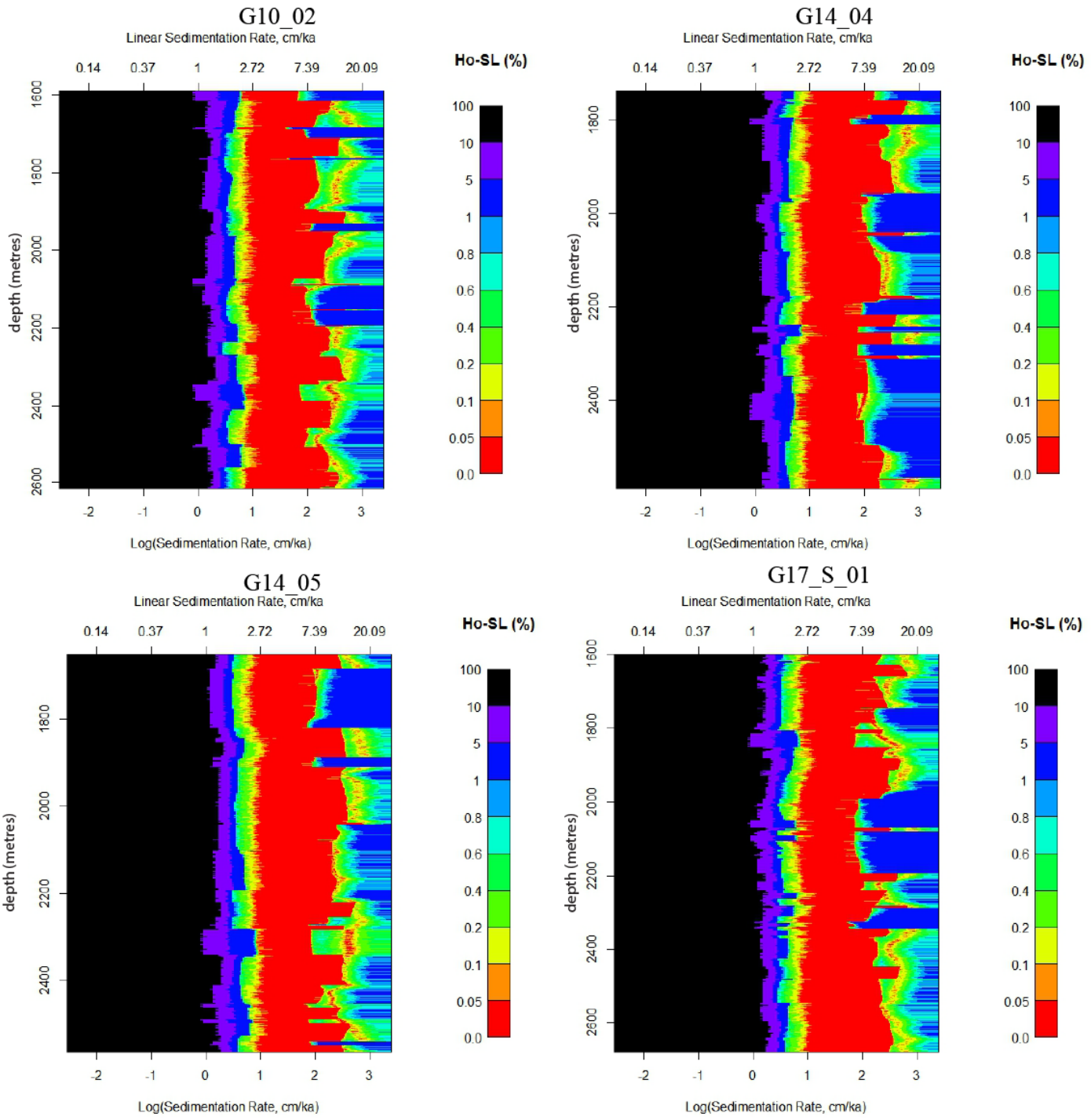

Figure 106. eASM plots seismic trace data

10.10 Seismic data filtering

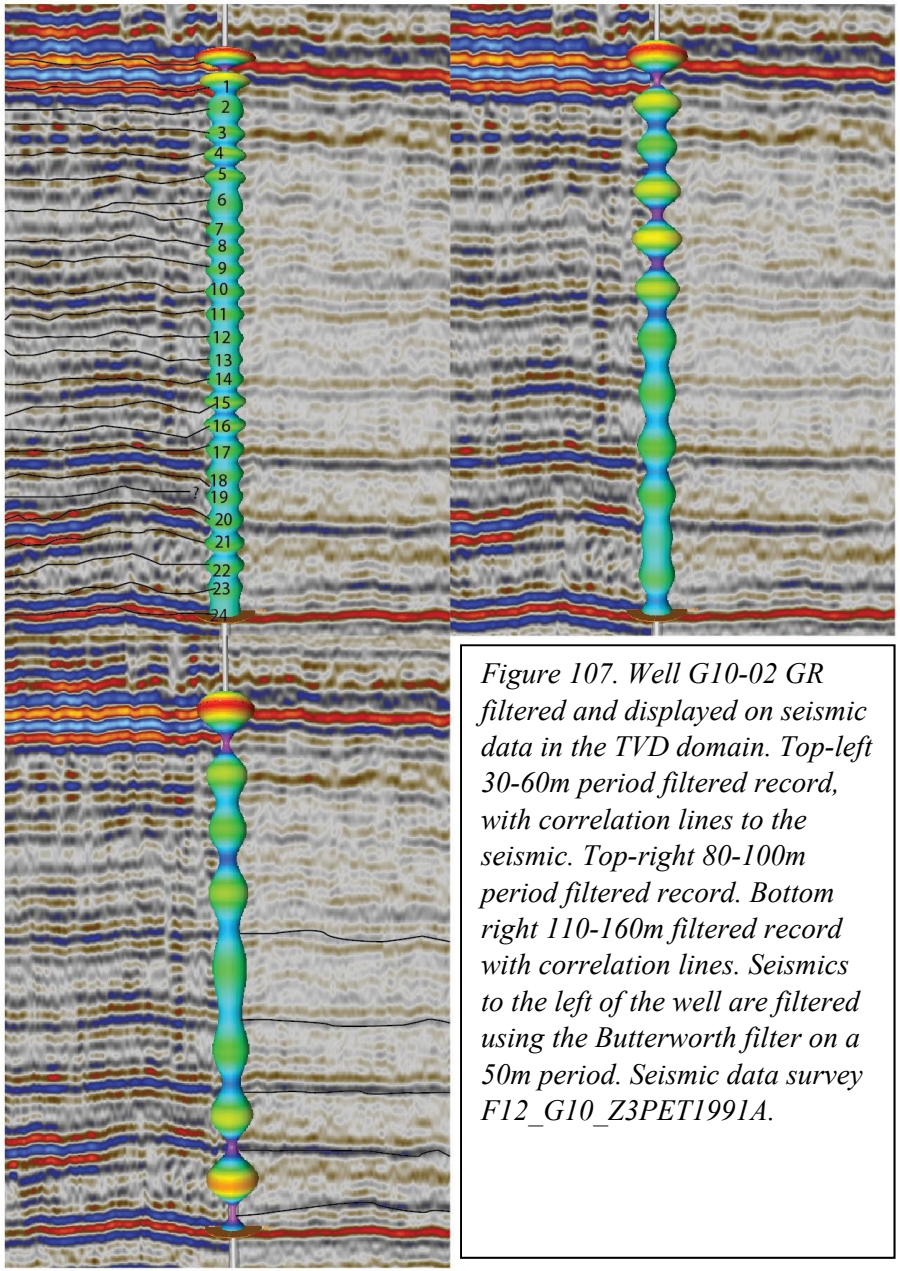

Figure 107. Well G10-02 GR filtered and displayed on seismic data in the TVD domain. Top-left 30-60m period filtered record, with correlation lines to the seismic. Top-right 80-100m period filtered record. Bottom right 110-160m filtered record with correlation lines. Seismics to the left of the well are filtered using the Butterworth filter on a 50m period. Seismic data survey F12_G10_Z3PET1991A.

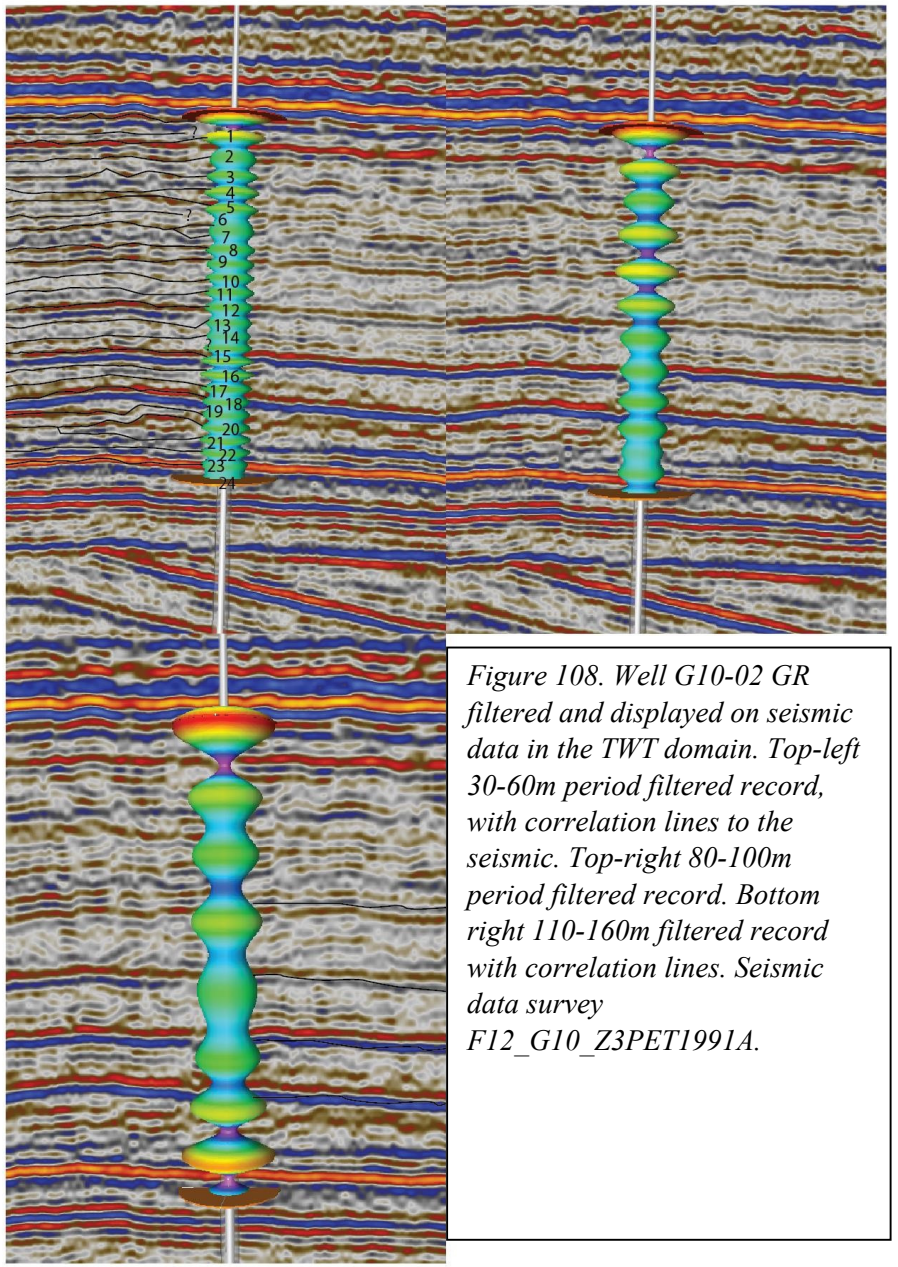

Figure 108. Well G10-02 GR filtered and displayed on seismic data in the TWT domain. Top-left 30-60m period filtered record, with correlation lines to the seismic. Top-right 80-100m period filtered record. Bottom right 110-160m filtered record with correlation lines. Seismic data survey F12_G10_Z3PET1991A.

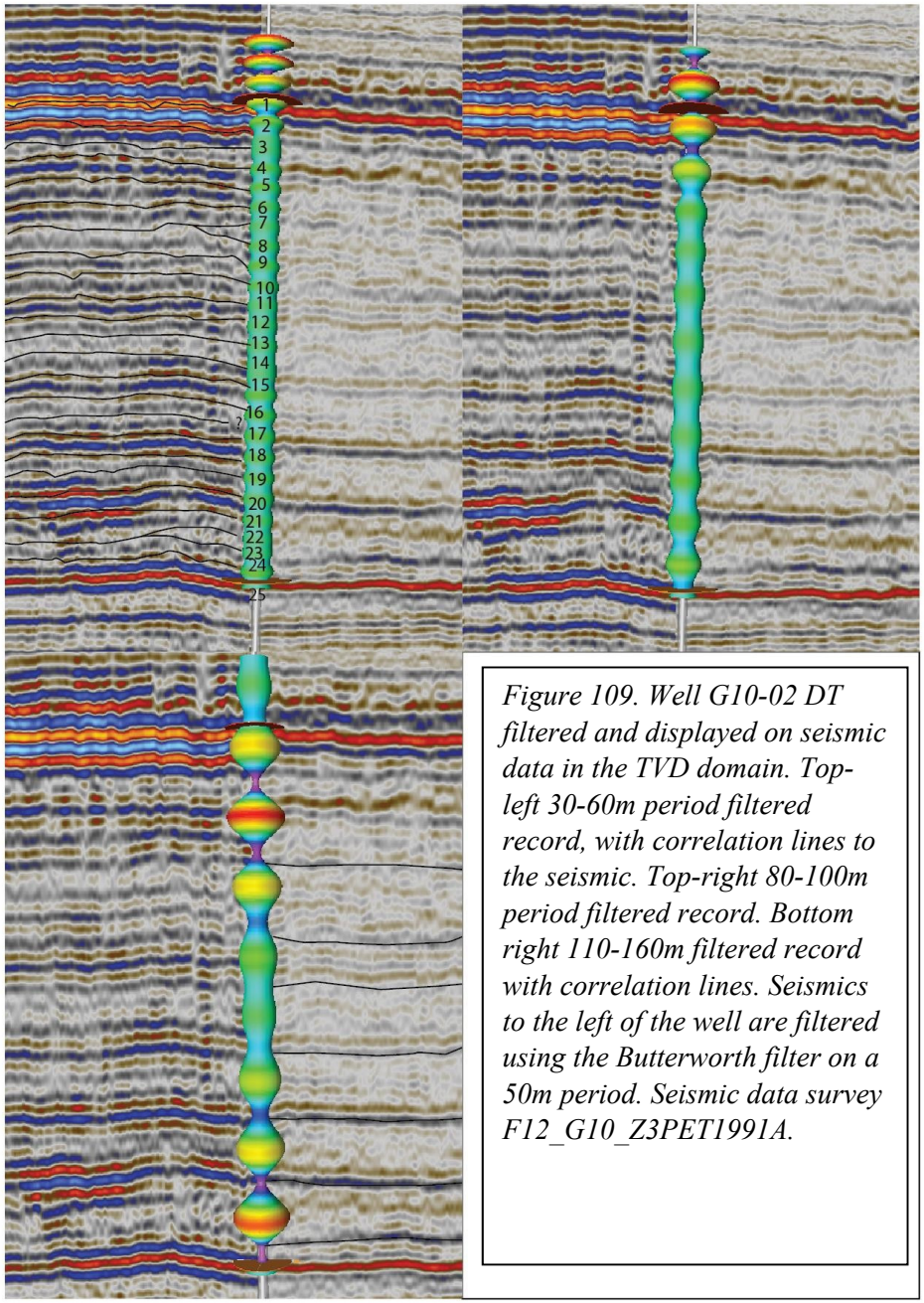

Figure 109. Well G10-02 DT filtered and displayed on seismic data in the TVD domain. Top-left 30-60m period filtered record, with correlation lines to the seismic. Top-right 80-100m period filtered record. Bottom right 110-160m filtered record with correlation lines. Seismics to the left of the well are filtered using the Butterworth filter on a 50m period. Seismic data survey F12_G10_Z3PET1991A.

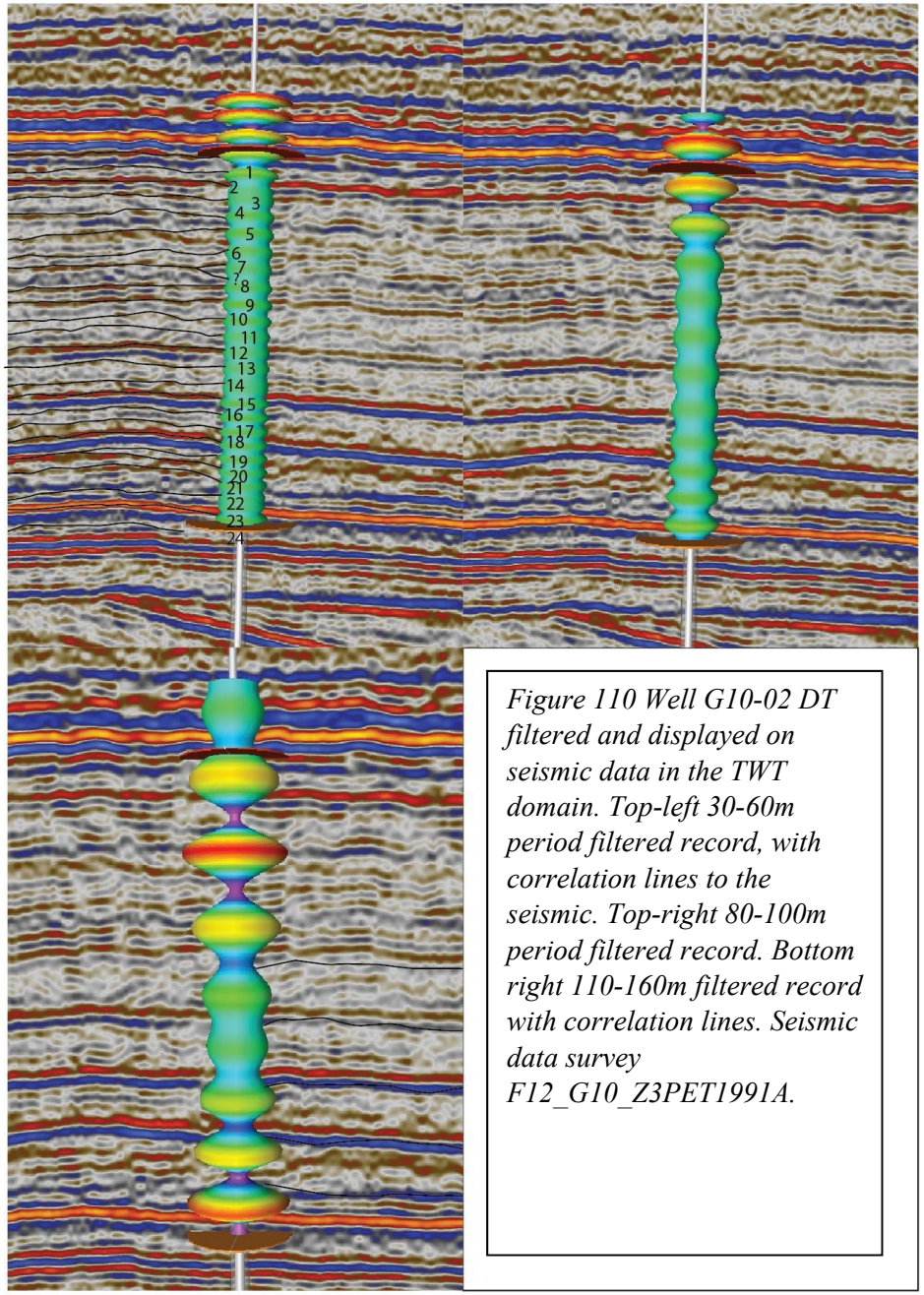

Figure 110 Well G10-02 DT filtered and displayed on seismic data in the TWT domain. Top-left 30-60m period filtered record, with correlation lines to the seismic. Top-right 80-100m period filtered record. Bottom right 110-160m filtered record with correlation lines. Seismic data survey F12_G10_Z3PET1991A.

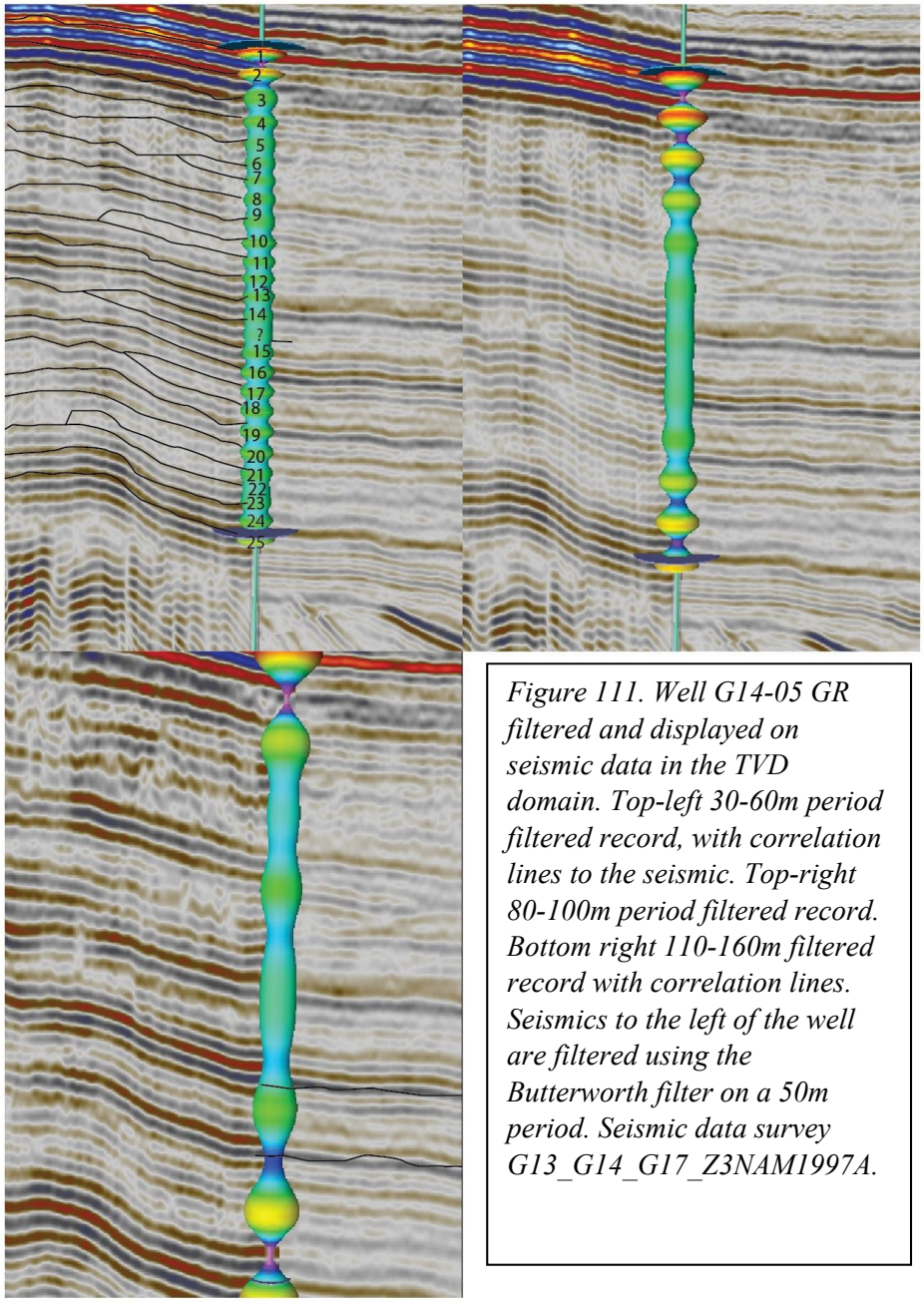

Figure 111. Well G14-05 GR filtered and displayed on seismic data in the TVD domain. Top-left 30-60m period filtered record, with correlation lines to the seismic. Top-right 80-100m period filtered record. Bottom right 110-160m filtered record with correlation lines. Seismics to the left of the well are filtered using the Butterworth filter on a 50m period. Seismic data survey G13_G14_G17_Z3NAM1997A.

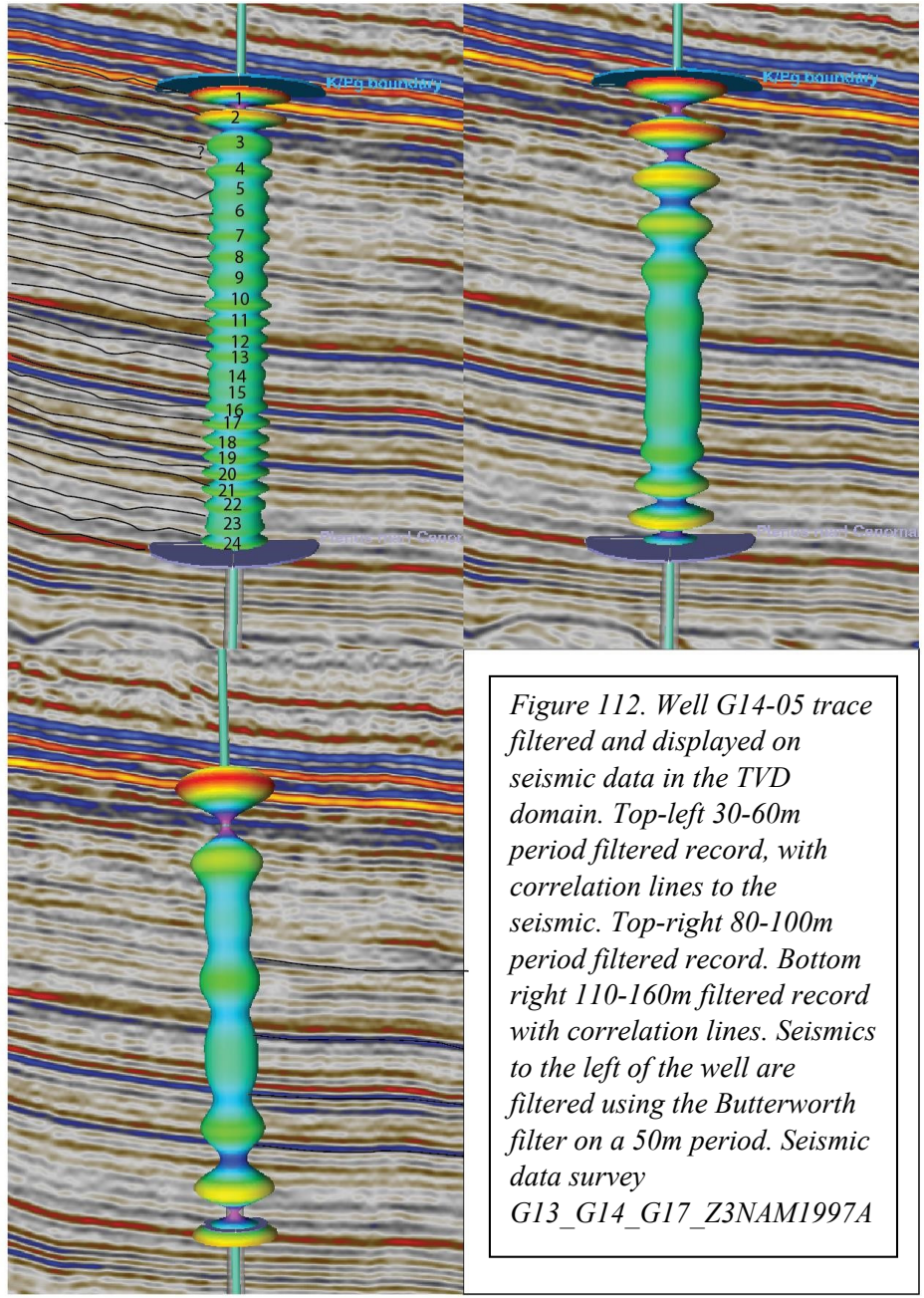

Figure 112. Well G14-05 trace filtered and displayed on seismic data in the TVD domain. Top-left 30-60m period filtered record, with correlation lines to the seismic. Top-right 80-100m period filtered record. Bottom right 110-160m filtered record with correlation lines. Seismics to the left of the well are filtered using the Butterworth filter on a 50m period. Seismic data survey G13_G14_G17_Z3NAM1997A

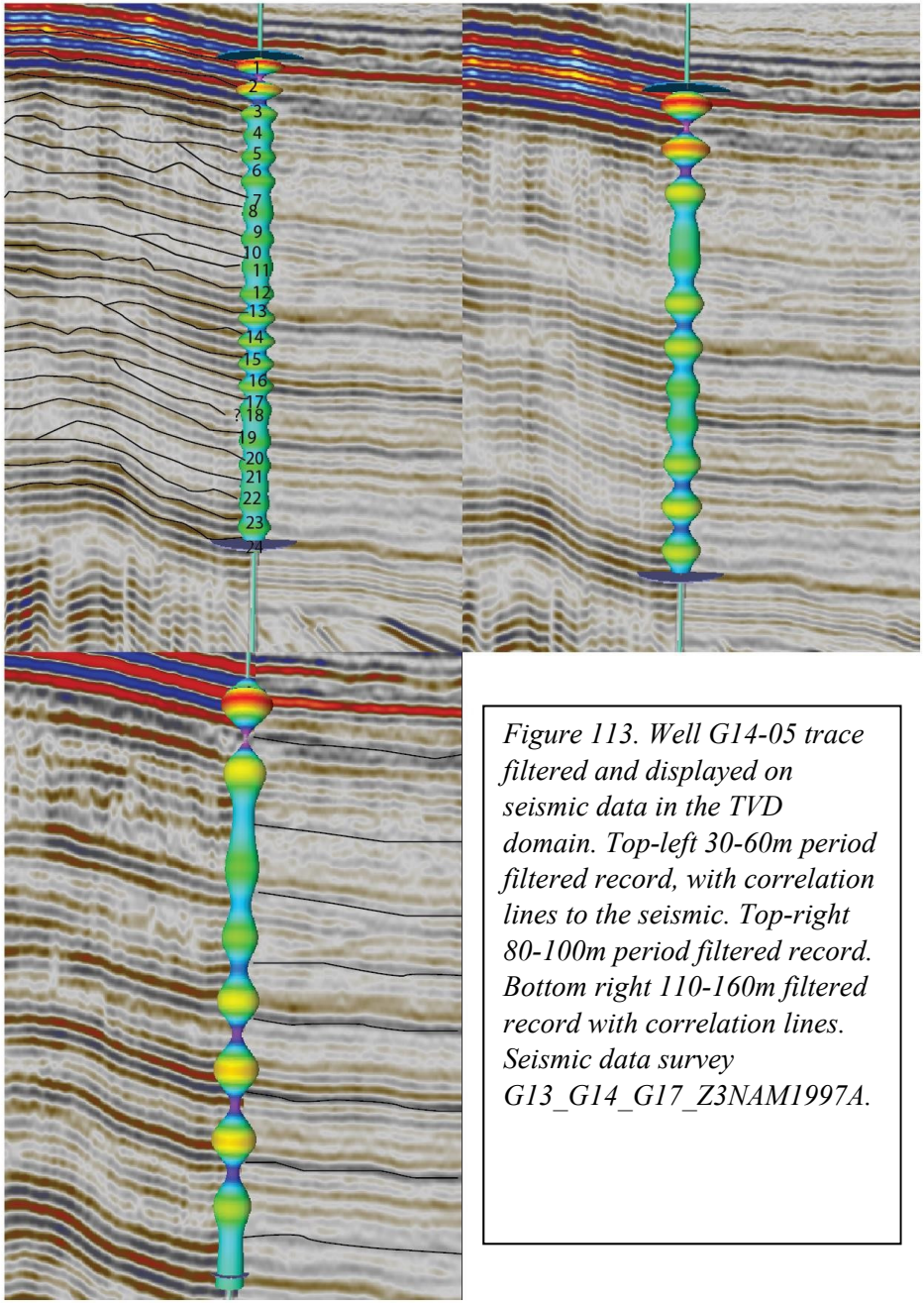

Figure 113. Well G14-05 trace filtered and displayed on seismic data in the TVD domain. Top-left 30-60m period filtered record, with correlation lines to the seismic. Top-right 80-100m period filtered record. Bottom right 110-160m filtered record with correlation lines. Seismic data survey G13_G14_G17_Z3NAM1997A.

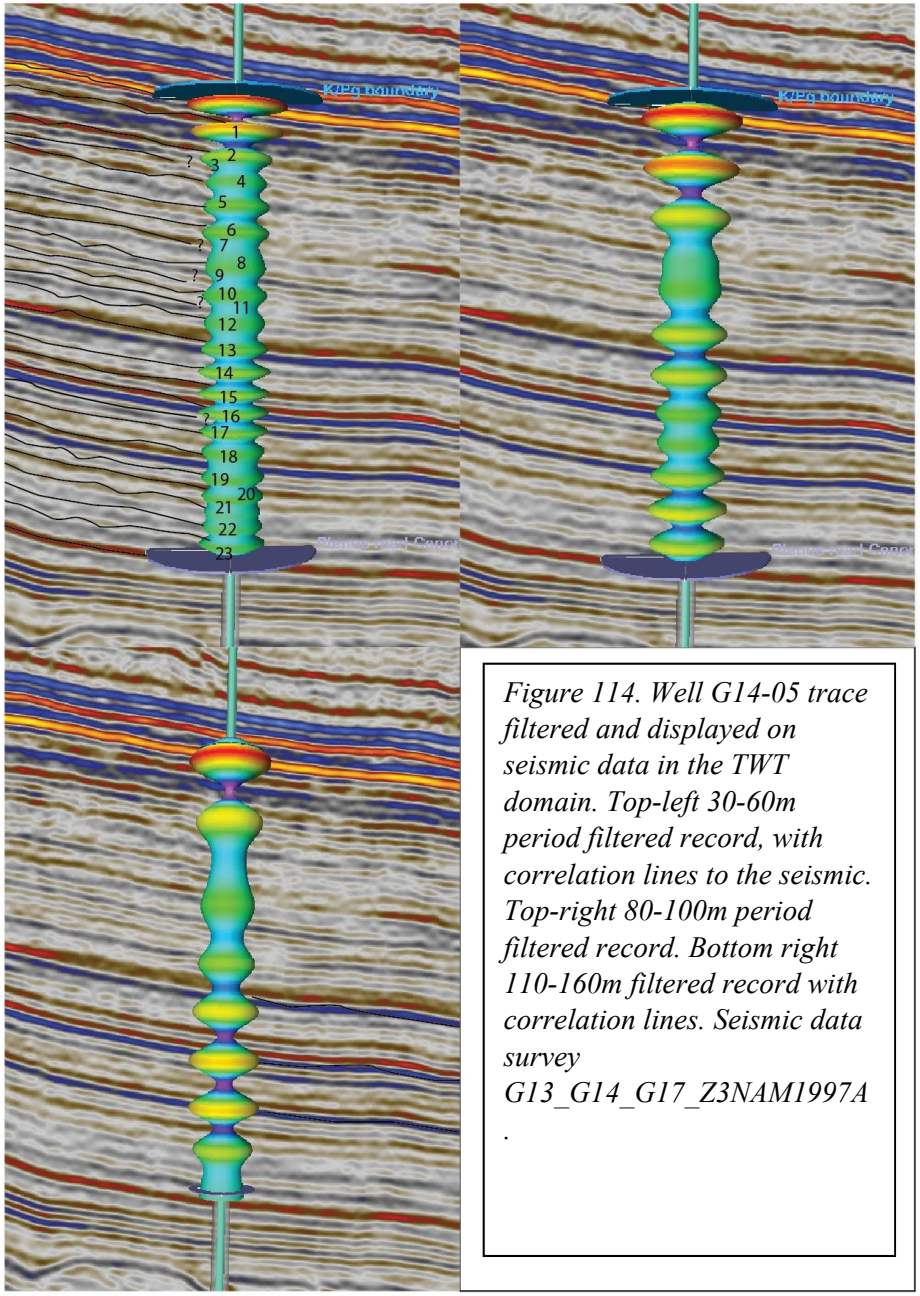

Figure 114. Well G14-05 trace filtered and displayed on seismic data in the TWT domain. Top-left 30-60m period filtered record, with correlation lines to the seismic. Top-right 80-100m period filtered record. Bottom right 110-160m filtered record with correlation lines. Seismic data survey G13_G14_G17_Z3NAM1997A .

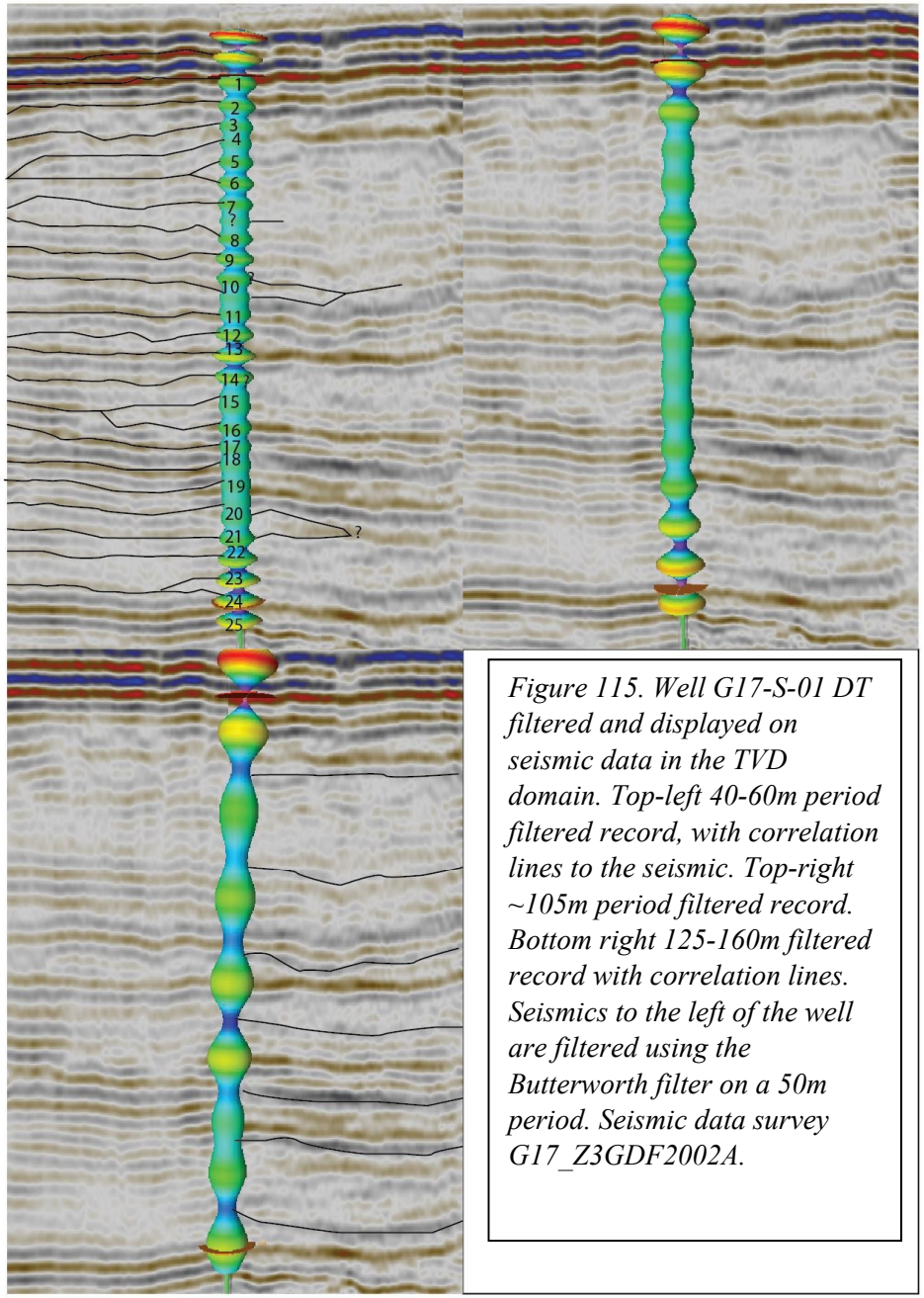

Figure 115. Well G17-S-01 DT filtered and displayed on seismic data in the TVD domain. Top-left 40-60m period filtered record, with correlation lines to the seismic. Top-right ~105m period filtered record. Bottom right 125-160m filtered record with correlation lines. Seismics to the left of the well are filtered using the Butterworth filter on a 50m period. Seismic data survey G17_Z3GDF2002A.

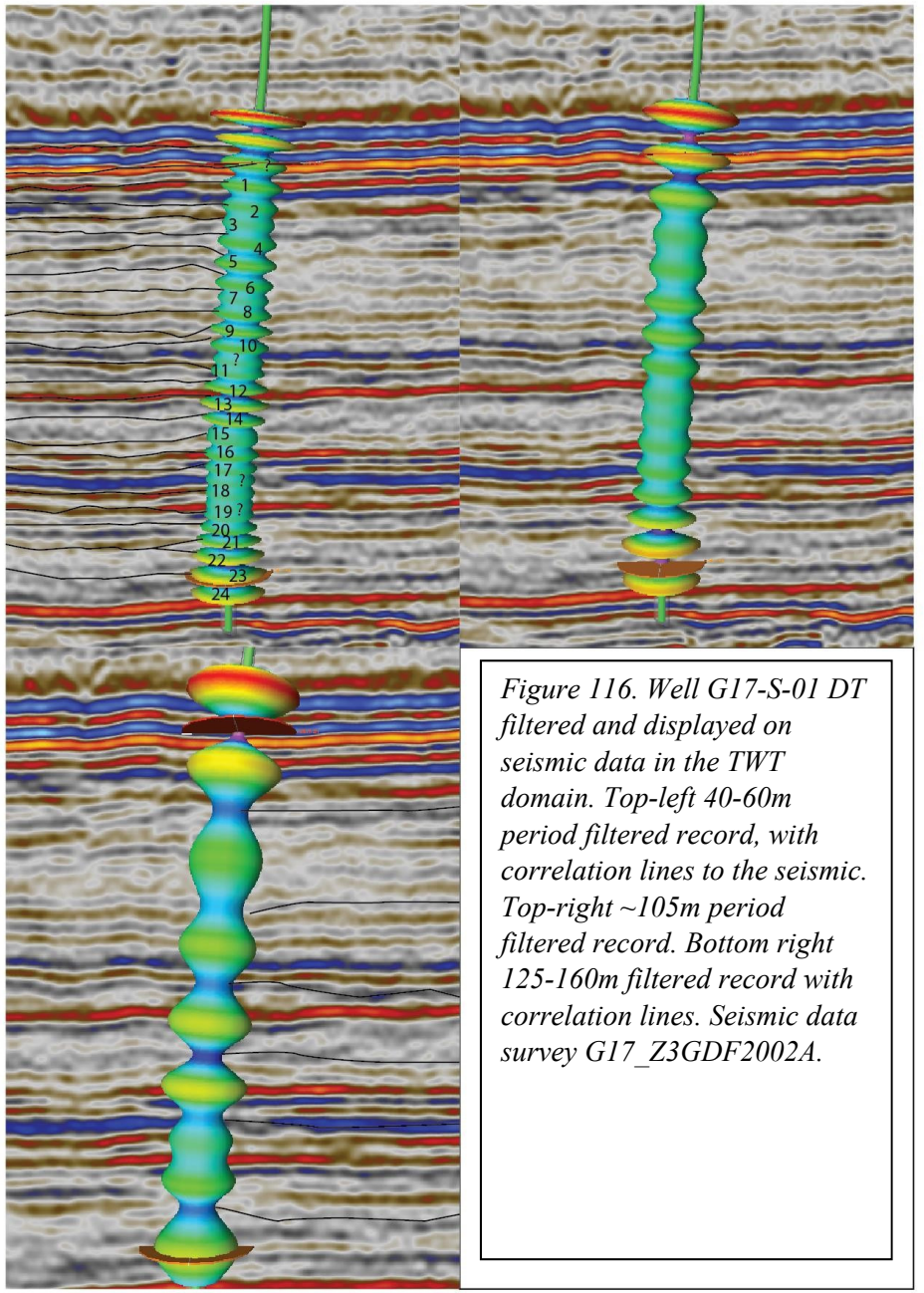

Figure 116. Well G17-S-01 DT filtered and displayed on seismic data in the TWT domain. Top-left 40-60m period filtered record, with correlation lines to the seismic. Top-right ~105m period filtered record. Bottom right 125-160m filtered record with correlation lines. Seismic data survey G17_Z3GDF2002A.

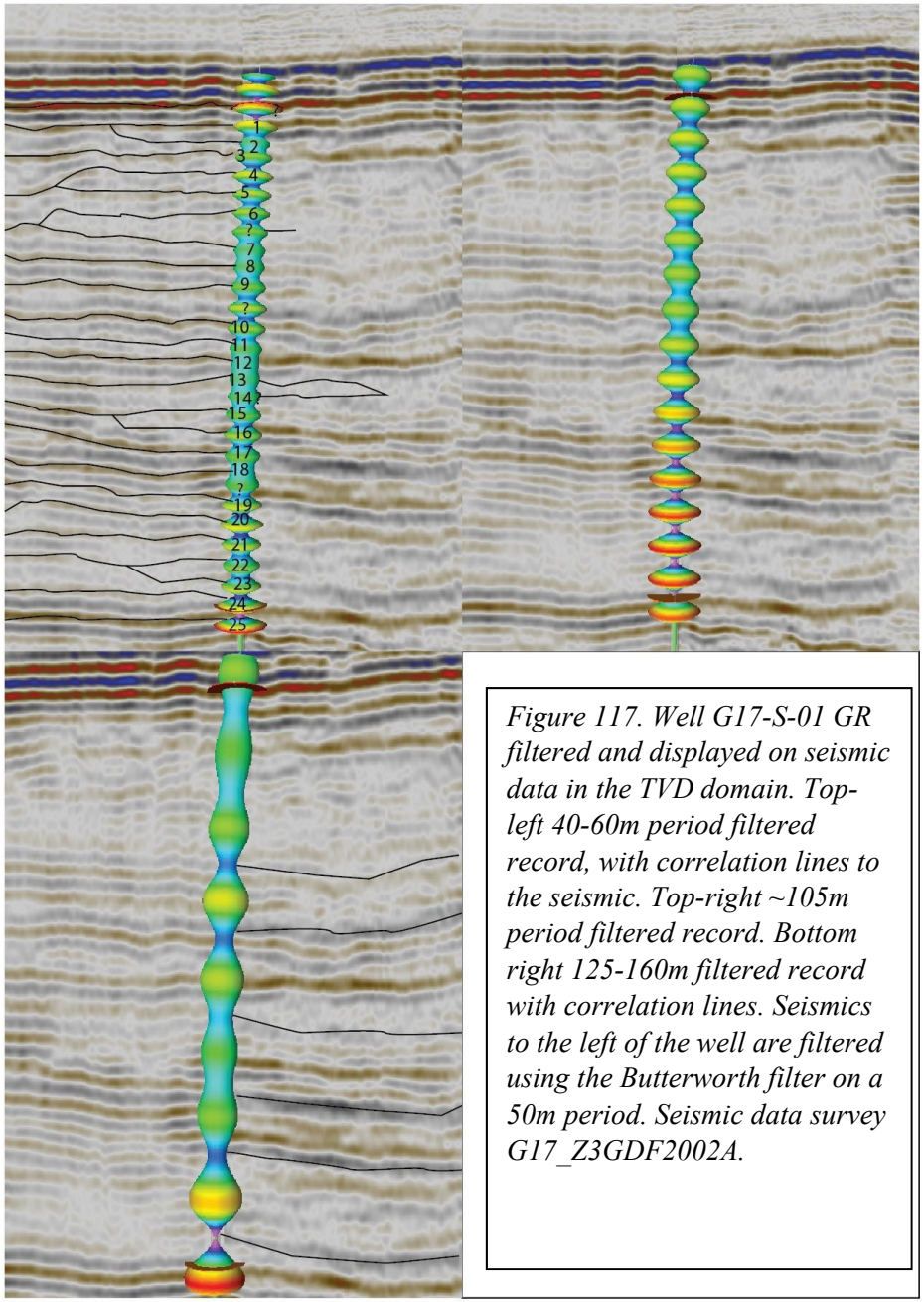

Figure 117. Well G17-S-01 GR filtered and displayed on seismic data in the TVD domain. Top-left 40-60m period filtered record, with correlation lines to the seismic. Top-right ~105m period filtered record. Bottom right 125-160m filtered record with correlation lines. Seismics to the left of the well are filtered using the Butterworth filter on a 50m period. Seismic data survey G17_Z3GDF2002A.

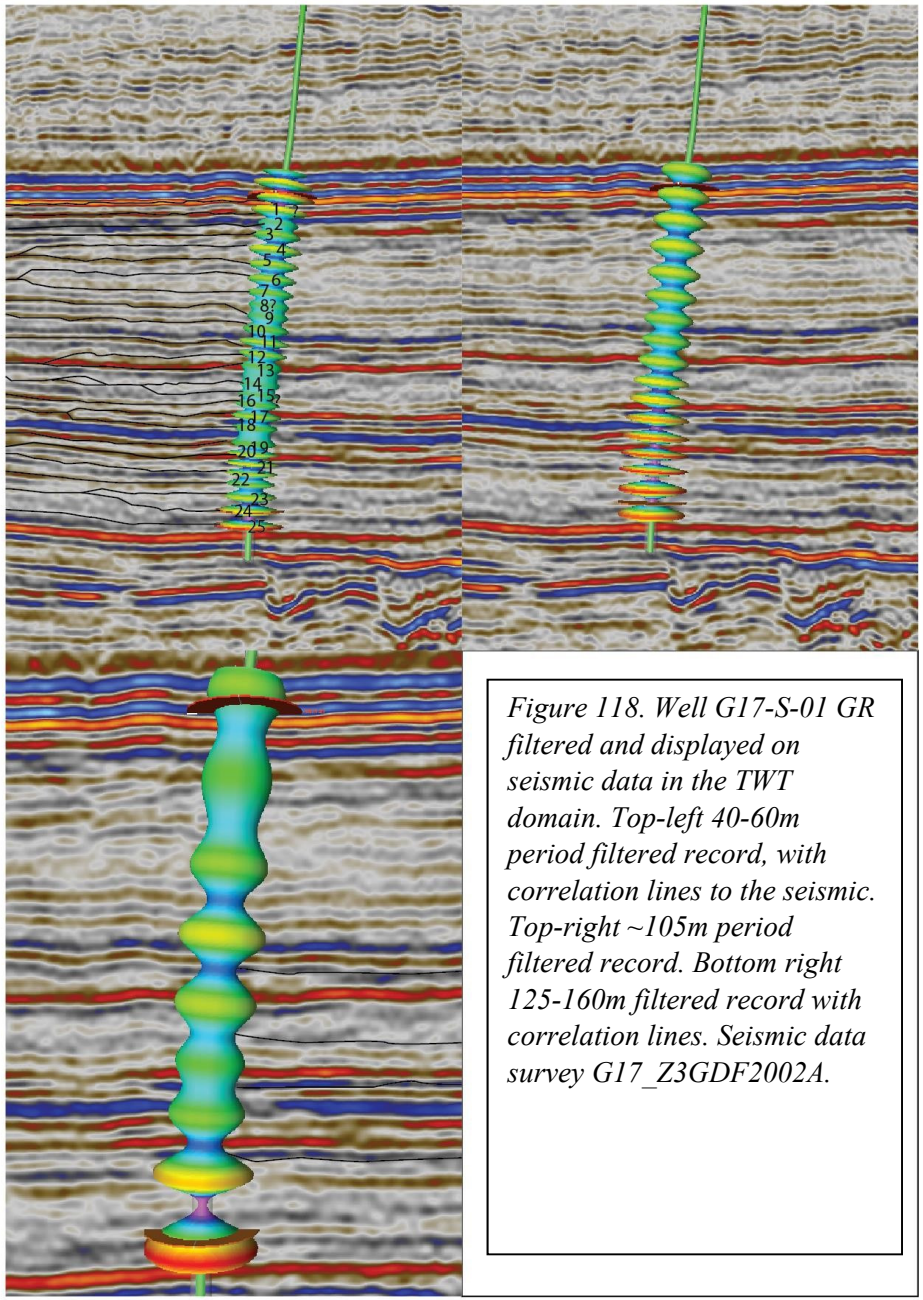

Figure 118. Well G17-S-01 GR filtered and displayed on seismic data in the TWT domain. Top-left 40-60m period filtered record, with correlation lines to the seismic. Top-right ~105m period filtered record. Bottom right 125-160m filtered record with correlation lines. Seismic data survey G17_Z3GDF2002A.

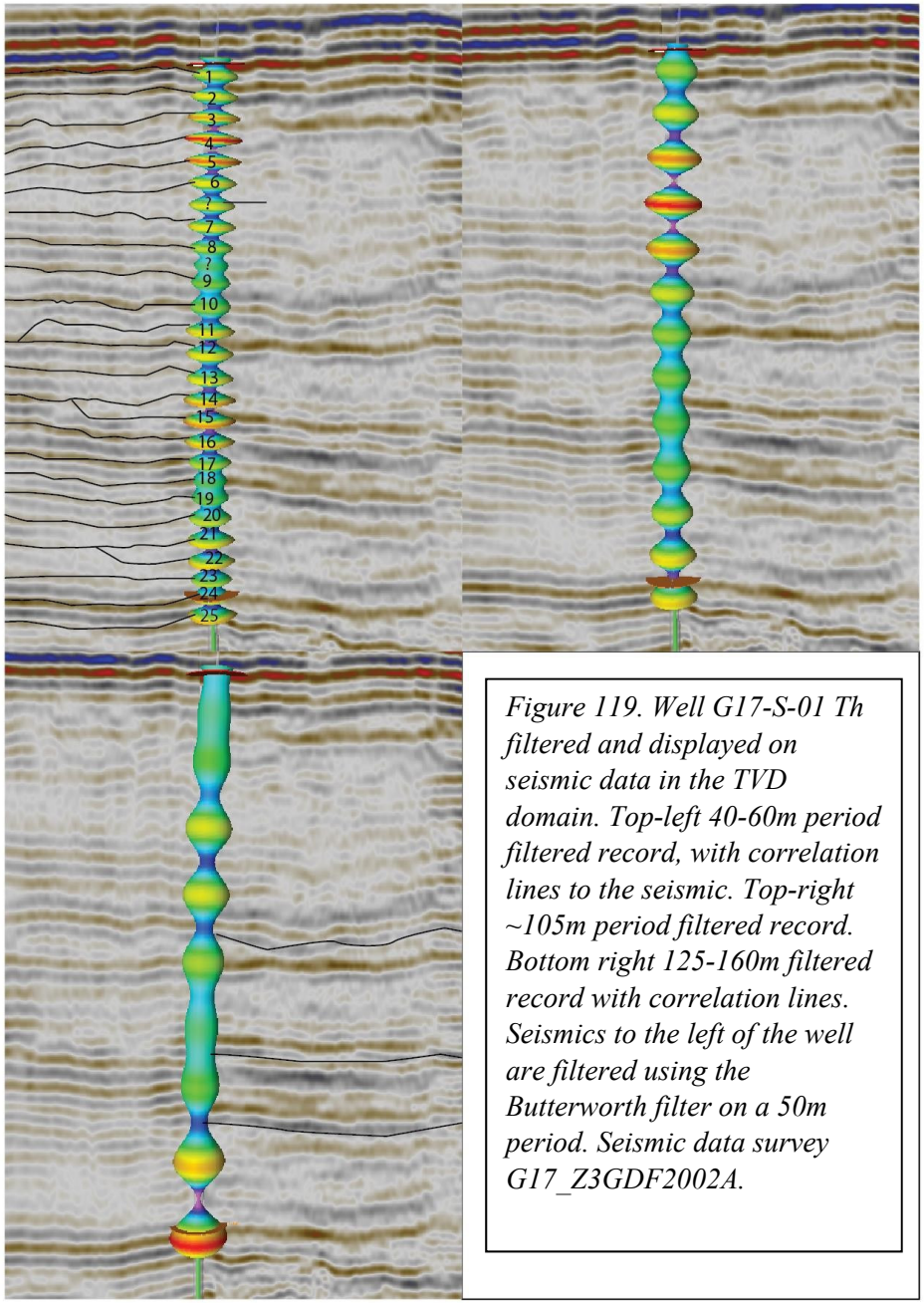

Figure 119. Well G17-S-01 Th filtered and displayed on seismic data in the TVD domain. Top-left 40-60m period filtered record, with correlation lines to the seismic. Top-right ~105m period filtered record. Bottom right 125-160m filtered record with correlation lines. Seismics to the left of the well are filtered using the Butterworth filter on a 50m period. Seismic data survey G17_Z3GDF2002A.

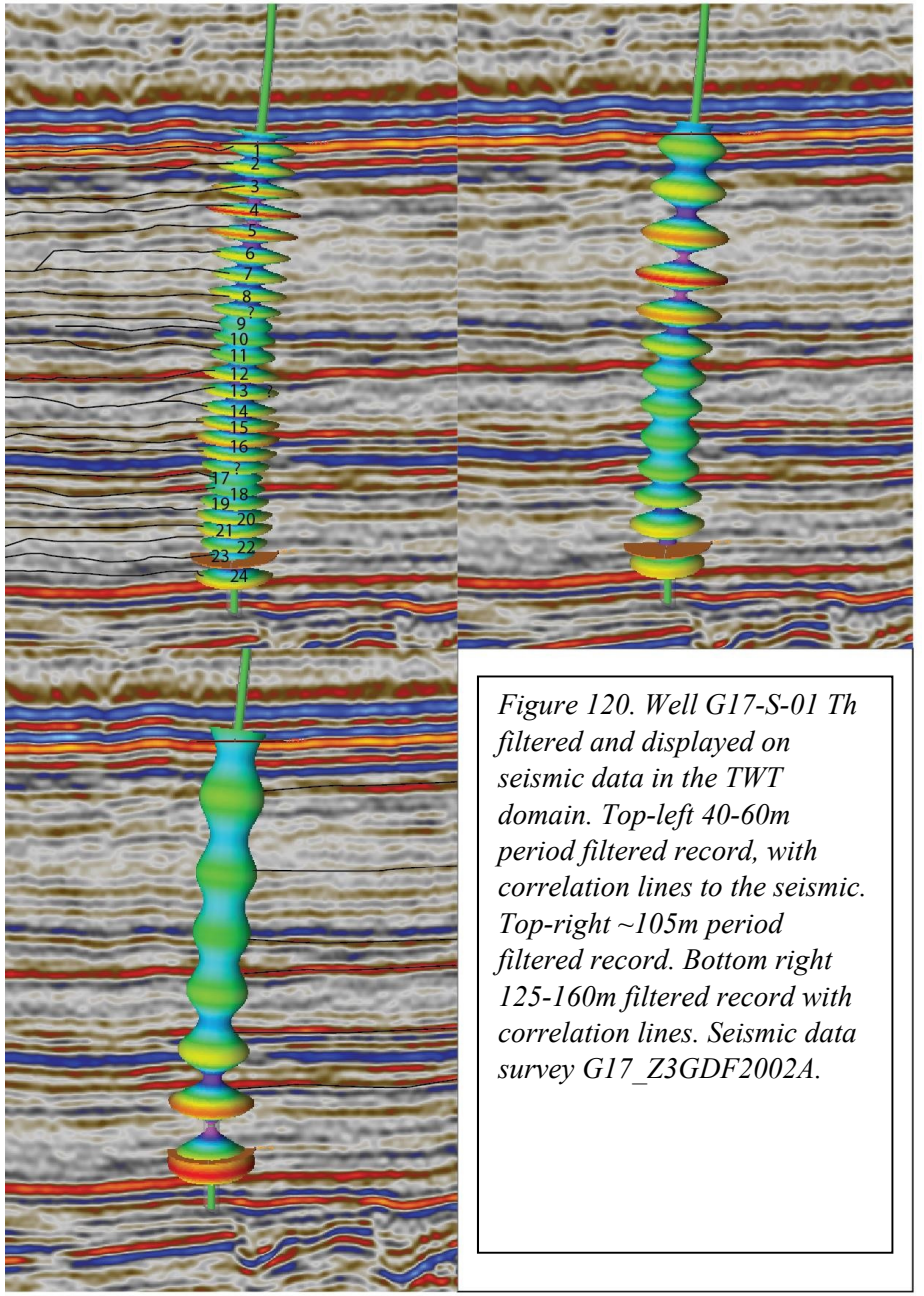

Figure 120. Well G17-S-01 Th filtered and displayed on seismic data in the TWT domain. Top-left 40-60m period filtered record, with correlation lines to the seismic. Top-right ~105m period filtered record. Bottom right 125-160m filtered record with correlation lines. Seismic data survey G17_Z3GDF2002A.

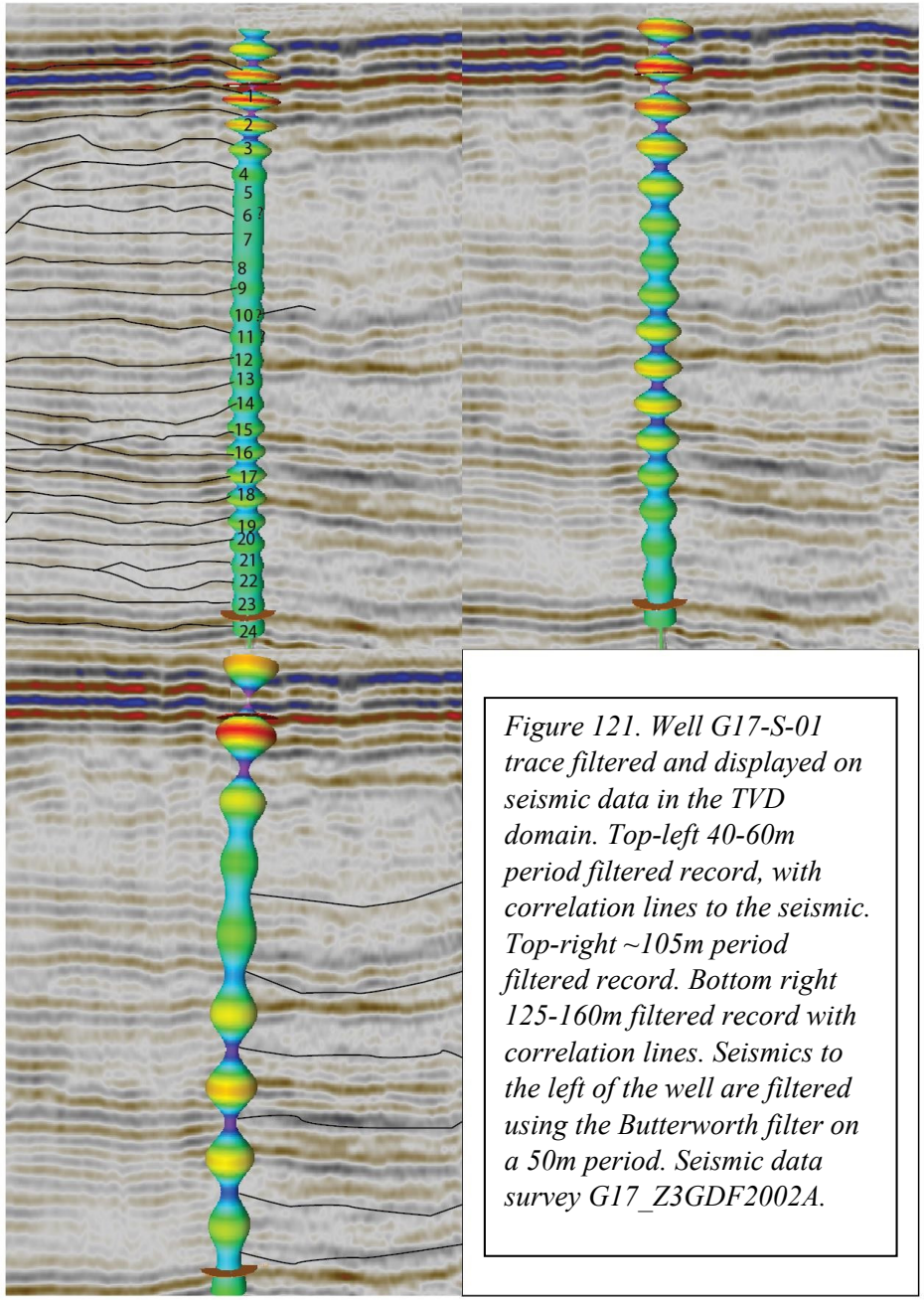

Figure 121. Well G17-S-01 trace filtered and displayed on seismic data in the TVD domain. Top-left 40-60m period filtered record, with correlation lines to the seismic. Top-right ~105m period filtered record. Bottom right 125-160m filtered record with correlation lines. Seismics to the left of the well are filtered using the Butterworth filter on a 50m period. Seismic data survey G17_Z3GDF2002A.

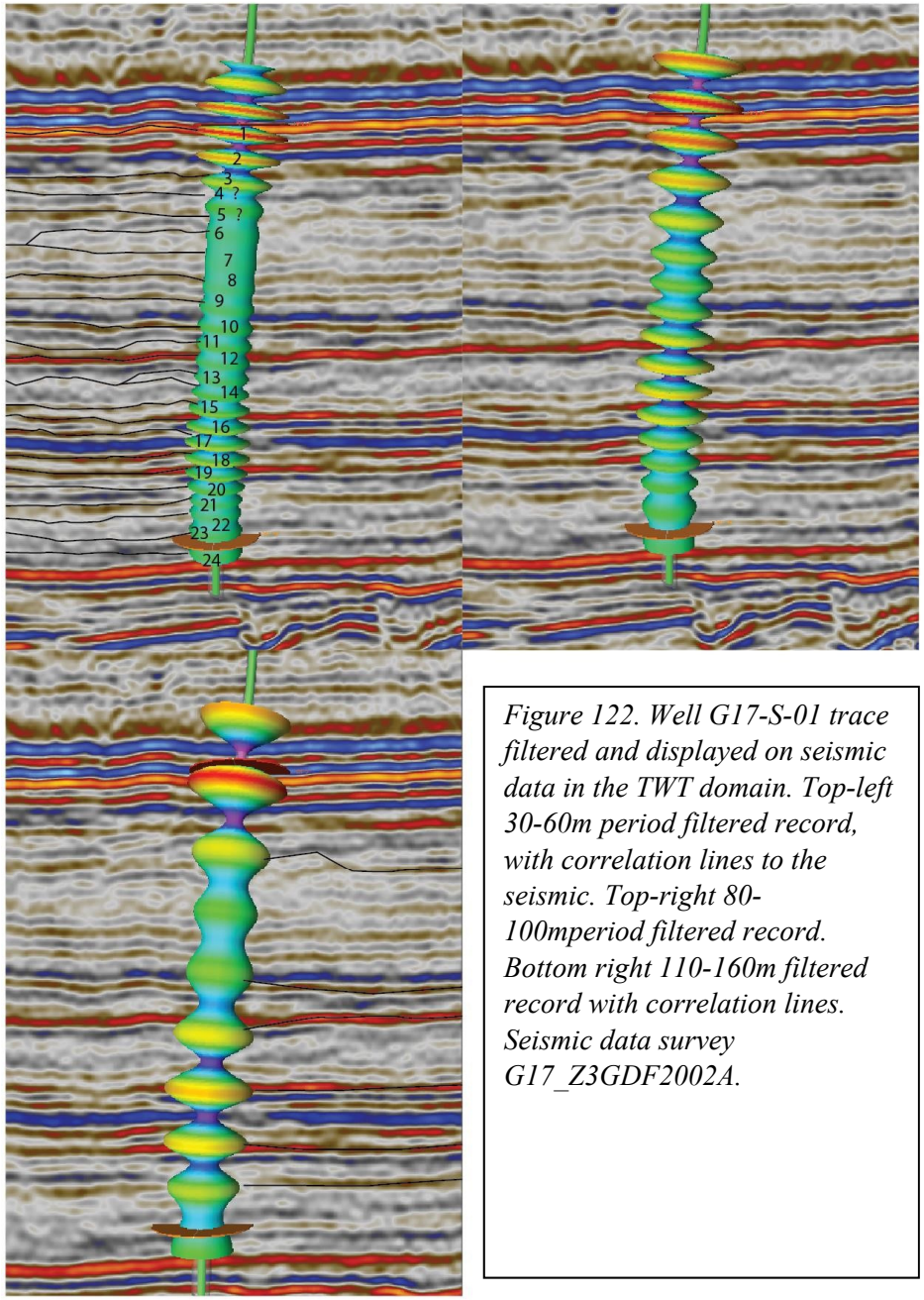

Figure 122. Well G17-S-01 trace filtered and displayed on seismic data in the TWT domain. Top-left 30-60m period filtered record, with correlation lines to the seismic. Top-right 80-100mperiod filtered record. Bottom right 110-160m filtered record with correlation lines. Seismic data survey G17_Z3GDF2002A.

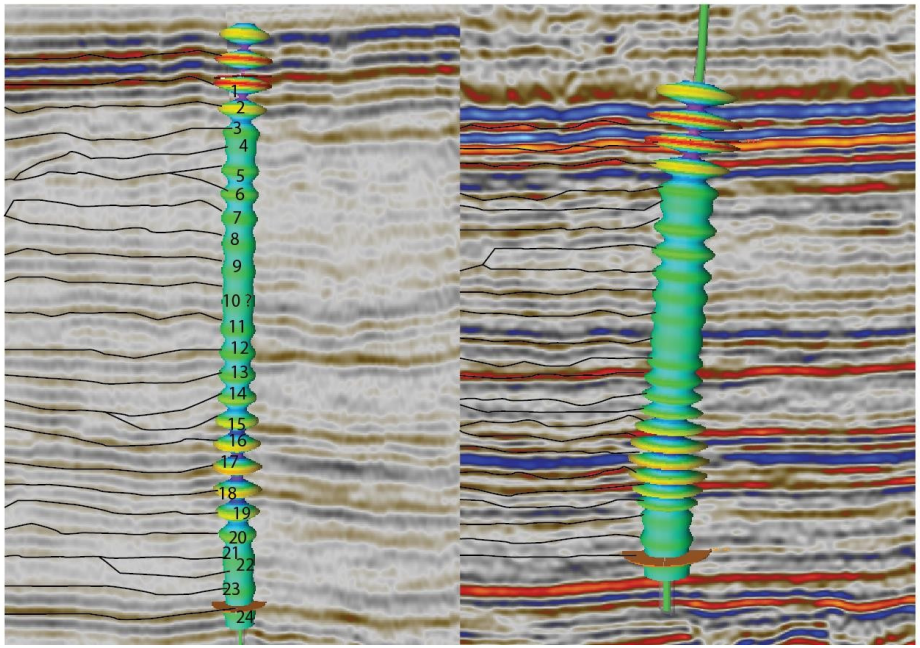

Figure 123. Well G17-S-01 VSP trace filtered and displayed on seismic data in the TWT domain. Top-left 30-60m period filtered record in TVD domain with correlation lines to the seismic. Top-right 30-60m period filtered record in TWT domain with correlation lines. Seismics in the left image and to the left of the well are filtered using the Butterworth filter on a 50m period. Seismic data survey G17_Z3GDF2002A.

10.11 Astronomical cycles in literature

10.11.1 300-kyr cycle in literature

A +99% significant peak with a 294-kyr duration found in the early-Turonian to early-Campanian terrestrial/lacustrine succession of the Singliao Basin in north-eastern China (Wu et al., 2013). That Wu et al. (2013) found a ~300-kyr cycle is peculiar especially so because the work of Wu et al. (2013) also spans the same time interval as this study. The presence of the ~300-kyr was not explained by Wu et al. (2013) so the origin of the 300-kyr remains enigmatic.

10.11.2 1200 and 2400-kyr cycle in literature

A strong 1200-kyr cycle is observed in the Maastrichtian Zumaya section in northern Spain (Batenburg et al., 2014, 2012). The 1200-kyr cycle is observed in the cyclic alternation of limestones and marls deposited in a hemipelagic setting. The 1200-kyr is manifested as changes in the grey/redness and resistance measurement. Mitchell et al. (2008) did find the 1200-kyr cycle in the alternating cherts and carbonates of the Cenomanian Scaglia Bianca in Italian Apennines. Mitchell et al. (2008) even postulated that the timing of OAE 2 is controlled by a 2.4 minimum insolation minimum. A 1200-kyr cycle was also found in the early-Turonian to early-Campanian terrestrial/lacustrine succession of the Singliao Basin in north-eastern China (Wu et al., 2013). Beside the 1200-kyr cycle, cycles with durations of 1.17Myr and 1.44Myr were also observed by Wu et al. (2013). Because of a large variation in the spectral peaks produced by different spectral analysis techniques for different logs an astronomical origin for some of these is peaks is called into question by Wu et al. (2013). A similar situation as that of Wu et al. (2013) is observed in this research with spectral peaks at 1.1Myr and 1.4Myr in the Redfit spectra in the time domain. A non-astronomical forcing behind some of the spectral peaks is something which should be accounted for

10.11.3 3500-kyr cycle in literature

Niebuhr and Prokoph, (1997) did find a similar ~150-125M cycle in the Chalk Group in Germany, however they did not give this cycle any interpretation. Assuming similar sedimentation rates, it could well be that this cycle in the German Chalk Group is the 3500-kyr cycle. The 3500-kyr cycle was also found in Albian-Campanian alternating chert and carbonate record of the Botaccione section in the Italian Apennines (Sprovieri et al., 2013). In a 70Myr long record of Triassic-Jurassic bedded chert sediments from Japan the 3.5 Myr cycle was also observed (Ikeda et al., n.d.; Ikeda and Tada, 2014, 2013). The 3500-kyr cycle has also been found in the continental to lacustrine sediments of the Newark Basin (Olsen and Kent, 1999). A 3500-kyr cycle was also interpreted for the Devonian prograding marginal marine muddy shoreline sediments of the Catskill delta (Tassell, 1988).

10.11.4 9500-kyr cycle in literature

To investigate long duration astronomical cycles a composite record approached is often used. The $\delta^{13}C$ record of Martinez and Dera (2015) is a such a composite record. Multiple records across western Europe were combined together to create a Jurassic to early Cretaceous $\delta^{13}C$ record. Martinez and Dera (2015) did find a 9.5 Myr cycle. The exact duration of the cycle varies between 8 and 10Myr. Two explanations for the relative high spectral power of the 9500-kyr cycle are given by Martinez and Dera (2015). The first explanation is due to the a “memory” effect of the carbon cycle. long residence times of carbon in the ocean enable the transfer of power from the low frequencies to the high frequencies. The second explanation is linked to quasi-stable high latitude terrestrial environments. The accumulation and release of organic matter from quasi-stable these reservoirs is claimed to be modulated by the eccentricity signal. Ikeda and Tada (2014) also found a 10Myr cycle in a 70Myr long record of Triassic-Jurassic bedded chert sediments from Japan. The 10Myr cycle was linked to an amplitude modulation effect of the eccentricity cycle. In a combined $\delta^{13}C$ record for the Cenozoic a 9Myr cycle was found (Boulila et al., 2012). The 9Myr cycle was attributed to the modulation of the 2400-kyr ecc cycle. An 8.1Myr cycle was also found in Albian-Campanian alternating chert and carbonate record of the Botaccione section in the Italian Apennines (Sprovieri et al., 2013). The 8.1Myr cycle was explained by the amplitude modulating effect of the 2400-kyr eccentricity cycle.

10.12 Review of cyclicity in the western European Chalk Group record

A review and comparisons of the literature on the Chalk Group will enable to put the current findings into regional (cyclo)stratigraphic context. The current findings will be compared from a (cyclo)stratigraphic point of view to the studies from other regions in western Europe where the Chalk Group was deposited. The regions which will be review and compared are the Dutch Offshore, South Limburg, Danish Central graben, Danish Basin, northern Germany, the Anglo-Paris Basin and the Bohemian Basin.

10.12.1 The Dutch Offshore

The work of van der Molen (2004) investigated the cyclicity of the Chalk Group in the Dutch Offshore. As with this research well-logs (DT and GR) were analysed for their cyclicity. van der Molen (2004) interpreted a ~5m cycle as the 100-kyr cycle and a 2-3m cycle as an obliquity cycle. The cycle lengths are in agreement with the with 15-22 m / 405-kyr hypothesise of this research. van der Molen (2004) interpreted a spectral peak with a period of 10m as the 405-kyr cycle. The spectra of the same wells indicate a period between 15 and 22 m for the 405-kyr cycle. The lower identified frequency of van der Molen, (2004) is probably due to the 15m maximum period restriction used for the Maximum Entropy Spectral Analysis (MESA) routine of the cyclolog software package which was used by van der Molen (2004) used. The 10m cycle identified by van der Molen, (2004) most likely corresponds to the 8m 200-kyr cycle of this research.

10.12.2 South Limburg

The Campanian-Maastrichtian limestone record in the south Limburg area consists of multiple decimetre to metre thick fining upwards cycles capped by a calcite cemented layers or hardground (Molenaar and Zijlstra, 1997; Zijlstra, 1995, 1994). The lithology mainly consists of well-sorted fine-grained carbonate mudstones and silt- to fine sand-sized bioclastic grainstones. The origin of the fining upwards sequences is hypothesised to be related to changes in the hydrodynamic energy. During periods of increased storm activity there is an increase in the hydrodynamic energy and as a result the sedimentation rate decreases. The hardgrounds are indicative of periods of enhanced storm erosion and prolonged exposure of bed to water interface. The wavy laminations found in the chalk of the south Limburg area indicative of high energy conditions and reworking. No astronomical cycle was assigned to these tempestite cycles. Beside the Tempestite cycles flint cycles area also present in the South Limburg area (Zijlstra, 1995, 1994). It is stated that that the flint layers formed within the sediment in the anoxic redox zone or slightly below the anoxic redox zone. Slow sedimentation means a long residence time in the anoxic redox zone thus thicker flint layers indicate slower sedimentation rates. Flint cycles therefore represent changes in the sedimentation rate. Diagenesis accentuates the flint layers by re-precipitating dissolved silica around the flint layers. Zijlstra (1995, 1994) interpreted the primary flint cycle as the precession cycle. Any modulating of the expression of the flint cycles is ascribed to the 1.3 Myr, 405-kyr eccentricity, 126-kyr eccentricity and 98-kyr eccentricity cycles.

10.12.3 Danish central graben

In the Danish part of the Danish-Norwegian central graben Perdiou et al. (2015) conducted a cyclostratigraphic analysis on the Adda core. $\delta^{13}C$, Fe concentration and gamma ray measurement were analysed using the MTM spectral analysis method. A spectral peak with a period of ~4m was identified as the 405-kyr cycle, the ~1m cycle was identified as the 100-kyr eccentricity cycle and the ~25cm period was interpreted as the 20ky cycle. Perdiou et al. (2015) did investigate cycles longer than the ~4m eccentricity cycle and which might have given more confidence to the identification of the ~4m 405-kyr cycle. The resulting sedimentation rate is ~9.9 mm/kyr, which relatively low in comparison to other literature (see sub-chapter sedimentation rate). An $\delta^{13}C$ excursion within the core was identified as the Late Campanian isotope excursion (LCE). The Plenus Marl is located just 85 metres below the LCE and has a Cenomanian Turonian age (Schlanger et al., 1987a). If the sedimentation remains constant between the LCE and the Plenus Marl then this would indicate there is a hiatus of ~19 Myr within this 85m interval. In the article of Perdiou et al. (2015) no hiatus was mentioned, but it was mentioned that previous research inferred the age of the Adda core as being Cenomanian to Santonian. When taking the Plenus Marl age into account a negative excursion event such as the Haven brow event near the Coniacian Santonian boundary (Jarvis et al., 2006) might be a better fit with the old age model.

Stage (2001b) and (1999) studied a 23 metre-long core of Maastrichtian age from the Dan Field in the Danish Central graben. A simple Fourier transformation was used to create periodograms of the Gamma ray, porosity and magnetic susceptibility data. Spectral peaks with periods of 2.5m, 1.4-1 and 0.5 were observed. The 2.5m period was interpreted as the 100-kyr eccentricity, the 1.4-1 period was interpreted as the obliquity cycle and the 0.5m period was interpreted as the precession cycle. the 2.5m period of Stage (2001b) and (1999) would extrapolate into a 10m long 405-kyr eccentricity cycle. The period for the 405-kyr eccentricity cycle is significantly shorter than the 15-22m 405-kyr cycle found in this study. The core is only 23m long and taken from the top of a salt dome where salt tectonics-induced induced redeposition is prevalent. The location of the core and the relative short sampling interval may explain the difference in cycle length between the research of Stage (2001b) and (1999) and this study.

Scholle et al., (1998) has conducted research on the same area as (Stage, 2001b, 1999) and found a 1m cyclicity and linked it to precession. The chalk sediments were divided into three distinct types of facies. Facies A consists of parallel laminae with 5-10cm beds alternating with non-laminated sediments. Facies B consists of 5-100cm thick bioclast rich chalk and are heavily bioturbated. Facies C consists of a stylolitic facies with bioturbation. Facies C was deposited during events of reduced sedimentation rates. The 1m cycles consists of and alternation between laminated chalks and stylolitic bioturbated bioclastic chalks. The alternations are believed to be related to changes in the productivity. Towards a palaeo high section becomes condensed and the risk of hiatuses or very condensed sections increased. On top of the highs the cycles are influenced by winnowing. Sediment transport from highs to lows is proposed as one of the reasons why the cycles are thicker in the lows. A 1m precession cycle would translate into a ~4.5m / 100-kyr cycle and a ~18m long 405-kyr cycle. The ~18m cycle length is comparable to cycle lengths found by van der Molen, (2004), and this study.

Damholt and Surlyk (2004) conducted a study on multiple Maastrichtian chalk cores from multiple locations in the Danish central graben. The cores contain 300– 200 cm thick cycles alternating between bioturbated and non-bioturbated laminated beds. The cycles have been interpreted as an alternation between slow background sedimentation, which is extensively bioturbated and rapid deposition of laminated sediments origination from local turbiditic re-sedimentation processes. The laminated sediments are protected from being erased by bioturbation by anoxic bottom conditions. The 200-300cm cycles are interpreted as being precession. Individual laminae are linked to individual turbidites which are proposed to be deposited in only days to months. The whole laminated anoxic interval is proposed to have a duration of 10-kyr. Damholt and Surlyk (2004) did not perform any spectral analysis to discriminate between obliquity and precession, which does call into question the precession interpretation. A 200cm would indicate that the 405ecc cycle is 50m thick. The 405-kyr cycle in this research only has a thickness of 15-22m. The difference in the thickness of the 450-kyr cycle would indicate that the sedimentation rate is 3-4x higher in the Danish Central Graben in comparison to the Schill Grund Platform.

Petersen et al. (2003) found 1–1.5 m thick porosity cycles in the Dan fields in the Danish Central graben. The high porosity intervals have a redepositional origin. the redeposition occurred by means of current and gravitationally induced processes. The low porosity intervals are the result of slow pelagic deposition. The main factor controlling the cyclicity is sedimentation rate. The cycles are proposed to have an astronomical origin but no astronomical cycle was assigned to the 1-1.5cycle.

10.12.4 Danish Basin

The Maastrichtian Rørdal Member in Rørdal quarry the Danish Basin contains 125 cm thick marl-chalk cycles (Lauridsen et al., 2011; Lauridsen and Surlyk, 2008; Schovsbo et al., 2006; Surlyk et al., 2010). The marl layers are enriched in $\delta^{13}C$ and $\delta^{18}O$, depleted in CaC03 and have higher Gamma ray values when compared to the chalk layers (Surlyk et al., 2010). There still uncertainty regarding the origin on the enrichment of in $\delta^{13}C$ and $\delta^{18}O$ in the marl layers. According to Surlyk et al., 2010 the enrichment of in $\delta^{13}C$ and $\delta^{18}O$ in the marl layers could be a primary signal or a diagenetic overprint. The marl contains the highest diversity of trace fossils in comparison to the chalk interval (Lauridsen et al., 2011). The higher clay of the marl enhances the expression of bioturbation features, which could lead to wrong interpretations. The palaeoecological studies by Lauridsen et al. (2011) and Lauridsen and Surlyk (2008) indicated that the highest diversity in the benthic epifauna was in the chalk layers. The chalk layers are interpreted as periods of better living conditions, higher environmental stability and higher nutrient influx in comparison to marl. Lauridsen and Surlyk (2008) interpreted the marl intervals as periods of water column stratification, nutrient depletion,

and decreased productivity in the surface waters. Schovsbo et al. (2006) interpreted the marl as being deposited in cooler water conditions. Lauridsen and Surlyk (2008) and Schovsbo et al. (2006) linked the Marl/chalk cycles to the precession cycle. If the 125cm cycle is indeed the precession cycle then this would result in 20-25m thick 405cycle. The 20-25m 405cycle is similar to the 15-22m / 405-kyr cycle found in this research.

Thibault et al. (2015) created a chronostratigraphic for the upper Campanian–Maastrichtian of the Skælskør-1 core in the Danish Basin. The records contain a lot of bryozoa and redeposited facies but no laminated bioturbated facies was observed. This might be due to shallower depositional location. The coring location is located on the Ringkøbing Fyn High core which was a palaeo-bathymetric high during the Cretaceous. The gamma ray log shows cyclitic with a period of 15–20 m. the $\delta^{18}O$ record shows a cyclicity of 10–15 m. No spectral analysis was conducted on the $\delta^{18}O$ and gamma ray record. The gamma ray log and $\delta^{18}O$ cycles are both interpreted as the 405-kyr eccentricity cycle. the 10-15 $\delta^{18}O$ and 15-20m gamma ray cycles are similar to the 15-22 m / 405-kyr cycle found in this research.

10.12.5 Northern Germany

Voigt et al. (2007) investigated the upper Cenomanian to lower Turonian Halle and lower to middle Turonian Oerlinghausen sections in the Munsterland Basin. Just Below the Cenomanian-Turonian boundary in the Halle section the lithology changes from a coccolithophore dominated limestone to an alternation of marls, black shales and limestones. The Oerlinghausen section consists entirely out of the alternation of marls, black shales and limestones. A relatively shallow depositional environment is interpreted for both sections. The record consists of CaCO3%, TOC, $\delta^{13}C$, $\delta^{18}O$ measurements. In both sections, low carbonate content correlates to high TOC values and low $\delta^{13}C$ and $\delta^{18}O$ values. For both sections Voigt et al. (2007) indicated that marine productivity and terrestrial input influence the organic matter composition. This dual origin for organic matter can explain the poor correlation between isotope values and the TOC and carbonate measurements. Spectral analysis using the Lomb–Scargle algorithm the was performed on the $\delta^{13}C$ record of the Oerlinghausen section. The spectral analysis showed indicated power peaks for the periods of ~9m and 2-3m. the ~9m peak was identified as the 405-kyr cycle and the 2-3m cycle was identified as the 100-kyr.

Voigt and Schönfeld (2010) created a Campanian–early Maastrichtian floating timescale for the Lägerdorf–Kronsmoor section. The floating timescale was linked to self-potential logs for a basin wide correlation. The record consists of chalk with varying amounts of detrital clay. The Blackman-Tukey power spectra of the carbonate record showed spectral peaks with periods of 9.6m and 2.5m. The 9.6m cycle is interpreted as the 405ecc cycle and the 2.5m cycle as interpreted as the 100-kyr eccentricity cycle. The 9.6m 405-kyr cycle is significantly thinner than the 15-22m cycle found in this research. A thinner cycle would indicate significantly lower sedimentation rates. The Lägerdorf–Kronsmoor section is located more proximal which might explain the lower sedimentation rate.

Niebuhr and Prokoph, (1997) analysed Cenomanian to Campanian pelagic well-logs of multiple wells located in Northern Germany. Wavelet spectrograms of self-potential record were used to analyse the record. For the upper Campanian cycles were assigned to specific orbital cycles. For the Taaken-Ottersberg the 6.9m cycle was interpreted as the 100-kyr cycle and the 27.5m cycle was interpreted as the 405-kyr cycle. For the Lehrte 37 well the 12m cycle was interpreted as the 100-kyr cycle and the 48m cycle was interpreted as the 48m cycle For the E Daehre 4/83 well the 8.5-5.8m cycle was interpreted as the 100-kyr cycle and the 29m cycle was interpreted as the 405-kyr cycle. The 405 cycles in the research of Niebuhr and Prokoph, (1997) significantly thicker than the 15-22 m / 405-kyr cycle of this research. The 405-kyr 30-50m cycle of Niebuhr and Prokoph, (1997) is has a comparable thickness as the 40-60 m / 1200-kyr cycle found in this research. If in fact the 405-kyr was wrongly identified in this research and the 40-60m cycle is the 405-kyr cycle then this would imply that there must be one or more hiatuses present on the Schill Grund Platform.

Niebuhr et al. (2001) studied the Cenomanian to lower Coniacian well-logs of the Konrad 101 borehole located in Lower Saxony. EHA spectra of the resistivity log were created for the upper Albian to Turonian record. There is a notable alternation between orbitally forced facies and chaotic facies. In the Albian interval, the 100-kyr cycle has a thickness of 3-4 m. During the late Cenomanian, the sedimentation rate decreases to 13m/Myr and then increases to 18 m/Myr. During the late Cenomanian, the 405-kyr is identified firstly decreases in thickness to 3.33m and then increases in thickness to 7m. The 100-kyr cycle has as thickness of 3.33-2.5 m in the Turonian interval. The sedimentation rate varies between 25 and 30 m/Myr during the Turonian. The 3.33-2.5 m thickness of the 100-kyr cycle the Turonian interval would infer that the 405-kyr cycle is 13.5 and 10.1m thick. The 13.5 and 10.1m thickness of the 405-kyr cycle of Niebuhr et al. (2001) is comparable to the 15-22m 405-kyr cycle proposed in this research.

Niebuhr (2005) analysed the middle to late Campanian chalk marl-limestone alternation of the western Lehrte Syncline in northern Germany. The marl–limestone alternation was inferred as being a two-component system with pure carbonate and shale being the endmember. The variation in the shale content were attributed to variations in either productivity and/or dilution. And EHA spectral analysis was performed on the carbonate content record. The spectral peak of the 18-20m thick cycle was interpreted as the 405-kyr eccentricity cycle, the 4.1-6m thick cycle was interpreted as the 100-kyr eccentricity cycle, the 1.7-2.5m thick cycle was interpreted as the obliquity cycle and the 0.8-1.1m thick cycle was interpreted as the precession cycle. the 18-20 m / 405-kyr cycle found by Niebuhr (2005) is similar to the 15-22m / 405-kyr cycle found in this research.

Voigt et al. (2008) investigated the Cenomanian to Turonian of the Wunstorf section in North Germany. The section consists of laminated black shales, dark organic-rich marls and marly limestones. Spectral analysis using Blackman-Tukey transformation and wavelet techniques was performed on the Titanium and gamma ray records. The Blackman-Tukey power spectra indicated 13.9, 3.2–3.3, 1.26 and 0.68 m thick cycles. The 13.9m thick cycles was interpreted as the 405-kyr cycle. the 3.2-3.3 cycle was interpreted as the 100-kyr cycle. The 1.26m thick cycle was interpreted as the obliquity and the 0.68m thick cycle was interpreted as the precession cycle. The wavelet also indicated high spectral power for the 3.3m / 100-kyr eccentricity and 0.7m precession cycle. The 13.9m / 405-kyr cycle identified by Voigt et al. (2008) is like the 15-22m / 405-kyr cycle found in this research**.**

10.12.6 Anglo-Paris Basin

Both Ditchfield and Marshall (1989) and Leary et al. (1989) studied a 120cm thick Cenomanian chalk on the Kent coast. The record consists 50cm thick marl-chalk couplets. Ditchfield and Marshall (1989) analysed $\delta^{18}O$ and $\delta^{13}C$. No clear relationship could between the lithology and the $\delta^{13}C$ record could be established. low $\delta^{18}O$ values corresponded to marls while high $\delta^{18}O$ values corresponded to chalk. The chalks were interpreted to be deposited in warm waters while the marls were interpreted as being deposited in colder waters. Leary et al. (1989) linked variations in the relative abundance of different foraminiferal species to changes in the sea surface productivity. The chalks were interpreted as warm water productivity blooms. Leary et al. (1989) interpreted the chalk-marl alternations as precession cycles.

Hart (1987) studied the cyclicity of the Cenomanian Campanian succession of Chalk Group on the Isle of Wight. the Cenomanian lower chalk succession contains a 0.5-1m thick clay-limestone cycles. The cycles are interpreted as obliquity cycles. The clay rich intervals are interpreted as being low oxygen environments. This interpretation is based on the presence of chondrites. The low oxygen environment is believed to be caused by productivity cycles. High productivity leads to dysaerobic conditions and thus enabling carbonate dissolution and marl deposition. In the Coniacian-Campanian there is alternation between black cherts and chalks. The 0.5 to 0.7m thick chert-marl alternation is linked to the precession cycle and the 1.4 to 1.6m thick chert-marl alternation is linked to the obliquity cycle.

Juignet and Breton (1992) studied multiple sections of the Chalk Group time equivalent in the Paris Basin. The multiple sections showed a transition from pelagic chalk sediments to shallow marine clastics. Multiple 0.5 to 15 m metre thick cycles are observed throughout the basin. The top of these cycles is often bound by omission, hardground or erosional surfaces. The larger cycles contain shorter 0.30 and 1.50m thick elementary cycles. The main cycles are associated with changes in the clay content or changes in the sea-level. Chalk rich intervals contain abundant trace burrows. Diagenesis often caused silica to be deposit in these burrows. The general shallow environment and lots of diagenetic features present inhibits a cyclostratigraphic interpretation.

Lauridsen et al. (2009) studied the Cenomanian chalk-marl cycles of the Southerham Grey Pit section south east England. The section is 60–80m long section. Sediments were deposited relatively shallow water (50-100m). The marl-chalk cycles are 40 to 90cm thick and interpreted as precession cycles. The marly intervals are associated with a higher nutrient flux. The biostratigraphic analysis showed that changes in the lithology did not influence the fauna which was present. No spectral analysis performed to confirm the presence of beside the precession cycle. Expanding the 40-90cm cycle to the 405-kyr eccentricity cycles leads to a 7.4 to 16.6m thick eccentricity cycle. the 7.4 to 16.6m thick 405-kyr eccentricity cycle is comparable to the 15-22m / 405-kyr eccentricity cycle of this research.

Cottle (1989) studied the foraminiferal record of the Turonian chalk of the Aker steps section in southern England. Spectral analysis was performed for the absolute counts of the foraminiferal species Gyroidinoides Nitida. Spectral peaks were observed for the 8.25m period and the 92cm period. The 8.25m period was interpreted as the 405-kyr

eccentricity cycle and the 92cm period was interpreted as the obliquity cycle. No correlation with the stratigraphic record was made. The 8.25m thickness of the 405-kyr cycle is much thinner than the 15-22m / 405-kyr cycle and indicates a lower sedimentation rate for the Aker steps section.

Gale et al. (1999) created a composite greyscale record for Folkestone and Eastbourne sections in South eastern England. Blackman-Tukey spectral analysis of greyscale reflectance data indicates spectral peaks for the 20-50cm and 4-10m period. The 20-50cm thick period is interpreted as the precession cycles and the 4-10m thick cycle is interpreted as the 405-kyr eccentricity cycle. the record 20ky precession cycle was used for the tuning of the record. Tuning was compared to a tuning from the Crimea (also Gale et al. (1999)) indicated a hiatus of roughly 80ky. The 10m thickness of the 405-kyr cycle is much thinner than the 15-22m / 405-kyr cycle and indicates a lower sedimentation for the Cenomanian English chalk.

Thibault et al. (2016b) studied the upper Coniacian to Lower Campanian succession at the Seaford Head section in south eastern England. bulk $\delta^{18}O$ and $\delta^{13}C$ measurements were performed on samples from this section. Spectral analysis using the MTM was performed on the $\delta^{13}C$ $\delta^{18}O$ record. Spectral analysis indicated peaks with periods of 16m, 1.18m and 0.75-0.56 meter. The 16m period was interpreted as the 405-kyr eccentricity cycle. the 4.2m period was interpreted as the 100-kyr eccentricity cycle. The 1.18m period was interpreted as the obliquity cycle. The 0.75-0.56m period was interpreted as the precession cycle. the MTM spectra the obliquity peak for $\delta^{18}O$ was much larger than that of $\delta^{13}C$. Thibault et al. (2016b) explained the larger expression of obliquity for the oxygen isotope by the fact that organic carbon has a long residence time of 200-kyr . The average spectral misfit method was used to check the interpretation which confirmed the MTM spectral data. Evolutive harmonic analysis and MTM spectral analysis was performed in the depth domain. The results time domain was the same as results in the depth domain. Two phase relationships were proposed. In the first relationship, the $\delta^{13}C$ maxima correspond to eccentricity maxima and in the second relationship the $\delta^{13}C$ maxima correspond eccentricity minima. The Eccentricity minima option is favoured by Thibault et al. (2016b). Thibault et al. (2016b) did not make a correlation between the $\delta^{18}O$, $\delta^{13}C$ and the lithological records. The $\delta^{13}C$-lithology-orbital phase relationship was extrapolated from the Western Interior Basin. The Anglo-Paris Basin and the Western Interior Basin can have different lithological responses to orbital forcing so to extrapolate the $\delta^{13}C$-lithology-orbital phase relationship is problematic. The 16m 405-kyr cycle identified by Thibault et al. (2016b) is similar to the 15-22m 405-kyr cycle proposed in this research.

10.12.7 Bohemian Basin

Laurin et al. (2014) used multiple wells in the Bohemian Basin to create a astrochronology for the Mid Turonian to early Coniacian. The Turonian succession consists of hemipelagic carbonate sediments marl limestone alternations. Resistivity, gamma ray and $\delta^{13}C$ data was used for analysis. High gamma ray values correspond to low $\delta^{13}C$ values. MTM spectral analysis was performed on the gamma ray well-log data of boreholes RPZ-37 and RPZ-24. Spectral peaks with periods of 9m-14m, 3.6m-2.5m and 1.4m-0.9m were observed. The 9m-4m period was interpreted as the 405-kyr eccentricity cycle. the 3.6m-2.5m period was interpreted was the 100-kyr eccentricity cycle. The 1.4m-0.9m period was interpreted as the obliquity cycle. EHA spectra of the gamma ray logs of wells RPZ-37 and RPZ-24 showed similar cycles as the MTM spectra. The 9m-14m 405 cycle of Laurin et al. (2014) is thinner in comparison to the 15-22m / 405-kyr cycle of this research. The thinner cycle of Laurin et al. (2014) indicates slower sedimentation rate for the Bohemian Basin.

10.13 Proxy records of the chalk in literature

The References in this chapter which have an * have their location, lithology, cyclicity and age already described in the chapter 10.12 of this research and these aspects will therefore not be discussed in this chapter. Low $\delta^{18}O$ values can be interpreted as warmer temperatures and high $\delta^{13}C$ values can be interpreted as high productivity or high carbon burial (Ruddiman, 2014)

In Voigt et al. (2007)* low carbonate content correlates to high TOC values and low $\delta^{13}C$ and $\delta^{18}O$ values. This indicates that during warm periods (low $\delta^{18}O$), productivity was low (low $\delta^{13}C$) and high TOC marly carbonates were deposited.

In Surlyk et al. (2010)* low carbonate content (marl lithology) correlates to a high gamma value, high $\delta^{13}C$ and high $\delta^{18}O$. this indicates that the marls were deposited during cold periods (high $\delta^{18}O$) when productivity was high.

According to Surlyk et al. (2010)* the difference in the $\delta^{18}O$ values between the marls and the carbonates can be attributed to primary environmental signal or a diagenetic overprint.

Scholle and Arthur (1980) created a composite $\delta^{13}C$ record for the Cretaceous based on multiple site around the north Atlantic. Scholle and Arthur (1980) found multiple $\delta^{13}C$ excursion in the Cretaceous. These $\delta^{13}C$ excursions were linked to high TOC anoxic events linked to elevated temperatures and sea-level. These elevated temperatures are believed to have created a sluggish circulation and a poor water mass oxygenation.

Jenkyns et al. (1994) created a composite $\delta^{13}C$- $\delta^{18}O$ record of the Cenomanian to Campanian of the English Chalk Group. The composite based on multiple locations along the English coast. In the Chalk Group record positive $\delta^{18}O$ excursion seem to correlate to marls, but the sampling density is generally too low to make any definite conclusion about this observation. Upwelling is postulated as mechanism for marl-chalk alternation. The upwelling of cold low $\delta^{18}O$ nutrient rich water would have increased the productivity and the carbon burial and thus increased the $\delta^{13}C$ values.

Jarvis et al. (2006) also created a composite $\delta^{13}C$ record of the Cenomanian to Campanian of the English Chalk Group, which was also based on multiple locations along the English coast. The sampling resolution for $\delta^{13}C$ is generally too low to indicate a lithology- $\delta^{13}C$ relationship but often positive $\delta^{13}C$ excursion correspond to flints or marls.

Thibault et al. (2015)* observed a positive correlation between the GR log and the $\delta^{13}C$ log. A similar climatic control on the GR and $\delta^{13}C$ record is therefore proposed. $\delta^{13}C$ and $\delta^{18}O$ do not correlate. Thibault et al. (2015)* does not specify the relationship between the GR and the $\delta^{18}O$ signal. A visual inspection of the graphs of Thibault et al. (2015)* does appear to show a positive correlation between $\delta^{13}C$ and $\delta^{18}O$.

Voigt and Hilbrecht (1997) studied the Cenomanian to Coniacian at the Salzgitter Salder, Söhle, Dresden-Blasewitz locations in the Saxony Basin in Germany. The Salzgitter Salder section is of middle Turonian to Coniacian age. The Söhle section is Cenomanian to upper Turonian. Both sections consist of coccolith/calcisphere limestones intercalated with marls deposited in a pelagic epicontinental setting. The Dresden-Blasewitz borehole is of upper Cenomanian to lower Coniacian age. The sediments in the Dresden-Blasewitz borehole were deposited in an hemipelagic setting. The early late Cenomanian to sediments in the Dresden-Blasewitz borehole show a transition from calcareous sandstones to calcareous siltstones in the lower Turonian. The middle Turonian to early Coniacian sediment consist of calcareous/marly siltstones. The $\delta^{18}0$ and $\delta^{13}C$ records correlate positively at all the locations. No connection between the $\delta^{13}C$, $\delta^{18}O$ and lithology were made. Voigt and Hilbrecht (1997) linked high $\delta^{13}C$ values to high sea-level. It was hypothesized that during that during a high sea-level organic matter was deposited in shallow water. The previously deposited sediment was eroded/oxidized during a sea-level fall, which resulted in a negative $\delta^{13}C$ excursion

(Thibault et al., 2016)* proposed two phase relationships between $\delta^{13}C$ and insolation. In the first relationship, the $\delta^{13}C$ maxima correspond to eccentricity maxima. (Thibault et al., 2016)* linked carbonate poor intervals in the Western Interior Basin to insolation maxima. The continental weathering rate increases during insolation maxima, which leads to higher nutrient flux. An increase in the nutrient flux results in an increase of marine productivity and thus a higher organic burial rate. Due to preferential fractionation of 12C during photosynthesis $\delta^{13}C$ increases. In the second relationship, the $\delta^{13}C$ minima correspond eccentricity maxima. During eccentricity maxima weathering rates increase and the continental flux of (lighter $\delta^{13}C$ HCO3-) increases leading to a decrease in $\delta^{13}C$. During eccentricity minima $\delta^{13}C$ increases by higher removal as $\delta^{13}C$ in form of carbonate. The eccentricity minima option is favoured by Thibault et al. (2016b)*. Thibault et al. (2016b)* did not make a connection between isotope measurements signals and the lithology. It was not indicated if there was a correlation between $\delta^{18}O$ and $\delta^{13}C$, but a visual inspection does show that most peaks in the $\delta^{18}O$ record correlate positively to peaks in the $\delta^{13}C$ record.

Schönfeld et al. (1991) measured $\delta^{18}O$ from the middle Coniacian to lower Maastrichtian Chalk Group at the Lägerdorf section in Northwest Germany. Bulk carbonate and Inoceramid shells were measured. Bulk carbonate has a negative trend with carbonate content, which is attributed to a diagenetic overprint. The $\delta^{18}O$ signal also contains a positive depth trend. $\delta^{18}O$ measurements on the Inoceramid shells indicates a mean temperature of 16°C for the late Campanian early Maastrichtian bottom waters.

Jarvis et al. (2015) studied the Bch-1 borehole in Bohemian Basin in the Czech Republic. The sediments are of Turonian to Coniacian age and consist of dark grey marlstones and calcareous mudstones. Jarvis et al. (2015) indicates that Al2O3 correlates negatively to CaCO3, TOC positively correlates with Al2O and $\delta^{13}Corg$ is generally positively correlated to

δ^{13}Ccarb. Visual inspection of the data indicates that when δ^{18}O is positive, gamma ray is negative, δ^{13}C is positive, Toc is positive and CaCo3 positive. The negative correlation between Al2O3 and CaCO3was linked to a dilution trend. The noisy signal of the δ^{18}O curve is linked to the diagenetic overprinting of the original signal. These is additional uncertainty in the δ^{18}O signal due to effect of salinity on the δ^{18}O signal and the presence of an aquifer beneath the formation. The δ^{13}C record is linked to sea-level changes (positive values correspond to higher sea-levels). The combination of the δ^{13}Corg and δ^{13}Ccarb record records indicates that the organic matter flux is higher than the carbonate flux in Bohemian Basin.

Laurin et al. (2014)* simulated a δ^{13}C record for the Middle Turonian to upper Coniacian. Laurin et al. (2014) used a model where the δ^{13}C signal acted in a non-linear way to the obliquity cycle. This modelled record was compared to the δ^{13}C records from Salzgitter-Salder and Liencres and showed great similarities. The distinct asymmetry of the compared δ^{13}C signal could be related enhanced marine and/or terrestrial organic accumulation related to a monsoonal forcing at high eccentricity.

Pearce et al. (2009) studied the Cenomanian Turonian chalk-marl alternation near Eastbourne in the southern England. Above Ocean Anoxic Event 2 both δ^{13}C and δ^{18}O have positive excursions in the marls. The positive δ^{18}O excursion are attributed upwelling. According to Pearce et al. (2009) the location and airflow patterns could have enabled Ekman transport induced upwelling. Upwelling would have increased the nutrient supply leading to deposition of TOC rich marls. The shales of OAEII are believed to formed by a period of intense upwelling of nutrient rich bottom-waters. During the early-Turonian elevated temperatures reduced upwelling rates and hyperstratification ensued.

Pearce et al., (2003) studied the Upper Cretaceous of the Banterwick Barn Chalk borehole in south east England. During the late Cretaceous the Banterwick barn section was located in a shallow part of the Anglo-Paris Basin. This shallow location was confirmed by a dinocyst assemblage which is indicative of a shallow water setting. No upwelling related Dinocyst species were observed and principal nutrient supply is believed to be of detrital origin. Marls coincide with negative δ^{18}O indicating cool water deposition of the marls. Pearce et al., (2003) did not indicate if δ^{18}O and δ^{13}C correlated.

In Perdiou et al. (2015)* δ^{13}C and δ^{18}O do not correlate, while Fe and the gamma ray do. Perdiou et al. (2015)* did not indicate if δ^{13}C and gamma data correlate and a visual inspection of the data does not clarify this issue. The decreasing trend. The decrease in Fe values towards the top of the formation is linked to a decrease in the detrital input or a higher carbonate productivity.

Jorgenson (1987) measured δ^{13}C and δ^{18}O of the Chalk Group for multiple locations in the Danish Basin and Danish central graben. δ^{18}O decreases with depth, carbonate content and increases with porosity. The expression of the δ^{18}O signal is attributed to a digenetic overprint but a primary signal cannot be excluded. δ^{18}O and δ^{13}C correlate positively. δ^{13}C increases with a lower carbonate content. The δ^{13}C signal is believed to represent the palaeoenvironmental signal.

Boussaha et al. (2016) created an integrated stratigraphy of the late Campanian to Maastrichtian of the Danish Basin. A new age model was created for the Danish Basin using calcareous nanofossil data. The observed sedimentation rate was higher during warm intervals and lower during the cool intervals, except during the late Maastrichtian the opposite was observed. The changes in the sedimentation rate was linked to changes in the carbonate productivity by the calcareous nanoplankton and/or variations in the intensity winnowing currents.

Van Helmond et al. (2015) studied Cenomanian to Turonian laminated black shales, dark organic-rich marls and marly limestones of the Wunstorf section in north Germany. TEX 86, Toc, δ^{13}C and biostratigraphic data (e.g. pollen, spores, palynomorphs, dinoflagellates) were used for a palaeoenvironmental interpretation. Shale layers are believed to be formed as a consequence of runoff induced stratification. An enhanced productivity due enhanced runoff cannot be ruled out.

Ditchfield and Marshall (1989)* indicated that variation in the δ^{18}O record represent changes in temperatures. The δ^{18}O record indicated a palaeotemperature of 24°C for the marl and 27° chalk. The marl layers were linked to cool low productivity conditions and not increased terrigenous input and the chalk intervals were linked to higher surface productivity.

Stage (2001a) studied the insoluble residue from late Maastrichtian chalk samples from the Dan field in the Danish Central graben. Chalk contains illite, smectite and quartz, which are interpreted as being of a detrital origin. (Stage, 2001a) measured the Magnetic susceptibility of bulk chalk samples. Changes in the magnetic susceptibility are linked to changes in the continental runoff.

The records of Stage (2001b) and (Stage, 1999)* consists of a gamma ray and magnetic susceptibility record of the Chalk Group in the Danish central graben. Magnetic susceptibility is a proxy for detrital input (Da Silva et al., 2013). The Correlation between the Gamma ray and the magnetic susceptibility records is substantial and therefore peaks in gamma ray can be attributed to changes in the detrital input. Changes in the clay fraction are interpreted as changes in precipitation and continental runoff, changes in carbonate production, changes in the detrital source area or changed in the bottom water currents.

Niebuhr (2005)* suggests that there are two processes which may explains the marl-chalk alternations. The first process in changes in the carbonate productivity. CaCO3 %, Mg/Al, Mn/Al and Sr/Al proxies support the first process. the second process is changes in the detrital input (illite/smectite ratio). The K/Al, Ti, Rb, Si, Zr and Na, proxies do not vary greatly which indicates that the detrital flux was constant. The redox potential indicates oxidizing conditions for the whole interval.

Leary et al. (1989)* indicated that that the variations in the foraminiferal record were due to changes in the productivity. The marl layers were linked to cool low productivity conditions while the chalk intervals were linked to higher surface productivity.

Ineson et al., (2006) studied the late Maastrichtian M-10X and E-5X cored sections in the Danish Central graben. The nanofloral assemblages indicate a stable, cool water (Boreal), oligotrophic (low nutrient) conditions. In the lower cored part Ineson et al., (2006) inferred a cool-water, oligotrophic, deep shelf setting which was prone to stratification which resulted in anoxic conditions.

Rasmussen and Sheldon (2015) analysed the foraminifera in late Maastrichtian chalk samples from two locations in the Danish Central Graben. The planktonic/benthic ratio indicated a mostly stable outer-shelf environment with pelagic sedimentation and suboxic bottom waters. In the lower sampling interval, oligotrophic and dysoxic to anoxic conditions prevailed. Rasmussen and Sheldon (2015 correlated the anoxic phases to a higher productivity pulses. From the P/B ratio water depths between 200 and 800 metres were inferred.

10.14 Seismic cycles in literature

Weigelt and Uenzelmann-Neben (2007) performed spectral analysis on the seismic data the Cape Basin offshore Namibia and South Africa. To date the research of Weigelt and Uenzelmann-Neben (2007) is the only research were spectral analysis has been conducted on seismic data. The seismic data of Weigelt and Uenzelmann-Neben (2007) covers the top 500m of the sedimentary column which the presents present to Pliocene. Productivity and upwelling are proposed as the main drivers of changes in density. Density itself is proposed as the main factor influencing the reflector strength. The spectral analysis indicated the presence of the 40-kyr obliquity, 100-kyr eccentricity and 405 eccentricity cycle. Similar cycles were found in the density record. There is a notable shift from 100-kyr dominated (0-2 Ma) to 40-kyr (2-3 Ma) and back to 100-kyr (3 Ma-4.4 Ma). After 4.4 Ma, no clear cycles were present.

Cycles were observed In Bahama bank record spanning back to 23.9 Ma (Eberli et al., 1996, 2002). The hypothesis is that they can be stacked into seismic sequences with an astronomical origin. Biostratigraphy indicates that the cycles are indeed chronostratigraphic lines but no spectral analysis or hypothesis was made for the origin of the reflectors.

Scholz (1995) observed 7 ~100m thick couplets a seismic survey of lake Malawi. These couplets are hypothesised to be the result climatically induced fluctuations in lake levels and sediment supply. The high-amplitude reflectors are interpreted as highstand deposits. Cohen et al. (2000) proposed a 100-kyr eccentricity origin for the couplets. Cohen et al. (2000) observed similar cycles in Lake Tanganyika.

Lobo and Ridente (2013) and Ridente et al. (2009) investigated the marine isotope stages in the Adriatic.

Ridente et al. (2009) identified marine isotope stages from $\delta^{18}O$ and warm planktonic species in well data and linked the isotope stage to seismic reflectors. Ridente et al. (2009) traced the different marine isotope stages in a seismic cross-

section. The Record does not go further back than 375000 years (MIS10) and is based on high resolution shallow seismic data. (Lobo and Ridente, 2013) dealt with the sequence stratigraphic expression of the 100-kyr and 20-kyr cycles.

Hernandez-Molina et al. (2015) integrated seismic and well-log data from the Gulf of Cadiz. The focus of investigation spanned sediments ranging in age from the late Miocene to present. MTM spectral analysis of Pliocene-Pleistocene Gamma ray records from two well in the Algarve Basin indicated cycles with durations of 1.7-2 Ma, 800, 405, 275-288, 161-170, 96-107, 85, 55-44 and 22-24.5-kyr. Hernandez-Molina et al. (2015) proposes that the reflector pattern is a combination of tectonic and (cyclical)climatic influences.

Baker (1994) investigated seismic lines and synthetics of Triassic to Jurassic ages lake sediments of the Newark Basin. No spectral analysis was possible on the seismic data due to presence of a weathering zone. The weathering layer distorted the seismic signal making it impossible be processed. The reflection coefficient is the combination of the density and sonic log and was used as an approximation of the seismic signal. Spectral analysis on the synthetic reflectivity coefficient found similar cycles as ones already found in sedimentary records.

10.15 OAEII

The origin of OAEII has been linked to a volcanic nutrient input (Adams et al., 2010), extensive stratification (Lanci et al., 2010), an intensification of the hydrological cycle (Trabucho Alexandre et al., 2010) or an orbital perturbation (Mitchell et al., 2008). The orbital perturbation option is especially interesting because this study has a tuned record. Mitchell et al. (2008) did propose that OAEII coincided with a 2400-kyr eccentricity minimum.

The filtering in the time domain (Figures 54 and 55) does not show a consistent correlation between OAEII and the 2400-kyr eccentricity minima. The 2400-kyr eccentricity cycle did not have a noticeable large spectral peak and was not the focus of this study. If the 2400-kyr eccentricity cycle is given more attention in future research the 2400-kyr eccentricity might well correspond a 2.4 Myr eccentricity minima for OAEII but with the current data OAEII does not correspond to a 2400-kyr eccentricity minimum. The role orbital forcing in OAEII is still a matter of debate. Figure 124 shows multiple records of OAEII on the Schill Grund high. The peak identified as the upper marl is usually referred to as the Plenus Marl Member in literature. The lower marl has a peak which is much larger/broader when compared to the peaks above the upper marl. In other sections the Plenus Marl is often subdivided into two marls with a limestone in the middle (Gale et al., 2005; Jarvis et al., 2011; Keller et al., 2001; Schlanger et al., 1987a; Voigt et al., 2007). The lower marl on the Schill Grund Platform could well be lower marl in other studies. Laurin et al. (2016) used the frequency modulating aspects of the Furlo section in the Italian Apennines to infer an orbital phase. The phase relationship indicated that the onset of OAEII is linked to a 405-kyr eccentricity maximum, the build-up of $\delta^{13}C$ is related to the transition from a 405-kyr eccentricity maximum to a 405-kyr eccentricity minimum, the $\delta^{13}C$ plateau is linked to a 405-kyr eccentricity maximum and the recovery of the $\delta^{13}C$ record is linked to a transition from a 405-kyr eccentricity maximum to a 405-kyr eccentricity minimum. If the upwelling model eccentricity maximum tuning option is used then the Ce2 405-kyr eccentricity peak of the lower marl responds to the onset of OAEII and the Ce1 405-kyr eccentricity peak of the upper marl corresponds to the eccentricity maximum within OAEII. The duration of OAEII can be interpreted as being 1.5 405-kyr eccentricity cycles which results in a duration of ~600-kyr. The 600-kyr duration is comparable to the Western Interior Basin pueblo section (520 to 560-kyr) (Locklair and Sageman, 2008; Meyers et al., 2012), the Western Interior Basin Aristocrat-Angus-12-8 core in northern Colorado (516 to 613-kyr) (Ma et al., 2014), Demerara Rise (500–550) (Meyers et al., 2012a), Tarafaya (450 to 500-kyr) (Meyers et al., 2012a), the Western Interior Basin Iona core in Texas (~540-kyr) (Eldrett et al., 2015), Umbria Marche (490-kyr) (Batenburg et al., 2016), the Wunstorf quarry in northern Germany (435 to 500-kyr) (Van Helmond et al., 2015) or (430 to 445-kyr) (Voigt et al., 2008). The exact boundaries of OAEII are imprecise. The durations which are in the range of ~400ky are most likely an interpretation as a single 405-kyr cycle. If the duration is close to ~600-kyr then the interpretation is most likely a 1.5 405-kyr eccentricity cycle interpretation. The duration of OAEII in the Vocation Basin in France is 847 to 885-kyr (Takashima et al., 2009), which is significantly longer when compared to other literature. The duration of OAEII in the Vocontian Basin is based on the slightly older age model of Sageman et al. (2006), which might explain the difference or the interpretation does represent 2 full 405-kyr eccentricity cycles.

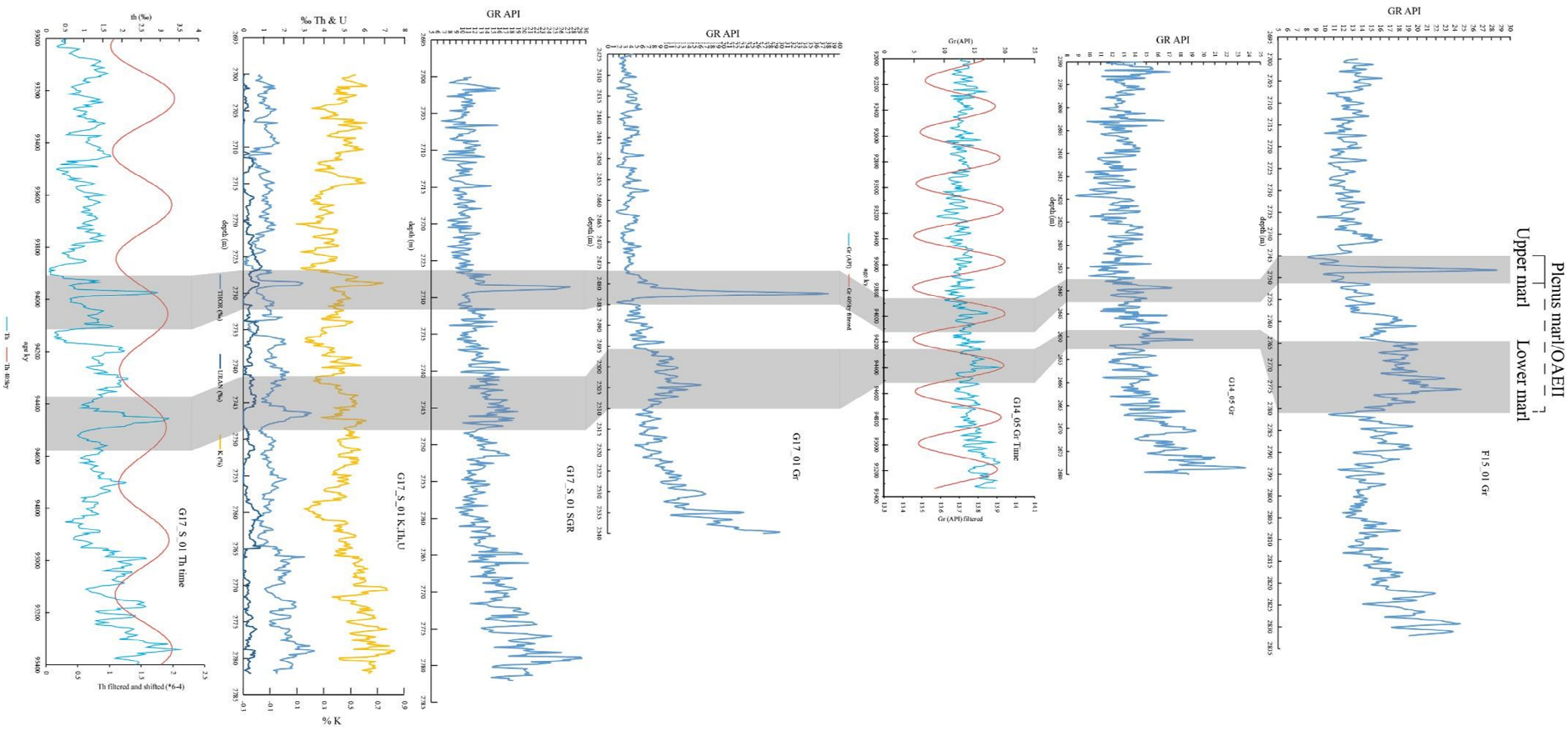

Figure 124. Lower and upper Plenus Marl beds correlation

10.16 Seismic intersections

10.16.1 Top view seismic intersection

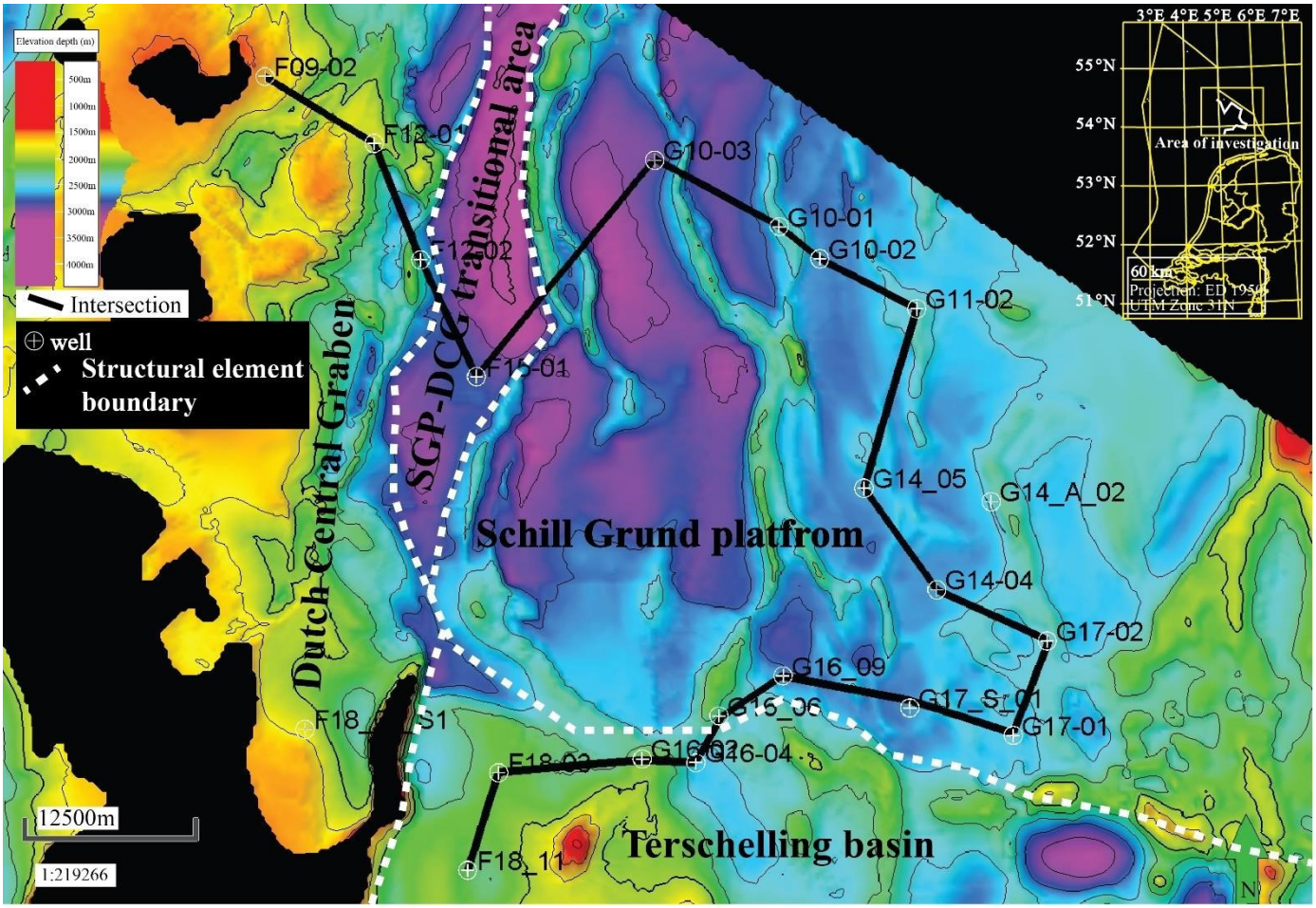

Figure 125. Top view cross-section Schill Grund Platform. The coloured surface is the depth surface of the bottom of the Chalk Group. For cross-section see figures 120 and 121 For the Cross-section Schill Grund Platform with K/Pg boundary and the cross-section Schill Grund Platform with all stage boundaries see supplementary information 10.14.2 and 10.14.3.

10.16.2 Seismic intersection with only K/Pg

For Figure 126. See file Figure-125-cross-section-schill-grund-platform-only-K-Pg.pdf

10.16.3 Seismic intersection with all stage boundaries

For Figure 127. See file Figure-126-cross-section-schill-grund-platform.pdf

10.17 Petrel seismic to well-tie, trace extraction and spectral analysis instruction manual

This manual is an instruction on how to extract a seismic trace/wiggle from seismic data with help of the seismic to well-tie function in the Schlumberger Petrel program. This trace can then be analysed, filtered and quality checked with well-log data.

10.17.1 Seismic to well tie extract using TWT method (used in this thesis)

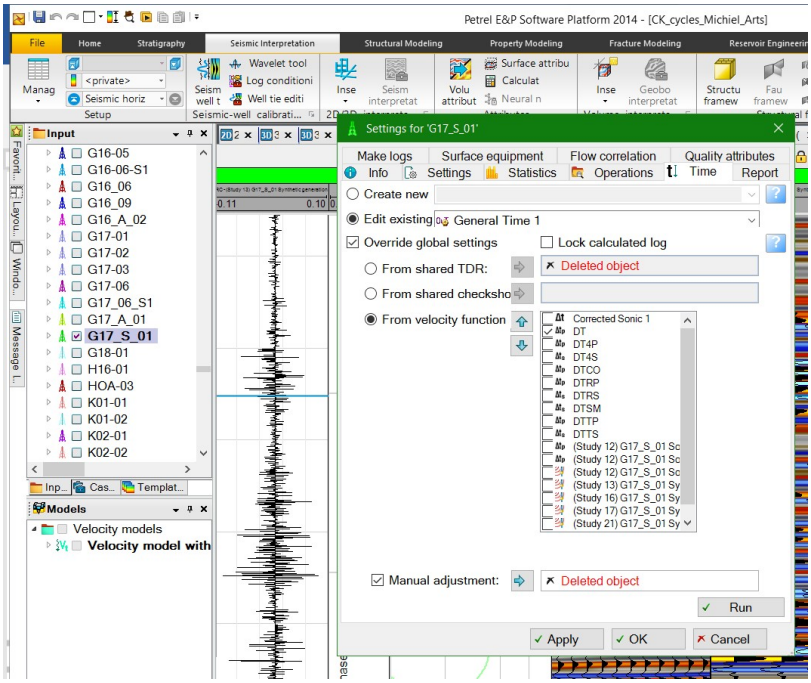

)

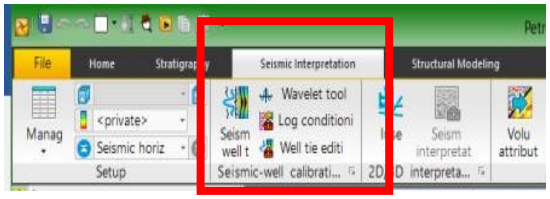

Figure 128. Give well time depth relation, either checkshots or Sonic (DT) (See setting tab)

Figure 129. Start seismic to well-tie option in Petrel

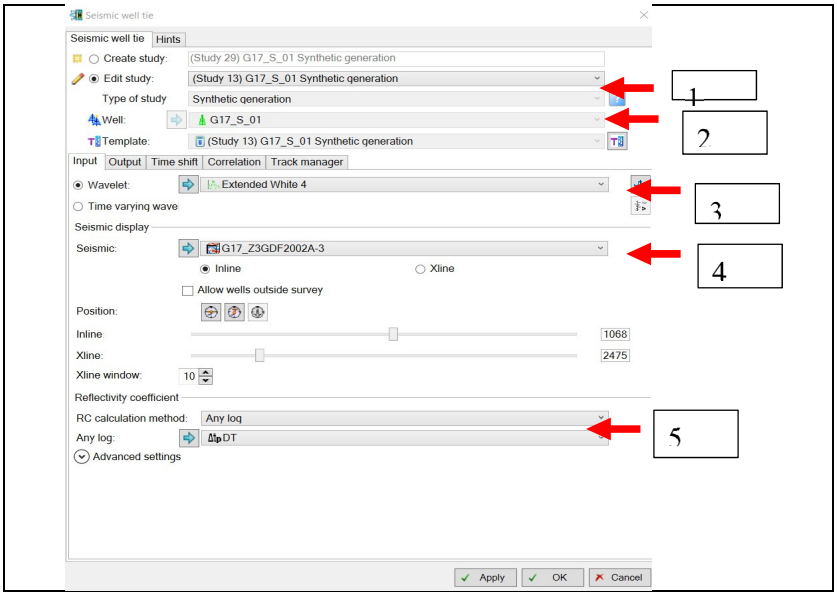

Figure 130. (1) Select synthetic generation. (2) Choose well. (3) Create or choose wavelet (usually ricker wavelet is good enough) otherwise create wavelet. (4) Select seismic crossing the well. (5) For RC calculation method select (acoustic impedance or Sonic and density option) if not possible choose Sonic (DT). One can also put in the filtered record to check fit with seismics

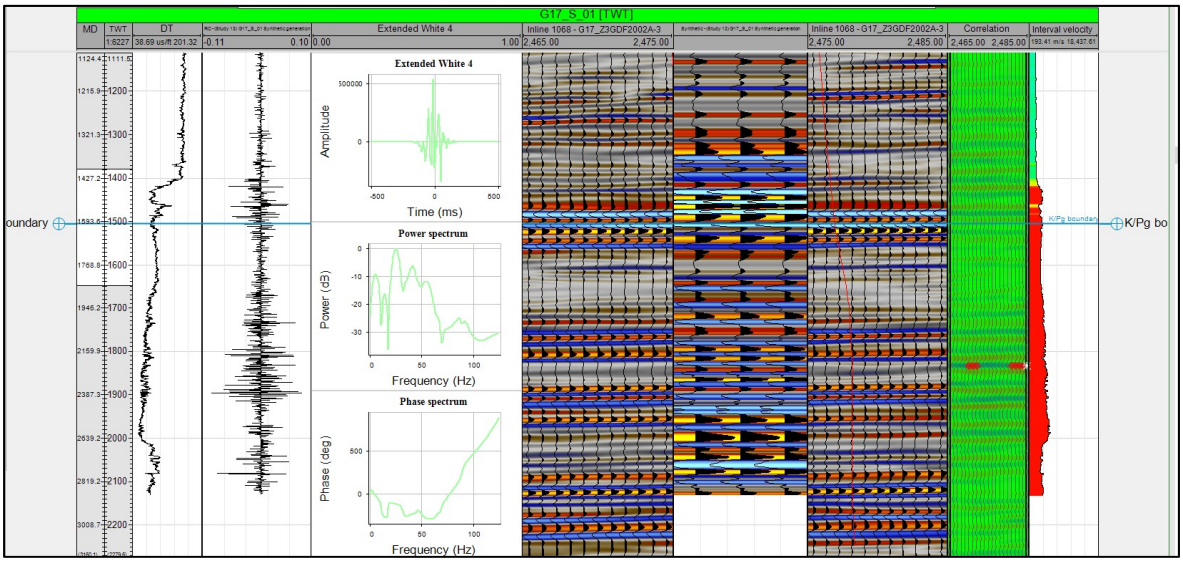

Figure 131. Check relationship between log derived synthetic log and well-logs.

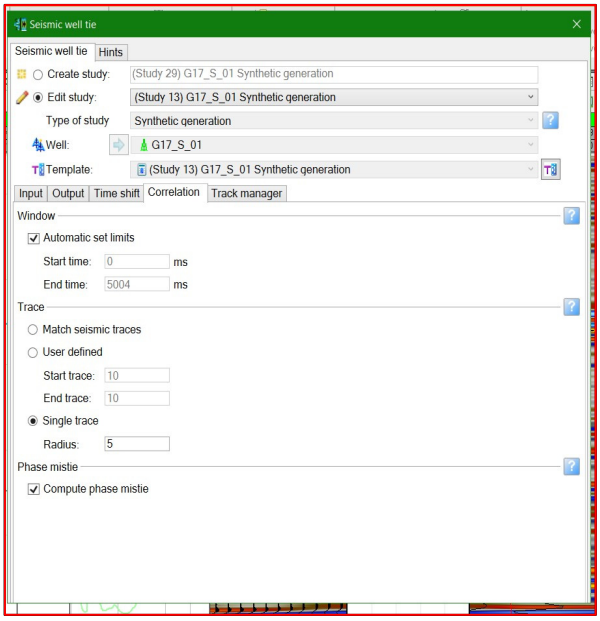

Figure 132. Go into correlation tab. Select single trace option, (choose radius anything between 1-10 is acceptable) larger radius more smoothing of seismic signal.

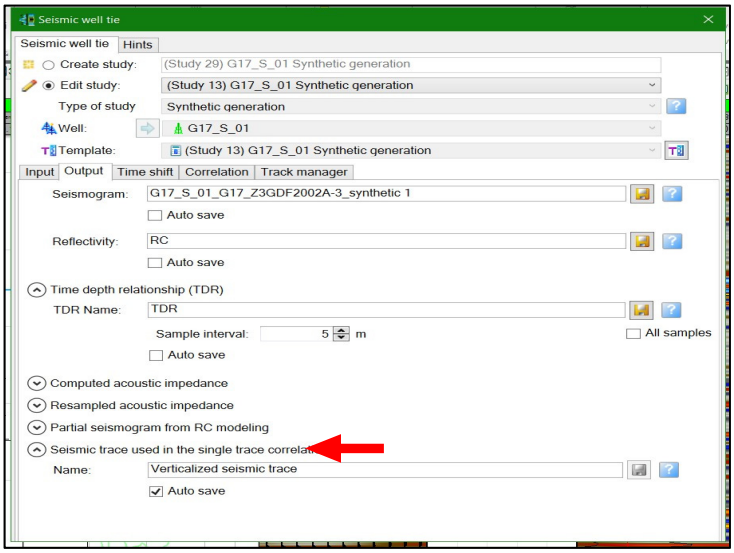

Figure 133. Select auto save option in seismic trace used in the single trace correlation option.

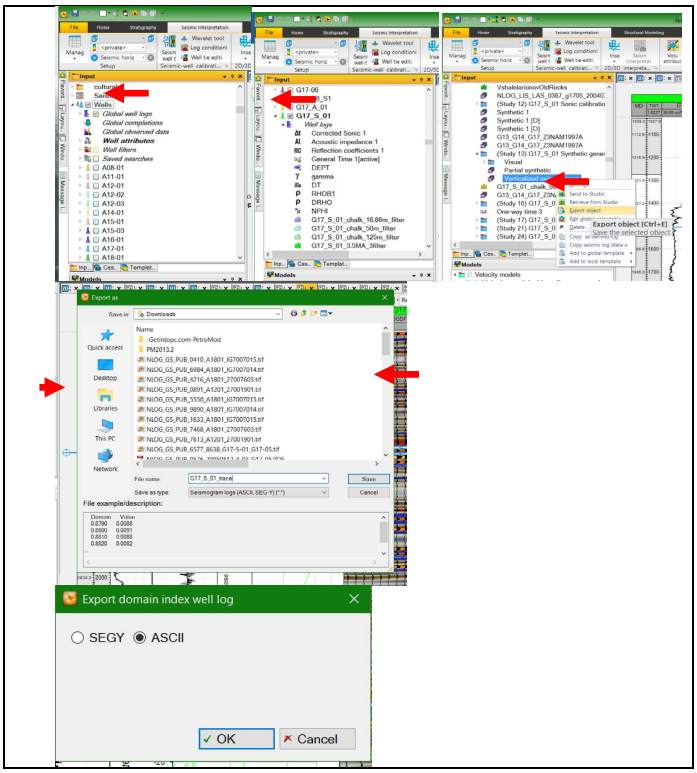

Figure 134. Export trace, important export as an ASCII file

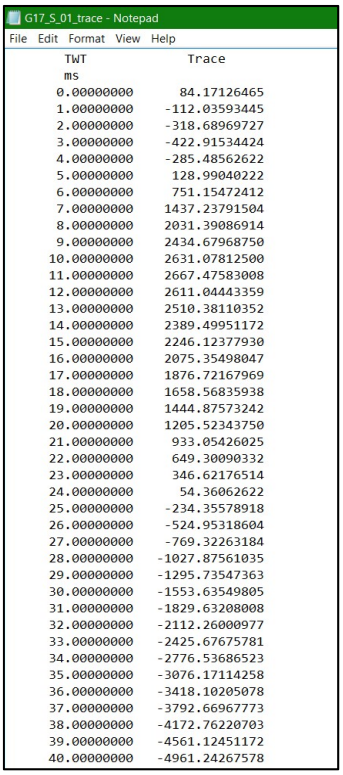

G17_S_01_trace - Notepad

File Edit Format View Help

TWT ms	Trace
0.00000000	84.17126465
1.00000000	-112.03593445
2.00000000	-318.68969727
3.00000000	-422.91534424
4.00000000	-285.48562622
5.00000000	128.99040222
6.00000000	751.15472412
7.00000000	1437.23791504
8.00000000	2031.39086914
9.00000000	2434.67968750
10.00000000	2631.07812500
11.00000000	2667.47583008
12.00000000	2611.04443359
13.00000000	2510.38110352
14.00000000	2389.49951172
15.00000000	2246.12377930
16.00000000	2075.35498047
17.00000000	1876.72167969
18.00000000	1658.56835938
19.00000000	1444.87573242
20.00000000	1205.52343750
21.00000000	933.05426025
22.00000000	649.30090332
23.00000000	346.62176514
24.00000000	54.36062622
25.00000000	-234.35578918
26.00000000	-524.95318604
27.00000000	-769.32263184
28.00000000	-1027.87561035
29.00000000	-1295.73547363
30.00000000	-1553.63549805
31.00000000	-1829.63208008
32.00000000	-2112.26000977
33.00000000	-2425.67675781
34.00000000	-2776.53686523
35.00000000	-3076.17114258
36.00000000	-3418.10205078
37.00000000	-3792.66967773
38.00000000	-4172.76220703
39.00000000	-4561.12451172
40.00000000	-4961.24267578

Figure 135. Open file in notepad and check for TWT and Trace values

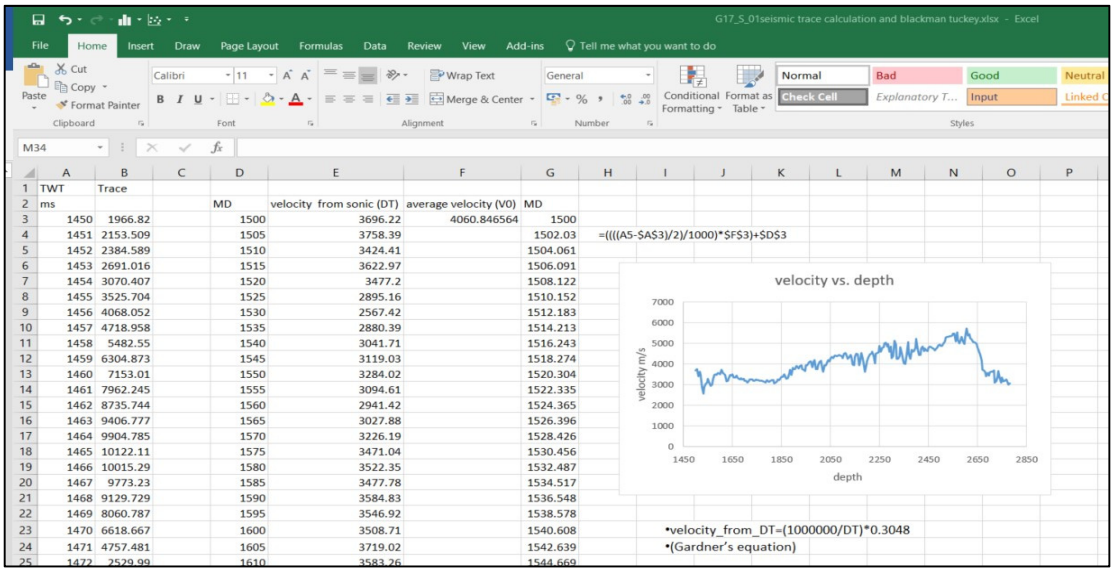

G17_S_01seismic trace calculation and blackman tuckey.xlsx - Excel

	A	B	C	D	E	F	G	H
1	TWT	Trace						
2	ms			MD	velocity from sonic (DT)	average velocity (V0)	MD	
3	1450	1966.82		1500	3696.22	4060.846564	1500	
4	1451	2153.509		1505	3758.39		1502.03	=((((A5-A3)/2)/1000)*F3)+D3
5	1452	2384.589		1510	3424.41		1504.061	
6	1453	2691.016		1515	3622.97		1506.091	
7	1454	3070.407		1520	3477.2		1508.122	
8	1455	3525.704		1525	2895.16		1510.152	
9	1456	4068.052		1530	2567.42		1512.183	
10	1457	4718.958		1535	2880.39		1514.213	
11	1458	5482.55		1540	3041.71		1516.243	
12	1459	6304.873		1545	3119.03		1518.274	
13	1460	7153.01		1550	3284.02		1520.304	
14	1461	7962.245		1555	3094.61		1522.335	
15	1462	8735.744		1560	2941.42		1524.365	
16	1463	9406.777		1565	3027.88		1526.396	
17	1464	9904.785		1570	3226.19		1528.426	
18	1465	10122.11		1575	3471.04		1530.456	
19	1466	10015.29		1580	3522.35		1532.487	
20	1467	9773.23		1585	3477.78		1534.517	
21	1468	9129.729		1590	3584.83		1536.548	
22	1469	8060.787		1595	3546.92		1538.578	
23	1470	6618.667		1600	3508.71		1540.608	
24	1471	4757.481		1605	3719.02		1542.639	
25	1472	2529.99		1610	3583.26		1544.669	

velocity vs. depth

velocity m/s

depth

•velocity_from_DT=(1000000/DT)*0.3048

•(Gardner's equation)

*Figure 136. Export trace to Microsoft excel. Choose interval of interest, in this case 1500m to 2780m. look up corresponding TWT which is in this case 1450ms to 2080ms. Re-calculate sonic record to velocity (crains petrophysical handbook **Vp=10^6 / DT** equation). Use this to calculate average velocity. Use the average velocity to recalculate from TWT to MD (sometimes a V0*k function or other functions might be more appropriate, however V0 is the quickest and usually a good approximation).*

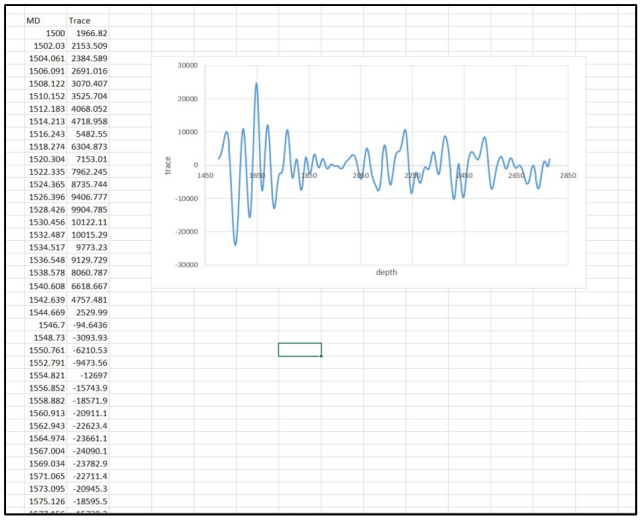

Figure 137. Trace is now converted to depth. Save MD and trace columns to notepad file. Now the Fun starts! One can export the MD and trace to any program which accepts notepad files!

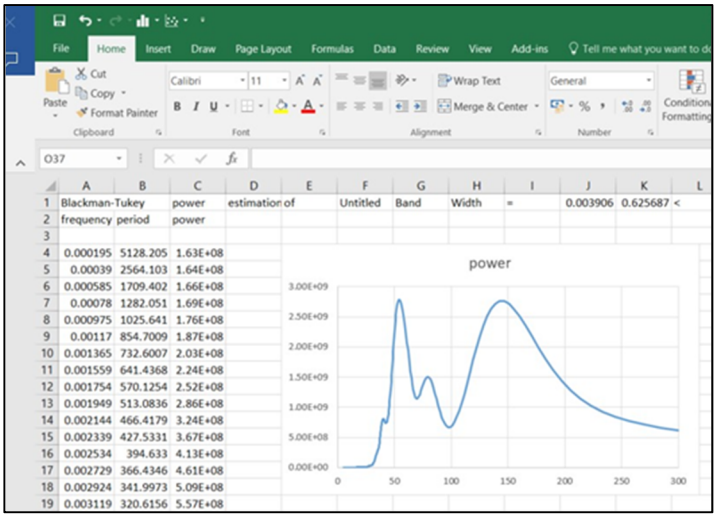

Figure 138. Simple Blackman-Tukey spectral analysis with the help of ardi-executor. 50m expected in well-logs also shown in seismic dataset.

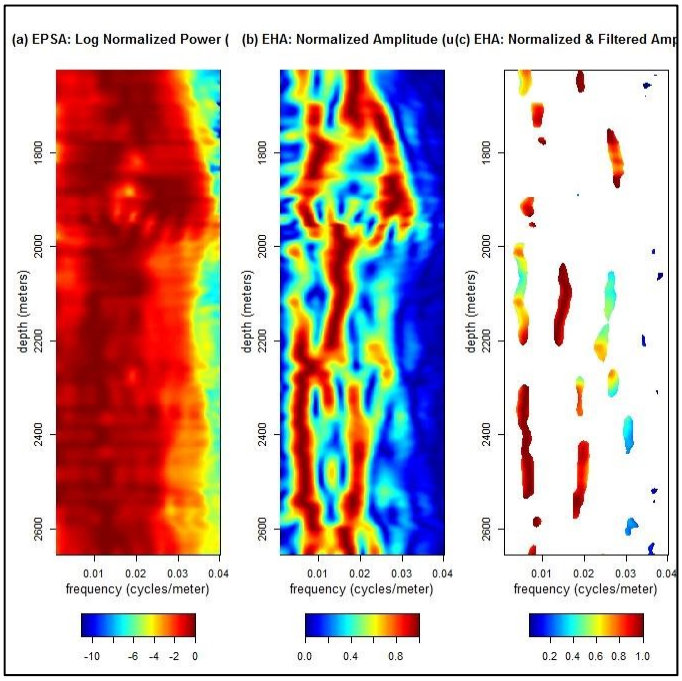

Figure 139. An EHA spectrum of the trace made with the help of Rstatistics. Note the 0.02 frequency which corresponds to the 50m period in the Blackman-Tukey spectral analysis.

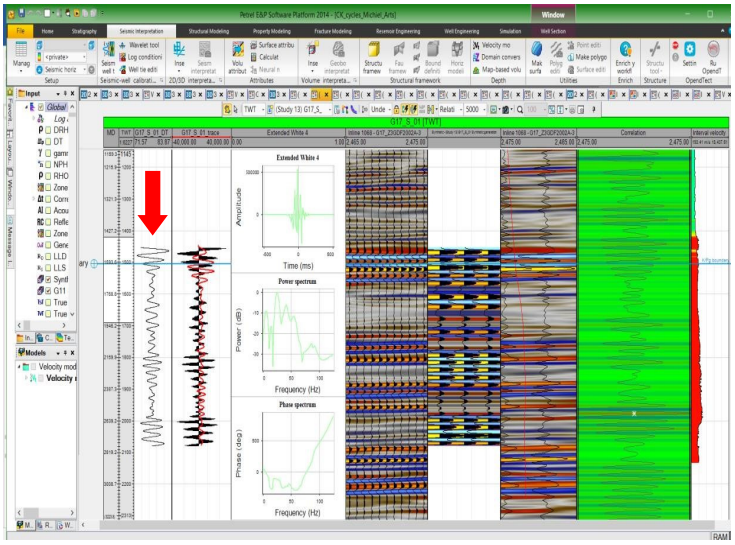

Figure 140. Synthetic seismics created from 50m filtered sonic. Good fit with real seismic signal. Look at the attractive fit between the sonic 50m filtered synthetic signal (black) and the 50m filtered seismic signal (red).

10.17.2 Trace extraction in TVD setting (not used in this thesis only used as an extra method to quality check the TWT method)

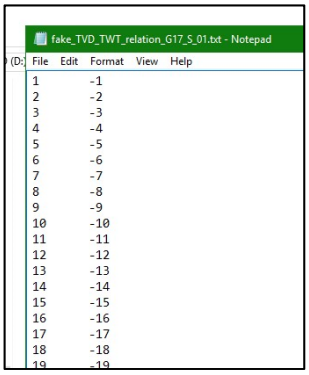

Figure 141. Make a fake MD-TWT relation which has a 1:1 ration -1 is because TWT goes down into the ground.

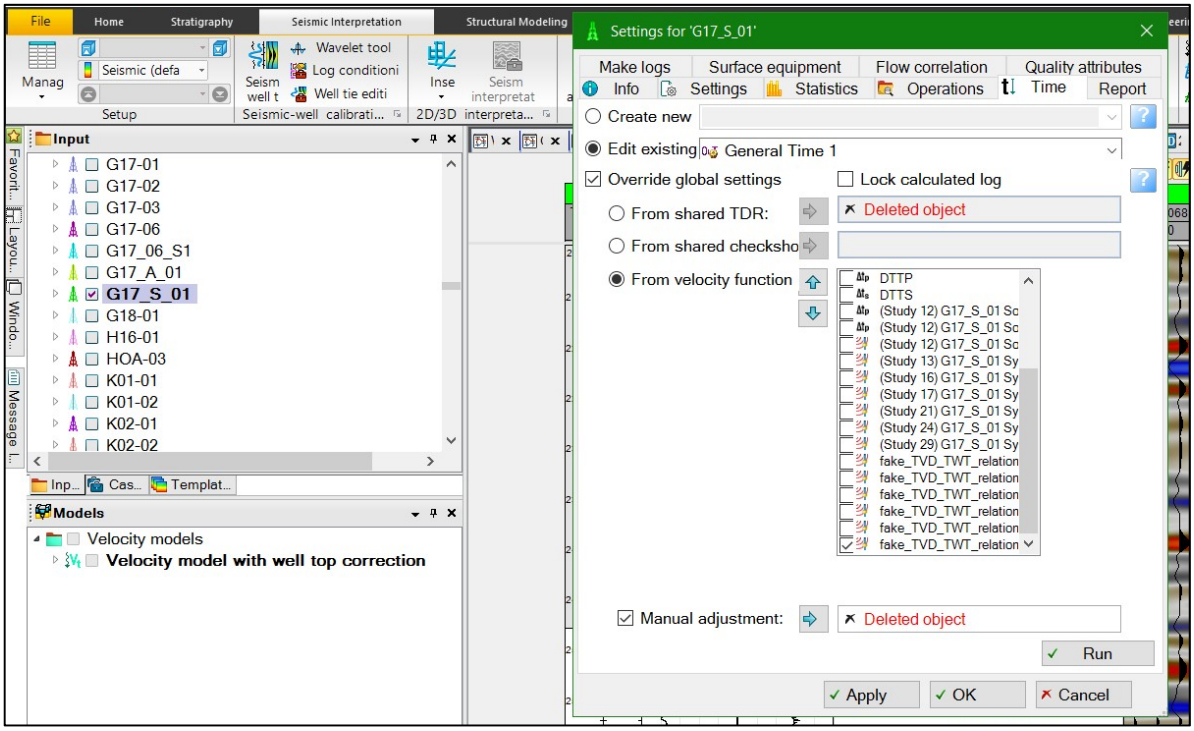

Figure 142. Set Fake TWT-TVD depth relationship for the individual wells.

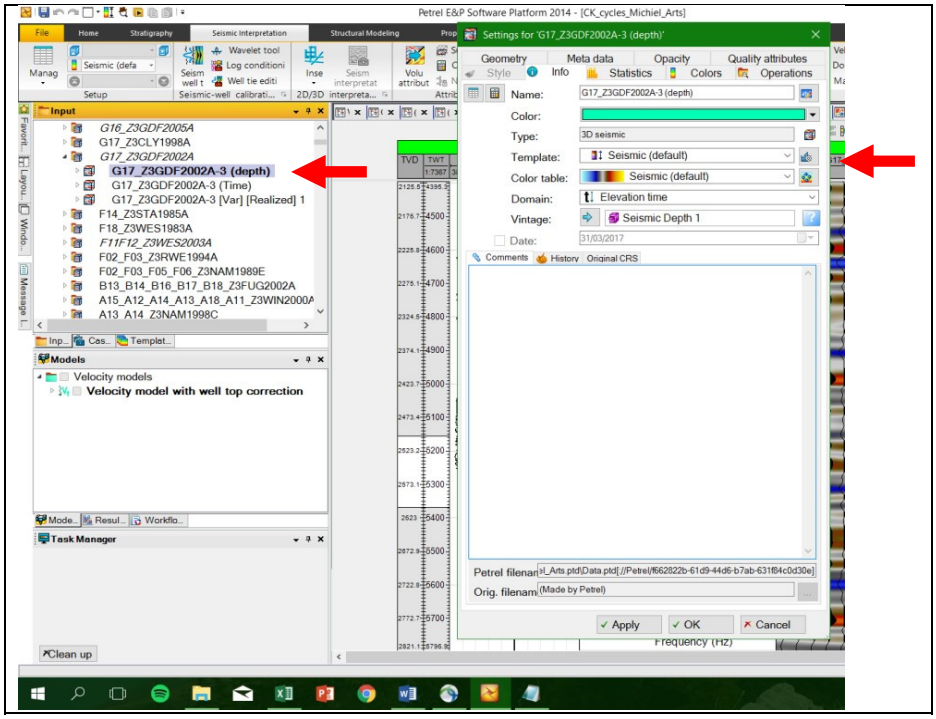

Figure 143. Set seismic cube which is in depth to elevation time. This way petrel thinks the cube is in time

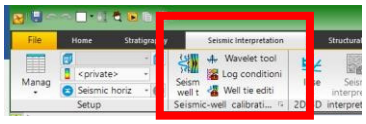

Figure 144. Start seismic to well-tie option in Petrel

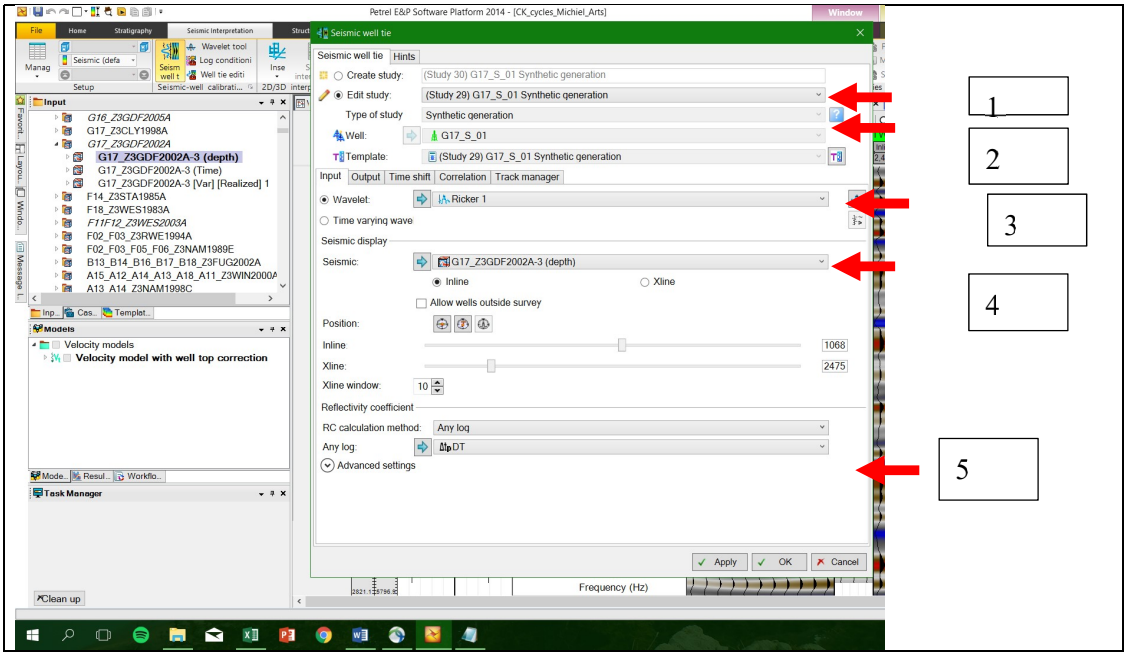

Figure 145. (1) Select synthetic generation. (2) Choose well. (3) Create or choose wavelet (usually Ricker wavelet is good enough) otherwise create wavelet. (4) Select seismic crossing the well (in this case it should be the seismic which is in depth but has been changes tot TWT). (5) For RC calculation method select (acoustic impedance or Sonic and density option) if not possible choose Sonic (DT). One can also put in the filtered record to check the fit with seismics

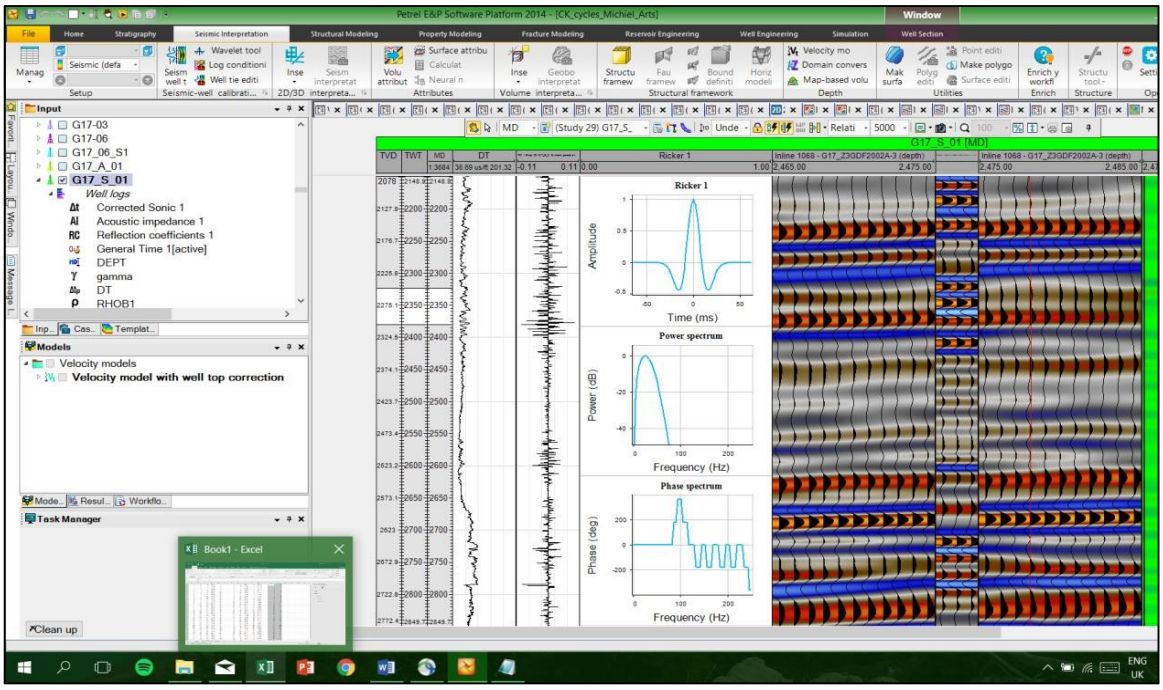

Figure 146. check correlation between the seismic data and the synthetic seismogram

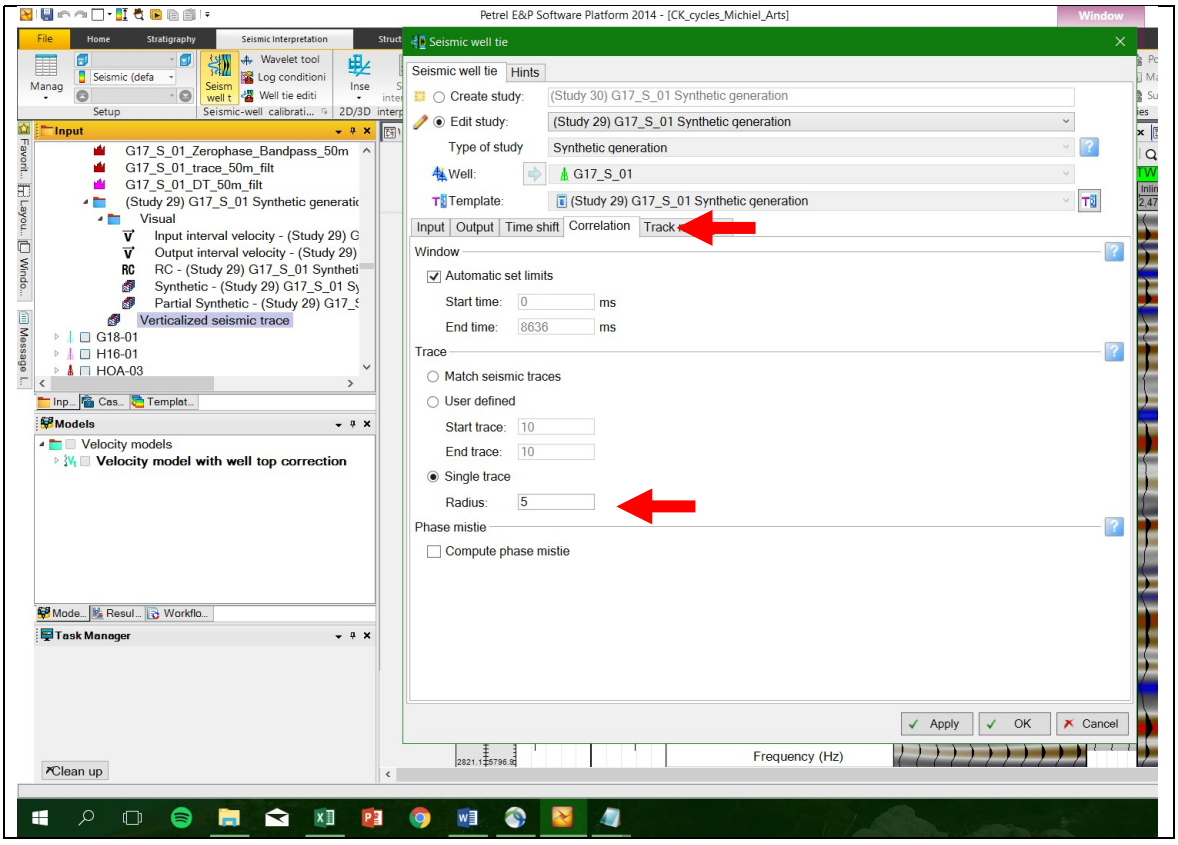

Figure 147. Go into correlation tab. Select single trace option, (choose radius anything between 1-10 is acceptable) a larger radius creates more smoothing of the seismic signal.

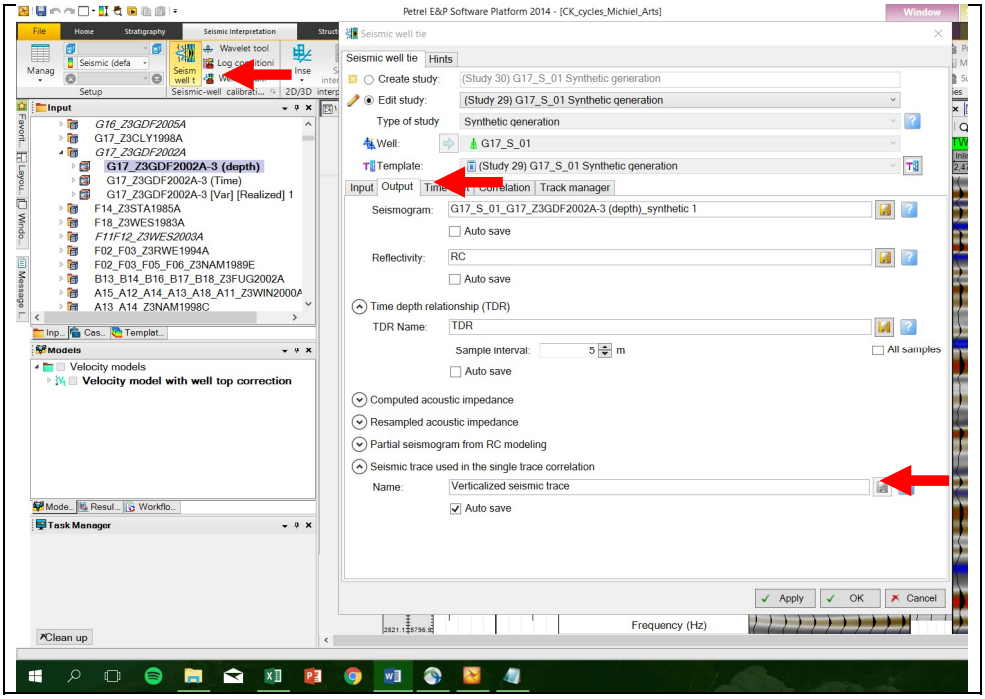

Figure 148. Set trace auto save on in output options

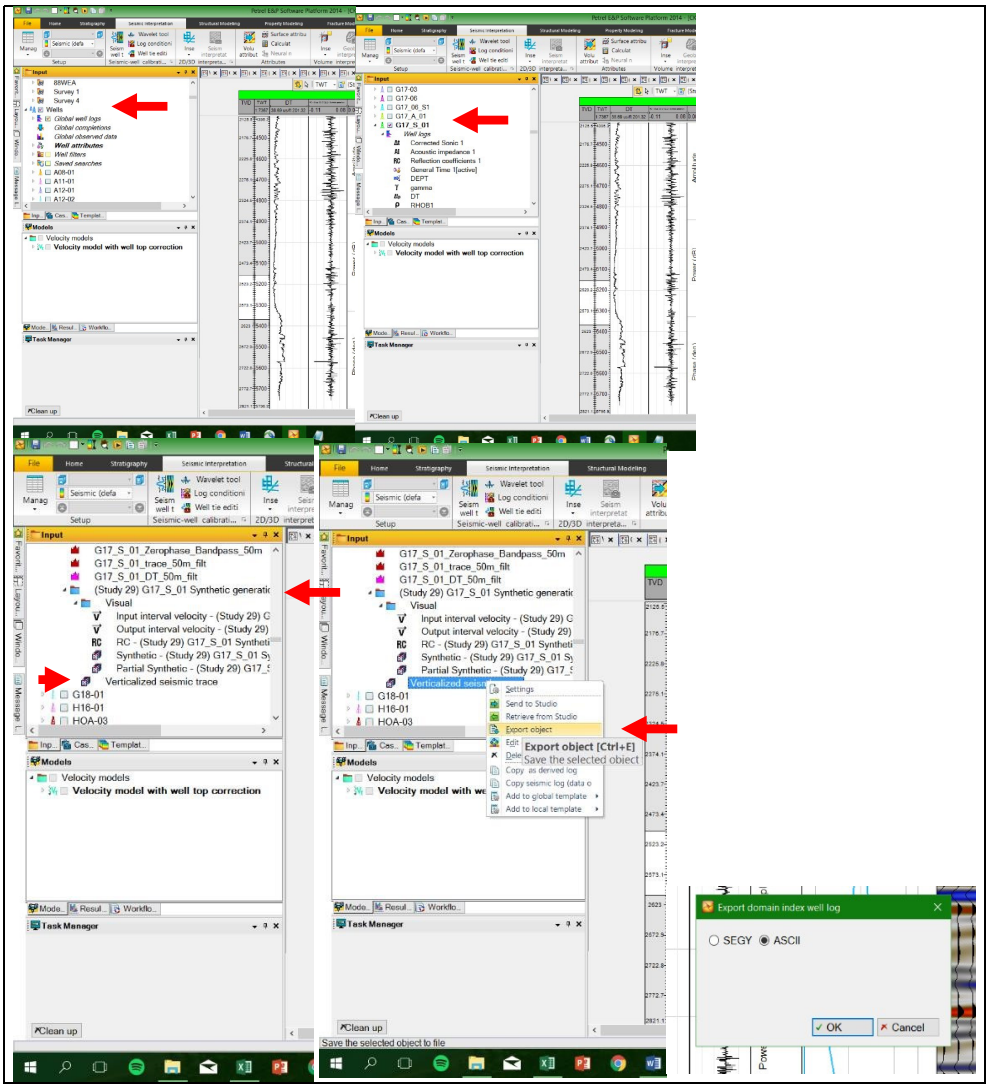

Figure 149. Export trace, important export as an ASCII file

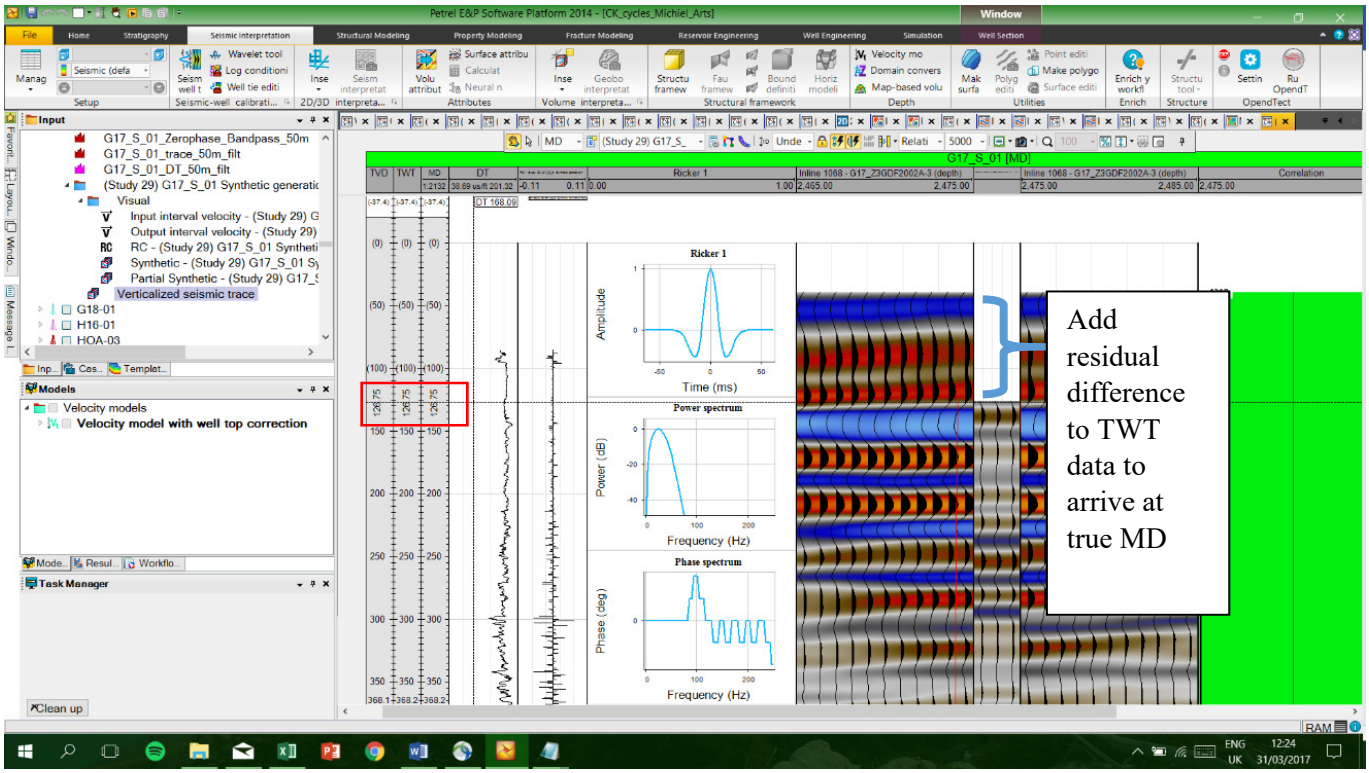

Figure 150. Add residual

TWT	Trace		
ms		MD true	trace
0	86.90369	126.19	86.90369
1	220.1234	127.19	220.1234
2	389.0385	128.19	389.0385
3	589.6149	129.19	589.6149
4	827.4053	130.19	827.4053
5	1076.87	131.19	1076.87
6	1331.741	132.19	1331.741
7	1578.006	133.19	1578.006
8	1801.247	134.19	1801.247
9	1988.137	135.19	1988.137
10	2127.761	136.19	2127.761
11	2234.104	137.19	2234.104
12	2264.359	138.19	2264.359
13	2221.496	139.19	2221.496
14	2099.1	140.19	2099.1
15	1896.166	141.19	1896.166
16	1619.16	142.19	1619.16
17	1282.78	143.19	1282.78
18	943.7305	144.19	943.7305

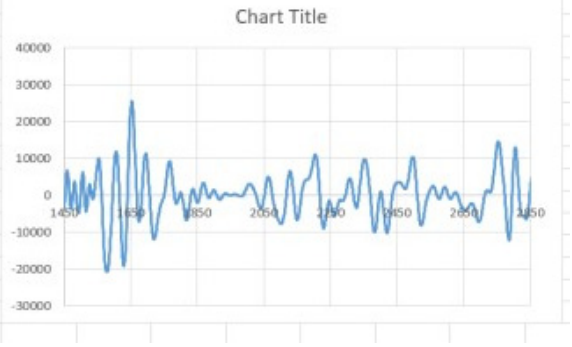

Figure 151. True md with seismic trace

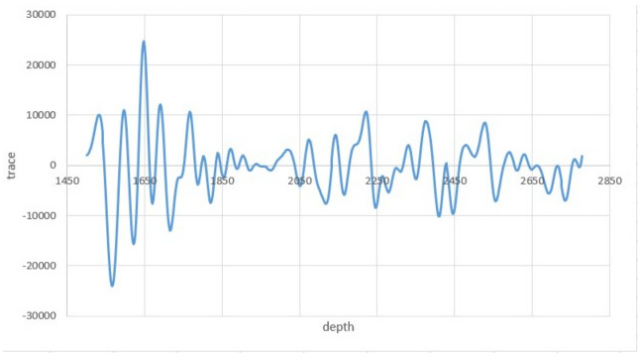

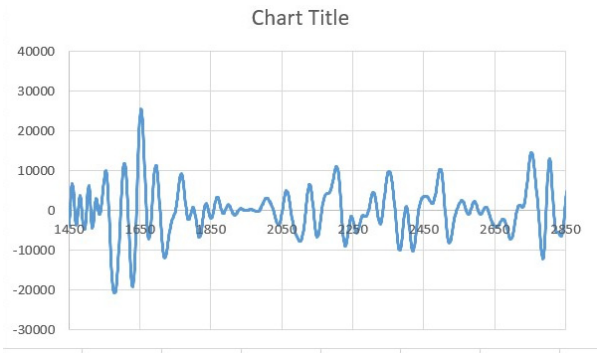

Figure 152. left: resulting wiggle from the TWT way to arrive at seismic trace. right: resulting wiggle from the TVD way to arrive at seismic trace

10.18 Well and seismic itinerary

10.18.1 Well locations

For all locations of the wells which were used see well locations Figure 153 in file Figure_153_well_locations.pdf.

10.18.2 Well data and applied techniques

well	biostrat.	petrophysical measurements present in Chalk Group							XRF	seismic to well tie	trace	Analytical techniques used						bandpass filtered logs				Used in long distance correlation Across Schill Grund Platform
		GR	DT	spectral gamma ray	porosity	density	calliper	SP			extracted	Blackman Tukey in depth domain	Redfit depth domain	Redfit time domain	EHA depth domain	Hilbert transformation in time domain	EHA time domain	eASM	depth domain	time domain	seismic domain	
A12-01	y	y	y																			
A12-02	y	y	y		y	y			y	y		GR	GR		GR				Gr			
A18-01	y	y	y			y																
B14-01	y	y	y		y	y				y												
B17-02	y	y	y																			
F02-03	y		y			y																
F09-02	y	y	y		y	y	y	y														y
F12-01	y	y	y			y																y
F12-02			y																			y
F15-01	y	y	y							y		DT, GR	DT, GR		DT, GR			DT, GR				y
F18-03	y	y	y																			y
F18-11		y	y			y																y
G10-01		y	y		y	y						DT, GR	DT, GR		DT, GR			DT, GR				y
G10-02		y	y			y				y	From survey F12_G10_Z3PET1991A	DT, GR, trace	DT, GR, trace		DT, GR, trace			DT, GR, trace	GR, trace		DT, GR, trace	y
G10-03		y	y	y								Gr	GR		GR							y
G11-1	y																					
G11-02		y	y		y	y						DT, GR	DT, GR		DT, GR			DT, GR				y
G14-A-02		y	y	y								spectral gamma ray	spectral gamma ray		GR spectral gamma ray							
G14-04		y	y							y	From survey G13_G14_G17_Z3NAM1997A							trace				y
G14-05		y								y	From survey G13_G14_G17_Z3NAM1997A	GR, trace	GR, trace	GR	GR, trace	GR	Gr, incl. GR Hilbert	GR, trace	GR, trace	GR	GR, trace	y
G16-02	y	y	y		y	y																y
G16-04		y	y																			y
G16-06		y	y																			y
G16-09		y	y																			y
G17-S-01		y	y	y						y	From survey G17_Z3GDF2002A and VSP NLOG_LIS_LAS_5023_g1705_20040714-4-01_G17-5-VSP_corzerophase	GR, DT, spectral gamma ray, trace/trace VSP	GR, DT, spectral gamma ray, trace/trace VSP	Th	GR, DT, spectral gamma ray, trace/trace VSP	Th	Th, incl. Th Hilbert	GR, DT, spectral gamma ray, trace	Th	Th	GR, DT, Th, trace/trace VSP	y
G17-01	y	y	y							y		GR	GR									y
G17-02		y	y																			y
M01-01	y	y	y		y	y																
M07-01	y	y	y																			

Table 9. Itinerary with all the wells which were used for in this thesis. Also indicated is for what the well data was used for and which processing techniques was used on the well data.

10.18.3 Seismic data

For all the used seismic date which was used see figure 154 in file Figure_154 _seismic_data.pdf.